THESIS

PETROLOGY AND GEOCHEMISTRY OF ALTERATION TYPES WITHIN A MULTIPHASE SYSTEM AND IMPLICATIONS FOR THE PRESENCE OF A PORPHYRY ROOT, HARRISON PASS PLUTON, NEVADA

Submitted by

Alexandra Racosky

Department of Geoscience

In partial fulfillment of the requirements

For the Degree of Master of Science

Colorado State University

Fort Collins, Colorado

Fall 2017

Master's Committee:

Advisor: John Ridley

Sally Sutton
Christopher Bareither

ABSTRACT

PETROLOGY AND GEOCHEMISTRY OF ALTERATION TYPES WITHIN A MULTIPHASE SYSTEM AND IMPLICATIONS FOR THE PRESENCE OF A PORPHYRY ROOT, HARRISON PASS PLUTON, NEVADA

The Eocene (~36 Ma), calc-alkaline, granodiorite-monzogranite multiphase Harrison Pass Pluton (HPP) intrudes a sequence of meta-clastic rocks and meta-carbonates within the southern portion of the Cordilleran metamorphic core complex of the Ruby Mountains East Humboldt Range (RMEHR), northeastern Nevada. Due to the unique (~5km) vertical exposure through the top of the pluton, numerous studies focused on the petrology, geochemistry, structural geology, temperature constraints, and hydrothermal fluids have been done on the HPP. To understand the effects multiphase plutonic systems have on the petrology and geochemistry of alteration, and on the fluids responsible for alteration, a petrological and geochemical analysis of the various alteration types: potassic, chlorite sericite (CS), silicification, endo-skarn, and exo-skarn (recognized using field and petrographic observation), was conducted. Additionally, due to previously discovered alteration geometries, the HPP was also assessed for porphyry root characteristics (the part of the pluton beneath a porphyry ore body). Increased knowledge of porphyry root zones can enhance exploration techniques, and lead to undiscovered ore bodies.

Petrological analysis using Harker diagrams, shows most samples are geochemically typical of evolving calc-alkaline magmas, however numerous samples also plot off evolution trends. Additional analyses using REE spider diagrams revealed a more complex

distribution of phases than previously recognized. Results indicate lenses of the early Toyn Creek granodiorite within the late two mica monzogranite unit are more abundant and spread to structurally lower levels than previously indicated, and the two mica monzogranite lenses spread to higher levels into the Toyn Creek granodiorite and Corral Creek monzogranite units. Even though the petrologic phases are clearly mapped (Barnes et al., 2001), the intermixed distribution of the Toyn Creek granodiorite and two mica monzogranite lenses throughout the HPP render field identification of the petrologic phases difficult.

REE and trace metal geochemical data was analyzed to determine mass balance of alteration. Well-defined patterns within data differentiated by alteration type, clearly show alteration signatures vary slightly between each unit. The variations are minor, but within a large data set could produce a wide data spread—therefore to further confine data spread when studying multiphase systems, data should also be differentiated by intrusion unit. Additionally, geochemical patterns are not affected in samples collected within a few meters of intrusion contacts, however more data is needed to further investigate and clearly understand the extent of interaction. Due to the intricacies within the multiphase HPP, alteration types cannot be identified based off only one to three trace elements.

Fluid inclusion analyses of samples from each intrusive unit showed pressure corrected temperatures of the hydrothermal fluids responsible for alteration ranged 400-500 °C for potassically altered samples, 330 to 450 °C for CS samples, 330 to 500 °C for the endoskarn samples, and 320 to 400 °C for the silicified samples. Temperatures were highest in the middle of the pluton and decreased outwards, corresponding to alteration

geometries throughout the system: potassic in the center, and CS along the flanks. Salinity of the hydrothermal fluids responsible for alteration were relatively low, ranging 0 to 7 wt. % NaCl and averaging 2.43 wt. %. Using median temperature values, isotope values of the hydrothermal fluids range from $\delta^{18}O_{water}$= -12.8 to 14 ‰, and δD_{water} data ranges -31 to -169‰. The mixing curve on the δD vs. $\delta^{18}O$ graph, along with hydrogen isotope ratios increasing towards the center of the intrusion, indicate pluton scale fluid pathways: depleted δD meteoric waters circulate along the flanks of the system and rose through the middle of the pluton, interacting with magmatic waters and rocks higher in δD.

Rare earth element, trace element, and isotope data emphasize local fluid pathways (3-20 m), associated with the many skarn/limestone enclaves/xenoliths scattered within the HPP. Concentrations of trace elements (Y, Zr, and small amounts of TiO_2, P_2O_5), REEs, and δD and $\delta^{18}O$ ratios in samples collected near limestone/ skarn xenoliths, indicate geochemical transport towards or away from xenolith contacts. Within the HPP, skarn/limestone pods may be eroded away, or not revealed at the surface, therefore depending on the distribution of the skarn/ limestone xenoliths, these alteration patterns can repeat and overprint one another and may be misinterpreted, or overlooked. Addressing how hydrothermal alteration and interaction between fluids and the limestone/skarn pods could affect geochemical results, is especially important when attempting to identify and define multiple petrologic phases within a multiphase system, and in regions where limestone wall rocks are present.

An assessment for porphyry root features within the HPP revealed numerous areas containing features indicative of root zones, such as large quartz±feldspar±muscovite

aplitic dikes and veins, potassic, CS, phyllic and endoskarn alteration. If an ore body formed above the HPP, the deposit could either be located to the west of the HPP (slid westward by the Ruby Mountain detachment fault), or displaced east under the adjacent Ruby Valley basin. However, additional field work within the HPP is necessary as the identified features are not enough to classify the HPP as a porphyry root system. Results show the importance of studying porphyry root systems, as undiscovered deposits may be close by.

ACKNOWLEDGEMENTS

This project was funded by the Rocky Mountain Association of Geologists.

I would like to thank my advisor Dr. John Ridley for his support, guidance, and instruction during this project. I would also like to thank my two field assistants Jake McCane and Mark Smith, for their help, encouragement, and input during field work. Additionally, I would like to thank my committee members Sally Sutton and Christopher Bareither for their input.

Most importantly I would like to thank my Family and Friends for their constant support.

DEDICATION

Dedicated in memory of Holly St. Clair: a smart, beautiful young woman. Thank you for your friendship, love, and support during our undergraduate studies.

TABLE OF CONTENTS

ABSTRACT ii

ACKNOWLEDGEMENTS vi

DEDICATION vii

1. INTRODUCTION 1

1.1 THESIS GOALS 3

2. REGIONAL GEOLOGY 4

2.1 THE GREAT BASIN 4

2.2 RUBY MOUNTAINS 5

2.3 GEOLOGY OF THE HARRISON PASS PLUTON 8

2.3.1 Harrison Pass Pluton 8

2.3.2 Magmatic petrology of the HPP 8

2.3.3 Alterations 15

2.3.4 Fluid activity and mineralization around and near the HPP 15

2.4 PORPHYRY ROOT CHARACTERISTICS 17

3. METHODS 21

3.1 FIELD WORK 21

3.2 PETROGRAPHY 22

3.3 WHOLE ROCK GEOCHEMISTRY 22

3.4 FLUID INCLUSION ANALYSIS 24

3.5 OXYGEN AND HYDROGEN ISOTOPES 25

4. DATA AND RESULTS 29

4.1 FIELD DATA 29

4.1.1 Transect overviews 29

4.1.2 Additional localities 34

4.2 ALTERATION TYPES 35

4.2.1 Summary of petrographic observation 39

4.3 PETROLOGY AND GEOCHEMISTRY OF THE HPP 41

4.3.1 Harker diagrams 41
4.3.2 Multi-element spider diagrams 43
4.3.3 REE diagrams 46
4.3.4 Trace metals 49
4.4 WHOLE ROCK GEOCHEMISTRY OF THE ALTERATION TYPES IN THE HPP 50
4.4.1 Pearce element ratio plots 50
4.4.2 Geochemistry results for mass-balance of alteration 52
4.5 FLUID INCLUSIONS AND TEMPERATURE CONSTRAINTS 78
4.6 STABLE ISOTOPES 81
5. DISCUSSION 87
5.1 PETROLOGY AND GEOCHEMISTRY OF THE HPP 87
5.2 GEOCHEMISTRY OF THE ALTERATION TYPES 92
5.3 FLUID FLOW-- ISOTOPE GEOCHEMISTRY OF THE HYDROTHERMAL FLUIDS 100
5.4 ROLE OF CARBONATE ASSIMILATION AND SKARN ALTERATION 106
5.5 IMPLICATIONS OF A PORPHYRY ROOT 118
6. SUMMARY AND CONCLUSION 120
REFERENCES 126
APPENDIX 1 131
SAMPLE I.D., TEST TYPE, AND LOCATIONS 131
TRANSECT DESCRIPTIONS 132
PETROGRAPHIC DESCRIPTIONS 136
PETROGRAPHIC IMAGES 143
APPENDIX 2 150
WHOLE ROCK GEOCHEMICAL RESULTS 150
UNALTERED DATA USED FOR MASS BALANCE CALCULATIONS 153
MASS BALANCE RESULTS 156
APPENDIX 3 186
MICROTHERMOMETRIC DATA 186
$\delta D_{mineral}$ *and* $\delta^{18}O_{mineral}$ RESULTS 190
CALCULATED δD_{water} *and* $\delta^{18}O_{water}$ RESULTS 191

1 INTRODUCTION

The Harrison Pass Pluton (HPP), a multiphase granitic pluton in the Central Ruby Mountains, Nevada, is the only known exposed intrusion coeval and similar in size and shape to the intrusions geophysically imaged beneath the Carlin-type (gold only) ore deposits in Nevada (Musekamp, 2011). Due to the tilting of the HPP (30° to 50° E), a ≈5 km vertical section through the top of the pluton is exposed (Barnes et al., 2001; Burton, 1997; Colgan et al., 2010). The unique exposure has led to studies of the fluids that migrated around and within the HPP, to help further understand the unexposed 'root zone' hydrothermal systems underlying the Carlin gold deposits. Other studies on the HPP have focused on the petrology and geochemistry within the HPP (Barnes et al., 2001), constraining temperature variations within the HPP magmas (Deans, 2010), and structural studies encompassing the extension and unroofing of the Ruby Mountains (Colgan et al., 2010).

However, studies have not been conducted on the chemistry and geometry of hydrothermal alteration zones within the HPP. Furthermore, studies on the relationship between multiphase intrusions and alteration are scarce, leaving the relationship unknown. This study aims to enhance what little is known about the effects multiphase plutonic systems have on the patterns and geochemistry of altered rocks and the fluids responsible for the varying alteration types. Whole rock geochemistry of the various alteration types will be used to measure major and minor trace elements and the geochemical mass balance of alteration.

Stable isotope ratios of oxygen and hydrogen have been used in the past to explore and vector into areas of increased hydrothermal mineralization (Nesbitt, 1996). However, with respect to multiphase intrusions, how isotope ratios vary throughout each zone of alteration and to what extent the various fluids effect fluctuating ratios, has not been extensively studied. Identifying fluid sources of each altered zone will demonstrate how multi-phase injections affect isotope ratios throughout the pluton.

Alteration geometries are typically associated with evolutionary paths of fluids, which produce varying zones of alteration that can be linked to certain water chemistries (Seedorff et al., 2008). Although the types of alterations found within the HPP resemble types found around porphyry deposits, the distribution of alteration zones determined in reconnaissance studies (Musekamp, 2011; Gates, 2016) does not fit alteration geometries typically displayed in and around porphyry systems. The unusual alteration geometries may be a result of the multiphase pluton, but may alternatively be a result of exposure of the region below the roots of a magmatic-hydrothermal system. Seedorff et al. (2008) characterized alteration facies found within porphyry root systems: the part of the pluton beneath a porphyry orebody, comprised of quartz veins, porphyritic dikes, and wide spread alterations including greisen, potassic, sodic, and calcic types. Based off field data collected by Barnes et al. (2001), Musekamp (2011), and Gates (2016), the geometries in the HPP could be a result of exposure of the roots of a magmatic-hydrothermal system.

Fluids responsible for porphyry ores originate in an intrusion below the ore body, however few studies have focused on porphyry roots as these features are rarely identified at the surface. Insight on the chemistry and fluids of the potential root zones can result in

enhanced exploration techniques, evaluation of new porphyry prospects, and improve upon the knowledge of the distribution and pathways of fluid flow around the HPP intrusion.

1.1 Thesis Goals

By analyzing the geochemistry and stable isotope ratios of samples from altered rocks, as well as mapping alteration geometries and porphyry root characteristics within the HPP, this project aims to

1.) Discern if the geochemistry of the alteration types were affected by the multiphase system of the HPP:
    a. By evaluating petrological data
    b. And by comparing data of like alteration types from the three major intrusion types
2.) Discern the source of, and if the isotope geochemistry of the waters responsible for alteration, were affected by the multiphase system of the HPP:
    a. By evaluating isotope data of varying alteration types from the seven separate transects
    b. And by evaluating isotope data of like alteration types from the three major intrusion types
3.) Determine the possibility of the HPP as a porphyry root system by mapping
    a. Alteration geometries
    b. Porphyry root characteristics described by Seedorff et al. (2008)

2. REGIONAL GEOLOGY

2.1 The Great Basin

The Great Basin (GB) spans ~2500 km, from the Pacific northwest to central Mexico, and constitutes the widest segment of the Basin and Range taphrogen, the bulk of which lies in the state of Nevada, and comprises of a vast area (600 km by 600 km) of rugged topography (Dickinson, 2006). Field work of the Harrison Pass pluton (HPP) took place in the Ruby Mountains East Humboldt Range (RMEHR), situated in the eastern Great Basin in northeastern Nevada.

Evolution of the GB started along the western edge of Precambrian Laurentia, and is best summarized by Dickinson (2006). The beginning of the tectonic evolutionary sequence started with the formation of the Archean Wyoming and Paleoproterozoic Mojave provinces. During continental rifting in the Mesoproterozoic (Belt age), Precambrian basement was incorporated into the Rodinian supercontinent. During late Neoproterozoic times, delineation of the Cordilleran miogeocline was accompanied by the onset of passive margin sedimentation that lasted through the late Devonian. Oceanic sediments were then deformed during the Antler orogeny (Devonian-early Mississippian), forming the Roberts Mountain thrust (Dickinson, 2006).

Post Antler Orogeny (late Mississippian- Permian), was a time in which marine and non-marine sediments deposited to the west, on top of, and to the east of the Antler Orogen. Following sediment deposition, the Sonoma Orogeny in the late Permian thrusted the oceanic sediments, and formed the Golconda allochthon over the Antler Orogen. This was followed by a period in the mid-Triassic, which encompassed the development of the

nascent Cordilleran magmatic arc. During the late Triassic, the Elko orogeny, characterized by Thorman et al. (1990) as southeast-vergent imbrication and crustal thickening of the northeastern Great Basin, caused several deformational events. Sedimentary rocks of the Neoproterozoic- Mesozoic, buried in the back arc of a fold thrust belt during the Sevier Orogeny, were subjected to polyphase metamorphism, several phases of brittle faulting, large-scale open folding**,** and uplift (Colgan, et al., 2010). Retro-arc thrust belt development along with episodes of back arc magmatism, well inland from the continental margin, occurred during mid-late Jurassic (Dickinson, 2006).

Migration of Laramide magmatism from the Sierra Nevada to the Rocky Mountain interior during Cretaceous-Paleogene times, was immediately followed by post-orogenic extensional collapse of the overthickened crustal highland. This resulted in exhumation of the RMEHR, achieved by brittle-ductile detachment faulting. Re-migration of magmatism across the GB from the interior to the continental margin in the late Eocene, resulted in the intrusion of the HPP into the RMEHR. Intra arc to back arc extensional deformation occurred during the Oligocene-Miocene, and caused tectonic denudation of basement rocks in some Cordilleran core complexes. Basin and range transtension and dispersed magmatism followed into the Neogene (Dickinson, 2006).

2.2 Ruby Mountains

The Ruby Mountains East Humbolt Range (RMEHR), situated within the eastern Great Basin in Northeastern Nevada, is a classic example of a Cordilleran metamorphic core complex. The RMEHR is bounded by recently active NNE striking, normal block faults (Burton, 1997). Tilting of the mountain range has exposed the polydeformed rocks, revealing four major elements of the complex: Tertiary sedimentary and volcanic rocks and

Neoproterozoic-Early Triassic miogeoclinal sedimentary rocks, a low angle normal fault system, with a ~1km thick extensional mylonitic shear zone (Ruby detachment fault), and a migmatic metamorphic and igneous infrastructure (MacCready et al., 1997; Wright and Snoke, 1993). Valleys adjacent to the complex are filled with Eocene-Miocene sedimentary and volcanic rocks, as well as overlying Quaternary deposits (Burton. 1997).

The Ruby Mountains experienced three deformational events, and two amphibolite-facies metamorphic events in the Late Jurassic (153 ± 1 Ma), all of which occurred simultaneously with emplacement of the Late Jurassic two-mica granites located in the Northern RMEHR. Uplift of the RMEHR in the Tertiary caused little to no deformation, preserving the Mesozoic fabrics (Hudec, 1992). The RMEHR can be split into three zones of metamorphism: infrastructure (=core complex), central transition, and suprastructure (=un-metamorphosed rocks). The northernmost section of the Ruby Mountains contains greenschist to upper amphibolite facies, polydeformed, in part migmatitic rocks. Towards the middle of the RMEHR a transition zone, is marked by lower amphibolite facies metamorphism. South of the central zone the rocks are un-metamorphosed. The calc-alkaline, granodiorite-monzogranite HPP is hosted within the transition zone between the high grade metamorphic rocks, and the low grade metamorphic and sedimentary rock units (Burton, 1997).

During and after the Mesozoic deformational events, erosional exhumation wore through a 2-3 km section of the RMEHR and surrounding area, leaving the Permian to Triassic aged rocks at/near the surface. The emplacement of the HPP occurred soon after, in the Eocene (~36 Ma) during a time of incipient extensional faulting and increased

magmatism induced by the delamination and flexure of the subducting Farallon slab (Humphreys et al., 2003). This time of increased magmatism presumably corresponds to the intrusions underlying the sediment-hosted Carlin-type Au deposits, as well as other precious metal deposits of the same age range in northeastern Nevada (Muntean et al., 2011; Henry and Boden, 1998).

Between 16-17 Ma and 10-12 Ma, the west dipping Ruby Valley detachment fault (part of a west rooted extensional fault system), initially dipping at ~55 W, slipped and rotated to a low angle (~20) (Maccready et al., 1997). Methods such as K-Ar dating and apatite fission track cooling ages indicate total slip estimates between 18 km and 4 to 8 km, (Kistler et al., 1981; Reese, 1986; McGrew & Snee, 1994). The extensional un-roofing of the Ruby Mountains is best recorded by postmylonitization cooling, which progressed east (30 Ma) to west (20 Ma)—coinciding with the un-roofing direction. Local evidence supports crustal extension starting as early as early Tertiary time, continuing up until today (Maccready et al., 1997). Extensional un-roofing induced by the Ruby Valley fault, in conjunction with erosion, has since downthrown the units overlying the HPP (a potential host to ore), and deposited a thick (~>2 km) sequence of coarse clastic rocks to the west (Colgan et al., 2010) (Figure 1). Ongoing erosion has since exposed an east dipping, 5km thick structural section of the HPP (Barnes et al., 2001).

2.3 Geology of the Harrison Pass pluton

2.3.1 Harrison Pass Pluton

The Harrison Pass Pluton, located in northeastern Nevada, occupies an area of ~110 km^2 in the central portion of the Ruby Mountains (Hudec, 1992; Burton, 1997). It lies 47 miles southeast of Elko, NV, constitutes part of the Humboldt National Forest, and borders the Franklin Lake Wildlife area to the east. The granitic rocks of the HPP are weathered at the surface, covered in lichen, and range from 6200-8600 ft in elevation along the main mountain ridges (Burton, 1997). Along the U.S. Forest roads, which provide access throughout most of the HPP, cattle guards and barbed wired fences enclose the grazing land used by the community of cattle ranchers.

2.3.2 Magmatic petrology of the HPP

The Harrison Pass Pluton, was emplaced in the Eocene (~36 Ma) during a time of copious magmatism in the Great Basin (Feeley and Grunder, 1991). The pluton intruded into metasedimentary rocks previously deformed during the emplacement of a Jurassic igneous complex to the north (Hudec, 1990). The HPP is surrounded by upper amphibolite facies rocks to the north, lower greenschist facies rocks to the south, and a contact metamorphic aureole that extends 0.5–1.5 km from the intrusion contact (Burton, 1997). The depth of emplacement of the HPP has been estimated by reconstructing the overlying stratigraphy (4-12 km) (Burton, 1997; Colgan et al., 2010), and by thermobarometric analysis (12.1–14.8±1.6 km) (Burton, 1997; Barnes et al., 2001). In 2016, Gates calculated the entrapment pressures of aqueous fluids, generating entrapment depths of 8.9–17.8 km. These data coincide with the thermobarometric depths determined by Barnes et al. (2001), and suggest that the stratigraphic reconstructions and simple interpretations of the

overlying Paleozoic rock units made by Burton (1997) and Colgan et al. (2010), are insufficient (Gates, 2016). On the other hand, the greater depth estimates have been inferred by Barnes et al. (2001) as evidence for partial crystallization of early stage magmas under higher pressures and/or deeper conditions, before final emplacement of the crystal rich magma at shallower depths. Inconsistencies between these depth estimates are still debated.

The HPP is a multiphase intrusive body emplaced in two major stages: tonalitic-monzogranite magmas, and monzogranite with sparse mafic dikes. Six lithologies were identified and described by Snoke and Lush (1984) and Wright and Snoke (1993). The intrusive phases are listed in order of oldest to youngest:

1.) Diorite—now preserved as mafic xenoliths
2.) Biotite granodiorite porphyry
3.) Porphyritic granodiorite-monzogranite
4.) Biotite-muscovite granite
5.) Alaskite-pegmatite
6.) Net-veined composite dikes

The petrology and geochemistry of Harrison Pass pluton was further investigated by Barnes et al., (2001). The sequence of intrusive phases was simplified and defines the classification scheme used in this thesis. The early stage began with an intrusion of the hornblende-biotite granodiorite of Toyn Creek (Ttc) and was immediately followed by the intrusion of the biotite monzogranite of Corral Creek (Tcc). Both granites contain mafic xenoliths from the earlier mafic stage. The late intrusive stage comprises sheets and dikes

of biotite and two mica monzogranite (Tmg), followed by the youngest intrusive suite, the two mica monzogranite of Green Mountain Creek (Tgm). Late stage, sparse mafic dikes can also be found intruding into the Tmg and Tgm units (Barnes et al., 2001) (Figure 2).

Geochemically the early and late stage intrusions can be easily distinguished from one another, as later stages generally contain lower magnesium and iron and higher silica, Nb, Y, and Rb concentrations. Upon further examination, Barnes et al. (2001) found that none of the plutonic units in the HPP share a liquid line of descent, suggesting the HPP consists of at least four distinct types of granitic magmas (listed above: Ttc, Tcc, Tmg, Tgm), and seemingly each type originates from magma batches derived from heterogeneous crustal source rocks. Furthermore, the non-systematic isotopic compositions of $\delta^{18}O$, Nd, and Sr proves that the different HPP units originate from a heterogeneous source region. In addition, a $\delta^{18}O$ stable isotope analysis of samples from the HPP display magmatic values between ~+9 to 11‰, however four late stage samples display lower values around <+7.8‰, suggesting interaction with ^{18}O depleted meteoric fluids (Barnes et al., 2001). General descriptions of each intrusive suite, listed oldest to youngest are included below.

Ttc: hornblende-biotite granodiorite

The Toyn Creek unit ranges from a biotite± hornblende tonalite (mafic endmember) to granodiorite, and predominantly crops out in the northeast and in some central parts of the HPP. The granodiorite is hypidiomorphic in texture, commonly containing large (3cm long) microcline phenocrysts. Biotite is the abundant mafic mineral, however amphibole is present in some mafic endmember samples. Mafic enclaves are abundant throughout the HPP, but are scarce in areas of flow aligned microcline megacrysts. Miarolitic cavities are

present, but sparse. Allanite-cored epidote is often found throughout this unit. Quenched equivalents of the Ttc are represented as porphyritic dacite dikes protruding into the structurally overlying wallrock. Geochemical data from Ttc samples indicate the granodiorite formed from a magma mixing and mingling event, between mantle and crustal melts (Barnes et al., 2001).

Tcc: biotite monzogranite

The Corral Creek monzogranite crops out in the southern part of the HPP, and is very similar to the Ttc granite in that it has similar grain sizes and microcline phenocrysts. In this unit, mafic enclaves and miarolitic cavities are present, but sparse. Quenched equivalents of the Tcc are represented as biotite granodiorite to granite porphyritic dikes protruding into the carapaces or roof zones. The contact between the Ttc and the Tcc truncates the magmatic fabric preserved in the Tcc (Barnes et al., 2001). The formation of the Tcc rock unit is the result of the combination of two different processes in magma generation: 1.) Magma from deep-seated crustal melting interacted with mafic mantle melts forming the hybridized, tonalitic endmember of the Ttc and 2.) The hybridized magma then mixed with a monzogranitic crustal melt that escaped hybridization, to form the Tcc (Barnes et al., 2001).

Tmg: sheets and dikes of biotite and two mica monzogranite

The two mica monzogranite sheets and dikes underlie most of the western part of the HPP, and outcrop in the mid-west and southwest portions of the pluton. In general, the unit ranges from coarse to fine grained and hypidiomorphic- aplitic in texture. The intrusive bodies classified as sheets strike N/S and dip ~30° E, predominantly cluster

around the Tcc contact, and are composed of composite pegmatite-aplite intrusions, while the Tmg dikes dip steep/sub-vertically. Mafic dikes in the area were also found to contain amphibole. Accessory minerals identified in the Tmg include titanite, allanite, apatite, and garnet. The Tmg is thought to be a smaller melt volume derived from the larger melt fraction of the Tcc that interacted with metapelitic source rocks upon ascent in the lower-middle crust (Barnes et al., 2001).

Tgm: two mica monzogranite

The muscovite-biotite monzogranite of Green Mountain Creek, outcrops in the northern part of the HPP. Older previously described units do not intrude into the Tgm, validating the Tgm as the youngest unit. The Tgm is relatively homogeneous, medium-coarse grained, and contains sparse enclaves of biotite-muscovite rich clots and fist sized quartz globules. Dikes ranging from mafic-intermediate composition were intruded later during the late stages of the Tmg emplacement. The Tgm monzogranite evolved from the older Tmg melt batch, interacting with a distinctly different metapelitic source, as backed-up by varying Sr and ε_{Nd} isotopic compositions (Barnes et al., 2001).

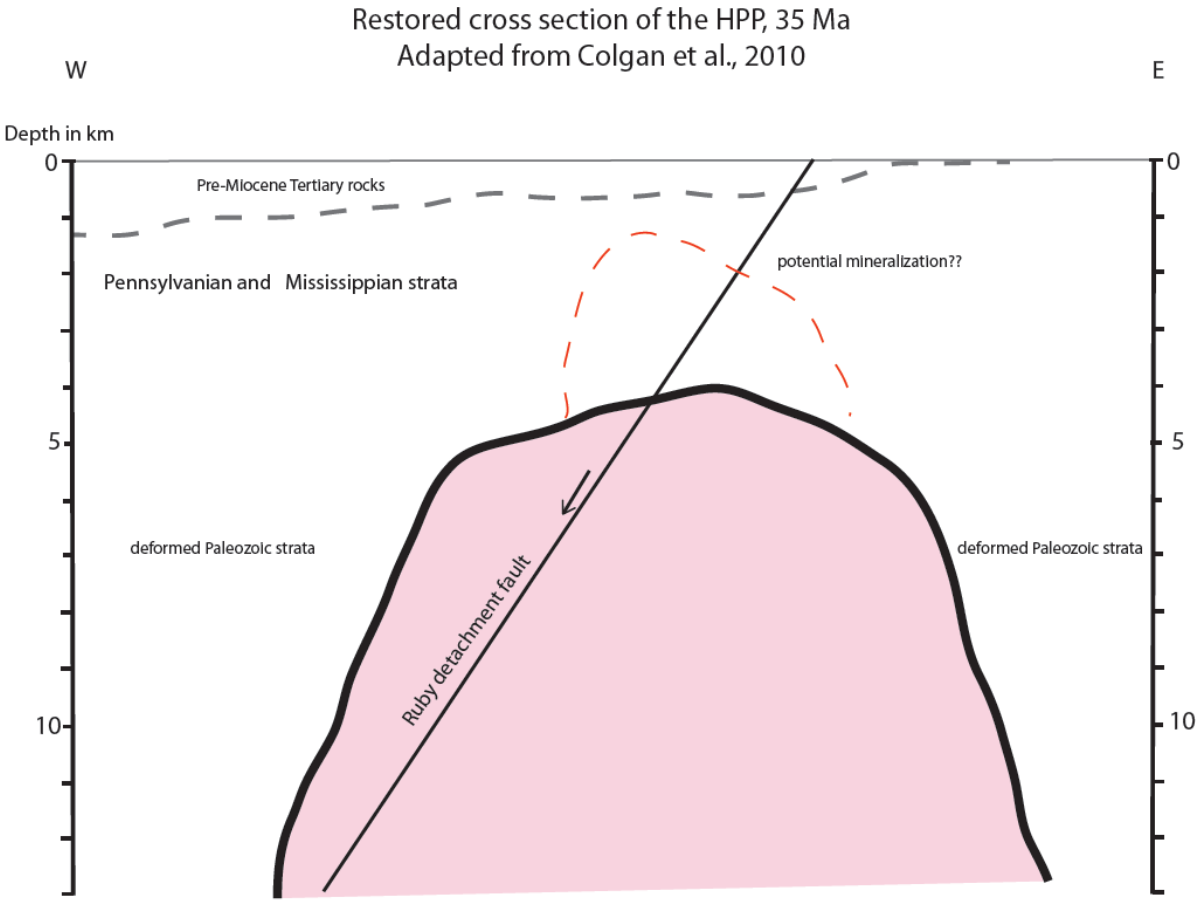

Figure 1: Restored cross section of the HPP, before eastward rotation (Colgan et al., 2010). The red outline is an interpretaion of possible hydrothermal ore above.

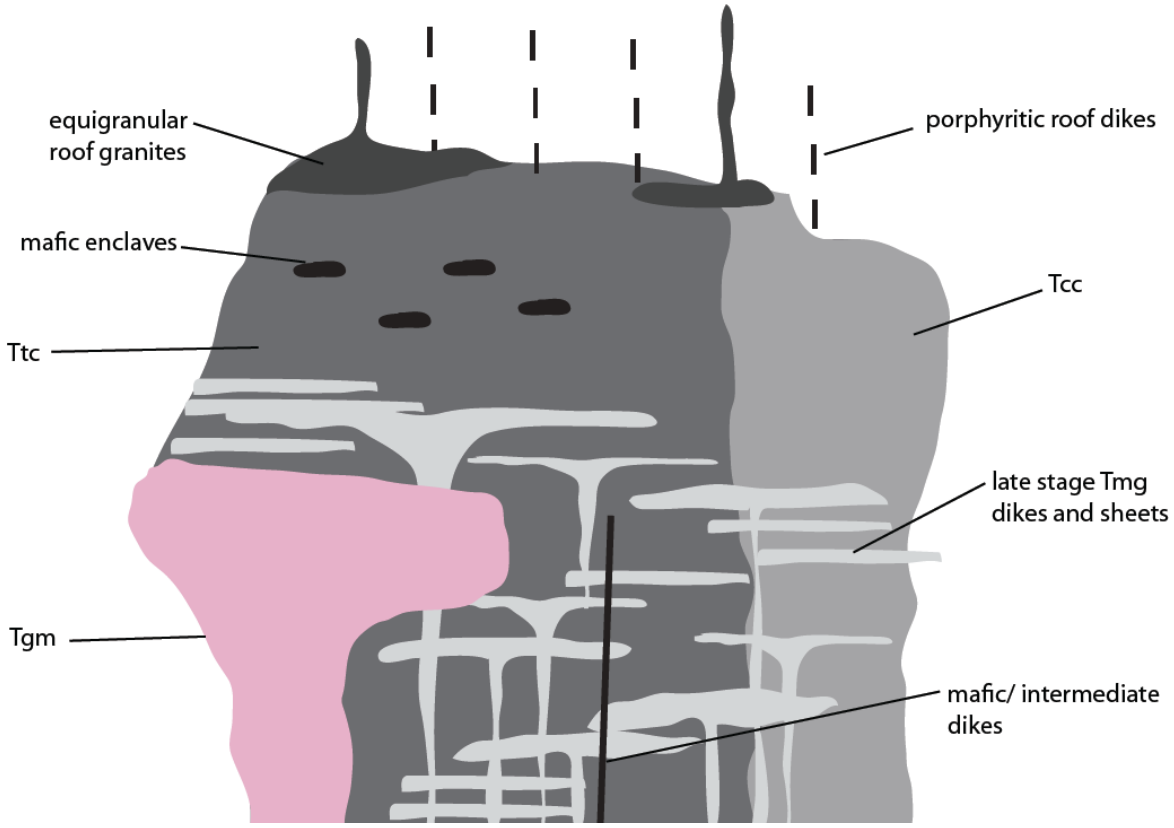

Figure 2: Schematic restored cross section through the HPP showing the sequences of emplacement within the HPP. Adapted from Barnes et al. (2001).

2.3.3 Alterations

During field work devoted to studying the fluid history in and around the Harrison Pass pluton, Musekamp (2011) and Gates (2016) assembled dot distribution maps of the alteration types identified. Before their work, alteration types had not been documented throughout the area. Musekamp documented potassic, phyllic, and skarn alteration around the HPP and the country rock contact, whereas Gates recognized potassic, phyllic, skarn, chlorite-sericite, and silicification alteration types in the HPP. When data from both Musekamp and Gates are compiled, the alteration geometries do not resemble that of a typical porphyry system (figure 3). Instead, the compiled map shows concentrated swarms of silicic alteration, and small isolated pods of the remaining types (potassic, phyllic, skarn, chlorite-sericite) scattered throughout the HPP.

2.3.4 Fluid activity and mineralization around and near the HPP

Based off fluid inclusion studies by Gates (2016), early stage fluid activity in the HPP involved the exsolution of aqueous fluids from the early stage magmas. These fluids were generally low salinity, ore metal-poor, and continued to circulate throughout the magmatic evolution of the pluton. $\delta^{18}O$ values within the HPP indicate only minor meteoric fluid mixing during this time (Gates, 2016). Musekamp (2011) suggested the fluid entrapment temperatures and $\delta^{18}O$ values outside the HPP demonstrate a pressure gradient favorable for the migration of fluids outward and upward towards the roof zone and margins of the HPP. These fluids were responsible for potassic and phyllic alteration, as well as the carbonate replacement and skarn deposits around the contact (Gates, 2016).

Late stage fluids were derived from an episode of magmatic-hydrothermal fluid activity, and were similarly low salinity, and ore metal-poor, but shift to pre-dominantly

aquo-carbonic as opposed to aqueous. The aquo-carbonic fluid type was interpreted to have derived from a later, distinctly more evolved magma (Gates, 2016). Post-intrusion fluid activity was characterized by the influx of large volumes of cooler, deeply circulating, surface derived fluids driven by extension on the Ruby Mountain Shear Zone (RMSZ) (Fricke et al., 1992; Gates, 2016). Evidence of meteoric infiltration ($\delta D_{biotite}$: -125 to -175‰; $\delta^{18}O_{quartz}$ down to -4.4‰) within the mylonites of the low angle structure was documented by Wickham et al. (1993), at paleodepths of 5–10 km. Gates (2016), interpreted these fluids to be a product of mixing of the deeply circulating meteoric groundwater and magmatic fluids.

Around the HPP, evidence of mineralization appears mostly as Cu, Pb, and Zn oxides in outcrop, however several small Pb-Zn carbonate replacement and W skarn deposits have been exploited along the HPP contact zone. During 1925 a portion of the southwestern contact was mined for Pb, Zn, Ag, Cu, and W ores. In 1916, scheelite was discovered at what is now the Star tungsten mine (Lapointe et al. 1991). Mining operations in the district did not start until 1940, but produced ~ 15,000 units of WO_3, 80% of which was produced by the Star mine (Stager and Tingley, 1988). Similar deposits, such as the Climax mine, can be found along the contact zones in the mid-southern to southeast portions of the HPP. During field work in 2016, the deposit locations were confirmed. In addition, weathered Tcc dikes in the adjacent country rock containing copper sulphides in the southeastern corner, and numerous mafic pyroxene-hornblende -pyrrhotite dikes (0.3-0.6m thick) in the northwest HPP near the Tgm unit, were also discovered.

2.4 Porphyry root characteristics

The ability to identify and recognize porphyry root systems is of much importance, as the presence of root zones may indicate an undiscovered deposit nearby (Seedorff et al., 2008). Porphyry deposits are one of the best modeled ore deposit systems, and yet while the tops of porphyry systems have been studied extensively, the bottoms have been studied little despite evidence indicating metal bearing fluids responsible for precipitating the ore minerals rose from somewhere below. These root systems constitute an important source region of ore fluids and likely extend for many kilometers beneath the ore body into the batholith: a critical region where porphyry fluids broke through the pluton cupola carapaces.

Seedorff et al. (2008) published one of the few papers to date which describes porphyry root features in detail: the region beneath a porphyry ore body, comprised of porphyry dikes merging down into the cupola/carapace of a larger igneous intrusion, concentrated fluid flow, and wide spread hydrothermal alteration. Because porphyry deposits average two kilometers of vertical exposure, known root zones that have been structurally brought to near surface levels are rare, and only six were examined: Yerington, Ann-Mason, Miami Inspiration, Sierrita- Esperanza, Ray, and Kelvin-Riverside (Seedorff et al., 2008).

General porphyry root features include: quartz veins, aplitic, porphyritic, and pegmatitic dikes, and wide spread alterations including greisen, potassic, and chlorite-sericitic types. All six examined root zones were found to have the following features in common: quartz veins with variably developed K-feldspar alteration envelopes, and

biotitic, greisen (muscovite)? , calcic, sodic-calcic and sodic alteration. Each system contained various vein types, including and is not limited to: quartz±feldspar, quartz±feldspar±biotite(pyrite>>chalcopyrite), quartz-biotite-magnetite, and greisen muscovite±pyrite (Seedorff et al., 2008). The nature of porphyry root features varies depending on the system. For more information on how alteration types grade up and out see Seedorff et al. (2008), and Figure 4 for a generalized distribution of alteration types.

Although mentioned by Seedorff et al. (2008), copper/ore grades in root zones are not discussed, but are generally very low. This along with many genetic questions are still left unanswered. Seedorff and his team of graduate students continue to study root zones, and are on the verge of publishing a paper discussing root zone greisen alteration (Runyon, oral correspondence, 2016).

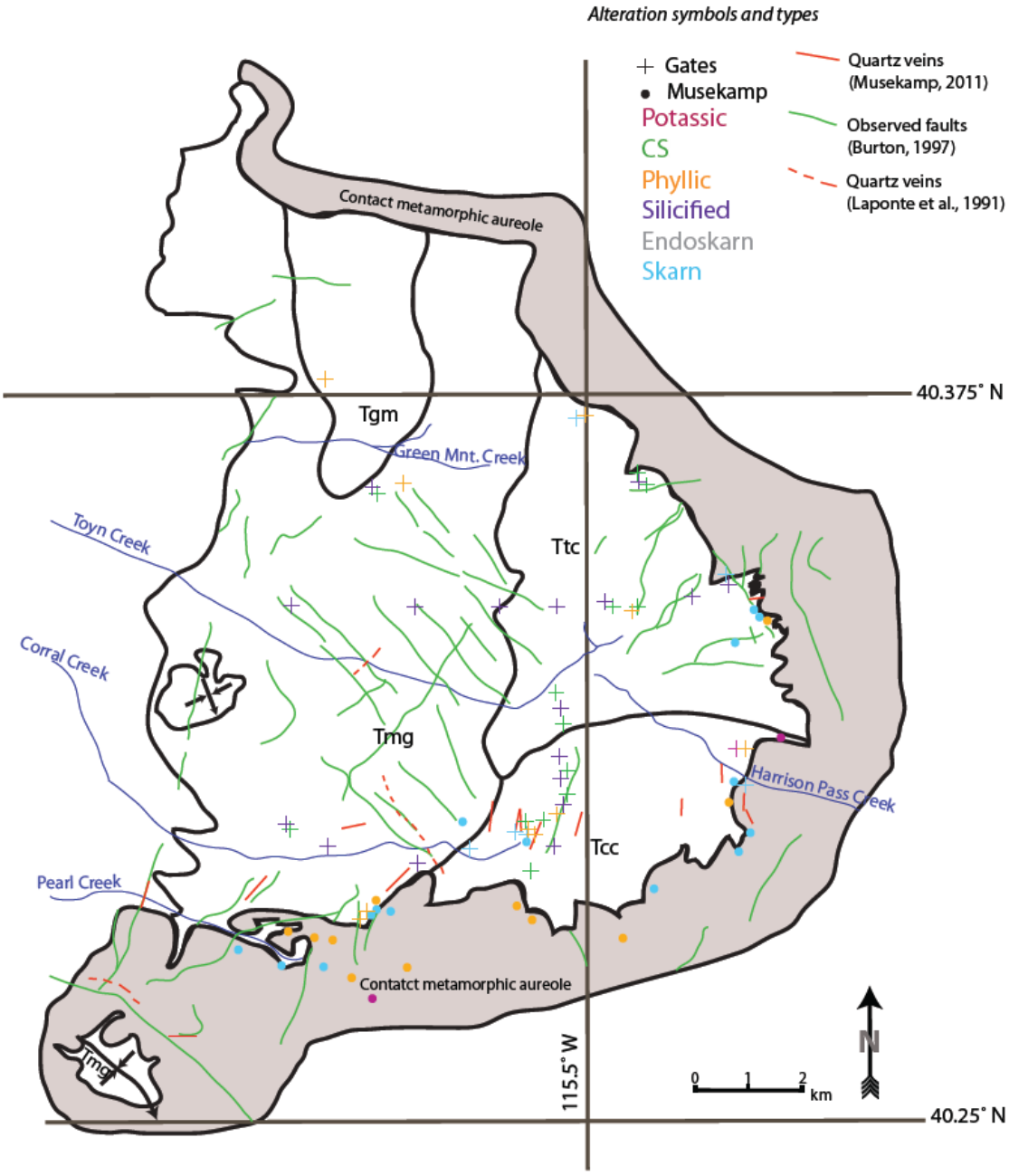

Figure 3: Geologic map of the Harrison Pass Pluton, including locations of known alteration types identified by Musekamp (2011) and Gates (2016). Positions of the alteration types are slightly distorted to enhance readability within the dense clusters of data. Map adapted from Burton (1997) and Barnes et al. (2001).

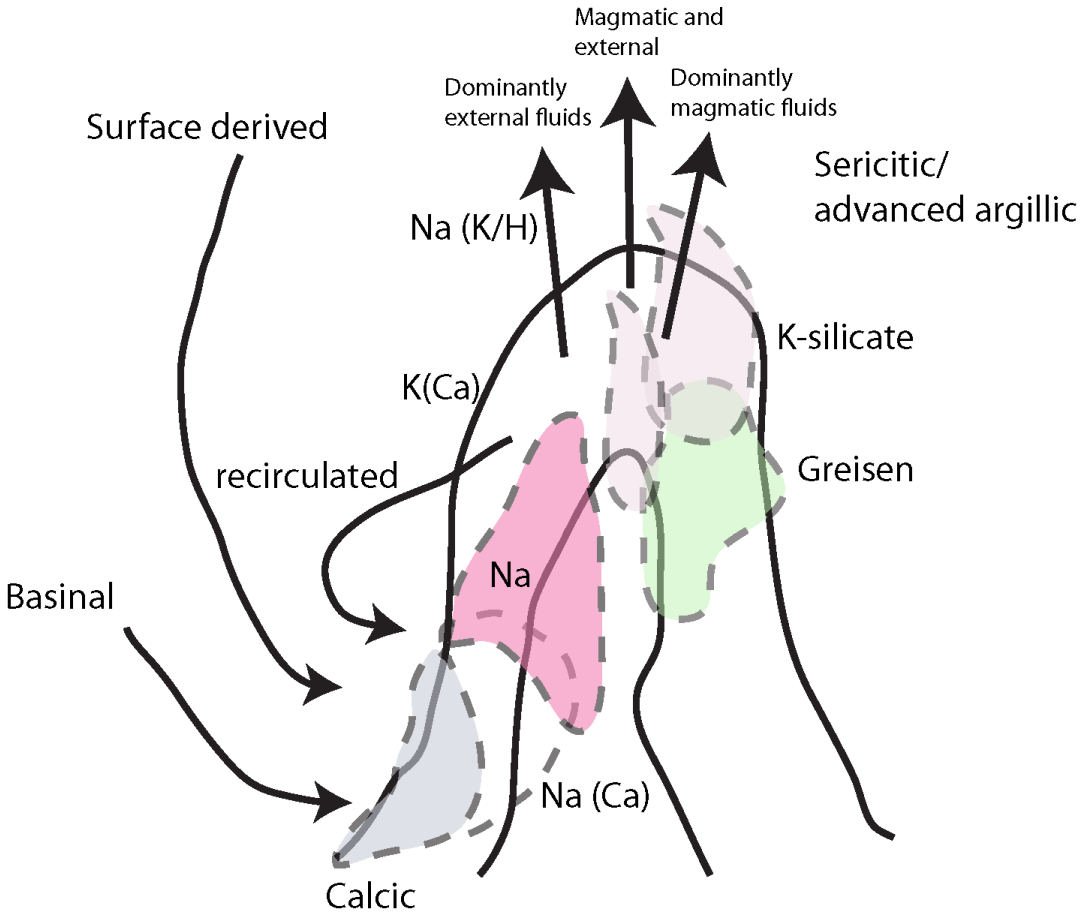

Figure 4: Schematic cross section and interpretation of a possible arrangement of alteration types in root zones, adapted from Seedorff et al. (2008). Alteration types include: calcic, sodic-calcic [Na(Ca)], sodic [Na], greisen [muscovite-rich greisen], potassic [K-silicate], potassic transitional to calcic [K(Ca)], sodic transitional to potassic and sericitic [Na(K/H)], and sericitic and advanced argillic types. Arrows indicate the origin of alteration types.

3 METHODS

3.1 Field work

Four major strips through the HPP, two trending EW and two NS, were identified as areas of interest and used as a guide for the three-week field work excursion during June 1st 2016 through June 20th 2016. Most areas were accessible by vehicle through jeep trails maintained by the US Forest Service, but hiking off trail was necessary to access most outcrops. Dot point maps of alteration types observed by Musekamp (2011) and Gates (2016) were overlaid and used to determine areas of interest (Figure 5). Each transect was carefully chosen, to ensure each alteration type would be collected and mapped. As alteration types were identified, the location of the outcrops were logged using a eTrex 10 GPS, field notes and pictures were taken, samples were labeled and collected for further analyses, and when appropriate, structures were measured using a Brunton compass. Samples near post magmatic zones of deformation and fluid circulation (i.e. the Ruby Detachment) were avoided due to the possibility of geochemical overprinting. Once an alteration type was identified and documented, additional shorter transects were made to trace the path of zoned alteration types. Through this method, 110 samples were collected and seven major transects were documented. Descriptions of each transect are crucial to fully grasp the implications of the geochemically zoned systems, and will therefore be given in detail in appendix 1. A list of the sample numbers, GPS locations, and alteration types for all samples in each transect is in Table 1 of Appendix 1.

In addition, where identified, porphyry root features such as quartz veins, aplitic, porphyritic, and pegmatitic dikes, and wide spread alterations including greisen, potassic,

and chlorite- sericite, were recorded (Seedorff et al. 2008; Runyon et al. 2016). Quartz veins have been well documented and mapped throughout the HPP by Lapointe et al. (1991), Musekamp (2011) and others, while Barnes et al. (2001) recorded porphyritic-equigranular roof dikes. Knowledge of the distribution of these features throughout the HPP allowed for a finer focus on finding veins and dikes cutting through topographically higher features, behaviors similar to those of porphyry root systems (Seedorff et al., 2008). A compilation of the alteration zones and locations of the veins and dikes within the HPP was used to compare to the maps of porphyry root systems published by Seedorff et al. (2008), to investigate the possible presence of a porphyry root system at the HPP.

3.2 Petrography

Forty-seven samples of altered rocks from the seven major transects were sent to Paula Leek Petrographics, and made into standard thin sections. Using transmitted light from a Leica DM-EP microscope, thin sections were predominantly analyzed for mineralogy, microstructures, and textural fabrics. The overall analysis was used to verify alteration types identified in the field, and to evaluate the integrity of quartz, biotite, and chlorite grains needed for oxygen and hydrogen isotope analysis. In addition, quartz grains were evaluated for the presence of fluid inclusions. Seventeen samples were selected based off fluid inclusion abundance and size, sent to Wagner Petrographics, and made into double polished thin sections for fluid inclusion analysis.

3.3 Whole rock geochemistry

Twenty-nine samples representative of the multiple rock types and alterations in the seven transects through the HPP were crushed to pebble sized pieces in house, and sent to the ALS laboratory in Reno for whole rock geochemical analysis. Samples were analyzed

for major element oxides and some trace elements using a Lithium Borate Fusion and ICP-AES, and analyzed for trace and rare earth elements (REE) by a Lithium Borate Fusion and ICP-MS. To compare the petrological and geochemical data in this study to the 2001 study conducted by Barnes et al., Harker and spider diagrams were used. Harker diagrams mimicked those found in Barnes et al. (2001). Multi-element spider diagrams, normalized using mid-ocean ridge basalt (MORB) data from Pearce (1983), were plotted to present the evolution and petrologic variation between each intrusive unit. Lastly, REE spider diagrams, normalized with chondrite values from Anders and Grevesse (1989), were plotted separated by intrusion type.

As a preliminary test for alteration, bivariate plots were constructed using the principles of Stanley and Madeisky (1994). To confirm the alteration type and quantify alteration intensity, Gresens' isocon plots (Leitch and Lentz, 1994) were made using the program EASYGRESGRANT, developed by López-Moro (2012). Unaltered data from each unit (Ttc, Tcc, and Tmg) was selected from Barnes et al., 2001, were averaged, and used for the alteration of mass balance calculations. (Table 3, Appendix 2). Alteration mass balance was calculated by the EASYGRESGRANT program, and used to produce spider diagrams in Excel to quantify the relative gain/loss of oxides and trace elements. Mass-balance results were calculated using the deviation of ΔC_i (change in amount of the component) from the slope of the isocon line, which represents immobile elements during hydrothermal alteration (in this study Al_2O_3) (see López-Moro, 2012). Data and reported as gain-loss in Wt.% or ppm (see Appendix 2). In addition, trace metals and REEs of each alteration type were plotted on spider diagrams.

3.4 Fluid inclusion analysis

Fluid inclusions from doubly polished thin sections were first mapped and logged using a LEICA DM 2500 P microscope coupled with a CLEMEX camera. Fluid inclusion origins (primary, secondary, and pseudosecondary) were assigned using criteria from Roedder (1984). Secondary fluid inclusions along/around healed quartz fractures (typically the result of hydrothermal alteration) were sought after. An Olympus BX-51 microscope coupled with a detachable Linkam 600 heating/freezing stage was then used for the microthermometric analysis. The following heating and freezing steps outlined by Roedder (1984) were used to obtain the following measurements:

1. Testing for the presence or absence of CO_2 (presence of a double bubble and low eutectic temperature)
2. Freezing to the temperature of meta stable freezing (T_{mf})
3. Warming to the temperature of eutectic (T_e)
4. Slow warming to temperature the of last ice melt ($T_{m\text{-}ice}$)
5. And finally, heated up to the total homogenization temperature (T_h)

The homogenization temperature values from the microthermometric analysis, were then corrected for pressure (1-4 kb) and salinity (0-5 wt. % NaCl) using isochore diagrams published by Bodnar (2003). The corrected range of temperatures, representative of the formation/alteration temperatures, were used to constrain and compare hydrothermal temperatures of the samples throughout all seven transects. In addition, temperature values were also used in the calculation of oxygen and hydrogen isotope ratios of the waters responsible for alteration, from the mineral data.

In addition to data published by Gates (2016), a general estimation of the salinity of the hydrothermal fluids was calculated using a new equation developed by Wilkinson (2017). By measuring the metastable freezing temperatures (T_{mf}) of the fluid inclusions, the following equation was used:

$$\text{Salinity (wt \% NaCl equiv)} = -69.7 - 2.617T_{mf} - 0.02603T_{mf}^2 - 0.0000994T_{mf}^3$$

In addition, an equation developed by Bodnar (2003), requiring use of $T_{m\text{-}ice}$, was used to confirm results from the equation above. Several $T_{m\text{-}ice}$ values were >0, hence the salinity of those fluid inclusions could not be determined by this method. Salinity of the fluids is used to establish the source of the fluids as: magmatic, meteoric, or saline brines.

3.5 Oxygen and Hydrogen isotopes

Twenty-four quartz, and twenty-three biotite/chlorite separates from representative alteration samples were crushed, and separated in house and sent to The Light Isotope laboratory at The University of Texas at Austin. Oxygen in quartz separates was first converted to gas by the laser fluorination oxygen extraction line, and then analyzed by the Thermo MAT253 stable isotope ratio mass spectrometer. Biotite and chlorite separates were put in silver capsules and heated in the Costech Zeroblank autosampler, producing a gas phase. The hydrogen gas was then separated, and sent to the MAT253 isotope ratio mass spectrometer. All $\delta^{18}O$ values were normalized to NBS-28 (~+9.65‰ SMOW), and δD values were normalized to biotite standard NBS-30 (~δD=–65‰ SMOW). To calculate the oxygen and hydrogen isotope ratio values for the waters responsible for alteration, the following equation for both oxygen and hydrogen were used:

Oxygen equation:

$$\delta^{18}\mathrm{O}\ \mathrm{H_2O} = \left[\frac{\left[\frac{\delta^{18}\mathrm{O\ quartz}}{1000} * \left(\frac{^{18}\mathrm{O}}{^{16}\mathrm{O}}\right)\mathrm{smow} + \left(\frac{^{18}\mathrm{O}}{^{16}\mathrm{O}}\right)\mathrm{smow}\right] \div \alpha - \left(\frac{^{18}\mathrm{O}}{^{16}\mathrm{O}}\right)\mathrm{smow}}{\left(\frac{^{18}\mathrm{O}}{^{16}\mathrm{O}}\right)\mathrm{smow}}\right] * 1000$$

$\boldsymbol{\delta^{18}O_{H_2O}}$=Amount of $\delta^{18}O$ in the waters that formed the mineral quartz

$\boldsymbol{\delta^{18}O_{quartz}}$ = Amount of $\delta^{18}O$ in the mineral quartz

$\left(\frac{^{18}O}{^{16}O}\right)_{smow}$ = A standard: ratio of ^{18}O to ^{16}O in standard mean ocean water

α= The fractionation coefficient —based off formation temperature

Hydrogen equation:

$$\delta\mathrm{D}\ \mathrm{H_2O} = \left[\frac{\left[\frac{\delta\mathrm{Dbio}}{1000} * \left(\frac{\mathrm{D}}{\mathrm{H}}\right)\mathrm{smow} + \left(\frac{\mathrm{D}}{\mathrm{H}}\right)\mathrm{smow}\right] \div \alpha - \left(\frac{\mathrm{D}}{\mathrm{H}}\right)\mathrm{smow}}{\left(\frac{\mathrm{D}}{\mathrm{H}}\right)\mathrm{smow}}\right] * 1000$$

$\boldsymbol{\delta D_{H_2O}}$ =Amount of deuterium in the waters that formed the mineral

$\boldsymbol{\delta D_{biotite\text{-}chlorite}}$= Amount of deuterium in the mineral biotite/chlorite

$\left(\frac{D}{H}\right)_{smow}$ = A standard: ratio of deuterium to hydrogen in standard mean ocean water

α= The fractionation coefficient—based off formation temperature

The calculated fractionation coefficient (α) for hydrogen used compiled fractionation curves in Taylor (1974). This method required relative Mg/Fe ratios for the biotite and chlorite samples, calculated using the whole rock geochemical data from each representative sample and Excel programs/files (Biotite.xls and Chlorite.xls) produced by The Open University. The fractionation factor for oxygen in quartz was determined using

the quartz-water fractionation equation from Clayton et al., 1972. It should be noted, however, that the equations assume pure water, a closed system at equilibrium (Taylor, 1997), and ignore factors such as pressure and salinity (Horita, 2005). The Ligang et al. (1989) Qtz-H_2O-salt fractionation study deemed values from Clayton et al., (1972) to be relatively reliable, and since the salinity of the HPP fluids are low (Gates, 2016), and pressure estimates vary in literature from 1-4 kbar (Burton, 1997; Colgan et al., 2010; and Barnes et al., 2001), the above equations were used in conjunction with assessment of the approximate uncertainties.

Once the $\delta^{18}O$ and δD values of the formation waters were calculated for each sample, the values were plotted on a $\delta^{18}O$ and δD diagram of isotopic values for different water sources (Taylor, 1974). Graphed results show whether single or multiple fluid types were responsible for the alterations, and define the source of each (i.e. magmatic, meteoric, metamorphic, or mixtures of these).

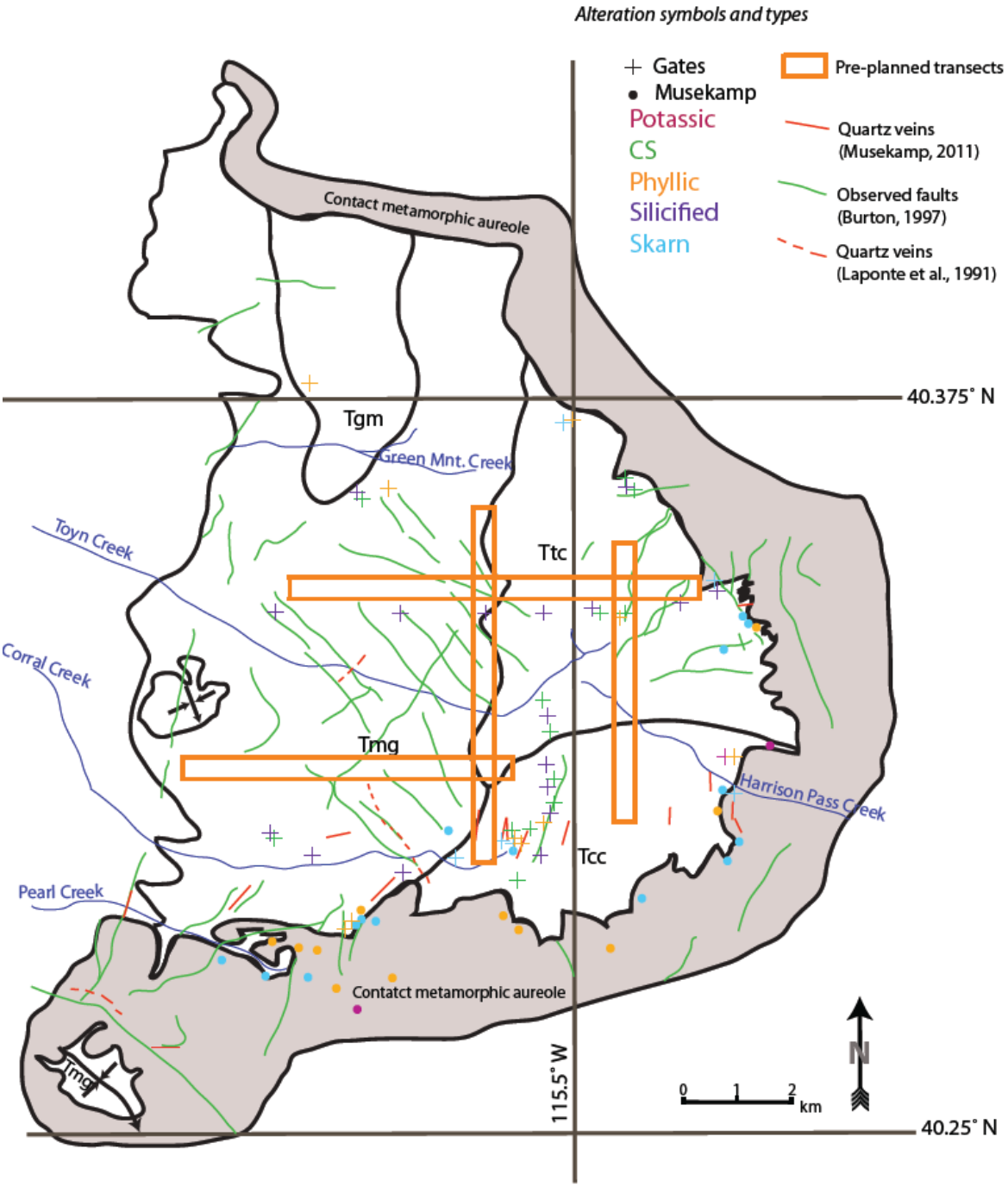

Figure 5: Geologic map of the HPP, showing pre-planned transects and alteration types mapped by Musekamp (2011) and Gates (2016). Positions of the alteration types are slightly distorted to enhance readability within the dense clusters of data. Map adapted from Burton (1997) and Barnes et al. (2001).

4 DATA AND RESULTS

4.1 Field data

4.1.1 Transect overviews

Modification of the pre-planned transects outlined in Figure 5 was necessary to observe outcrops of interest. For detailed transect descriptions see Appendix 1; for a visual of the updated transects along with sample I.D. numbers see Figure 6.

Transect 1 (Tmg): In view of the occurrences of potassic alteration recorded by Musekamp (2011) and Gates (2016), its presence was sought after as potassic alteration is present in most of the porphyry root systems studied by Seedorff et al. (2008).

Transect 2 (Ttc): The NE corner of the HPP, a large area consisting of a NW trending ridge-valley system, was targeted due to the amount of chlorite-sericite alteration (CS) recorded by Gates (2016), and the need for alteration data within the Ttc. Many outcrops were significantly fractured, tinted green, and displayed the typical mineralogy of CS alteration (Figure 7, picture C and D). Contact features such as endoskarns were sought after in this region. As a result, a bleached, K-feldspar rich sample was collected near a limestone contact. At the north-western most extent of the transect, a triple contact between CS altered, epidote rich, and unaltered Ttc was observed (Figure 7, picture E).

Transect 3 (Tmg): The northern mid-west part of the HPP was explored in order to encounter interleaved Tmg and Ttc (40.339 N, -115.559 W). The outcrops were made up of predominately a mixture of aplites, pegmatites, and quartz veins. Since the western portion of the HPP exposes a deeper position in the pluton, greisen alteration was sought for in the

region, but instead potassic alteration was found to be present. An isolated CS altered Ttc pod was encountered further south within the Tmg unit.

Transect 4 (Tmg): The southern middle portion of the HPP, was specifically chosen for observations in proximity of the Tmg- Tcc contact. Potassic alteration was found near the northern half of a ridge, which comprised of limestone-marble-skarn Tmg contact zone. Granite was silicified up to 15-20m north and south of the limestone xenolith.

Transect 5 (Tmg): The isolated Tmg inlier, in the southwest corner of the HPP was chosen as earlier data had not been collected in the area (40.245 N, -115.625 W). CS and endoskarn outcrops were found distributed around the flanks of the intrusion (Figure 7, picture F). A skarn pod—another feature of interest— was encountered in contact with the Tmg (Figure 8, picture G).

Transect 6 (Tcc): This area was chosen due to the proximity of the triple contact between the Tcc, Ttc, and Tmg phases. In the northwest portion of the Tcc, a large, 60cm wide vuggy quartz vein was found trending for 5m north (Figure 8, picture H). A small potassically altered Tcc outcrop along with CS alteration was encountered beyond the extent of the quartz vein trend.

Transect 7 (Tcc): This area was chosen for the proximity to the Star mine skarn and structural top of the exposed intrusion in the Tcc unit (40.311 N, -115.476 W). The west side of the skarn was in contact with potassically altered Tcc granite (Figure 8, picture I). A 4.5m band of CS altered granite was present 30m west of the skarn, and unaltered Tcc 60m further west.

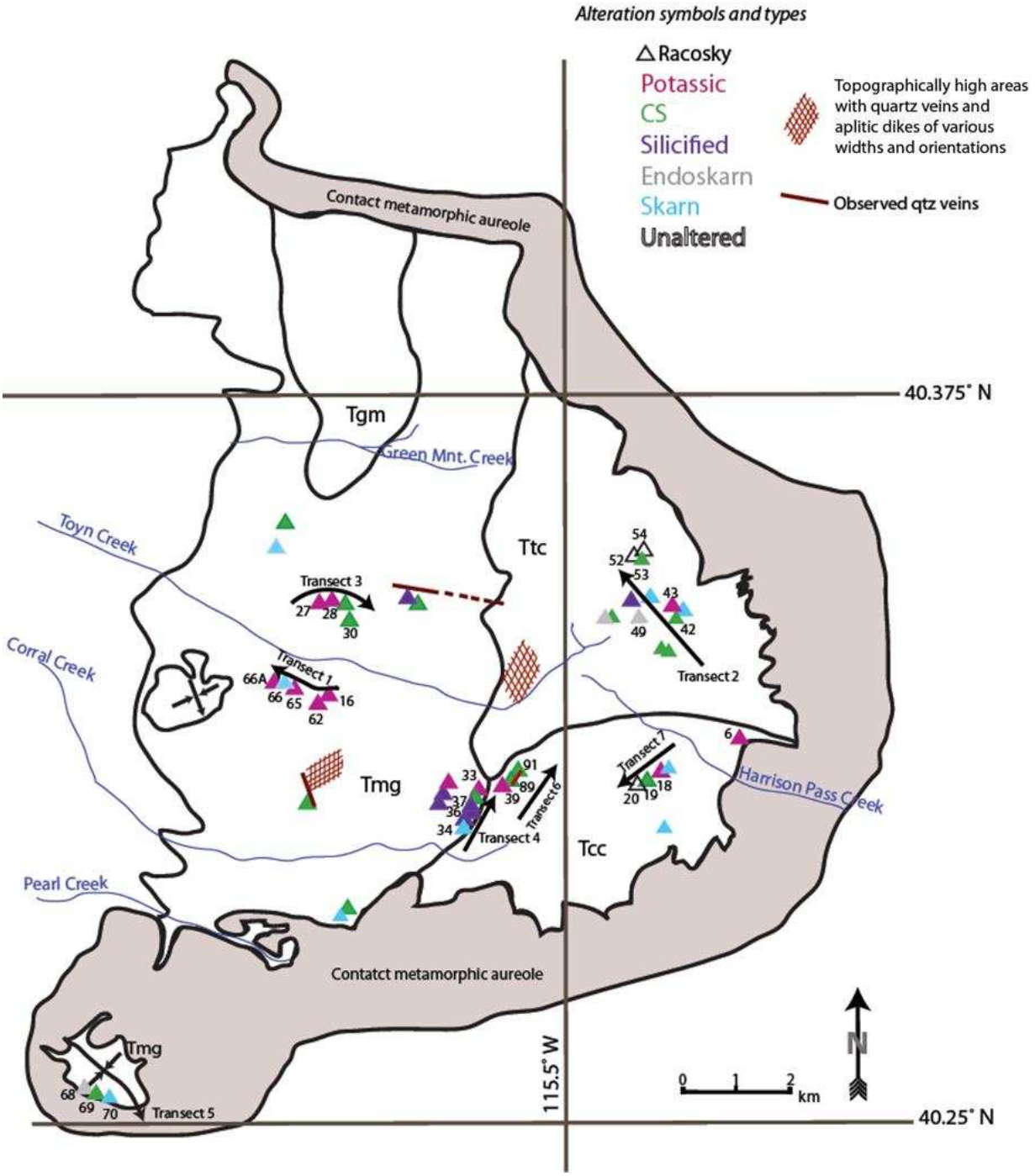

Figure 6: Map of sample locations and corresponding I.D. number. Positions of the alteration types are slightly distorted to enhance readability within the dense clusters of data. HPP map adapted from Burton (1997) and Barnes et al. (2001).

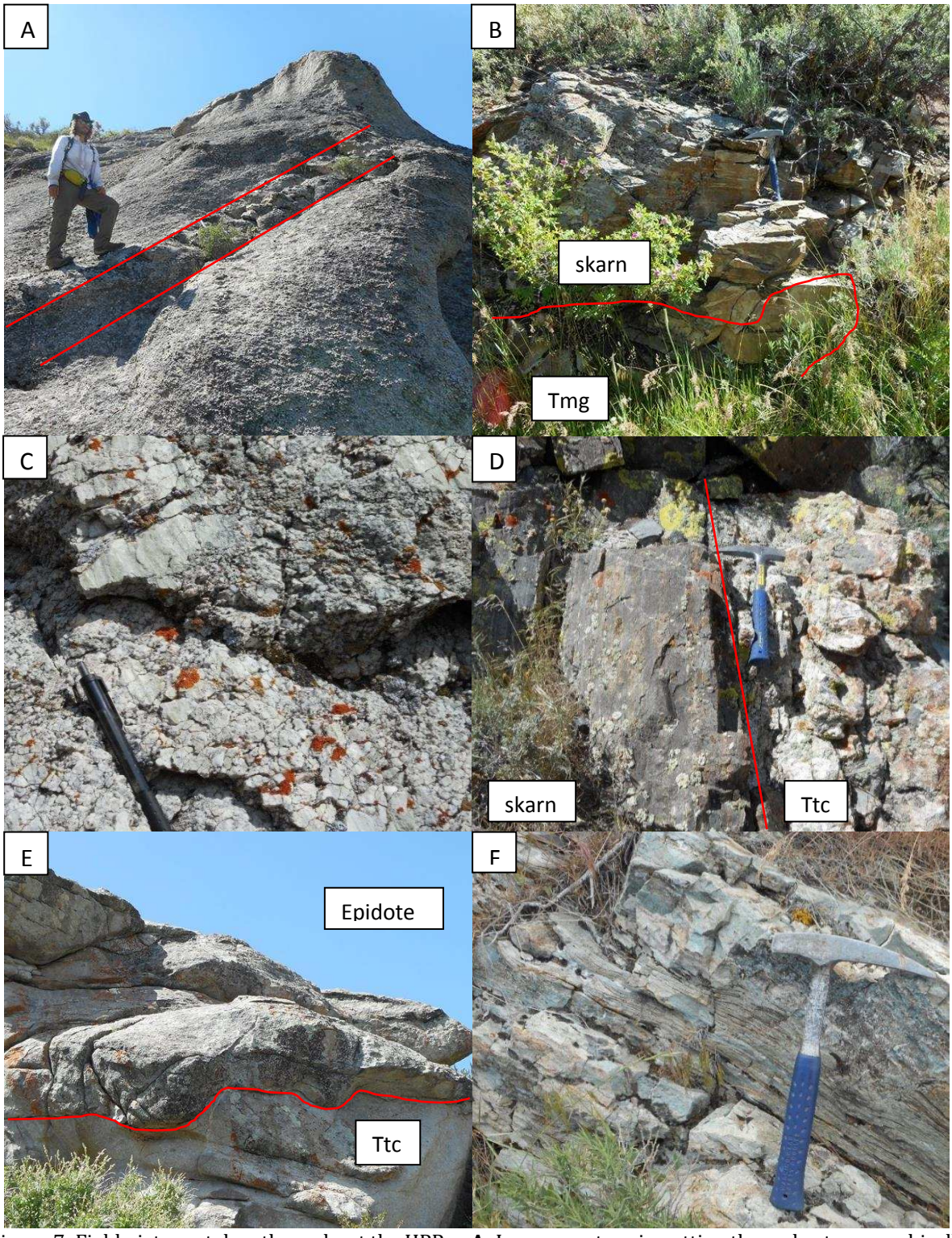

Figure 7: Field pictures taken throughout the HPP— **A:** Large quartz vein cutting through a topographically high, potassically altered outcrop in transect 1. **B:** Skarn and Tmg contact at the end of transect 1. **C:** Fractured CS altered Ttc outcrop in the southeastern portion of transect 2. **D:** Skarn Ttc contact in the central zone of transect 2. **E:** The epidote rich Ttc and unaltered Ttc contact, part of the triple contact found within the Ttc unit. CS contact (not shown) is to the right—found in the northern section of transect 2. **F:** Endoskarn outcrop found within the Tmg inlier along transect 5.

Figure 8: Field pictures taken throughout the HPP— **G:** Limestone xenolith in the Tmg inlier at the end of transect 5, looking east. **H:** miarolitic cavity within a quartz vein in the Tcc, at southern end of transect 6. **I:** Star mine in the Tcc unit with ~ 2m wide garnet skarn zone, located at the beginning of transect 7.

4.1.2 Additional Localities

Veins and dikes

Porphyry root zone features— described by Seedorff et al. (2008) as where porphyry fluids break through the crystalline carapace of magma intrusions, marked by an abundance of quartz veins, porphyry dikes, and alteration —were sought for near topographically high or "carapace" like features within the HPP. Concentrations of veins/dikes throughout the HPP are most widespread in the topographically high areas, in unaltered granite. Three major areas were found displaying one or both of these vein/dike types: Middle of the HPP near the Tmg-Tcc contact, SW portion of HPP in the middle of the Tmg unit, and northern-middle HPP also near the Tmg-Ttc contact (Figure 6).

1.) Middle of the HPP (40.332 N, -115.507 W): The investigation started at ≈2310m at the top of a topographically higher region within the Ttc, and continued south downwards towards the Harrison Pass road. Coarse and fine quartz, quartz-feldspar, and quartz-feldspar-muscovite veins, along with aplitic dikes, varying in width (.15-.3m), are present. Most the veins and dikes trend north to north-west, with a minor amount trending east, and all generally dipping vertically to sub-vertically in various directions (Figure 9, pictures A-G).
2.) SW HPP (40.309 N, -115.560 W): A large, 1.8-3m wide, NW trending, quartz vein cuts through a topographically higher region in Tmg, and pinches out at 2278m. Adjacent to the major quartz vein, a high density of small quartz veinlets cut through the Tmg, with CS alteration ~3m from the main quartz vein contact. The quartz vein dissipated at the top of the region, and smaller quartz±feldspar±muscovite veins became dominant. These veins cut through the

entirety of the topographically high "roof" and varied in width (.15-.6m), and were randomly oriented. The Tmg is found to be mostly unaltered, but muscovite is present along some of the vein selvages suggesting greisen alteration. The transect was followed around a horseshoe shaped ridge (~0.8 km long) until the vein density significantly decreased (Figure 10, pictures H-K).

3.) Mid-north HPP (40.344 N, -115.534 W): A large continuous, previously unmapped quartz vein was found in the mid-northern section of the Tmg (Figure 10, picture L). The vein trends 295, is 2-4.5m wide, and in contact with the Tmg producing a halo (~.3-.6m wide) of light CS alteration (Figure 10, picture M). The vein was a very distinctive landmark and was estimated to be ≈1.5 kilometers long.

4.2 Alteration types

Alteration types identified in the field throughout the HPP include:

- Potassic
- Chlorite-sericite (CS)
- Phyllic (identified by Musekamp (2011) and Gates (2016))
- Silicification
- Endo-skarn (similar to the calcic type described by Seedorff et al. (2008))
- Exo-skarn
- Greisen

An extrapolated interpretation of alteration geometries within the HPP, including data from Musekamp (2011) and Gates (2016), is presented in figure 11— A concentration of potassically altered rocks occurs in the middle portion of the HPP, while CS and phyllic alteration are distributed along the margins of the intrusion. While greisen alteration was not included in the alteration map, the alteration type was found and sampled in the southeastern portion of the Tmg (40.306 N, -115.526 W).

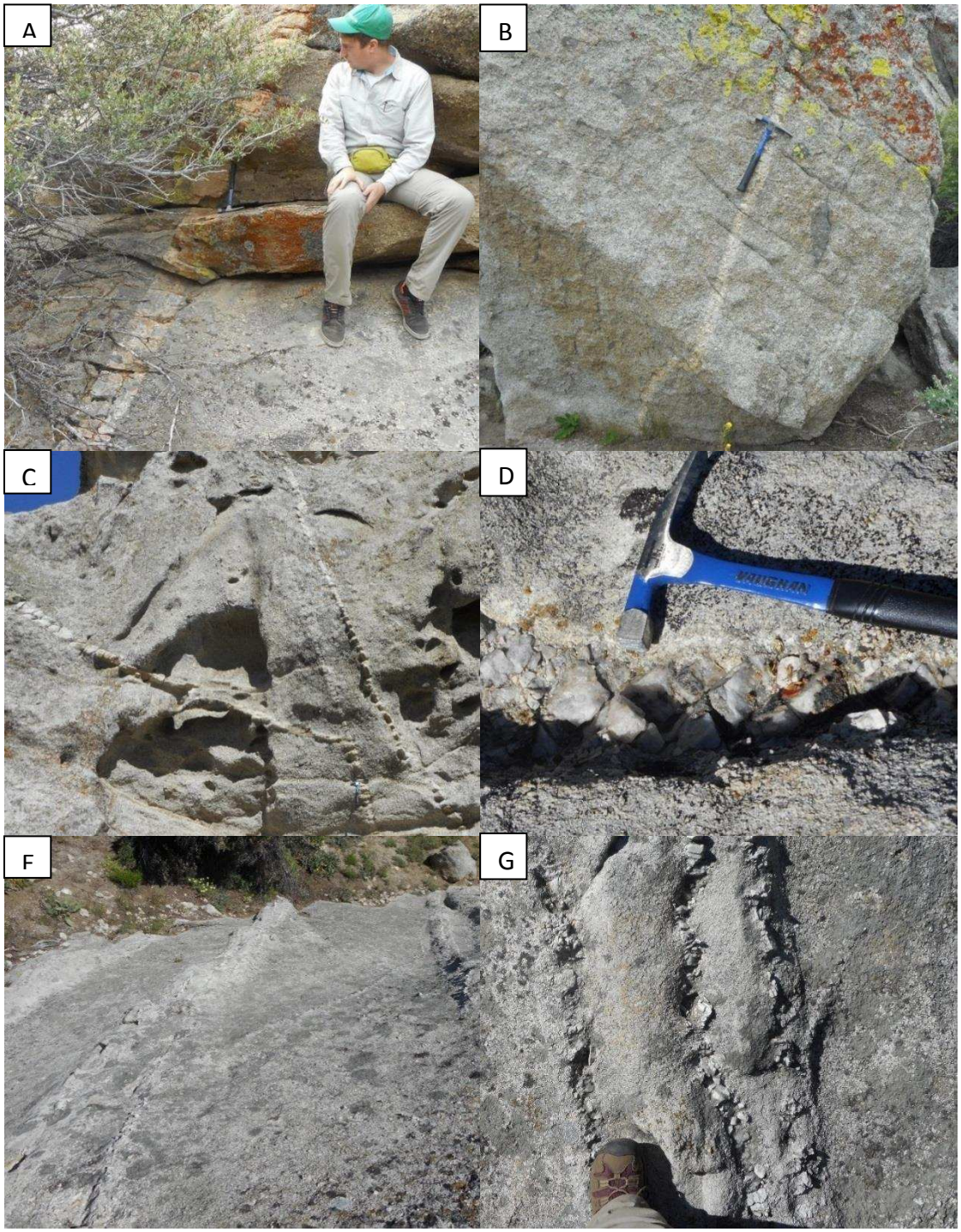

Figure 9: Pictures of porphyry root features within the HPP. Pictures A-G are all taken from a topograpically high area located in the southwest portion of the Ttc, represented by hash marks in Figure 6. **A:** Aplitic dike cutting through the Ttc unit. **B:** Aplitic dike next to a mafic enclave within the Ttc unit. **C-G:** Coarse grained quartz and feldspar veins cutting through the Ttc.

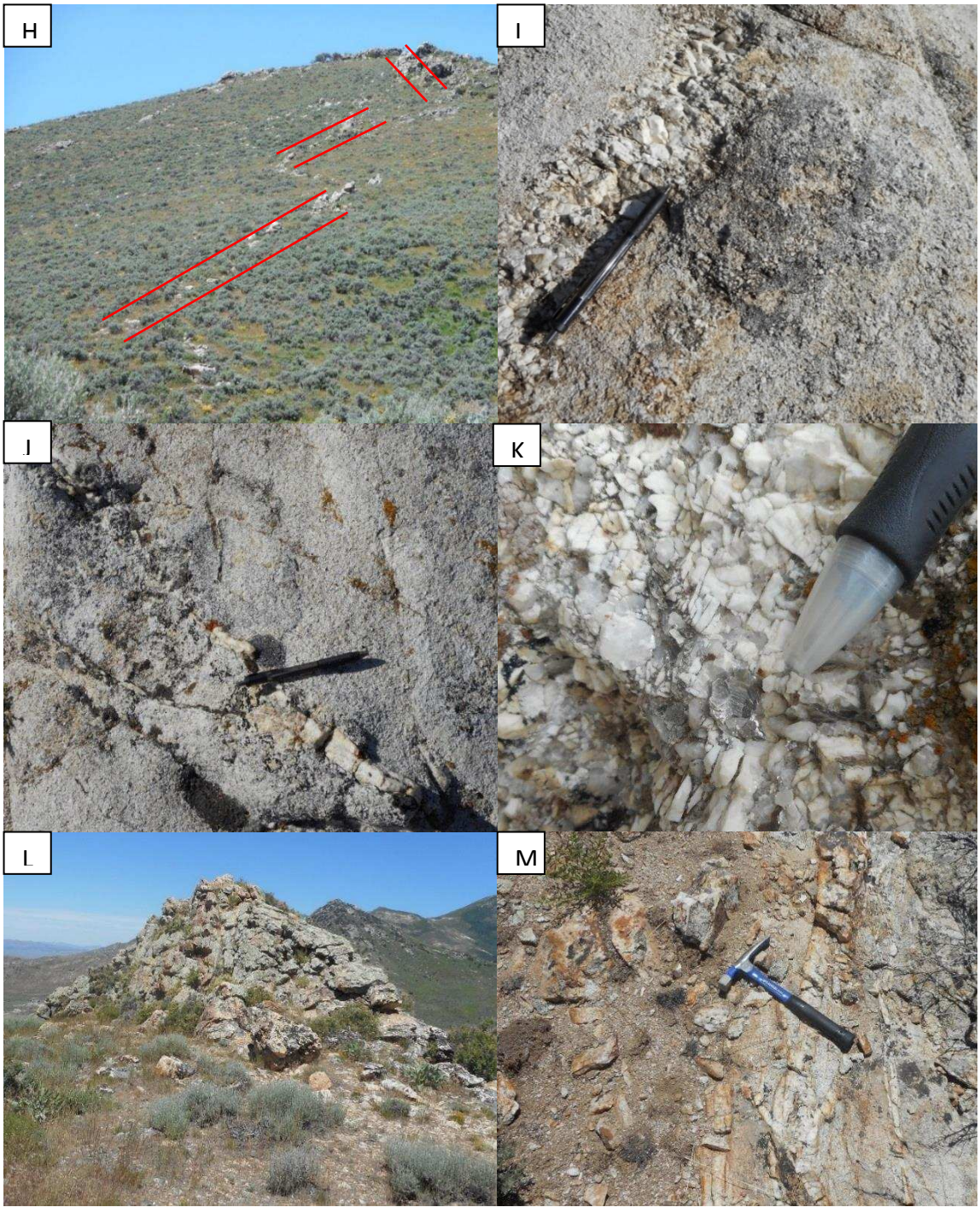

Figure 10: Pictures of porphyry root features within the HPP. Pictures H-K are all taken from a topograpically high area within southern portion of the Tmg (represented by hash marks in Figure 4). Pictures L and M are from the mideastern portion of the Tmg (marked by a bold amroon line in Figure 6)—H: Large quartz vein cutting through the Tmg. I-K : Smaller quartz+ feldspar±muscovite veins cutting through the Tmg unit. L: Large quartz vein cutting through the Tmg unit, looking northwest. M: light halo of CS alteration to the west of the large quartz vein in picture L.

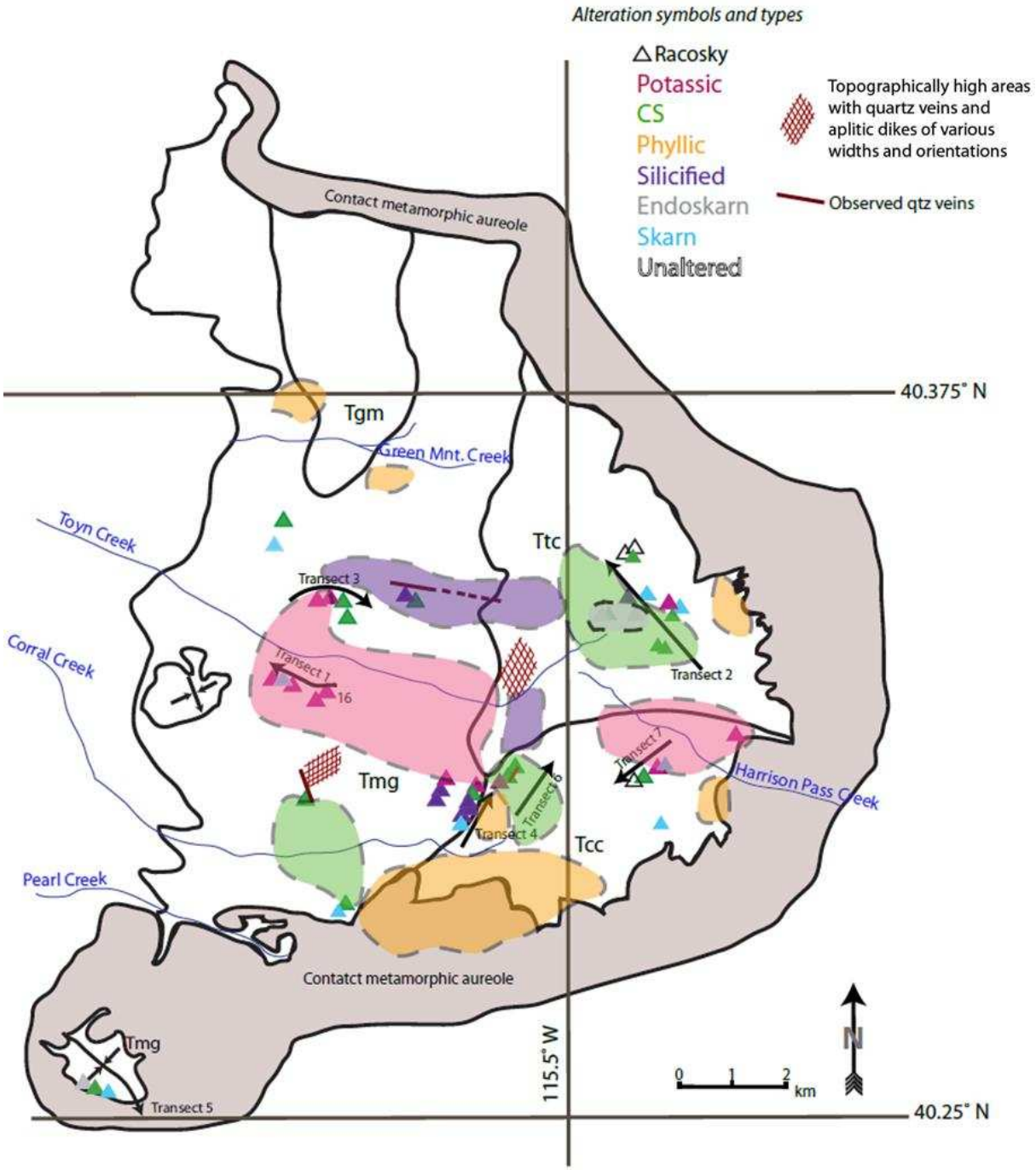

Figure 11: Interpretaion of the alteration geometries within the HPP. Data from both Gates (2016) and Musekamp (2011) was used to interpret the silicified and phyllically altered zones. Positions of the alteration types are slightly distorted to enhance readability within the dense clusters of data. HPP map adapted from Burton (1997) and Barnes et al. (2001).

4.2.1 Summary of petrographic observation

The petrographic descriptions below are summarized by intrusion unit and alteration type. For complete petrographic descriptions, see appendix 1.

Ttc

Petrographic analyses of the unaltered samples within the Ttc correlate with observations made by Barnes et al. (2001). Samples are generally coarse grained, hypidiomorphic, and contain large alkali-feldspar phenocrysts. Biotite is the predominant mafic mineral, however the more mafic samples contain hornblende.

CS altered samples on average consist of quartz (45%), plagioclase (40%), chlorite (10%), sericite (2%), ±hornblende (2%), and ±epidote (1%). All CS altered samples show the typical addition of chlorite and sericite. The only sample determined potassically altered by hand sample in the Ttc unit, contains intergrown K-feldspar and quartz (70%), quartz (25%), plagioclase (5%), and accessory epidote—not typical of potassic alteration. The epidote rich sample, found in contact with CS and unaltered rocks, consists of plagioclase (65%), epidote (20%), quartz (7%), chlorite (7%), and hornblende (1%).

Tcc

Unaltered samples of the Tcc are similar to Ttc samples described above in grain size and alkali-feldspar content, but differ in the presence of muscovite and the lack of hornblende. The potassic altered samples in the Tcc unit generally contain quartz (40%), plagioclase (35%), myrmekite (10%), biotite (8%), and microcline (2%). CS samples consist of plagioclase (45%), feldspar (25%), quartz (20%), chlorite (7%), sericite (2%), and biotite (1%), with minor hornblende, opaques, and apatite.

Tmg

Unaltered Tmg samples range from coarse to fine grained, with aplitic to pegmatitic textures, and generally contain plagioclase, alkali-feldspar, quartz, biotite and muscovite. Petrographic analysis confirms sample 76, in the field identified as greisen altered, as unaltered. Potassically altered samples contain quartz (35-45%)+ plagioclase (35-40%)+ K-feldspar (20-15%)+biotite (2-5%), with accessory minerals magnetite, muscovite, epidote and rutile. Some potassic samples in the Tmg contain up to ~20% myrmekite. The CS altered samples generally consist of plagioclase (40%), quartz (35%), biotite (15%), sericite (7%), chlorite (3%), with accessory epidote and minor apatite. Silicified samples consist of quartz (55%), plagioclase (40%), sericite (4%), and relict biotite (<1%), and minor apatite. All silicified samples contain two generations of quartz: magmatic quartz (medium to coarse grained and subhedral), and secondary quartz (fine to medium grained, euhedral to subhedral). The endoskarn sample in the Tmg unit consists of plagioclase (45%), calcite (27%), chlorite (15%), muscovite (7%), quartz (5%), biotite (1%), with minor rutile, apatite, and opaques.

4.3 Petrology and geochemistry of the HPP

Whole rock geochemical data of both unaltered and altered samples from three major granitic pulses of the HPP (Ttc, Tcc, and Tmg) obtained here are similar to data from Barnes et al. (2001) (Appendix 2, table 2 and 3). Weight percent SiO_2 ranges 58%-79% in the hornblende-biotite granodiorite to monzogranite unit (Ttc), and ranges 68%-77% in the biotite monzogranite units (Tcc and Tmg). On average the mafic end member (Ttc) has lower concentrations of SiO_2 and K_2O, and higher concentrations of Al_2O_3, CaO, MgO, Fe_2O_3, and REEs. Harker and spider diagrams are used below to initially compare data collected by Barnes et al. (2001) and that by the author and to identify patterns that may be related to alteration. Boundaries of the major granitic pulses and sheets depicted by the Barnes et al. (2001) map, are assumed throughout the data section.

4.3.1 Harker diagrams

Data collected from the three main phases, was used to compare with Harker diagrams published in Barnes et al. (2001) (Figure 12). In general, most of the data in this study clusters around the average trend line from Barnes's et al. (2001) data, but displays some minor variance. There are however, obvious outliers in the Ttc and Tmg samples, circled in figure 12. One Ttc sample plots high in SiO_2, and low in Na_2O, Al_2O_3, P_2O_5, and CaO concentrations. The other anomalous Ttc samples plot higher in Na_2O, and below typical P_2O_5 and CaO. One Tmg sample consistently has lower SiO_2, and either relatively higher or lower concentrations of Na_2O, Al_2O_3, P_2O_5, and CaO. Other Tmg samples plot distinguishably higher in Al_2O_3 and P_2O_5, than other Tmg samples.

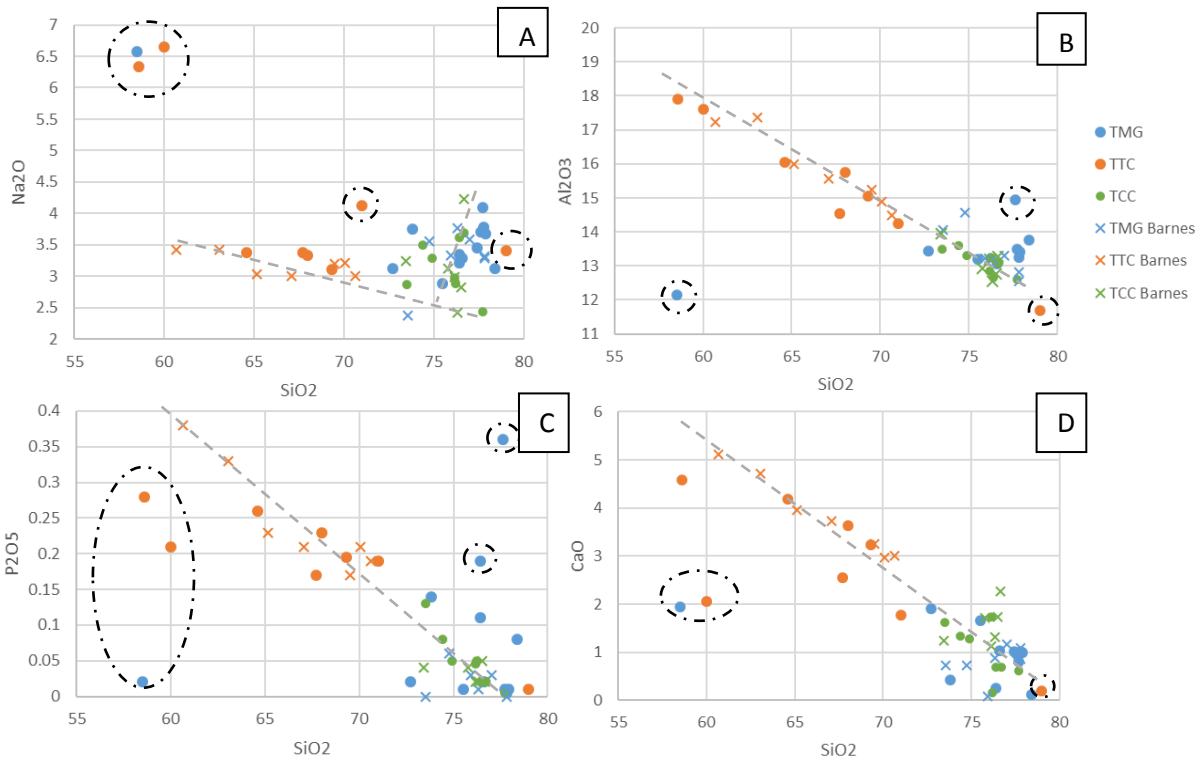

Figure 12: Harker diagrams plotted along with data from Barnes et al. (2001). Trend lines are drawn based on data from Barnes et al.. All data is in wt.% oxide. Circled anomalous points are discussed in the text.

4.3.2 Multi-element spider diagrams

Normalized multi-element data was plotted to present the evolution and petrologic variation between the three main intrusive units (Figures 13-15). In each unit, one to two major patterns, with various outliers are present. All units display, enrichment towards the least compatible elements, and depletion towards the most compatible immobile elements.

In the Ttc unit, Th, Rb, Ba comprise the highest normalized values, while TiO_2, Nb and Ta display a slight negative anomaly (Figure 13). The only outlier (sample 43, collected near a limestone xenolith along transect 2), displays a negative Ba anomaly, a stronger negative P_2O_5 trough, and in comparison, is significantly depleted in many HFSE's.

Within the Tcc, the largest enrichments occur in Rb and Th, which bound the negative Ba anomaly situated in-between (Figure 14). Noticeable negative anomalies are also present in P_2O_5 and TiO_2, while positive anomalies occur in Ce and Hf. Two outliers are present in the Tcc data. Sample 18 exhibits the largest negative P_2O_5 anomaly (< 0.1), while sample 6 displays the largest negative Ba anomaly (normalized concentration < 1), and is the only sample depleted in Sr.

The Tmg unit is more variable than the previous units—Sr, P_2O_5, Sm, Zr, Ce, and Hf are either depleted or enriched, while Ba enrichment varies greatly from 1 to >100 (Figure 15). TiO_2 displays two distinct sets of patterns, with one set depleted more than the other. These differences highlight the two distinct patterns: 1.) samples 68, 69, and 33, and 2.) the remaining samples.

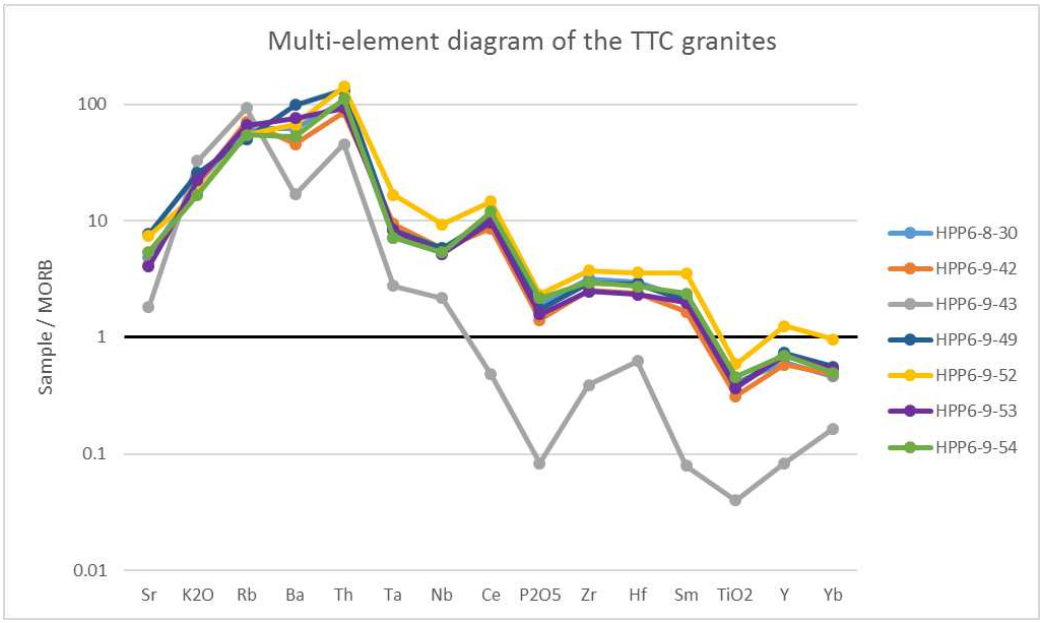

Figure 13: Multi-element diagram of all Ttc (hornblende-biotite granodiorite) samples collected within the HPP. All data normalized to MORB (Pearce, 1983). Immobile elements are situated to the right of the graph and increase in incompatibility right to left (Sr to Ba), while mobile elements placed on the left side of the graph increase in incompaibility from left to right (Yb to Th).

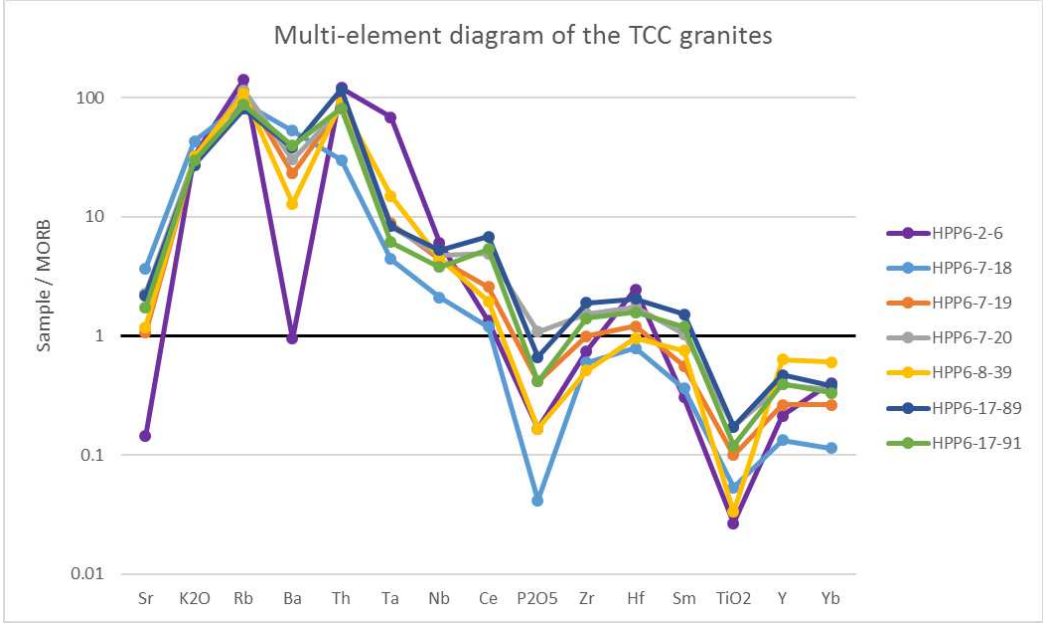

Figure 14: Multi-element diagram of all Tcc (biotite monzogranite) samples collected within the HPP.

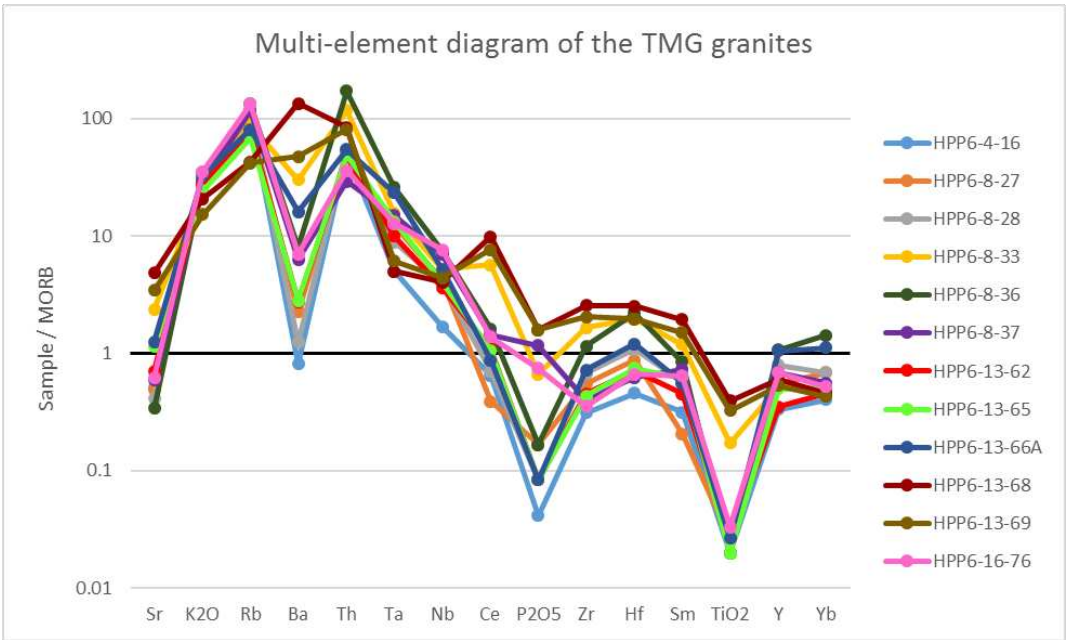

Figure 15: Multi-element diagram of all Tmg (biotite and two mica monzogranite) samples collected within the HPP.

4.3.3 REE diagrams

REE diagrams of each intrusive unit were plotted using data collected in this study, and then were overlaid with the respective range of REE data from Barnes et al. (2001). Within the Ttc unit, excluding sample 43, all samples cluster together and exhibit the same gentle negative slope (Figure 16). The outlier—sample 43—is relatively depleted in REEs, displays a flatter slope, and contains a positive Eu anomaly. The pattern of the Barnes et al. overlay matches well with data from this study.

Three trends are distinguishable within the Tcc data: 1.) gentle, relatively smooth negative slope (samples 19, 20, 89, and 91), 2.) flatter, negative slope with a negative Eu anomaly (samples 6 and 39), and 3.) a negative slope with a positive Eu anomaly (sample 18) (Figure 17). Barnes's et al. (2001) data overlays most of the Tcc range, however samples 6 and 18 do not fit within the trend. The outliers differ in anomaly patterns and contain lower REE concentrations.

Tmg samples also display 3 major patterns: 1.) steep, smooth, negative slope (samples 30, 33, 68, and 69), 2.) flatter, negative slopes with negative Eu anomalies, and 3.) flatter slopes, with positive trend through the HREE data (samples 16 and 27) (Figure 18). Barnes's et al. (2001) overlay only parallels the Tmg pattern with the negative Eu anomaly, and does not encompass the entire data range.

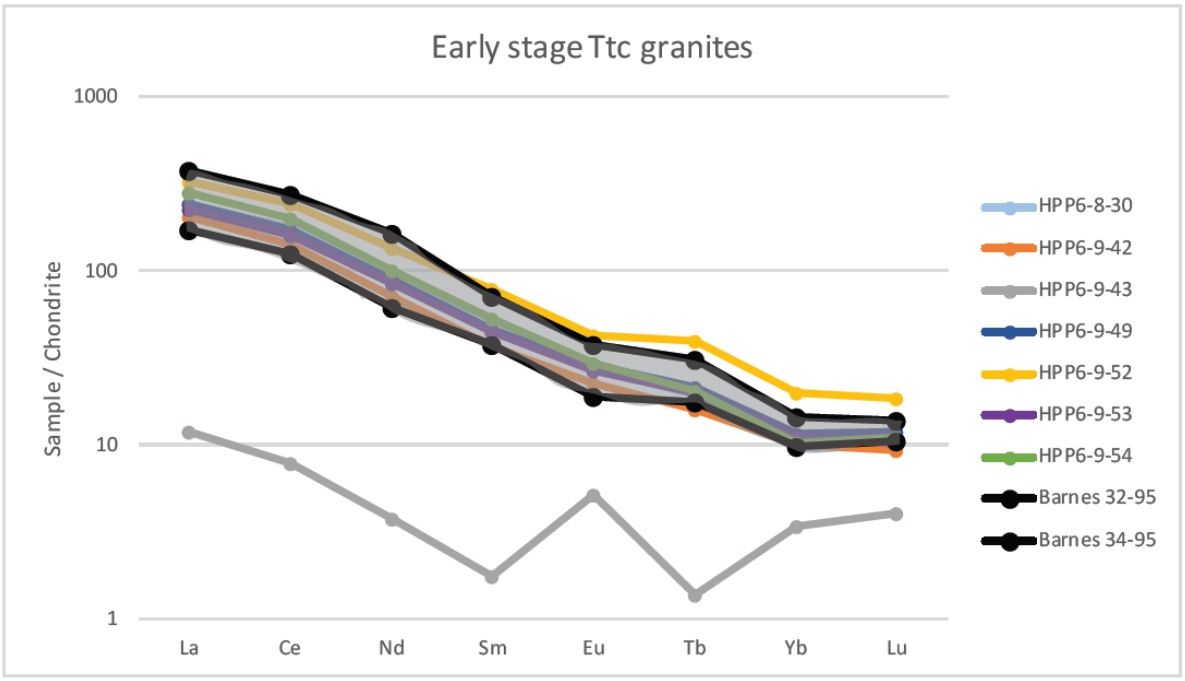

Figure 16: REE diagram of all Ttc (hornblende-biotite granodiorite) samples collected within the HPP. All samples are normalized to chondritic meteorites from Anders and Grevesse (1989). The range of Barnes et al.'s Ttc 2001 data, in black, was overlaid to compare to the results of this study.

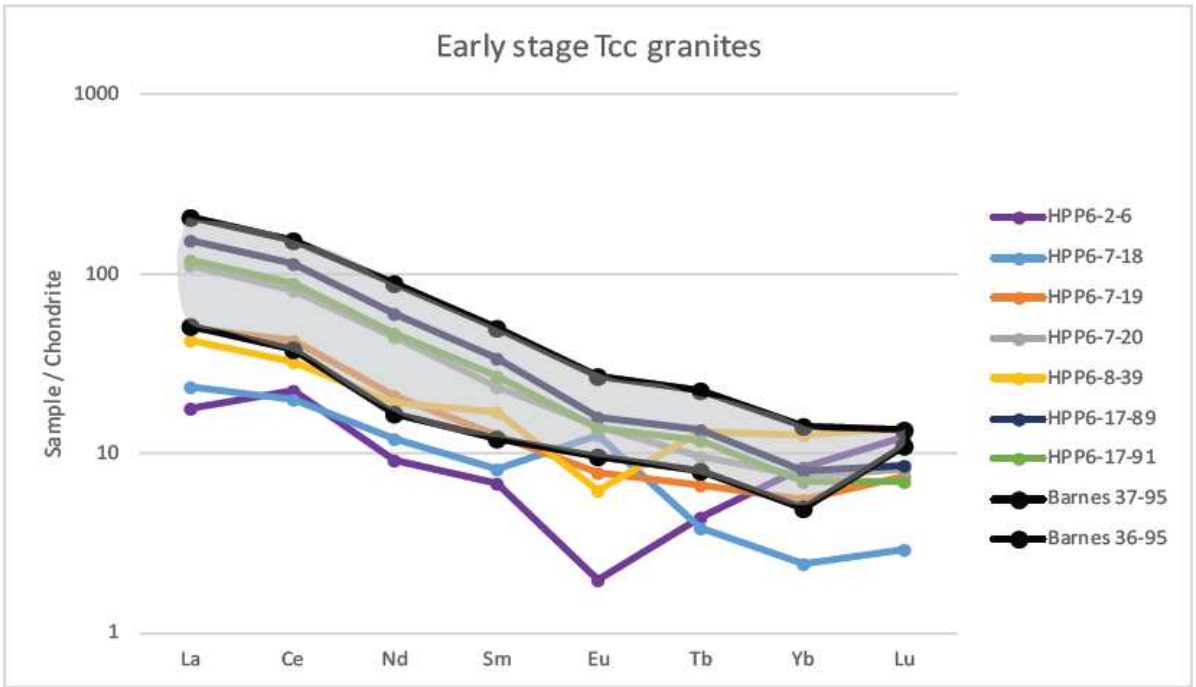

Figure 17: REE diagram of all Tcc (biotite monzogranite) samples collected within the HPP. The range of Barnes et al.'s Tcc 2001 data, in black, was overlaid to compare to the results of this study.

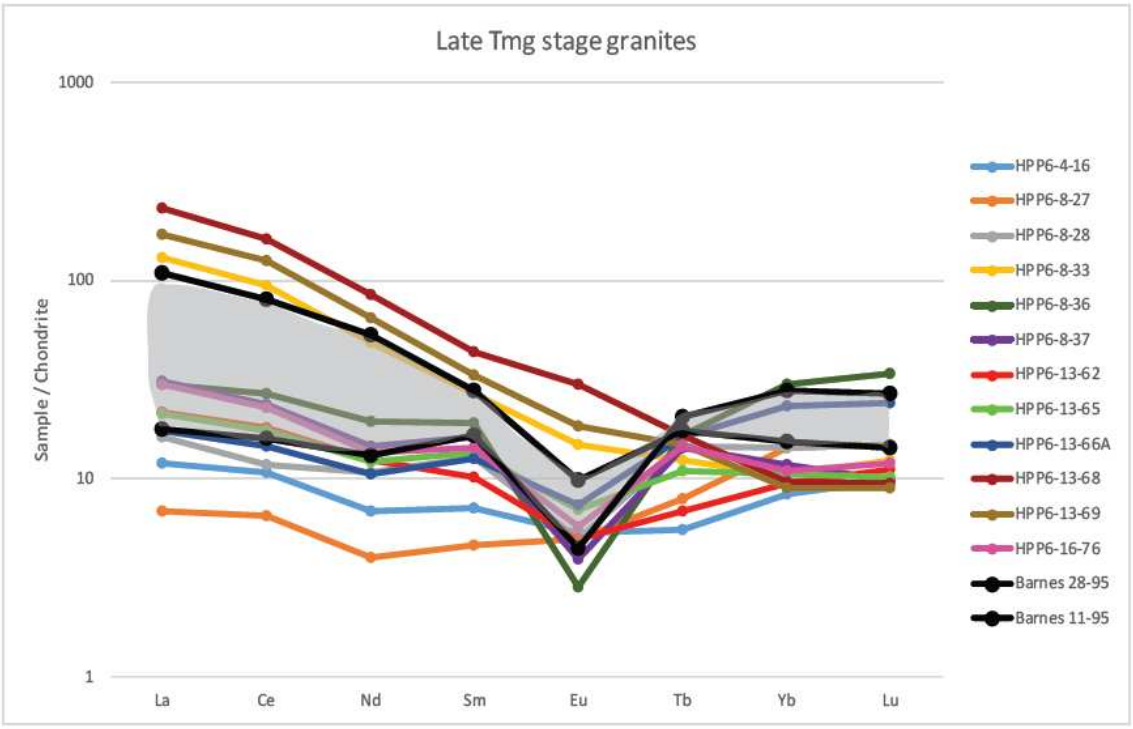

Figure 18: REE diagram of all Tmg (biotite and two mica monzogranite) samples collected within the HPP. The range of Barnes et al.'s Tmg 2001 data, in black, was overlaid to compare to the results of this study.

4.3.4 Trace metals

Trace metal data from unaltered rocks of the three main intrusive suites, were plotted together to model magmatic evolution, and are listed in the key in order from oldest to youngest unit (Figure 19). Co, Ni, Sc, and Zn acted compatibly during magmatic evolution, concentrations of which decrease in the more evolved magmas. Pb and Cu acted incompatibly and are most concentrated in the later magmas. Trace elements such as Ag Cd and Tl, are commonly below the detection limit throughout the study.

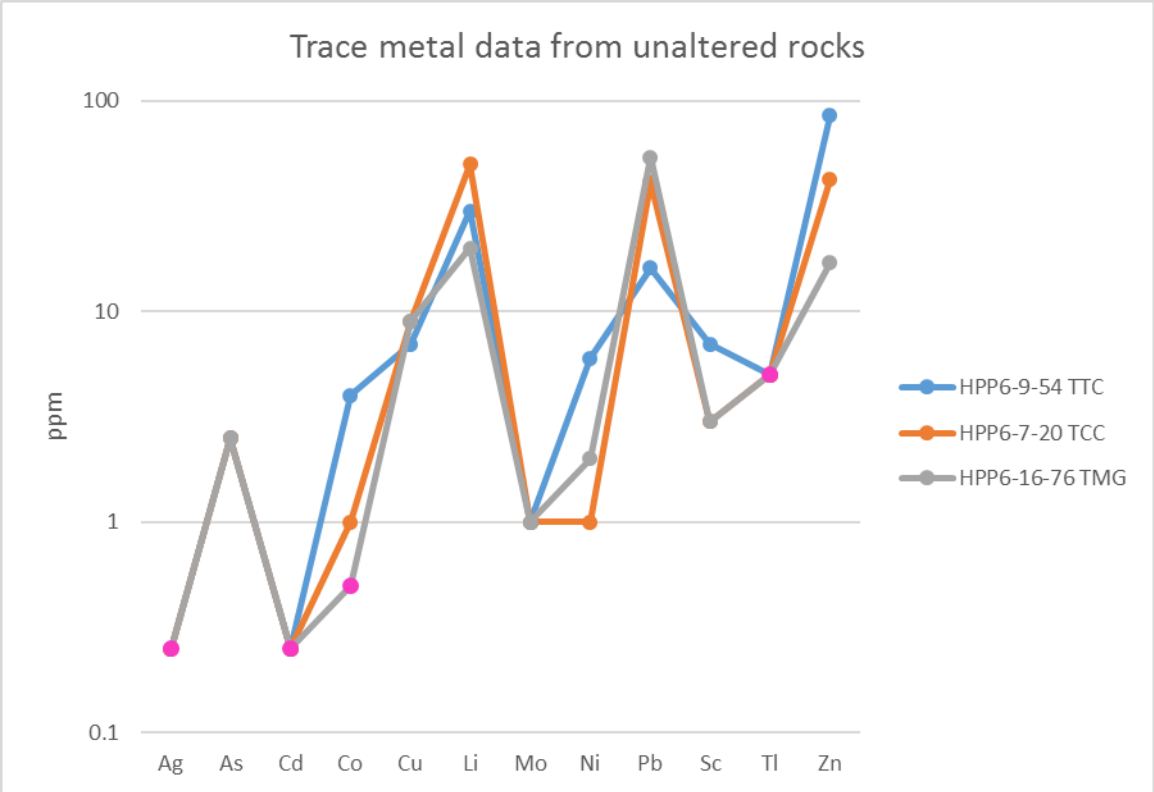

Figure 19: Trace metal concentrations in unaltered samples from the Ttc, Tcc, and Tmg units. Pink data points represent trace metals reported as below the detection limit, these points are as plotted half the detection limit.

4.4 Whole rock geochemistry of the alteration types in the HPP

4.4.1 Pearce element-ratio plots

Numerous Pearce element-ratio plots were made as a precursor to identifying mobile elements and to confirm the different alteration types, previously defined by petrographic analysis. Unaltered samples from Barnes et al. (2001), were added to the plot to better define magmatic trends. The three plots in figure 20 are illustrated here as they best represent the data. Alteration types are clearly differentiated and plot in clusters (Figure 20). Endoskarn alteration always plots highest in Al_2O_3 concentrations. Potassic and CS altered samples plot near each other but in distinct separate clusters— with CS samples higher in Fe_2O_3 and Sr. And finally, silicified samples always plot lowest in Al_2O_3 concentrations, and near the potassically altered samples.

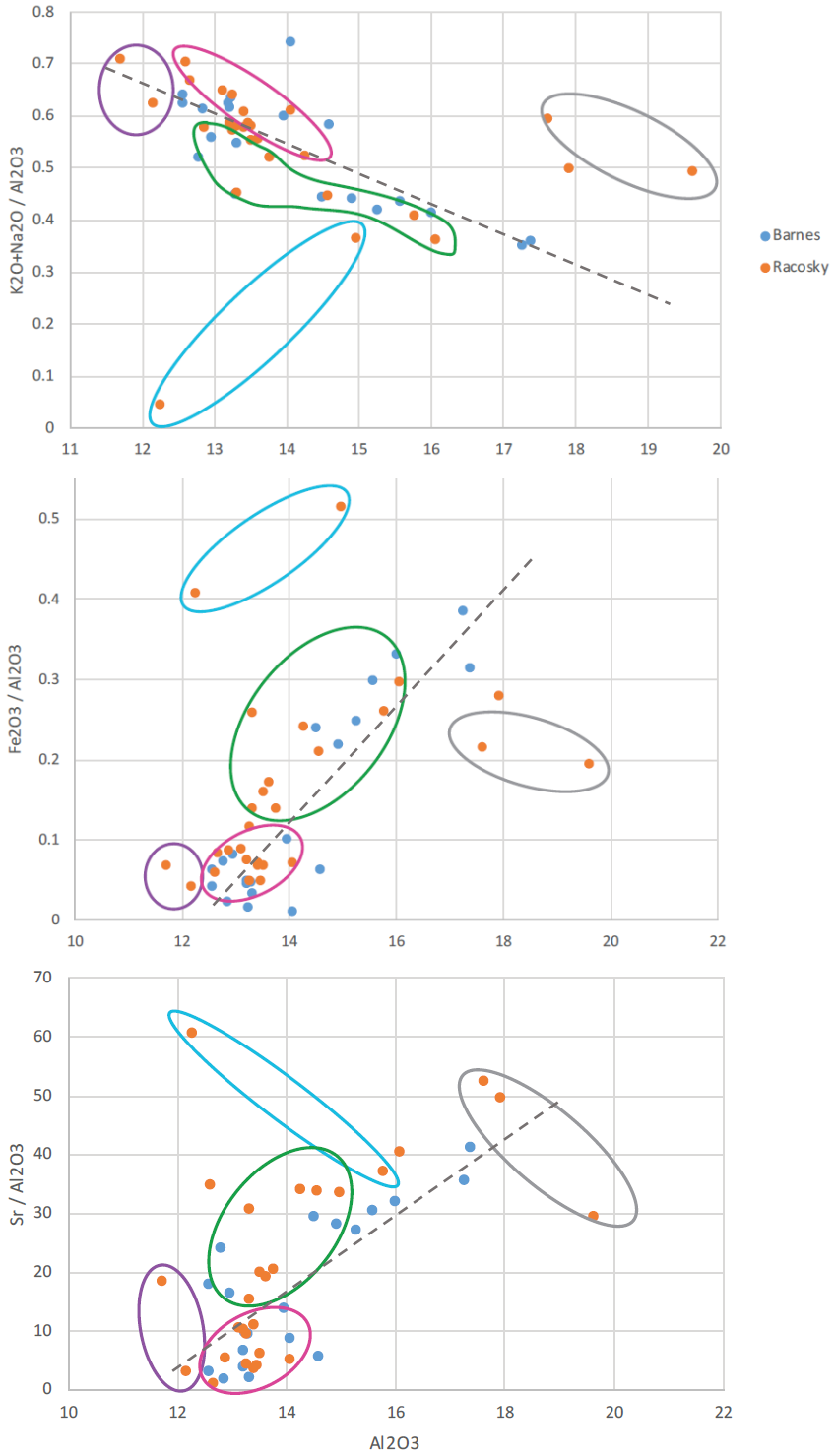

Figure 20: Pearce element-ratio diagrams, plotted along with data from Barnes et al. (2001). Trend line represents the trend of Barnes's et al. (2001) data. Alteration types are cricled to emphasize clusterings. Pink= potassic alteration, green=CS, purple=silicification, grey= endo-skarn, blue=exo-skarn

4.4.2 Geochemical results for mass-balance of alteration

To quantify the intensity of alteration and determine if the geochemistry of the alteration types were affected by the multiphase system of the HPP, mass-balance of alteration was calculated for the major oxide and trace element data (mass balance data in Appendix 2, Table 4). Each sample was normalized to an average of un-altered samples of the same unit from Barnes et al. (2001)(Unaltered data in Appendix 2, Table 3). Because exo-skarn data could not be compared to the unaltered HPP granite, data was plotted on multi-element spider diagrams. This spider diagram was normalized using MORB data from Pearce (1983) due to the lack of carbonate normalization data in literature. In addition, trace metals and REE concentrations (normalized using Anders and Grevesse (1989)) were plotted on spider diagrams. All data is differentiated according to alteration type and intrusion unit. Not all alteration types were recognized in each intrusive unit.

Potassic

Major oxides and trace elements

Mass balance varies in the potassically altered samples, and includes one major outlier (sample 43) (Figure 21). Sample 43 may have had a contrasting original composition, but will still be considered. Excluding outlier sample 43, gain-loss values vary moderately in SiO_2, K_2O, Fe_2O_3, MgO, CaO, and Na_2O.

When samples are differentiated based on unit, potassically altered samples collected in the Tmg unit display more consistent patterns (Figure 22). All K- altered samples in the Tmg are enriched in Fe_2O_3, while the concentrations of CaO and K_2O in the Tmg unit vary less. However, outliers persist in samples collected close to a contact (i.e.

skarn or different granitic phase/unit), in MgO and CaO (66A and 33), and SiO_2 and Fe_2O_3 (sample 33). Potassically altered samples collected in the Tcc unit also display more consistent patterns (Figure 23). However, sample 18, collected adjacent to a skarn, is comparatively more enriched in K_2O and SiO_2 and depleted of Na_2O. Sample 43, the only potassically altered sample collected in the Ttc unit, differs significantly from the other potassically altered samples in the pluton (Figure 21).

Trace element data in the all the potassic samples display variable trends (Figure 24). Excluding outlier sample 43, large ranges in gain-loss trends exist in Ba (-171 to 896 ppm), Rb (-129 to 152 ppm), and Sr (-173 to 236 ppm), while smaller gain-loss ranges occur in Nb, V, Y, and Zr. When data was differentiated by intrusion type, trace elements in the Tmg samples display a very confined trend in data with variable trends in Ba, Sr, and Zr (Figure 25). Trace elements in the Tcc share similarities, but contain variations in Ba, and Sr (Figure 26).

REEs and Trace Metals

Normalized concentrations of REEs for all potassically altered samples lack consistent patterns, with some slopes steep, others gentle (Figure 27). Eu anomalies are either slightly negative, strongly negative, or strongly positive. When data is differentiated by intrusion type, some patterns appear. The Tmg potassic altered samples consist of one major trend along with three outliers (samples 16, 27, and 33) (Figure 28). Generally, the Tmg data plots as gentle negative slopes with variably large negative Eu anomalies. The two outliers 27 and 16, do not share the negative Eu anomaly, while the remaining outlier (sample 33) displays a comparatively steeper slope and small negative Eu anomaly. Altered REE data correlated moderately well with unaltered data, except for samples 16, 27, and

62, which fall below typical unaltered Tmg ranges. REE data from the Tcc unit shows similar minor patterns between samples 39 and 6, however HREE patterns are variable (Figure 29). Sample 18 is the only potassically altered sample that displays a positive Eu anomaly. Altered Tcc data fits better within its corresponding unaltered REE ranges than the altered samples in the Tmg unit.

Trace metal contents in all the potassically altered samples are — minus a few outliers—very similar (Figure 30). Trace metal concentrations are low (~< 1 ppm) for: Ag, As, Cd. Co, Mo, and Ni. Higher Pb is apparent ~ 40 to 60 ppm. The Tmg potassically altered samples share the same trends (Figure 31). Compared to unaltered Tmg data, potassically altered Tmg samples contain higher concentrations of Co and Ni, and lower concentrations of Li. Potassic samples from the Tcc do not contain large concentrations of Zn or Li, but vary in Pb concentrations (20 to 60 ppm) (Figure 32). Zn concentrations are relatively lower, and Li and Sc higher in concentration compared to unaltered Tcc data.

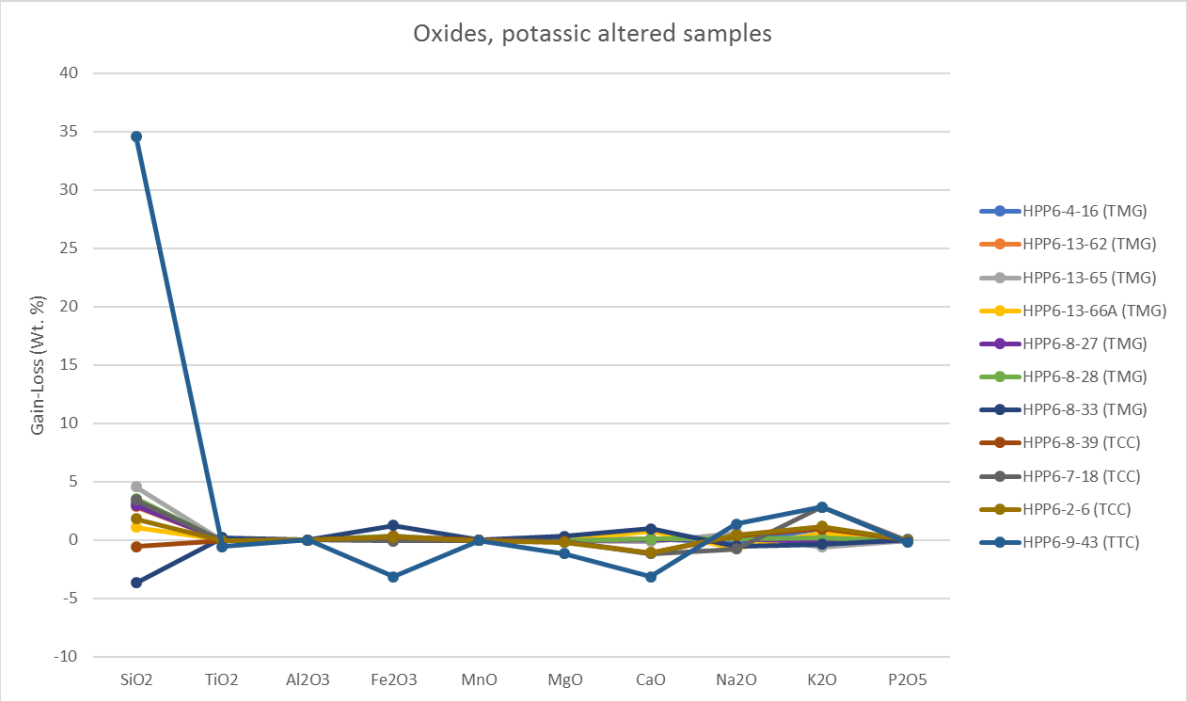

Figure 21: Mass balance alteration data of the oxides from potassically altered samples. Al_2O_3 used as immobile element for mass balance calculations.

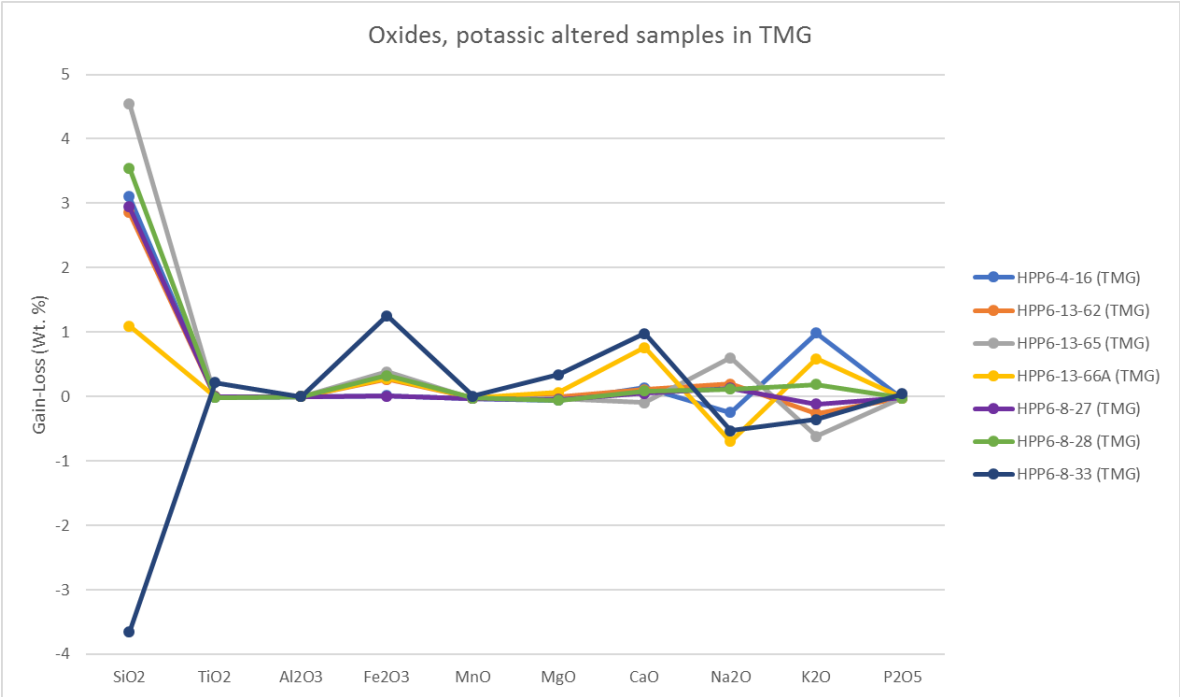

Figure 22: Mass balance alteration data of the oxides from Tmg potassically altered samples.

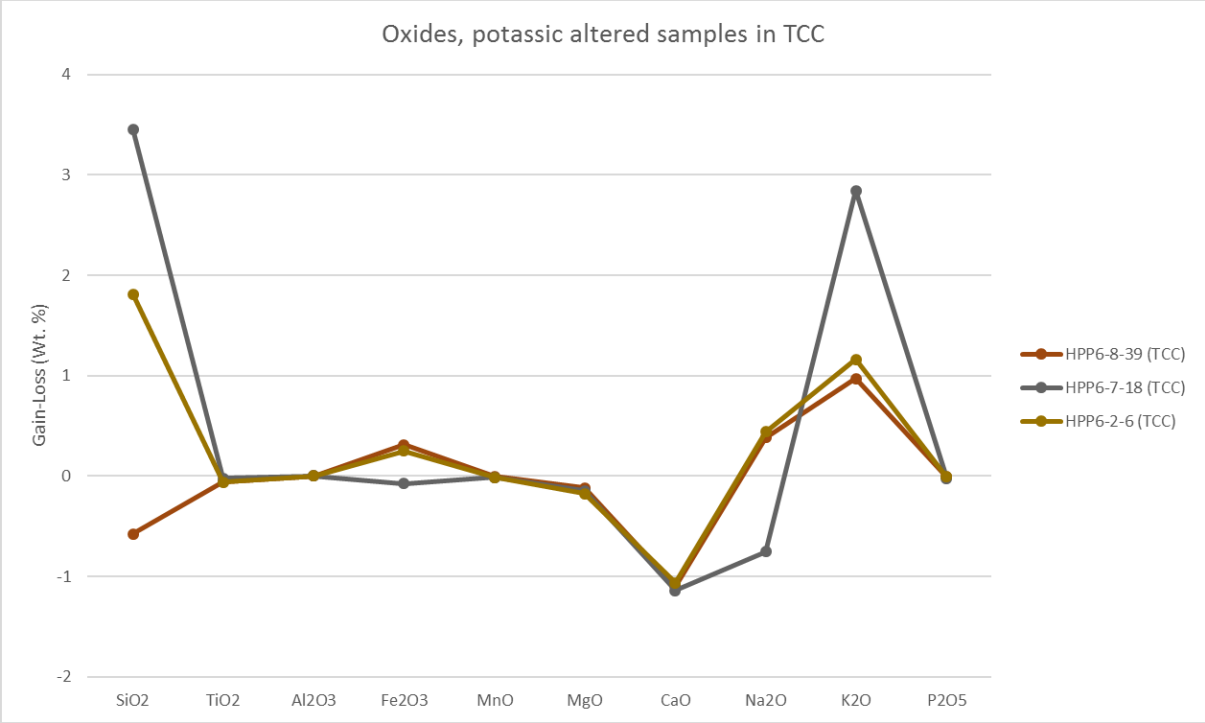

Figure 23: Mass balance alteration data of the oxides from Tcc potassically altered samples.

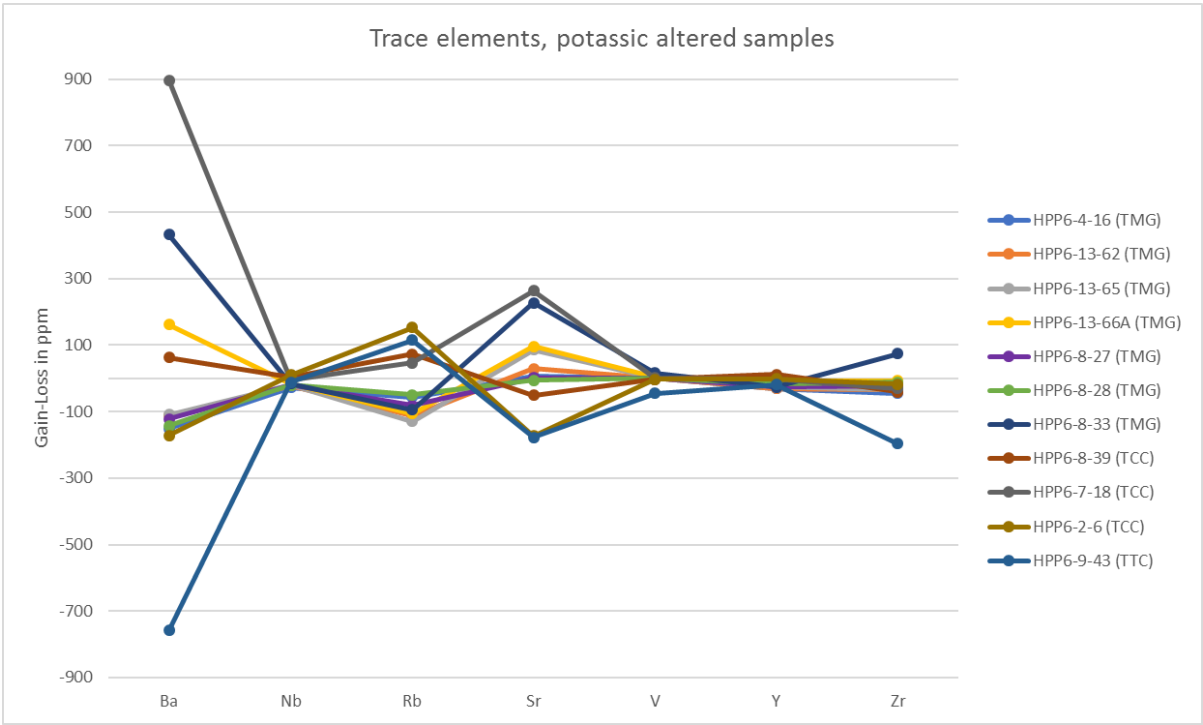

Figure 24: Mass balance alteration data of the trace elements from potassically altered samples.

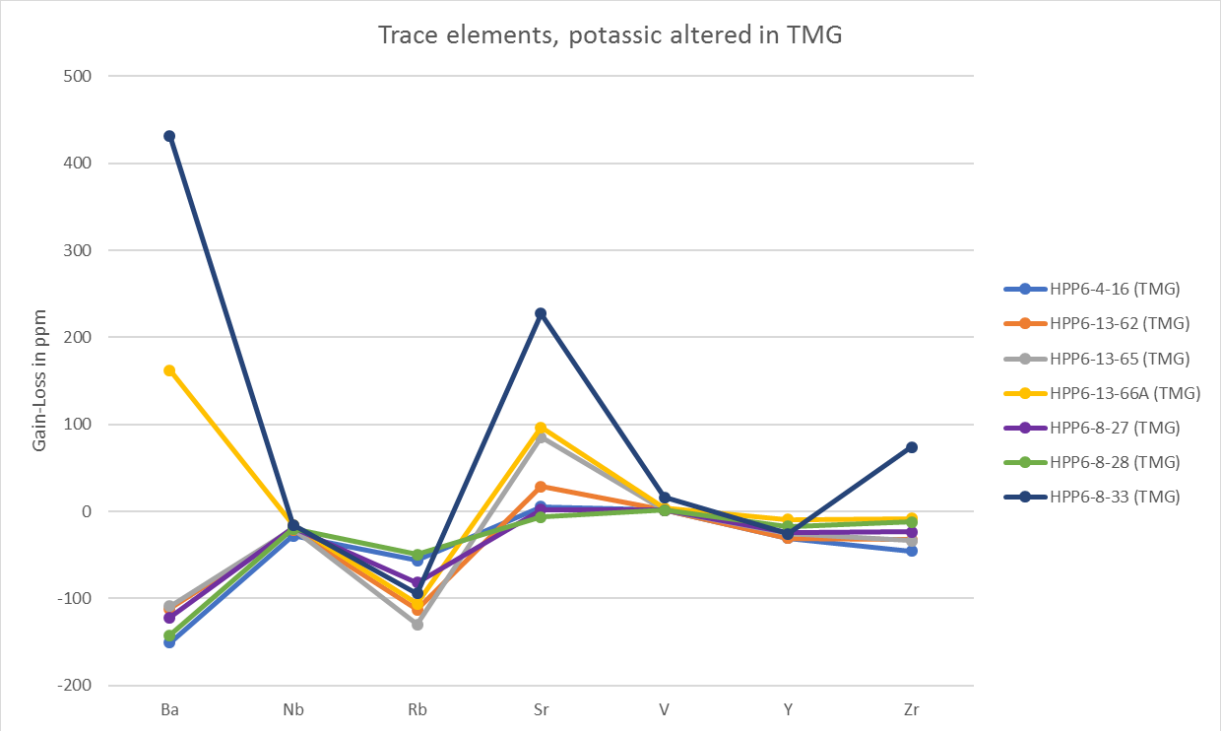

Figure 25: Mass balance alteration data of the trace elements from Tmg potassically altered samples.

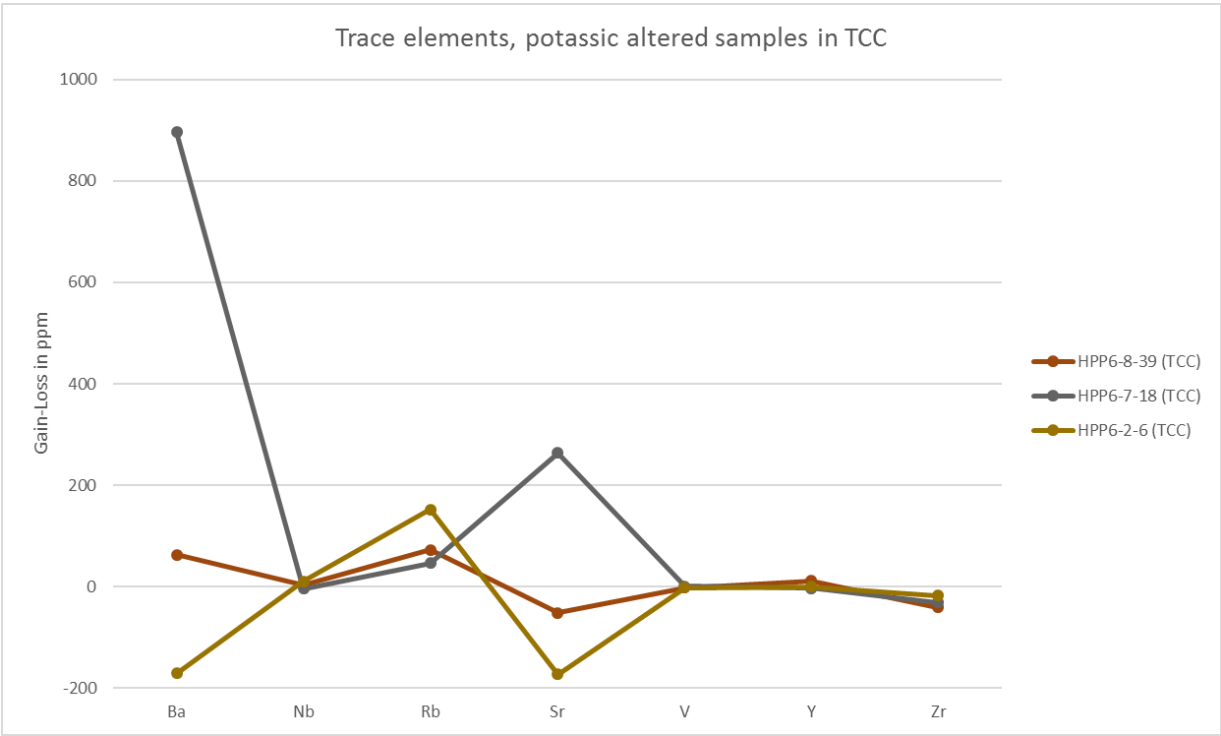

Figure 26: Mass balance alteration data of the trace elements from Tcc potassically altered samples.

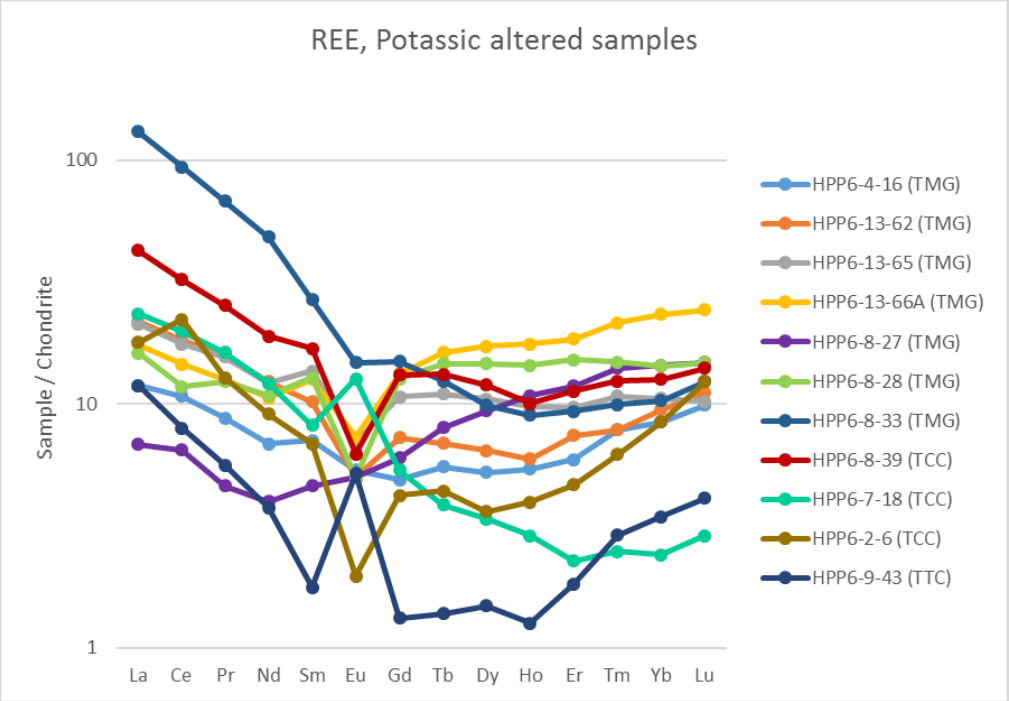

Figure 27: REE data of all the potassically altered samples. Note: sample 43 the sample did not petrographically show signs of potassic alteration. Samples are normalized to chondritic meteorites from Anders and Grevesse (1989).

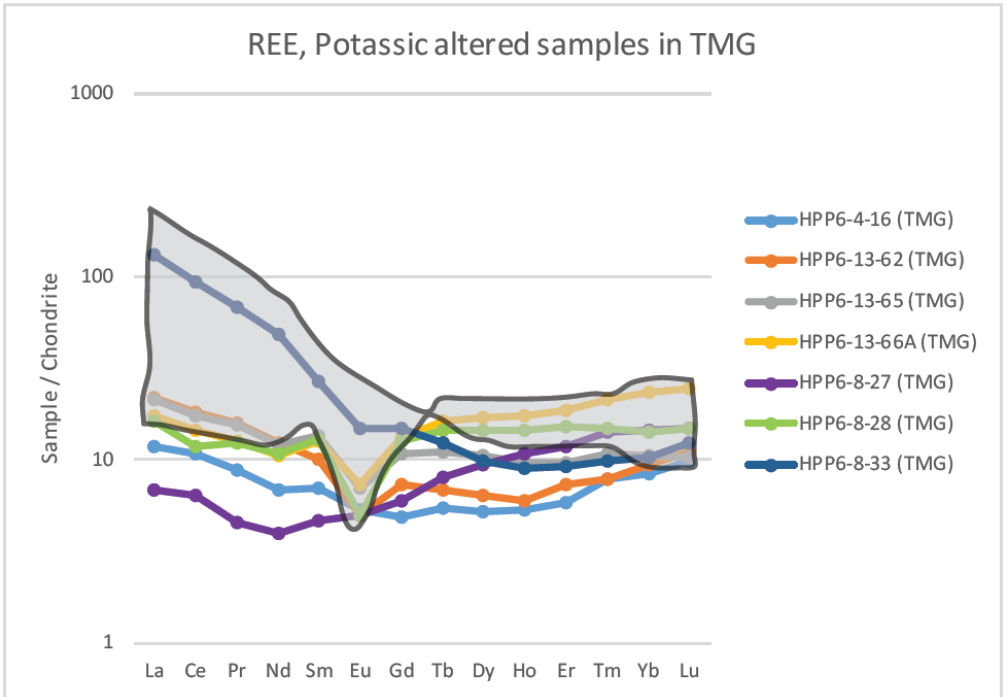

Figure 28: REE data of the Tmg potassically altered samples. Data overlaid by the range of REE data from this study and Barnes et al. (2001) Tmg samples. All samples are normalized to chondritic meteorites from Anders and Grevesse (1989).

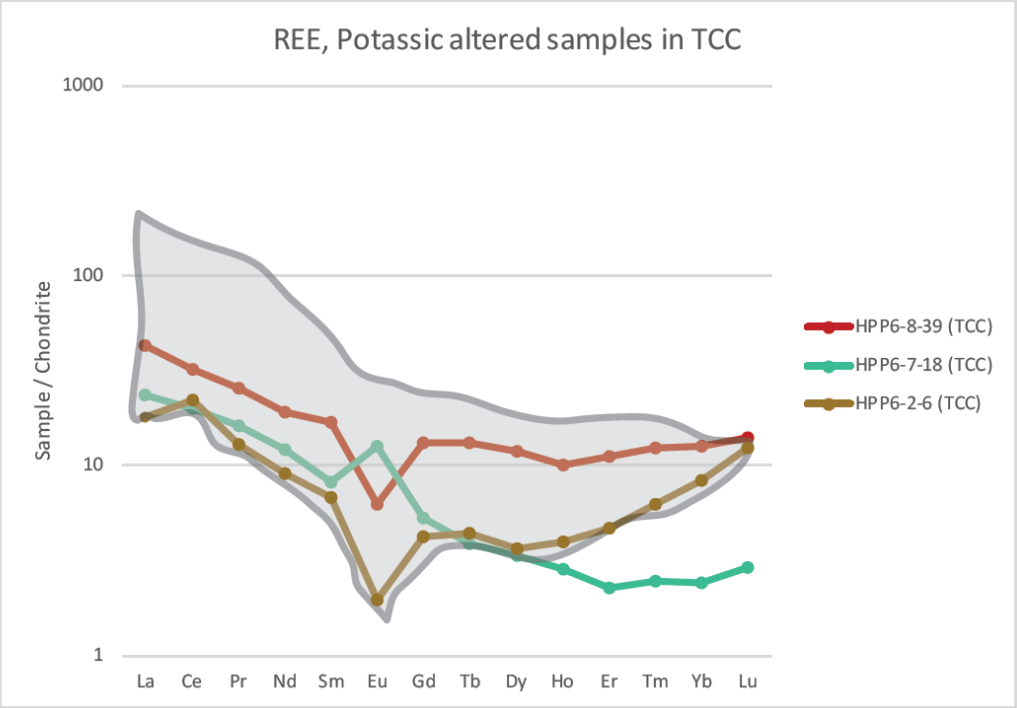

Figure 29: REE data of the Tcc potassically altered samples. Data overlaid by the range of REE data from this study and Barnes et al. (2001) Tcc samples. All samples are normalized to chondritic meteorites from Anders and Grevesse (1989).

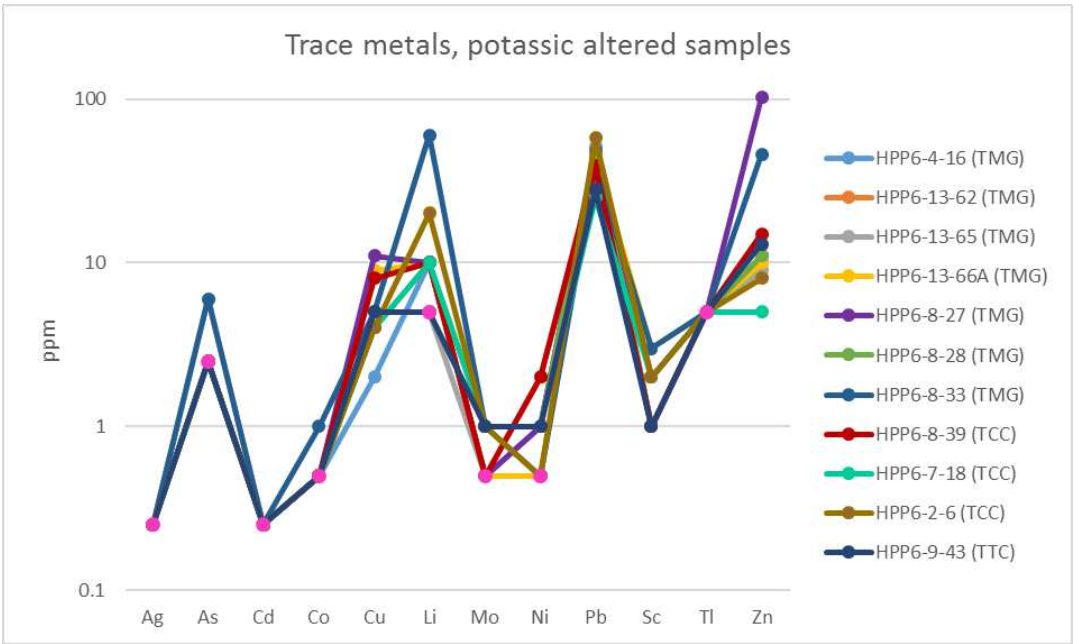

Figure 30: Trace metal data of all the potassically altered samples. Y-axis is in log scale. Figure 19: Trace metal concentrations in unaltered samples from the Ttc, Tcc, and Tmg units. Pink data points represent trace metals reported as below the detection limit, these points are as plotted half the detection limit.

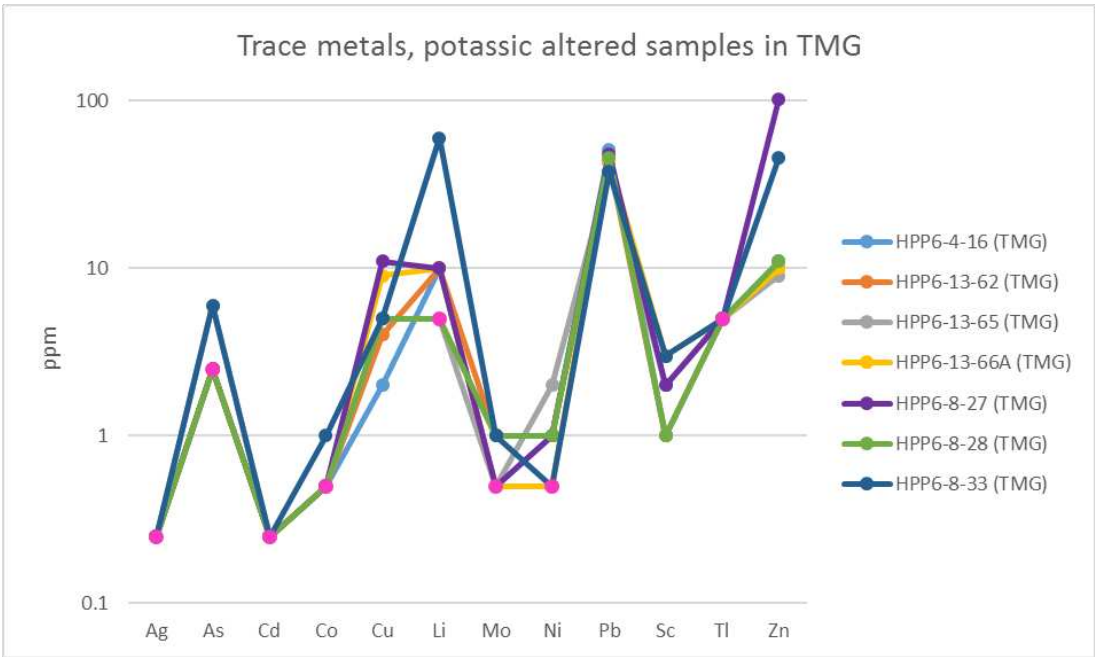

Figure 31: Trace metal data of the Tmg potassically altered samples. Y-axis is in log scale.

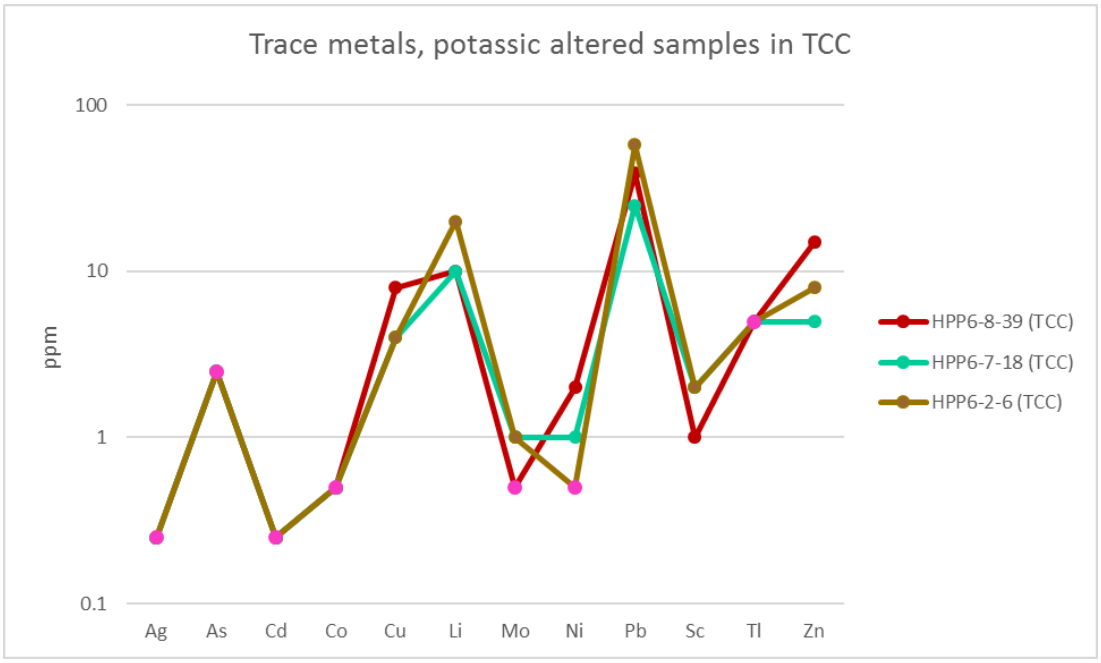

Figure 32: Trace metal data of the Tcc potassically altered samples. Y-axis is in log scale.

Chlorite-sericite

Major oxides and trace elements

Mass balance data vary in the CS altered samples when the different units are not separated out, and are equally as variable as the potassically altered data (Figure 33). Larger ranges in gain-loss values are noticeable in SiO_2 (-6 to 7.66 Wt. %) and Fe_2O_3 (-0.96 to 2.89), while the remaining oxides display smaller variations within the mass balance of alteration results. Ttc CS samples share relatively low ΔC_i —all gains and losses ~< 1.5 wt.%, except for SiO_2 (-2.4 to 7.6 Wt. %) (Figure 34). Excluding SiO_2 and CaO, the Tcc CS altered samples share similar gain/loss patterns (Figure 35). The only Tmg CS sample (69) plots as an outlier within the mass balance alteration results in oxides Fe_2O_3, and K_2O (Figure 33).

In contrast to the mass balance oxide data, and excluding outlier sample 69, all trace element data plots in a consistent trend. In general, Ba, Nb, Sr, V, Y, and Zr are enriched in various amounts. The Ttc CS samples all follow the same gain-loss trend, except for Ba (Figure 37). Gain-loss trends of the trace elements in the Tcc samples are similar in samples 89 and 91, and slightly differ in sample 19 (Figure 38). Sample 19, near a skarn contact, is notably more enriched in Rb, and less enriched of trace elements Ba and Sr. The remaining CS altered sample (69) was collected in the Tmg inlier unit adjacent to a skarn contact. This sample contains the most outliers within the sample suite, with a large enrichment of Ba, Sr, and Zr, and is heavily depleted in Rb (Figure 36).

REEs and Trace Metals

All CS samples display the same steep slope, small negative Eu anomaly, and contain similar REE concentrations (Figure 39). REE trends in the potassically altered samples, are widely variable in comparison to the tightly bounded CS data. Sample 19 is the only sample that noticeably contains smaller concentrations of REE. Trace metal concentrations are relatively similar in most of the CS samples, in comparison to the potassically altered samples, which display slightly more variable data (Figure 40). Li is noticeably higher in samples 30, 53, and 89, Ni concentrations are uncharacteristically high in sample 42, and Zn varies 25- 80 ppm. When data is differentiated by intrusion type, the concentration relations stay the same: very similar with a few outliers (Figures 41 and 42). Tcc CS altered samples contain lower concentrations of Li and Pb than un-altered Tcc sample 20.

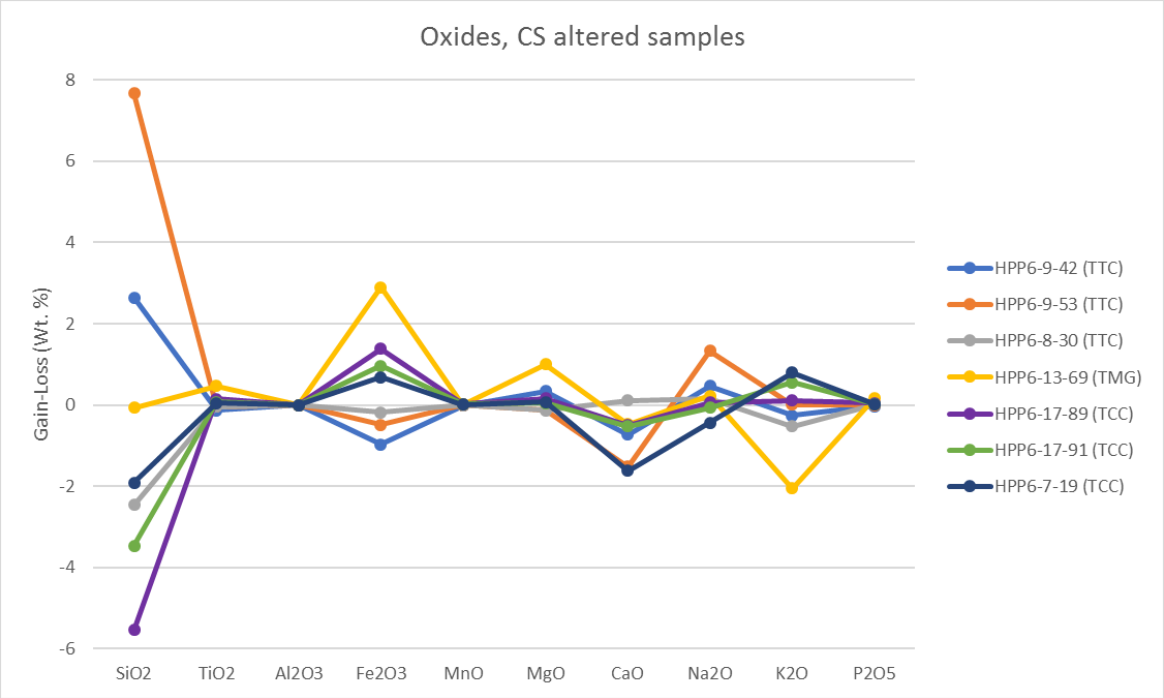

Figure 33: Mass balance alteration data of the oxides from all CS altered samples. Al_2O_3 used as immobile element for mass balance calculations.

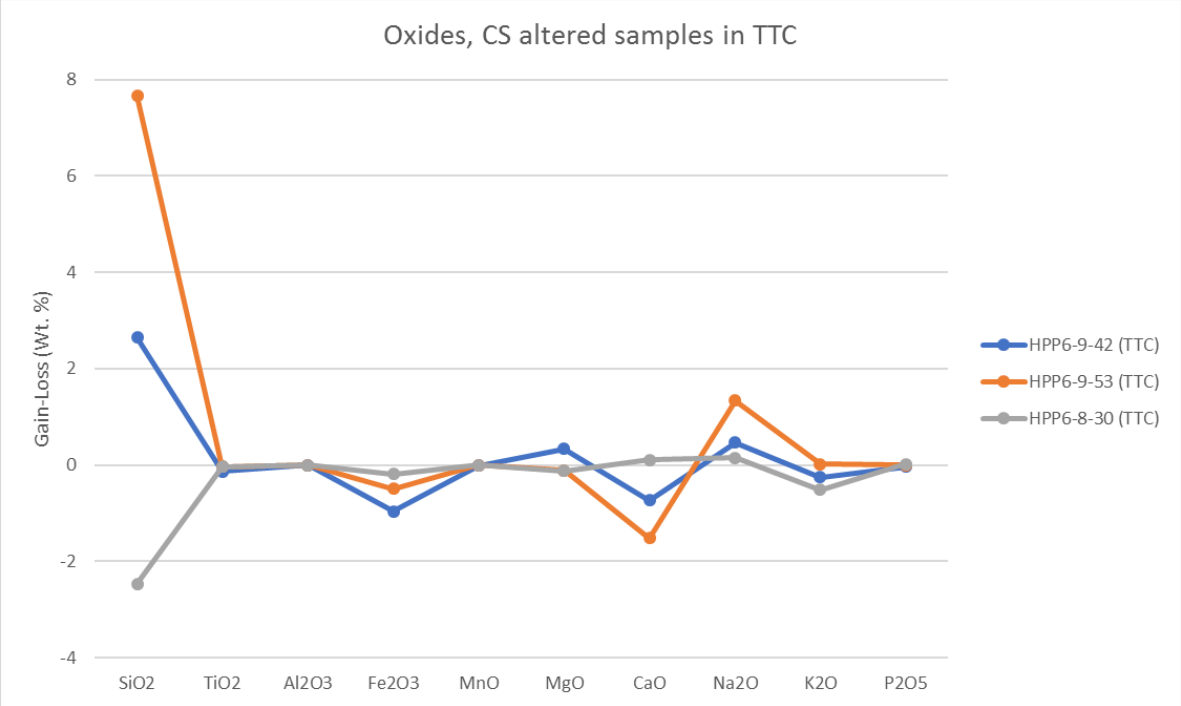

Figure 34: Mass balance alteration data of the oxides from Ttc CS altered samples.

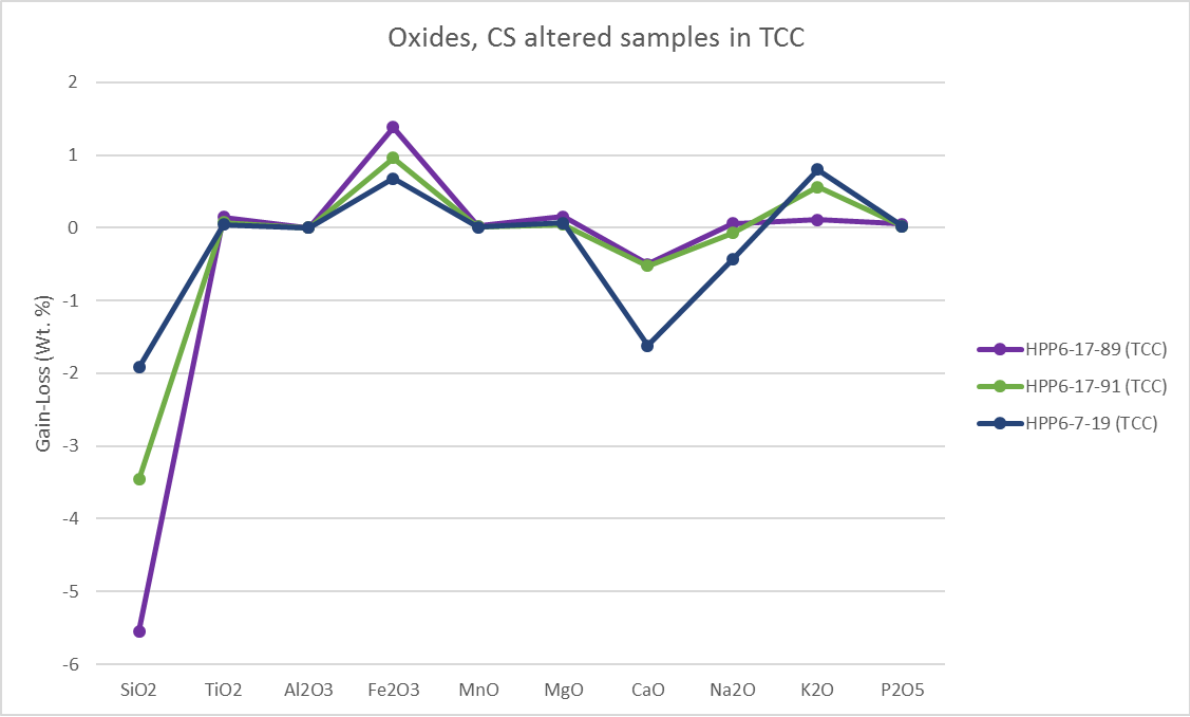

Figure 35: Mass balance alteration data of the oxides from Tcc CS altered samples.

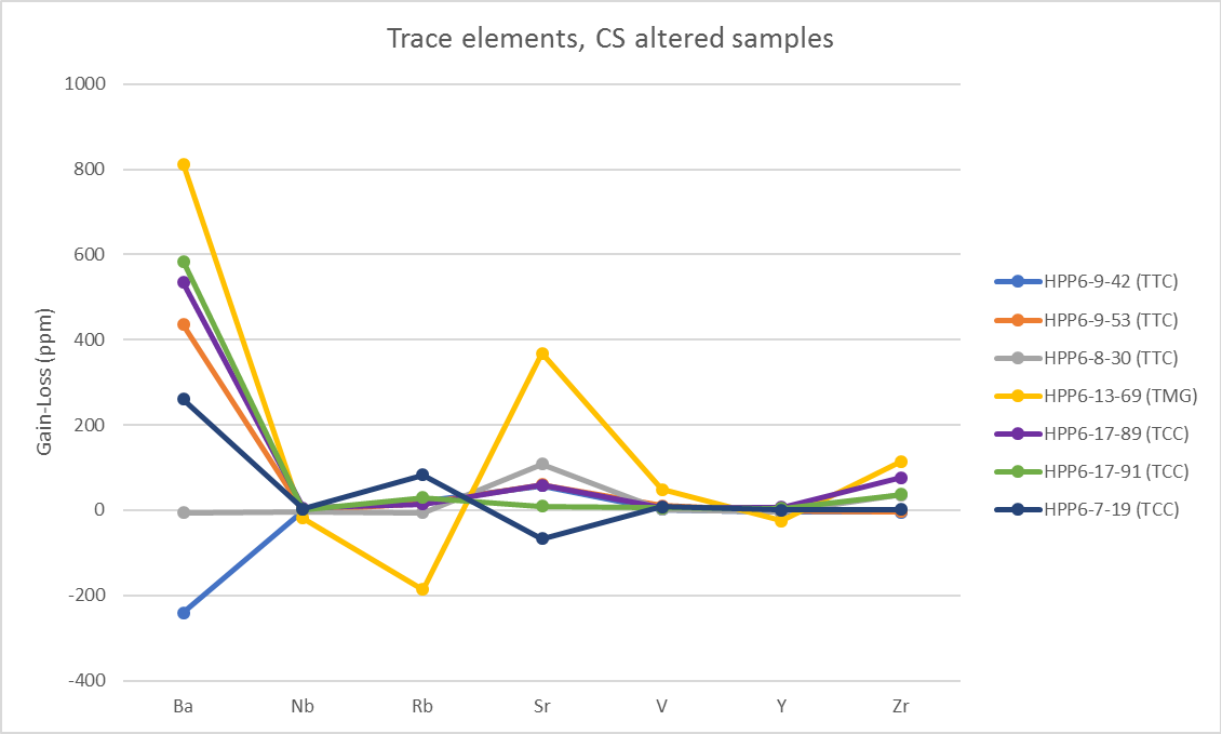

Figure 36: Mass balance alteration data of the trace elements from all CS altered samples.

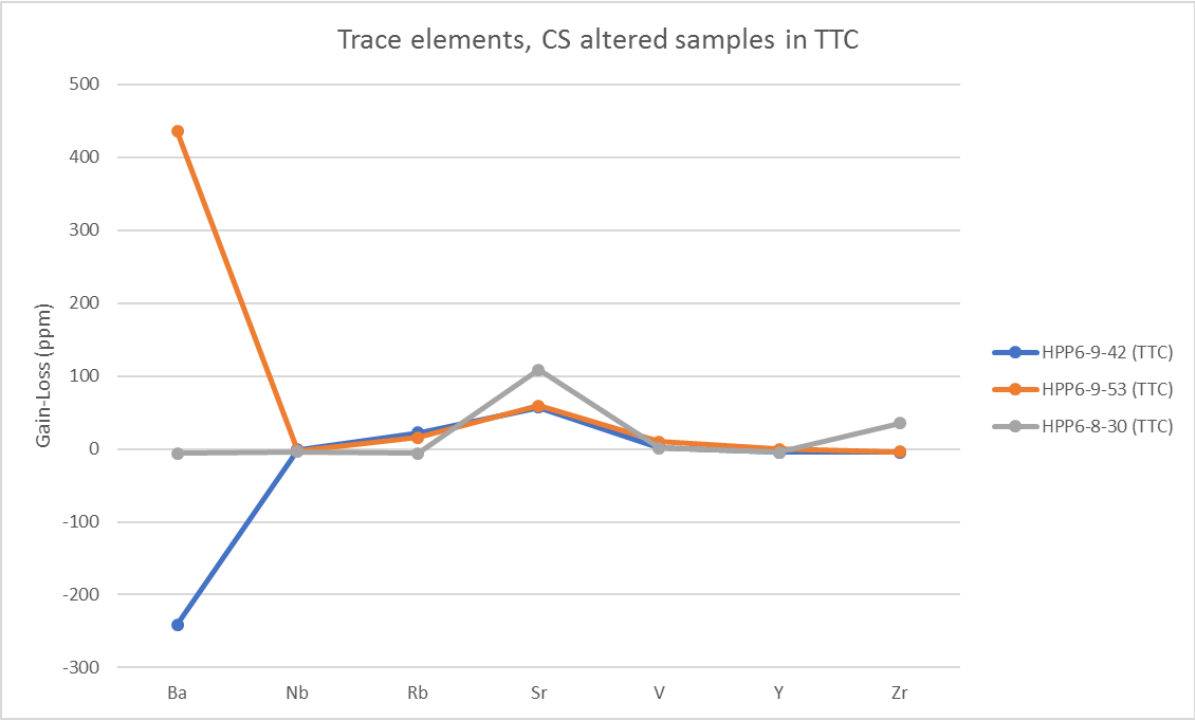

Figure 37: Mass balance alteration data of the trace elements from Ttc CS altered samples.

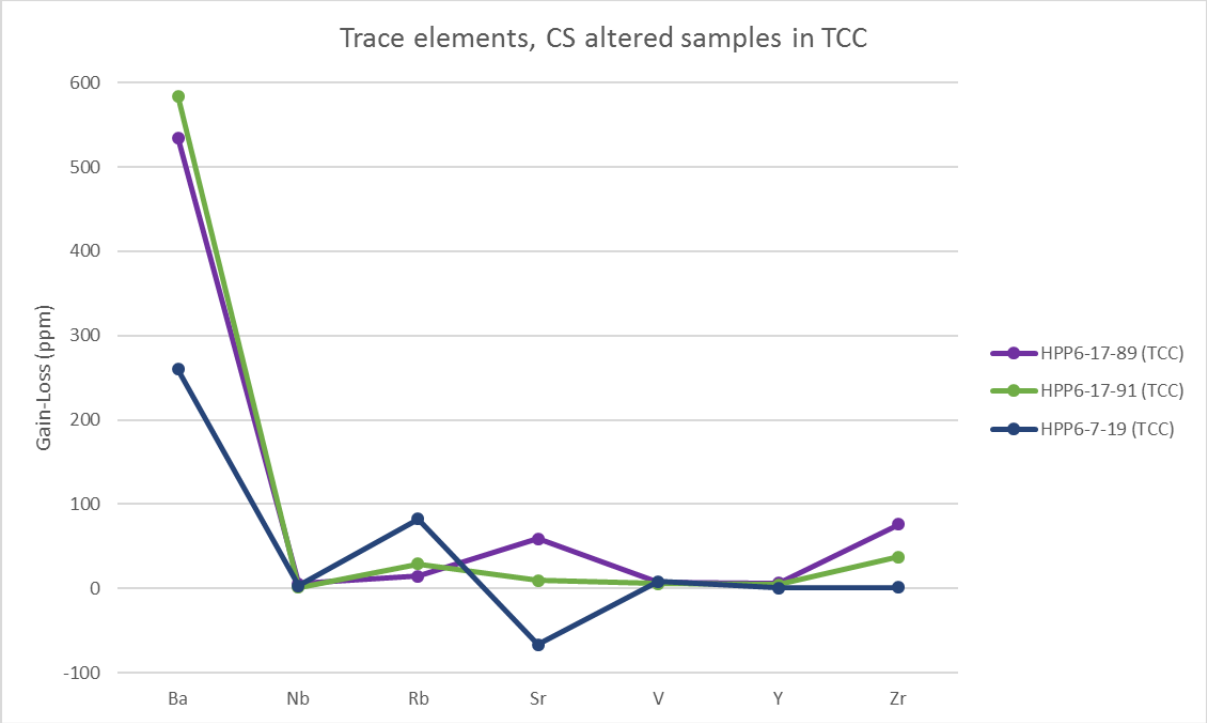

Figure 38: Mass balance alteration data of the trace elements from Ttc CS altered samples.

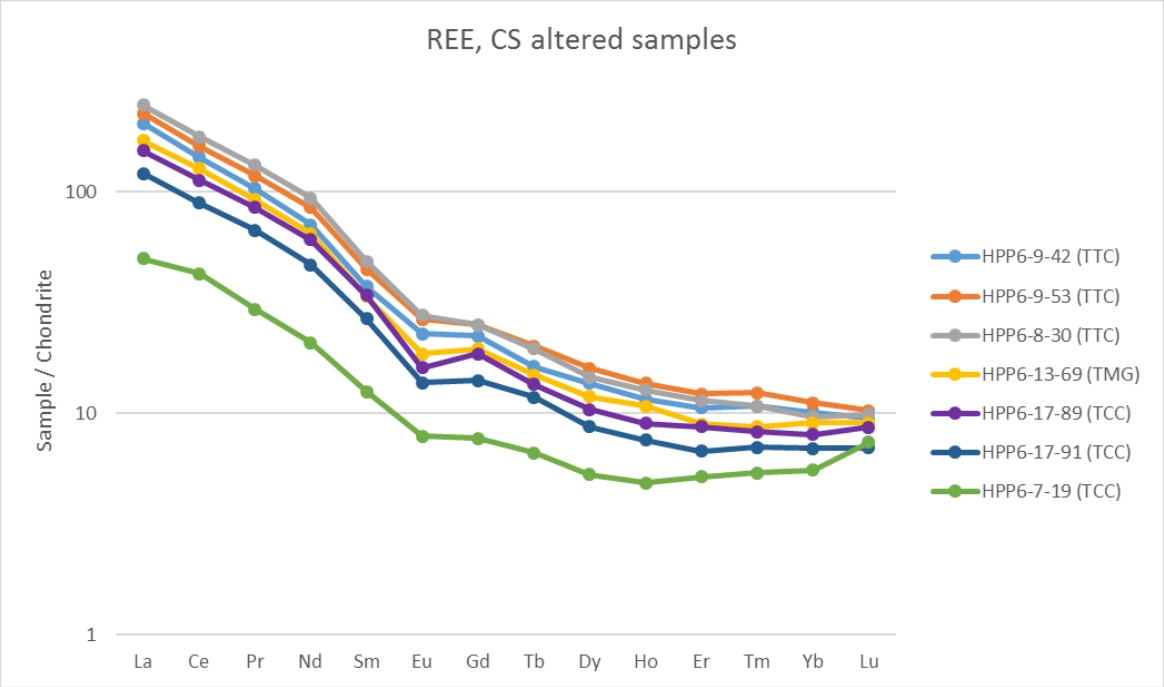

Figure 39: REE data of all the CS altered samples. All samples are normalized to chondritic meteorites from Anders and Grevesse (1989).

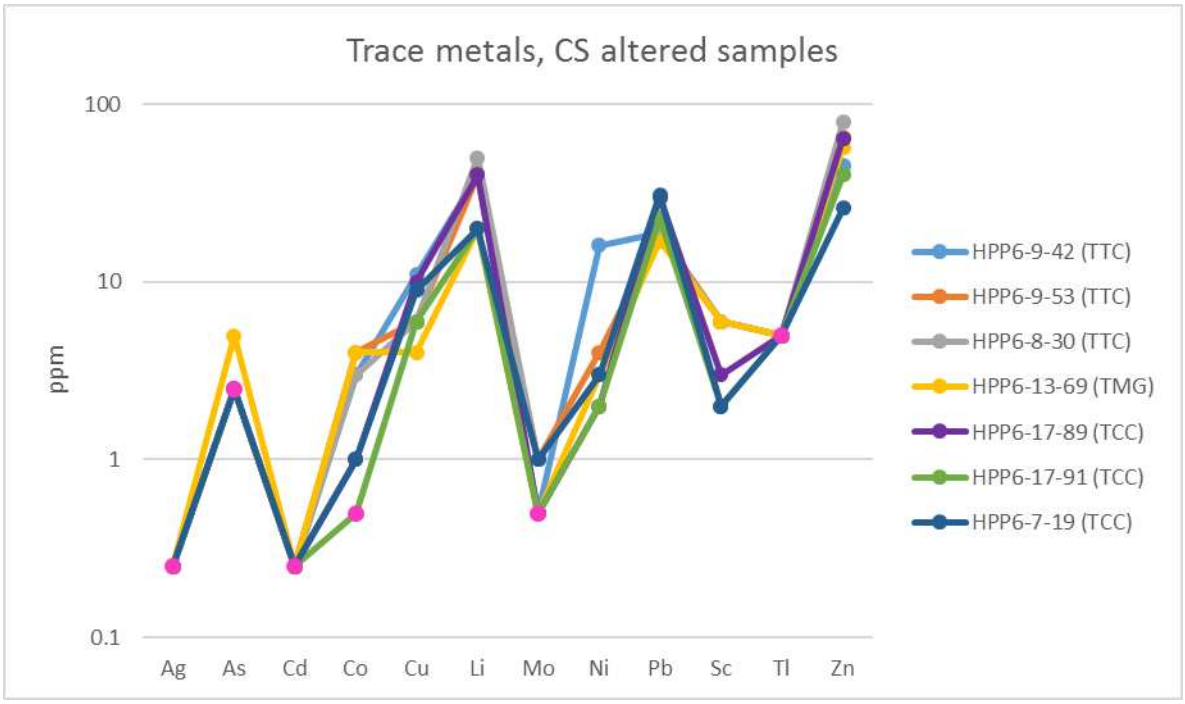

Figure 40: Trace metal data of all the CS altered samples. Y-axis is in log scale. Figure 19: Trace metal concentrations in unaltered samples from the Ttc, Tcc, and Tmg units. Pink data points represent trace metals reported as below the detection limit, these points are as plotted half the detection limit.

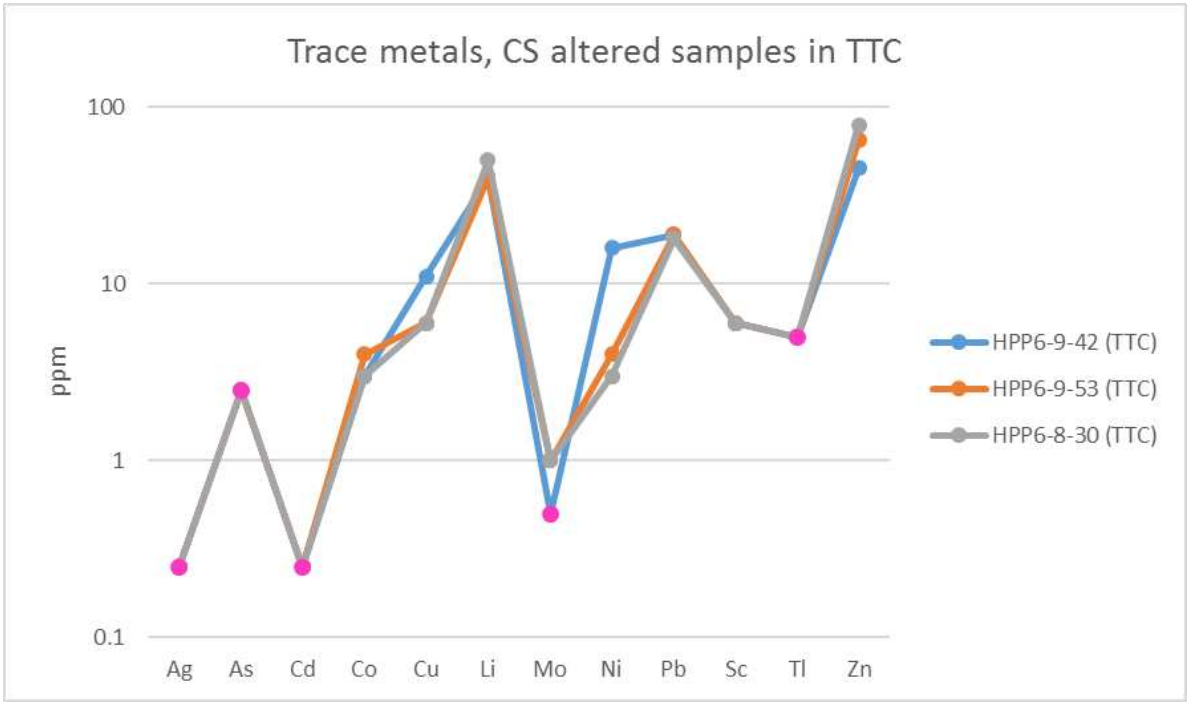

Figure 41: Trace metal data of the Ttc CS altered samples. Y-axis is in log scale.

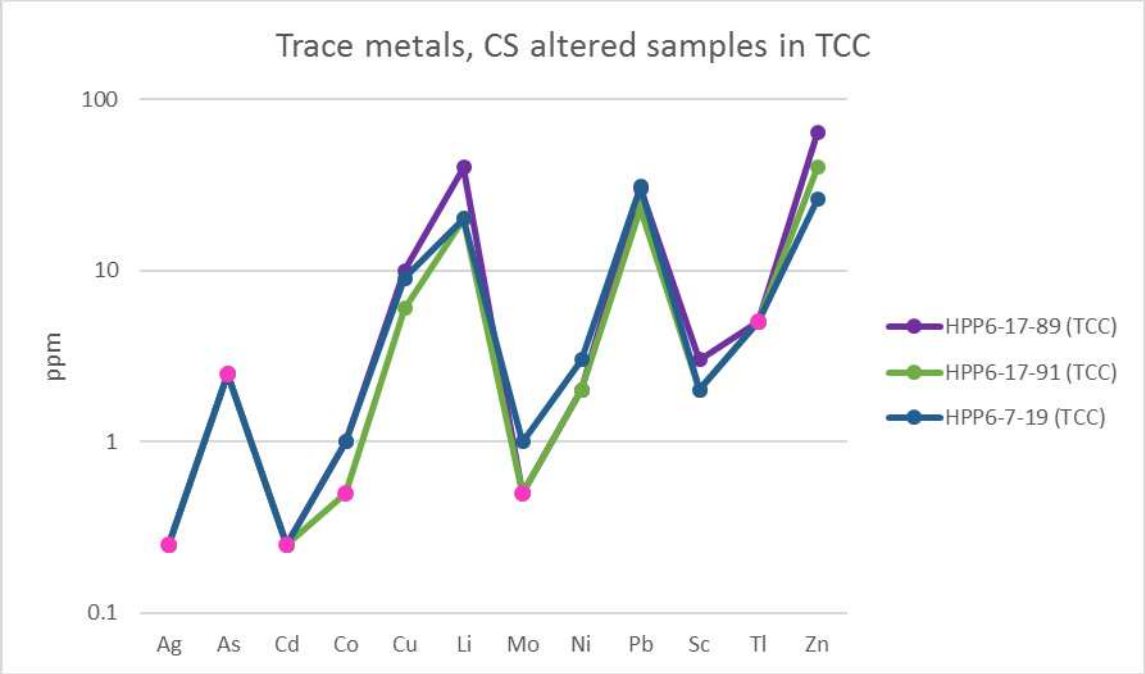

Figure 42: Trace metal data of the Tcc CS altered samples. Y-axis is in log scale.

Silicified

Major oxides and trace elements

In general, no major changes are apparent in the major oxide data (Figure 43). Thus, patterns in the silicified mass balance data are less variable than both the potassic and CS data. Both silicified samples from the Tmg unit, are enriched in SiO_2 and K_2O, and depleted of CaO and Na_2O. The silicified sample collected closer to the skarn contact (36), is significantly more enriched in SiO_2 (12 Wt.%) and slightly more enriched in K_2O and depleted in Fe_2O_3. The trace element mass balance data varies in the silicified samples (Figure 44). Gain-loss results range in Ba (-32 to 12.61 ppm), Rb (-21 to 29 ppm), Sr (-11 to 18 ppm), and Zr (-35 to 42.8 ppm). The sample closest to the skarn contact (36) is relatively enriched in Ba, Rb, and Zr, compared to the sample collected further away (37).

REEs and Trace Metals

REE concentrations in the silicified samples are nearly the same, with a flat slope and a strong negative Eu anomaly (Figure 45). However, the two samples contain marginally different HREE concentrations. Overall REE patterns of the silicified samples fit well within unaltered REE data ranges of the Tmg. Generally, no major changes are apparent in the trace metal data. Both silicified samples contain nearly the same concentrations of trace metals, which remain low, except for Li (10 ppm), Pb (~40 ppm) and Zn (17-21 ppm) (Figure 46). Silicified trace metal data is less variable, and more confined than both potassic and CS trends.

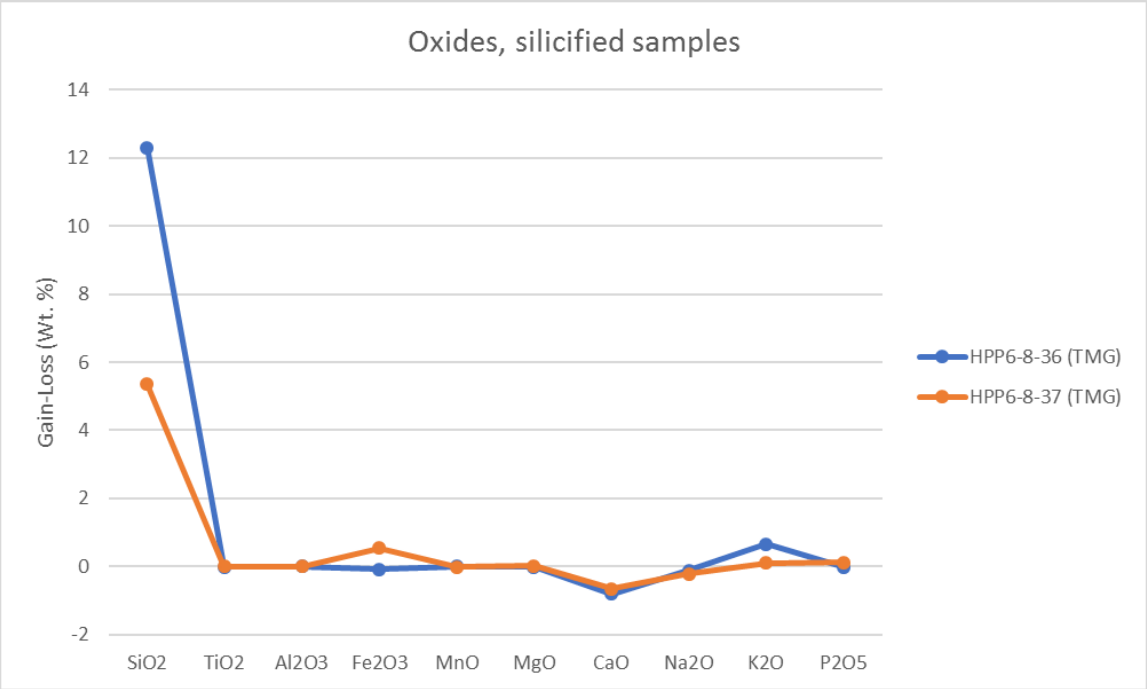

Figure 43: Mass balance alteration data of the oxides from all silicified samples. Al_2O_3 used as immobile element for mass balance calculations.

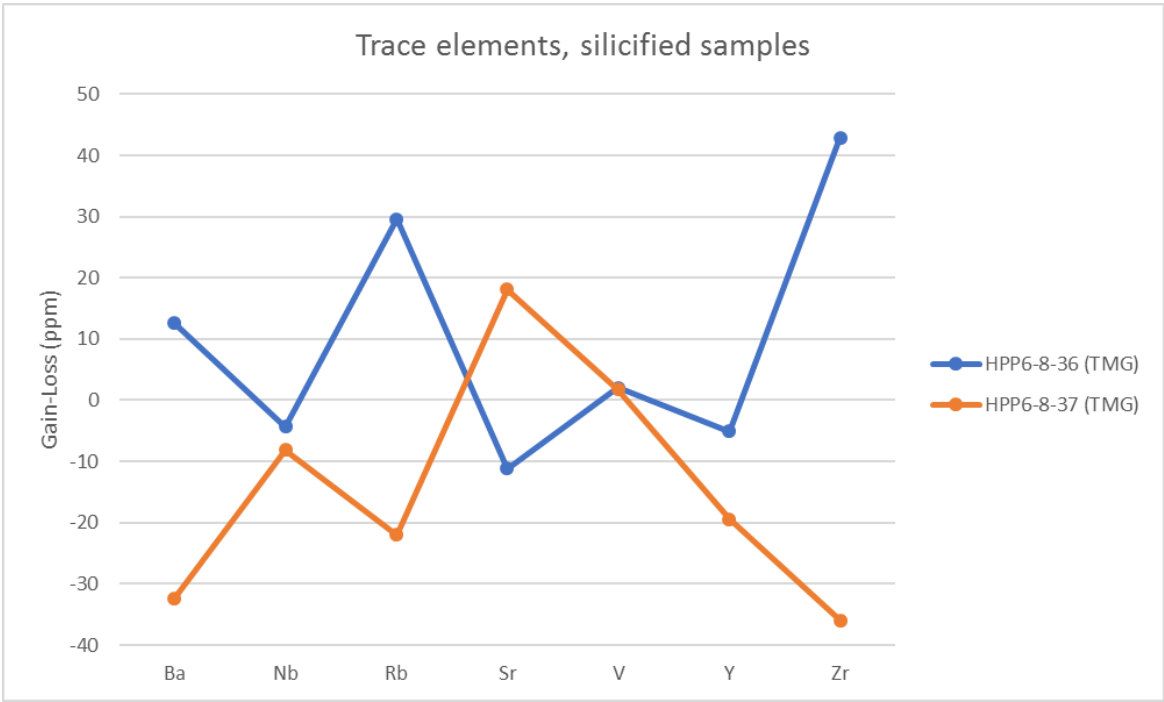

Figure 44: Mass balance alteration data of the trace elements from all silicified samples.

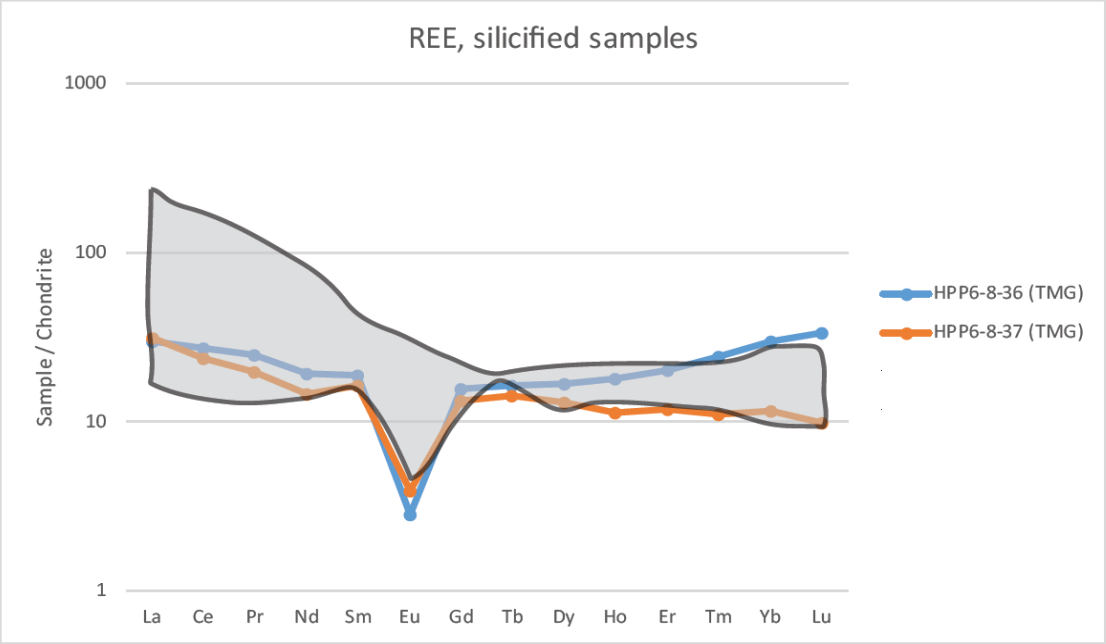

Figure 45: REE data of the Tmg silicified samples. Data overlaid by the range of REE data from this study and Barnes's et al.(2001) Tmg data. All samples are normalized to chondritic meteorites from Anders and Grevesse (1989).

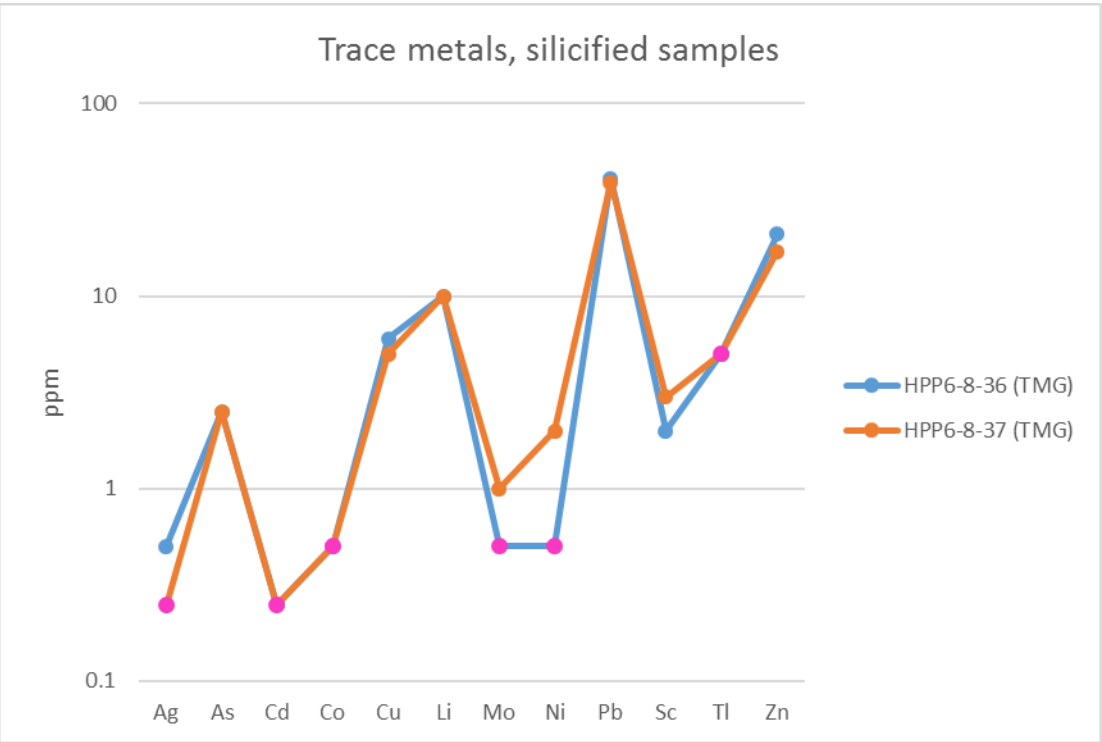

Figure 46: Trace metal data of all the silicified samples. Y-axis is in log scale. Figure 19: Trace metal concentrations in unaltered samples from the Ttc, Tcc, and Tmg units. Pink data points represent trace metals reported as below the detection limit, these points are as plotted half the detection limit.

Endoskarn

Major oxides and trace elements

Both endoskarn samples share consistent patterns. Both significantly depleted of SiO_2 (-35 to -16 Wt. %), slightly depleted of K_2O (-2.24 to -0.24 Wt. %), and enriched in Na_2O (0.95 to 2.6 Wt. %) (Figure 47). Trace element mass balance data shows the two endoskarn samples behaved similarly during alteration (Figure 48). Trace elements Ba and Sr are enriched, while Nb (-24 to -4.3 ppm) , and Rb (-212 to -38 ppm) are depleted.

REEs and Trace Metals

REE elements are nearly the same in both samples, with a shallow/nonexistent Eu anomaly, and a moderate negative slope (Figure 49). Endoskarn REE patterns fit well within the corresponding unaltered REE ranges. In both samples, trace metal concentrations are similar and all fall below concentrations of 10 ppm, except for Li (20 to 30 ppm), Pb (15 to 24 ppm), and Zn (61 to 78 ppm) (Figure 50). Ttc endoskarn samples contain higher Co and lower Li concentrations than un-altered Ttc sample 54.

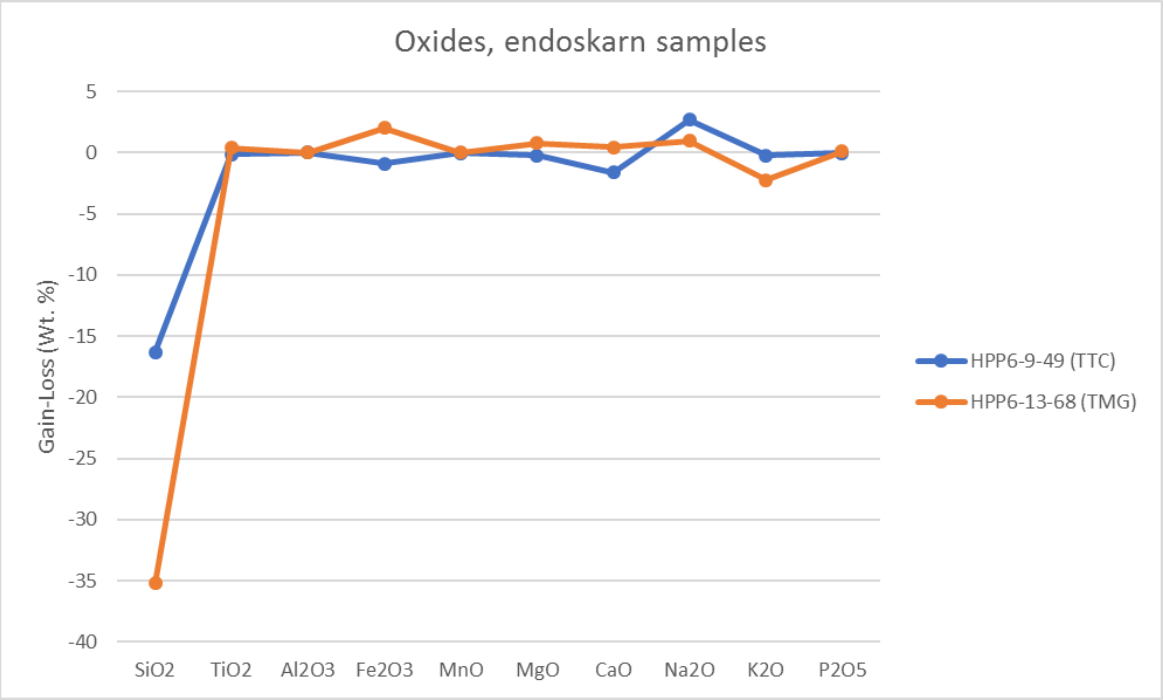

Figure 47: Mass balance alteration data of the oxides from all endo-skarn samples. Al_2O_3 used as immobile element for mass balance calculations.

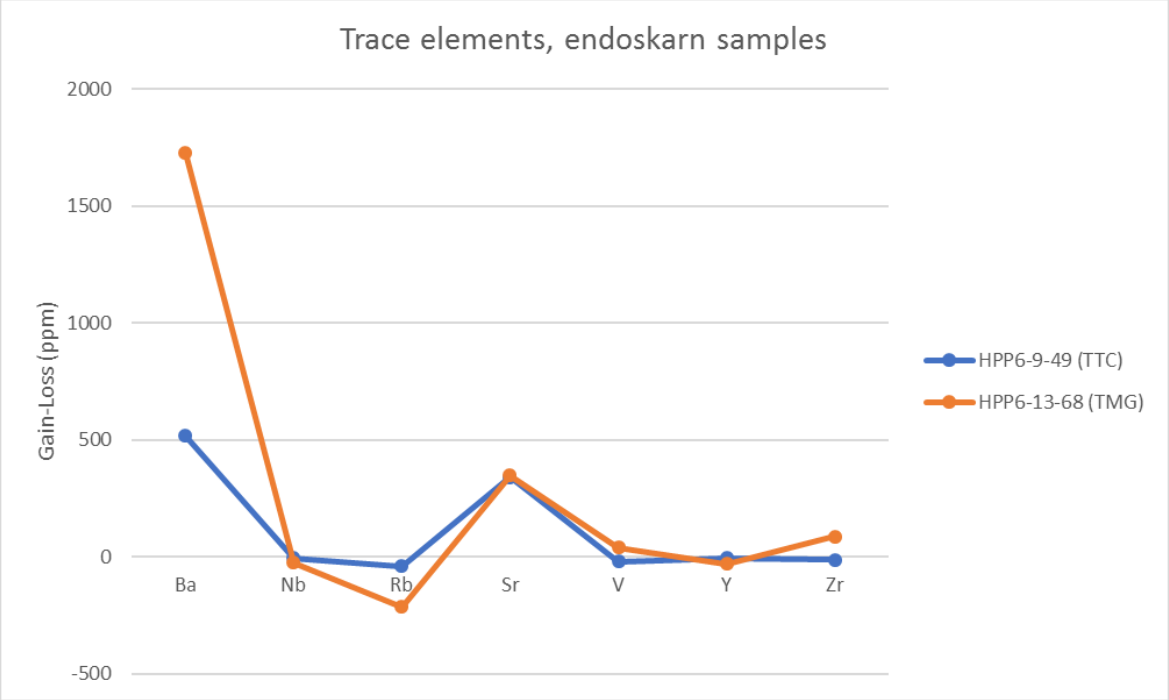

Figure 48: Mass balance alteration data of the trace elements from all endo-skarn samples.

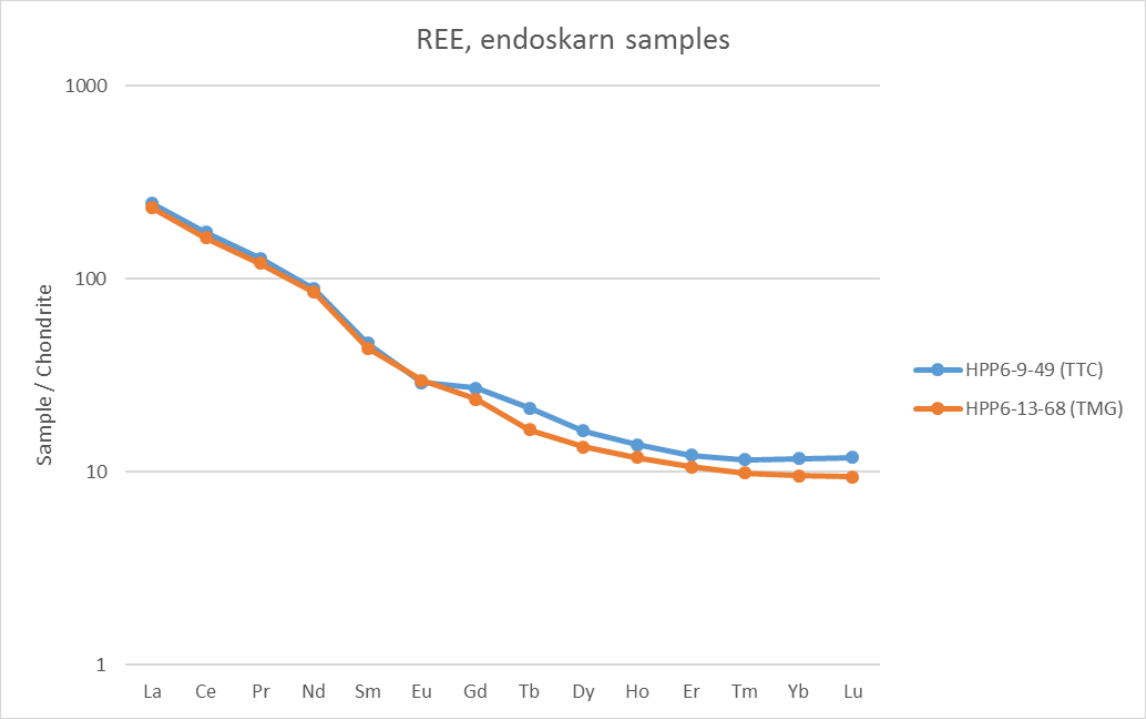

Figure 49: REE data of all the endo-skarn samples. All samples are normalized to chondritic meteorites from Anders and Grevesse (1989).

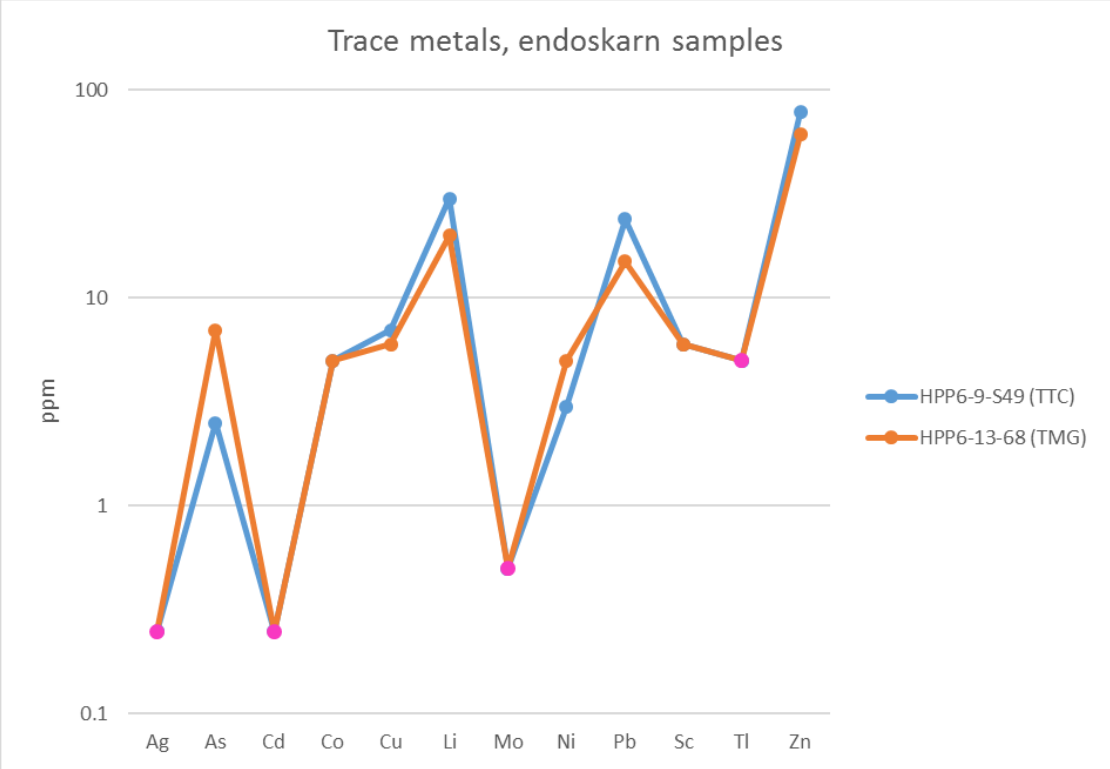

Figure 50: Trace metal data of all the endo-skarn samples. Y-axis is in log scale. Figure 19: Trace metal concentrations in unaltered samples from the Ttc, Tcc, and Tmg units. Pink data points represent trace metals reported as below the detection limit, these points are as plotted half the detection limit.

Exo-skarn

The three exo-skarn samples have very variable compositions (Figure 51). Samples are progressively depleted in elements towards the right of the graph—the less incompatible immobile elements. Sample 66 is enriched in most elements except for TiO_2 and Yb and contains concentrations similar to granites, while sample 34 bounds the bottom data range. REE elements in the exo-skarn samples plot with the same trend, however sample 34 contains significantly lower concentrations (Figure 52). All samples have small negative Eu anomalies. Between samples 66 and 70, trace metal concentrations differ (Figure 53). Sample 66 contains higher concentrations of Li (40 ppm) and Sc (20 ppm), whereas sample 70 contains an uncharacteristic concentration of Ni (26 ppm). Both samples contain relatively larger concentrations of Zn (86 to 106 ppm), and low/moderate amounts of Pb (7 to 14 ppm). In comparison, sample 43 contains very low concentrations of trace elements.

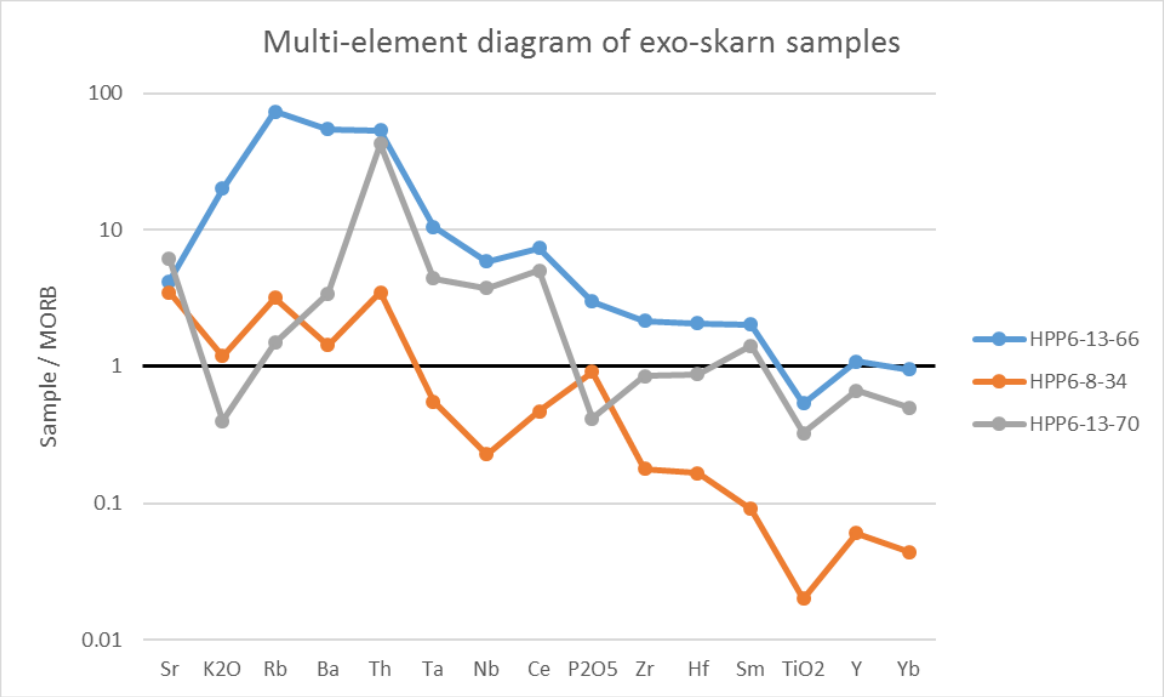

Figure 51: Multi-element diagram of all exo-skarn samples collected within the HPP. All data normalized to MORB (Pearce, 1983). Immobile elements are situated to the right of the graph and increase in incompatibility right to left, while mobile elements placed on the left side of the graph increase in incompaibility from left to right.

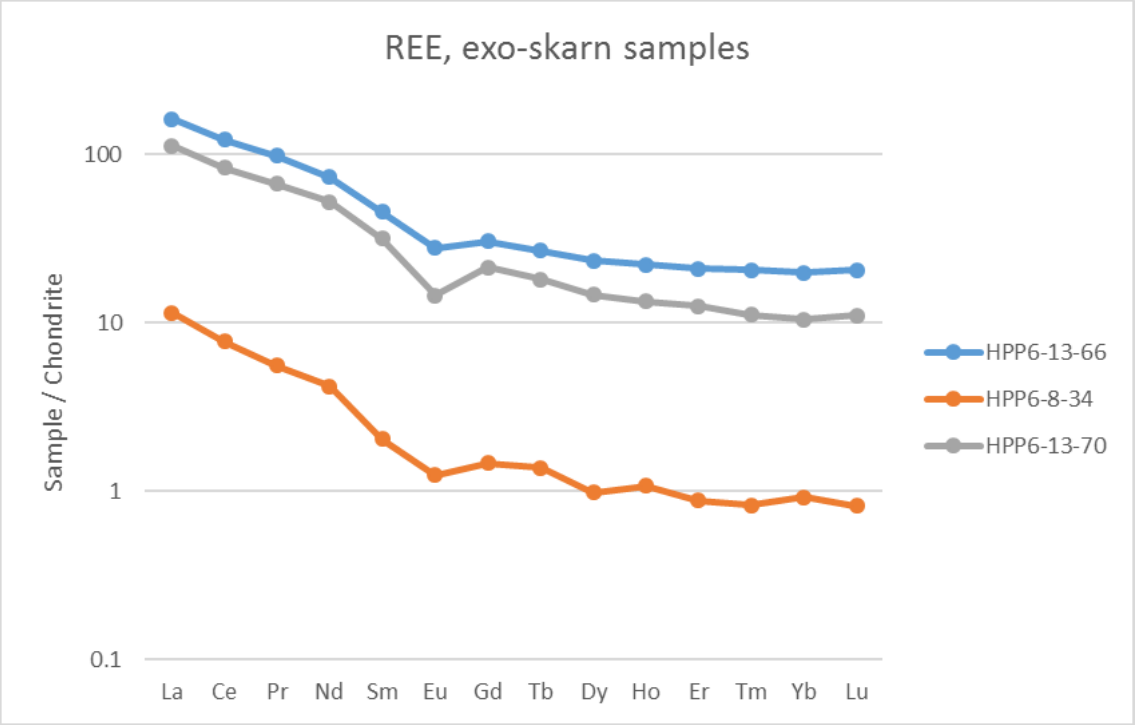

Figure 52: REE data of all the exo-skarn samples. All samples are normalized to chondritic meteorites from Anders and Grevesse (1989).

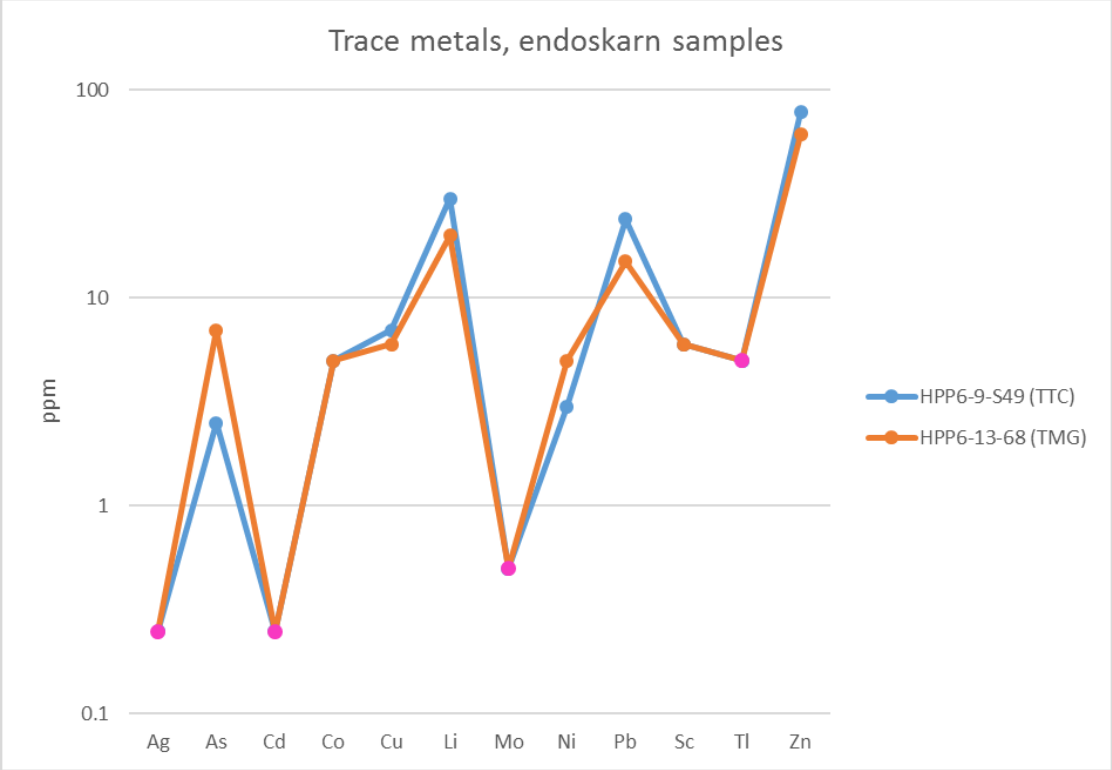

Figure 53: Trace metal data of all the exo-skarn samples. Y-axis is in log scale. Figure 19: Trace metal concentrations in unaltered samples from the Ttc, Tcc, and Tmg units. Pink data points represent trace metals reported as below the detection limit, these points are as plotted half the detection limit.

4.5 Fluid inclusions- temperature constraints

Depending on the number of generations of inclusions in a sample, approximately 20-30 fluid inclusions along healed fractures were analyzed microthermometrically per sample (Table 5, appendix 3). The inclusions range in size from 5 to 12 μm in diameter, are predominately equant and absent of solid inclusions. T_n values range from -40 to -30 °C, T_e: -55 to -10 °C, $T_{m\text{-}ice}$: -2.2 to 5.5 °C (values >0 due to possible minor gas content and/or metastability), and T_h: 110 to 250 °C. Using the equation from Wilkinson (2017), salinity values average 2.43 wt. % NaCl (with some outliers around ~7 wt.% NaCl). With low salinities and pressure estimates between 1 to 4 kb, isochore graphs representing 0% and 5% salinity yielded average pressure corrected temperatures of entrapment of 400-500 °C for potassically altered samples, 330 to 450 °C for CS samples, 330 to 500 °C for the endoskarn samples, and 320 to 400 °C for the silicified samples.

Overall entrapment temperatures varied throughout the HPP. A map with temperatures placed next to corresponding sample locations, showed hotter fluid temperatures near the center of the HPP and lower temperatures fanning outward (Figure 54). Temperatures were also slightly higher in the western half of the pluton, as these rocks were brought up from a deeper position in the pluton. Potassically altered samples (concentrated in the middle of the HPP) always corresponded to the highest hydrothermal fluid temperatures in the system, while CS alterations (clustered around the flanks of the HPP) corresponded to lower hydrothermal temperatures (Figure 55).

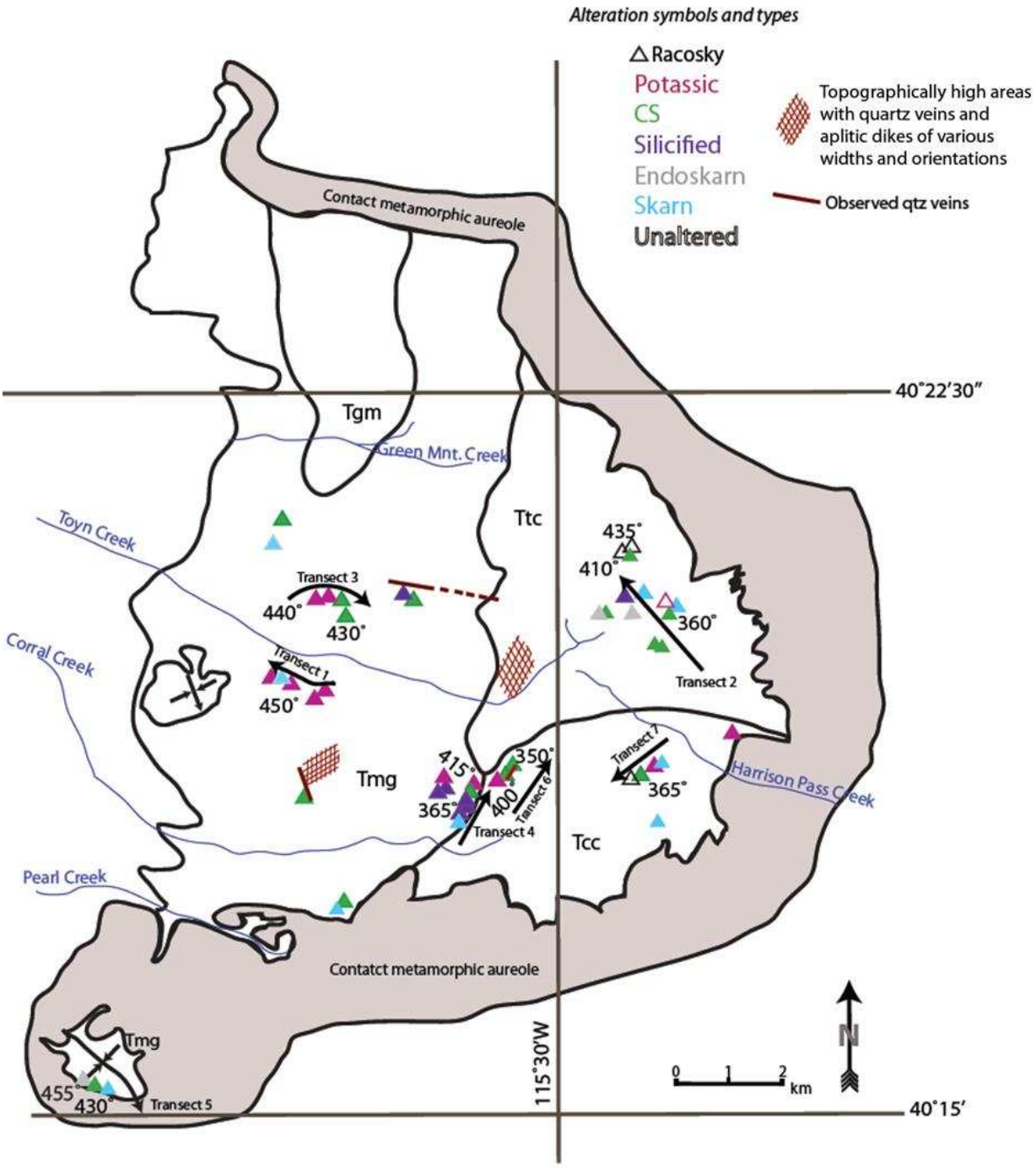

Figure 54: Map of median hydrothermal temperatures in °C. Positions of the alteration types are slightly distorted to enhance readability within the dense clusters of data. HPP map adapted from Burton (1997) and Barnes et al. (2001).

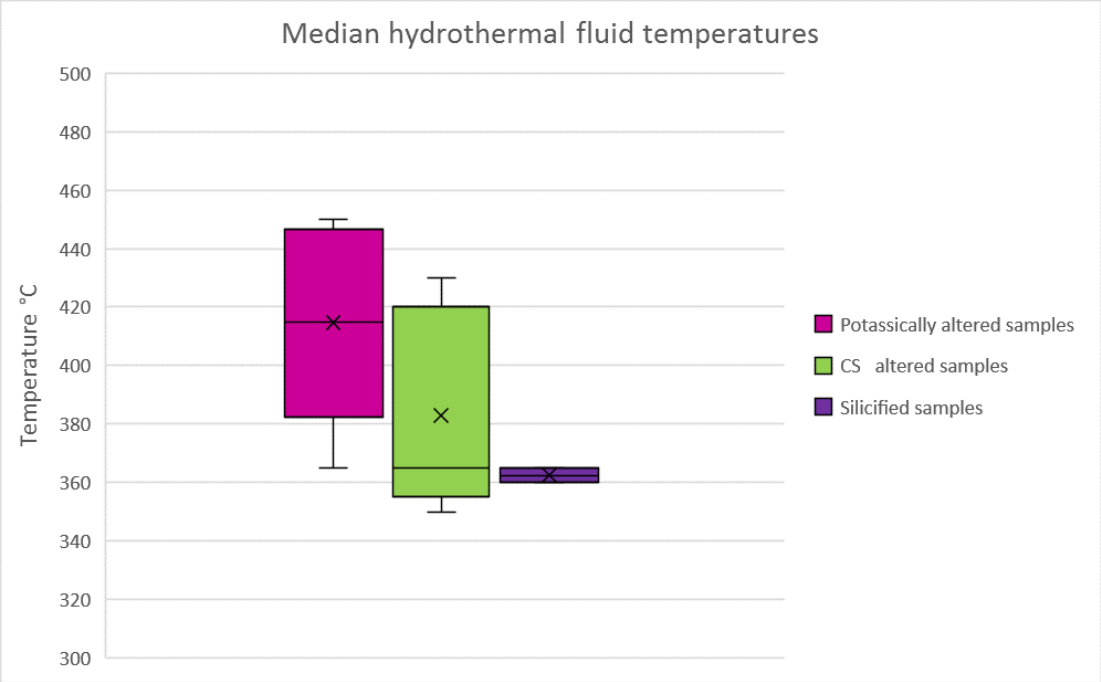

Figure 55: Median hydrothermal fluid temperatures of alteration types in the HPP. Potassic alteration, found in the middle of the HPP consistently plots higher than CS samples (clustered around the flanks).

4.6 Stable isotopes

$\delta^{18}O_{quartz}$ and $\delta D_{biotite\text{-}chlorite}$

Oxygen and hydrogen isotope results for the quartz, biotite, and chlorite separates, are listed in Table 6 in Appendix 3. $\delta^{18}O$ values in the quartz separates range from -8 to 18‰, whereas δD values range -189 to -91‰ in biotite, and -199 to -164 ‰ in chlorite. In the potassically altered samples, $\delta^{18}O$ is within a narrow range from 8 to 11.5‰, and δD varies significantly from -189 to -102 ‰. CS samples range in $\delta^{18}O$ from 4.8 to 18.2 ‰ and in δD from -198 to -176 ‰. The two endo skarn samples contain the same $\delta^{18}O$ values at -6.5‰ and chlorites with low δD values (-193 to -187 ‰). A wide range of $\delta^{18}O$ is present in the silicified samples (1.8 to 11‰), while the δD values differ between samples with biotite (-169‰) and chlorite (-181‰).

$\delta^{18}O_{water}$ and δD_{water}

Oxygen and hydrogen isotopic compositions of the hydrothermal waters responsible for alteration, along with the temperature ranges used for calculations, can be found in Table 7 in Appendix 3. Because of the narrow range of fractionation factors, the same patterns in the $\delta^{18}O_{quartz}$ and $\delta D_{biotite\text{-}chlorite}$ can be used to describe the calculated $\delta^{18}O_{water}$ and δD_{water} data. Compiled data curves towards the meteoric water line (Figure 56).

On a regional scale, δD_{water} is highest towards the middle of the intrusion, and decreases outwards, while the range of $\delta^{18}O_{water}$ from the center of the HPP overlaps with $\delta^{18}O_{water}$ in samples collected closer to the flanks of the intrusion (Figure 57). Data was also analyzed by transect as an attempt detect smaller-scale fluid pathways. For example:

samples collected furthest from the skarn contact in transect 1, contain water signatures of $\delta^{18}O$= 8.9‰ and δD= -79‰ (sample 16) (Figure 58). Samples collected closer to the skarn contact were altered by waters significantly lighter in δD, and slightly lighter in $\delta^{18}O$.

Data by alteration type

Alteration types are differentiated and appear to plot in clusters on the standard δD vs. $\delta^{18}O$ graph (Figure 59). Although isotopic data varies considerably for the potassically altered samples, the data still cluster vertically with δD_{water} data ranging -31 to -132 ‰ and $\delta^{18}O_{water}$ 2.5 to 9.6‰. CS samples cluster within a depleted δD zone, a small δD_{water} range of -140 to -169‰, and widespread range of $\delta^{18}O_{water}$ 1 to 14 ‰. The silicified samples plot with the potassic data, while the endoskarn samples (accompanied by the epidote sample) plot closest to the meteoric water line with δD_{water} values ranging -143 to -164‰ and $\delta^{18}O_{water}$ values ranging -12.8 to -10‰. Unaltered samples 20 and 54 ranged from $\delta^{18}O_{water}$ = 4 to 9.6‰ and δD_{water} = -31 to -92‰.

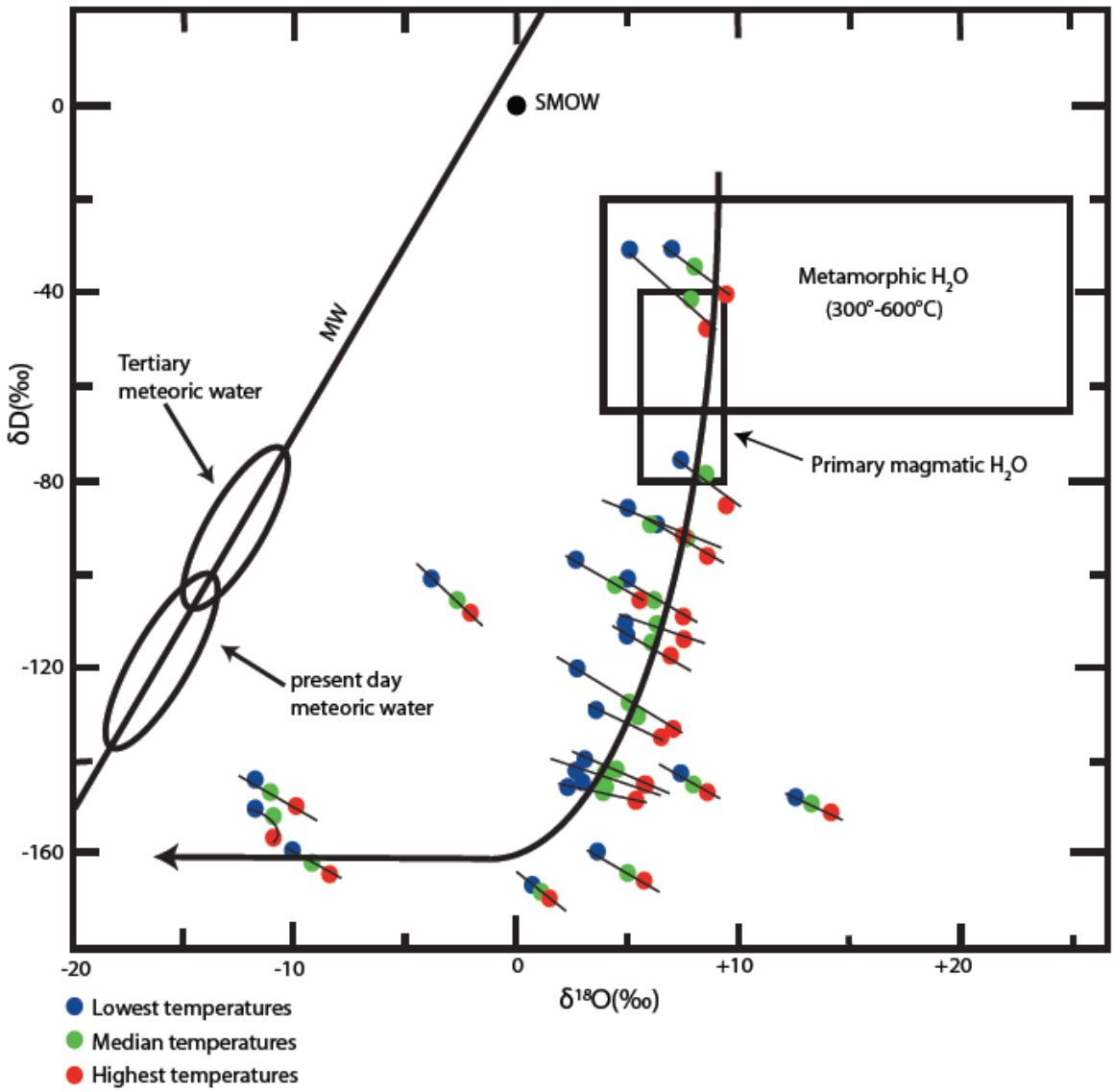

Figure 56: Graph of $\delta^{18}O_{water}$ and δD_{water}, calculated from quartz, and biotite and chlorite separates using a range of temperatures. Curved arrow is the interpreted reaction line. Small black lines represent the trend of each sample, produced from the temperature ranges. Local Tertiary and present day meteoric water data from Fricke et al. (1992).

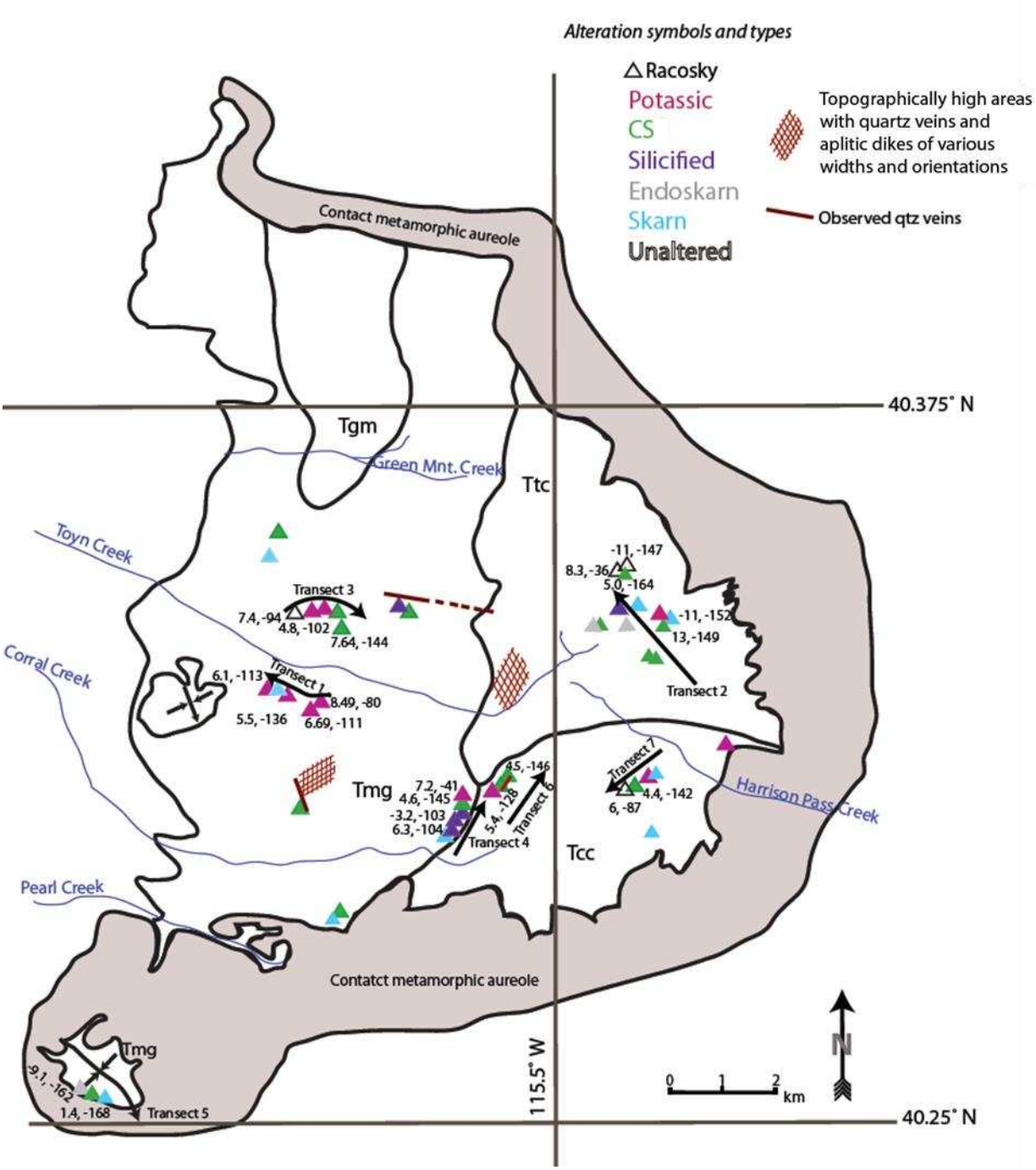

Figure 57: Map of $\delta^{18}O_{water}$ and δD_{water}, calculated from median hydrothermal temperatures. Positions of the alteration types are slightly distorted to enhance readability within the dense clusters of data. HPP map adapted from Burton (1997) and Barnes et al. (2001).

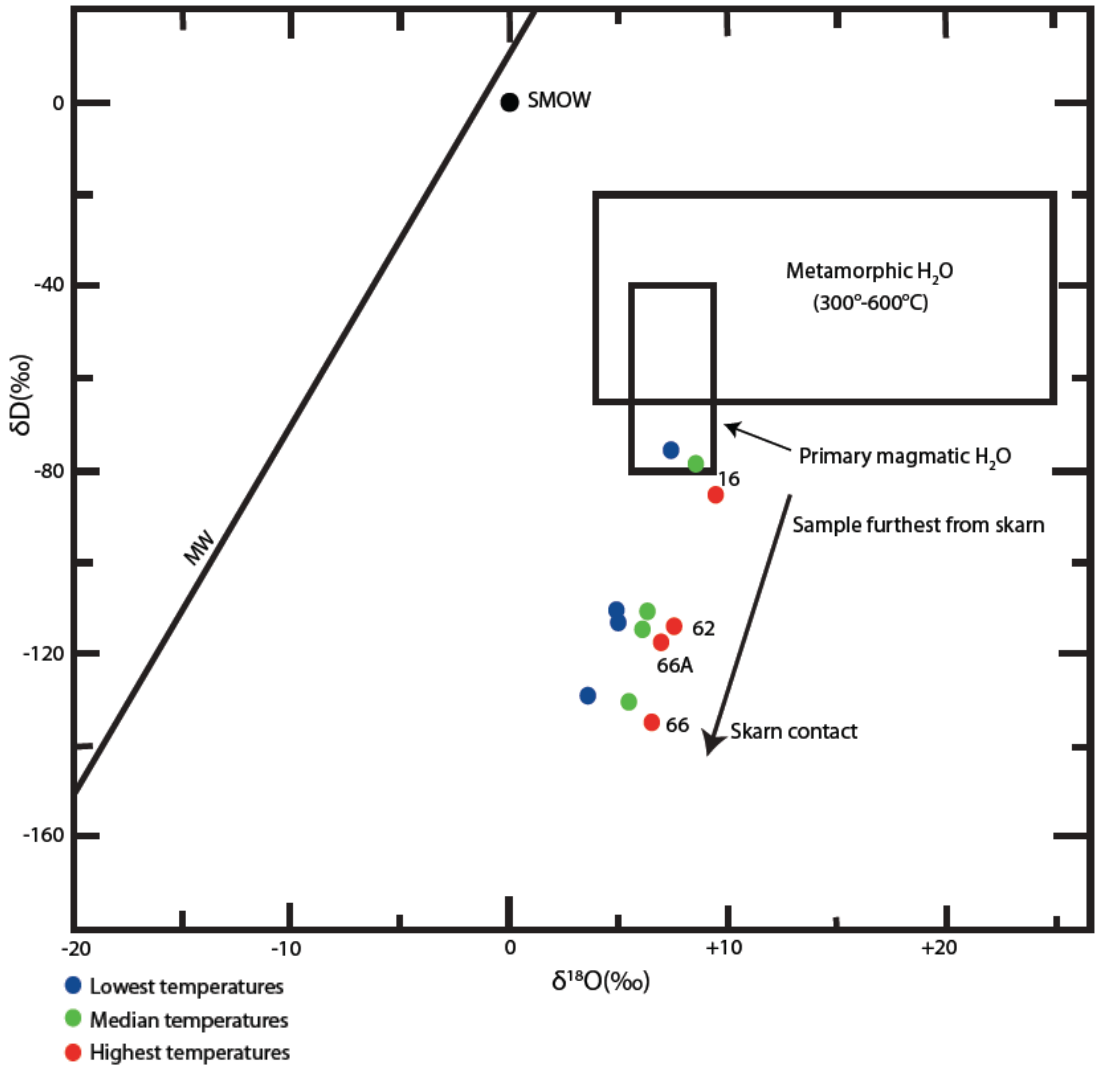

Figure 58: Graph of $\delta^{18}O_{water}$ and δD_{water}, from samples along transect one.

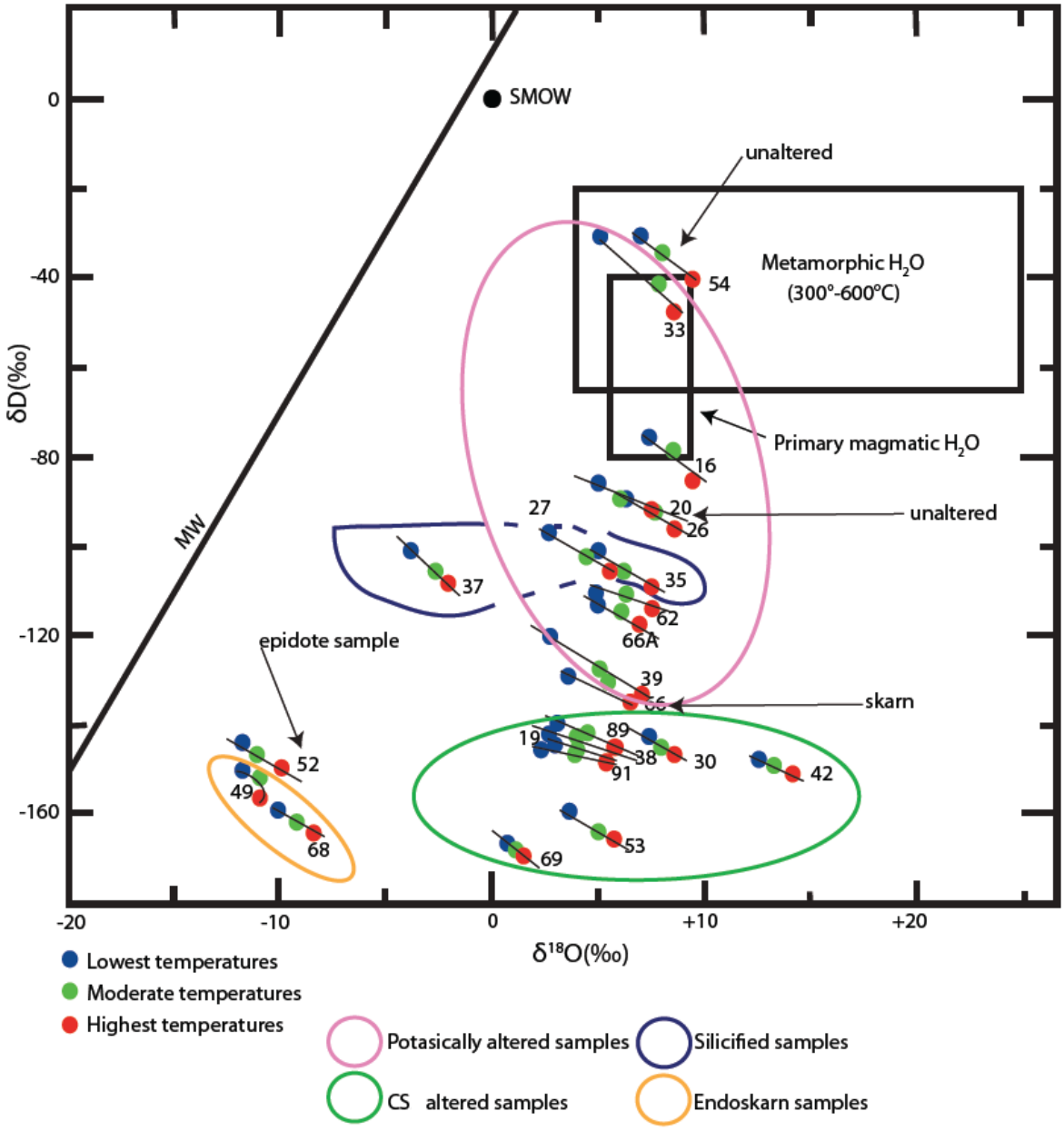

Figure 59: Graph of $\delta^{18}O_{water}$ and δD_{water} of all samples collected in the HPP. Samples are circled to highlight clustering by alteration type. Numbers correspond to sample I.D.

5 DISCUSSION

An in-depth analysis of the multi-element geochemical and isotopic data is needed to fully understand the petrologic evolution of the HPP and the affects the multiphase system, and country rock (suggested by data in this study) had on the geochemistry of alteration types in different parts of the system. Furthermore, evaluation of the isotope geochemistry of the hydrothermal waters is required to fully understand the source, nature, and flow geometries of the magmatic-hydrothermal fluids within the HPP. A combination of the following analysis, and the presence and nature of porphyry root features recognized in the HPP is used here to assess and discuss the prospect of the HPP as a porphyry root system.

5.1 Petrology and Geochemistry of the HPP

Harker diagrams, including data of this study and from Barnes et al. (2001), display general trends typical of evolving magmas: mafic samples (Ttc) plot lowest in SiO_2, and highest in oxides such as Al_2O_3, CaO, Na_2O, and P_2O_5, while the more evolved magmas (Tcc and Tmg) plot higher in SiO_2 and lower in oxides such as Al_2O_3 (Reid et al., 1993). This pattern was also noted by Barnes et al. (2001), and is typical to that of evolving granitic magmas. In addition to the narrow data trends (Figure 12), Harker diagrams clearly show that there are outliers within the Ttc and Tmg units. Data spread on the Harker diagrams, was the first indication of the variance between the data collected in this study and data published by Barnes et al. (2001). Ttc outliers with the lowest SiO_2 content, are interpreted as altered mafic endmembers of the Ttc unit. However, other anomalies present in the Ttc and Tmg data cannot be interpreted within the context of magmatic evolution. Although

the Harker plots define the evolution of the HPP magmas, petrological analysis based exclusively off Harker diagrams is not sufficient, as outliers could indicate a different/unrecognized intrusive phase, or alternatively be indicative of hydrothermal alteration— discussed further in the section.

An extensive examination using multi-element and REE spider diagrams, provides further insight on the petrology and also the distribution of the intrusive units. Sample 43, from the mid-northeast Ttc unit, is anomalous in the multi-element data, and does not correlate with any patterns in any intrusive units. REE data from the other Ttc samples in this study correlates well with Ttc data from Barnes et al. (2001). Sample 6 collected in the eastern edge of the Tcc, exhibits the same pattern as most of the Tmg samples on the multi-element spidergram— lows of Sr and TiO_2, and a large negative Ba anomaly. The second outlier in the Tcc data (sample 18) does not match trends of the other intrusive units. Approximately half of the Tcc data displays the same pattern and plots within the range of Barnes's et al. (2001) data. The remaining Tcc samples (6, 18, and 39) either fall below the range of Barnes's et al. (2001) data or display dissimilar trends and anomalies. Tmg samples exhibit two main patterns, one of which is a clear match to Ttc data (samples 33, 68, and 69), while the remaining samples in the Tmg sample suite are interpreted as the main Tmg signature—although data displays a broader spread than recognized by (Barnes et al., 2001). Samples 6 and 39 of the Tcc, parallel Tmg data. The majority of Tmg REE data correlates with Barnes's et al. (2001) data. However, samples 33, 68 and 69 match data ranges and patterns found in the Ttc samples. Tmg samples 16 and 27 do not correlate with Barnes et al.'s data or other data collected in this study.

Geochemical data suggest unit contacts on the geologic map of the HPP should be modified (Figure 60). The isolated granitic inlier, southwest of the main HPP intrusion, is currently mapped as the Tmg. However multi-element and REE data of samples collected from this inlier "Tmg" pod (68 and 69), clearly plot as Ttc. Similar results were found in sample 33, collected along the eastern most extent in the Tmg unit. In addition, both the multi element and REE data of Tcc sample 6 and REE data of Tcc sample 39, suggest the samples instead belong to the Tmg unit.

Cross-sectional interpretation of the HPP intrusive suites made by Barnes et al. (2001) presents the Tmg as sheets and lenses intruded through the Ttc and Tcc units (Figure 2). In addition, the detailed map by Barnes et al. (2001) exhibits several mafic Ttc lenses outcropping near the Ttc and Tmg contact in the middle of the HPP. Based off the cross-sectional interpretation by Barnes et al. (2001), the Ttc lenses could in theory extend further west than the map originally indicates. This interpretation is supported by geochemical data (samples 68 and 69), that indicates the Ttc outcrops as far as the southwest inlier. The mafic samples collected in the swarm of Ttc pods within the Tmg unit, also match the diagnostic Ttc trends seen in sample 68 and 69. Conversely, geochemical data of sample 6, collected from the eastern most extent of the Tcc, plots as Tmg. The cross-sectional interpretation by Barnes et al. (2001) only depicts the Tmg sheets intruded mid-way through the HPP, while current maps of the HPP do not place Tmg pods within the eastern half. However, geochemical data in conjunction with the HPP cross section support the possibility Tmg sheets intruded into the top portion of the pluton. An updated, schematic version of the HPP map was constructed to show the extent the Ttc and Tmg lenses (Figure 60). Remaining outliers in the REE data (16, 18, 27, and 43) do not fit or

match any of the prominent data trends. These outliers could indicate 1.) unidentified felsic/mafic pods 2.) new, undescribed intrusive units, or 3.) moderate to pervasive hydrothermal alteration.

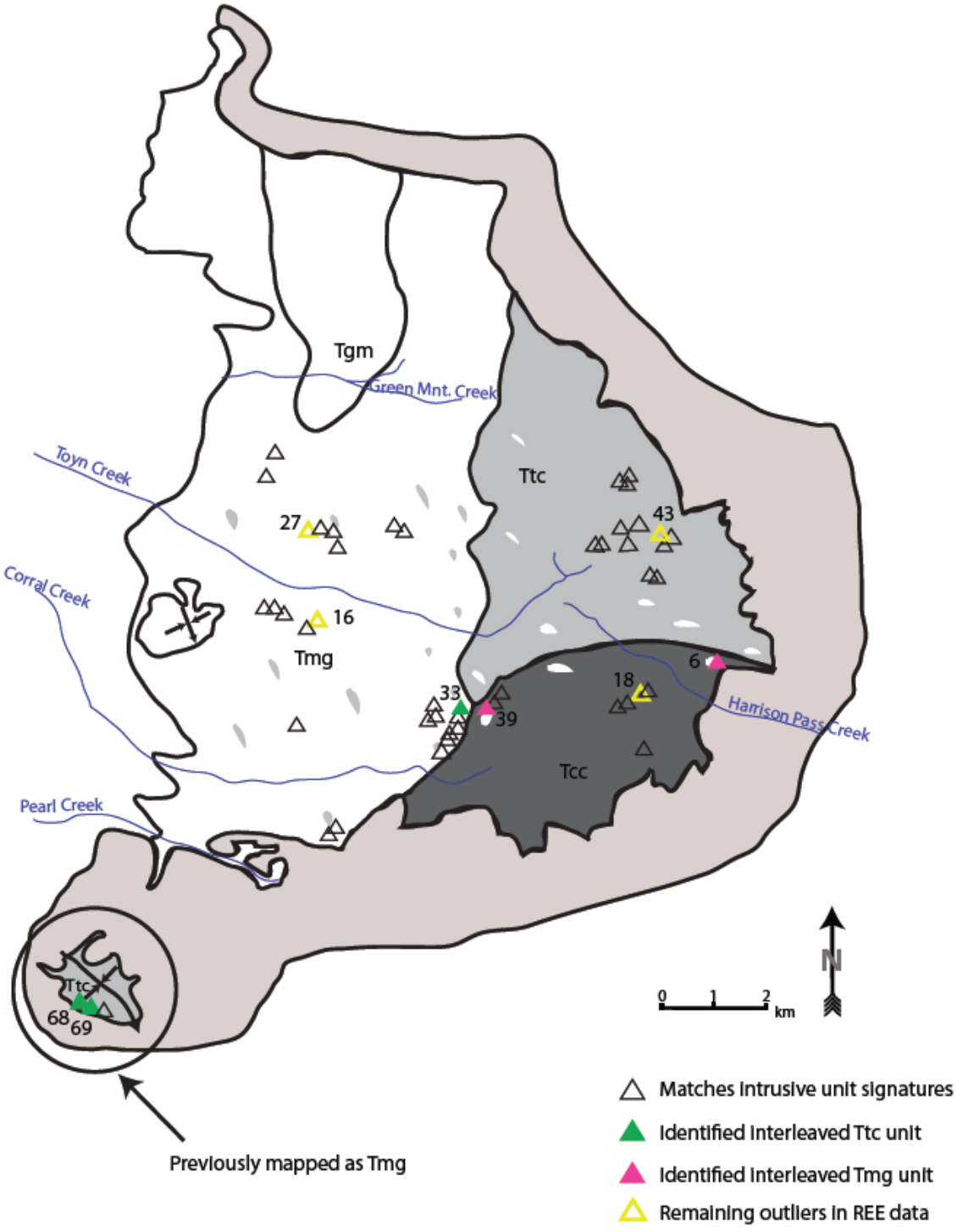

Figure 60: Updated map of the HPP—Interpretation of the positions of the interleaved units: white=Tmg and grey=Ttc.

5.2 Geochemistry of the alteration types

Mass balance alteration data of the major oxides and trace elements, along with REE, and trace metal data of each distinct alteration type display inconsistent enrichment/depletion patterns within the oxides and trace elements of the potassically altered rocks (Figures 21 and 24). However, with data differentiated by both alteration type and intrusion type (i.e. Ttc, Tcc, and Tmg), well defined patterns appear (Figures 22, 23, 25, 26). Tmg potassically altered samples have consistent enrichment and leaching patterns, while ranges in REE and trace metal data narrow. Abnormal samples highlighted in the Tmg potassic data include: samples 33, and 66A. Patterns in the Ttc potassically altered samples are also well defined.

Mass balance of the major oxides in the CS samples of both the Ttc and Tcc units vary (Figure 33). The range of trace elements and metals is narrower in the differentiated data, while REE patterns remain consistent (however samples do show differing enrichment and leaching trends) (Figures 36, 39,40). CS samples with anomalous enrichment and depletion include sample 19 of the Tcc and sample 69 from the Tmg units. Silicified samples in the Tmg lack consistent patterns in the mass balance alteration of the trace elements. However, REE, trace metal concentrations, and mass balance results of oxides, are consistent throughout the samples. Mass balance oxide and trace element data in the two endoskarn samples share similar trends (Figures 47 and 48). REE and trace metal data of the two endo-skarn samples are nearly the same (Figures 49 and 50). The multi-element diagram of the exo-skarn samples (all collected within the Tmg unit) shows a wide variance in patterns and concentrations. The three exo-skarn samples share the

same REE trend, but contain dissimilar concentrations, while trace metal data varies (Figures 51-53). Refer to figure 6 for sample locations.

Data differentiated by unit identify samples 18, 33, and 66A as the three main outliers within the potassically altered rocks. Mass balance of alteration for sample 33 was calculated using unaltered Tmg data, as these samples were collected within the Tmg unit boundary. However, using REE and multi-element analyses this samples was interpreted to be exposed lenses of a mafic Ttc lens (Section 5.1). Therefore, the use of an incorrect unaltered standard caused the sample to plot as an outlier. The other anomalous potassically altered sample collected in the Tcc unit (18), is also an outlier. The cause of the differing trends may be attributed to fluid conditions at the granite-skarn contact, as sample 18 was collected a few meters from a Tcc-skarn contact (Figure 23 and 26). The same can be interpreted for sample 66 A, which was also collected a few meters from a skarn pod contact, but within the Tmg unit (Figure 22 and 25).

The two distinct outliers in CS data were samples 19 of the Tcc and 69 of the Tmg. Sample 19 was collected near the Star Mine skarn-Tcc contact, while CS sample 69 was collected from the southwest satellite inlier, previously mapped as Tmg (Figures 35 and 38). But, from REE and multi-element analyses, sample 69 is proven to be part of the Ttc unit. Therefore, the incorrect comparison of CS sample 69 to unaltered Tmg data produced a false trend. The major difference between the two silicified samples (36 and 37) are the variances within the trace element trends of the mass balance data (Figure 44). Geology along the ridge from which the samples were collected, is complicated and riddled with

small (sometimes hidden—as indicated by isolated endo-skarn outcrops) limestone and exo-skarn pods.

The two endo-skarn samples analyzed in this study share similar trends in data, but contain minor variances. Sample 68, collected from the southwest satellite intrusion, is extremely depleted in SiO_2 and contains an uncharacteristic enrichment of Ba (1725 ppm) (Figures 47 and 48). Again, this satellite intrusion was originally mapped as Tmg, but REE and multi-element analyses suggests sample 68 is part of the Ttc unit. Therefore, incorrect comparisons between the endo-skarn sample 68 to unaltered Tmg data produced false mass balance trends. Finally, the three exo-skarn samples collected within the Tmg unit (34, 66, 70), contain considerable variances between composition, which clearly illustrate different degrees of alteration plus differences in original lithology (Figures 51-53). For example, sample 34, the least altered of the limestone pods, consistently contains lower concentrations of REEs and trace metals.

To validate the interpreted unit re-assignments, mass balance data of the mis-assigned samples were recalculated, while anomalous samples affected by fluid-skarn interaction were removed. Mass balance oxide results for samples 6 and 39—originally thought to be part of the Tcc— were reassigned to the Tmg unit and recalculated using unaltered Tmg data. Sample 33 was removed from the original graph (Figure 61) as the sample was interpreted to belong to the Ttc unit, while sample 66A was removed, as the sample was collected directly adjacent to a skarn xenolith. Corrected mass balance data and removal of anomalous data, eliminated data spread in SiO_2, Fe_2O_3, MgO, CaO, Na_2O and K_2O (Figure 62). For further justification, mass balance oxide and trace element results for CS

sample 69—originally thought to be part of the Tmg— was reassigned to the Ttc unit and recalculated using unaltered Ttc data. CS sample 19 was also removed from the original trace element graph (Figure 65 and 66), as the sample was collected adjacent to a skarn contact. Addition of the corrected data and removal of the anomalous samples, decreases data spread in both the oxide and trace element data. Although some elements still lack consistent patterns, data correction produces more defined and condensed patterns within the CS data (Figures 64 and 66).

Samples collected along intrusion contacts include: potassic altered samples 6, 33, and 39, CS samples 89 and 91, and silicified samples 36 and 37 (Figure 6). Potassically altered samples 6 and 39 only show slight variation within the potassically altered trace element data (Figure 26). In general, samples collected along intrusion contacts do not show signs of geochemical interaction between the neighboring intrusive unit.

Because of complexities within the multiphase HPP — such as varying geochemical patterns within the same alteration types, and interactions between skarn contacts, identification of alteration types cannot be simplified to the addition or loss of only one to three trace elements (e.g. Sr and Y patterns in potassically altered samples studied by Ulrich and Heinrich (2001)). Instead, within the multiphase HPP, a combination of hand sample, petrography, and bulk whole rock geochemical data, is required to identify and confirm alteration types. Differentiation of alteration types by intrusive unit, clearly show alteration type signatures vary slightly between each unit. The variations are minor, but within a large data set could produce a wide data spread of mass balance. In some cases, differentiation of the alteration types by intrusive unit, improves the correlation between

alteration types and trace elements. The geochemical patterns of each alteration type do not seem to be affected within a few meters of intrusion contacts. However, more data collected along intrusion contacts is needed to clearly define the extent of interaction between intrusive phases. On the other hand, the geochemistry of the alteration types collected near limestone/skarn pod contacts have been affected. The role of possible carbonate assimilation and skarn alteration will be discussed later.

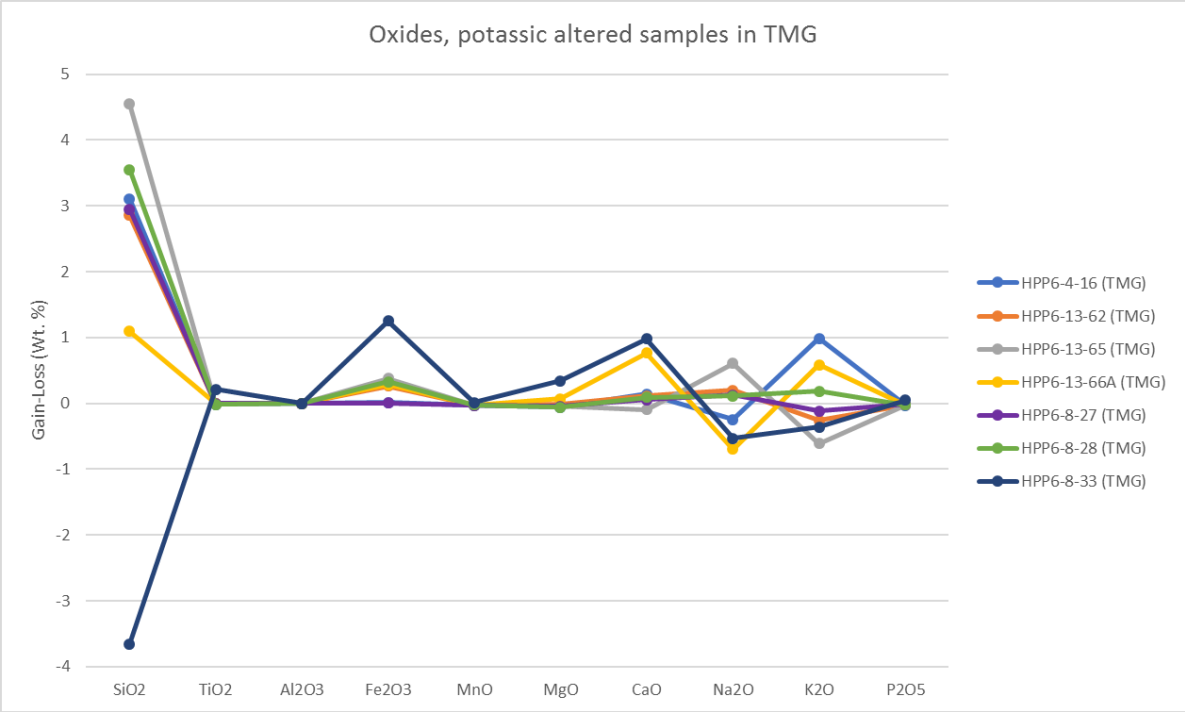

Figure 61: Mass balance data (including samples affected by unit mis-assignment) of the oxides in potassically altered Tmg samples—before corrections and deletions.

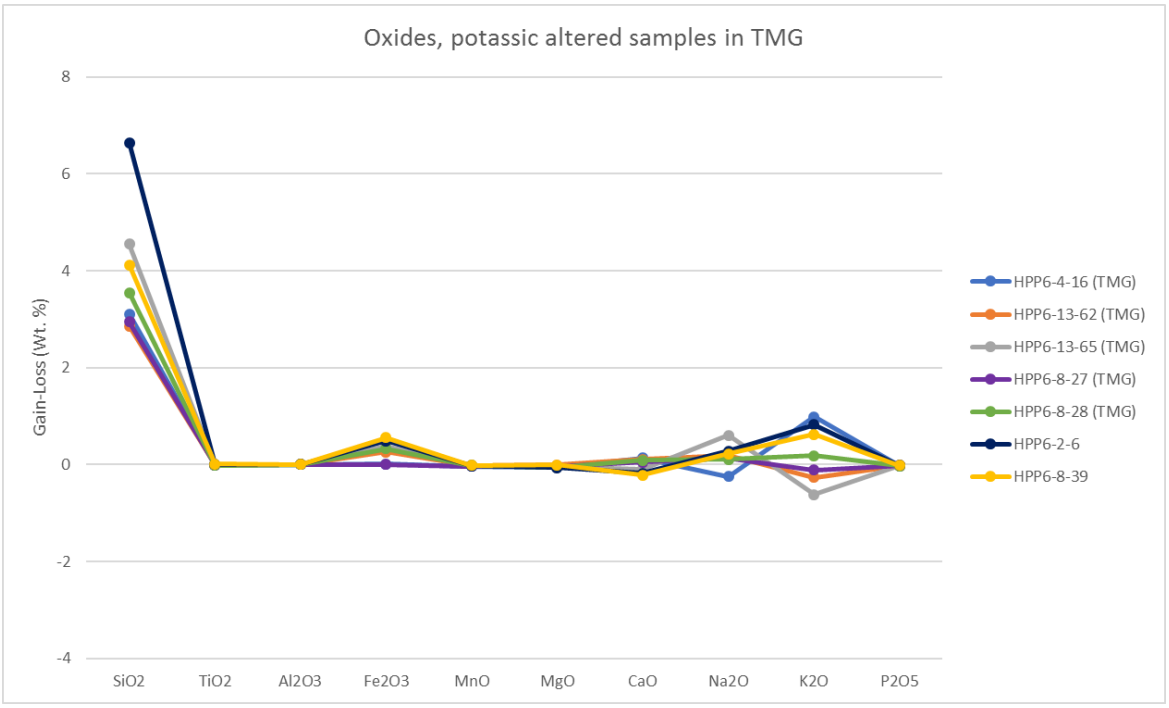

Figure 62: Corrected data for the mass balance of oxides in potassically altered Tmg samples. Samples 33 and 66A were taken out and sample 6 and 39 were added.

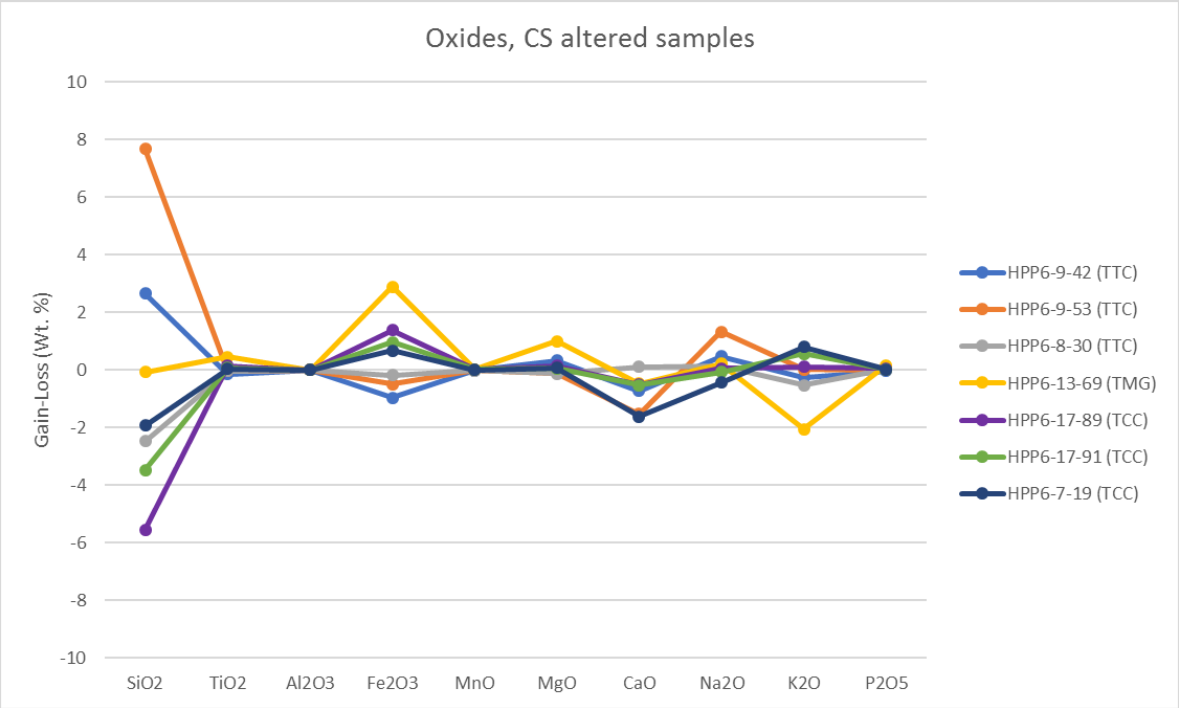

Figure 63: Mass balance data (including samples affected by unit mis-assignment) of the oxides in all the CS altered samples —before corrections and deletions.

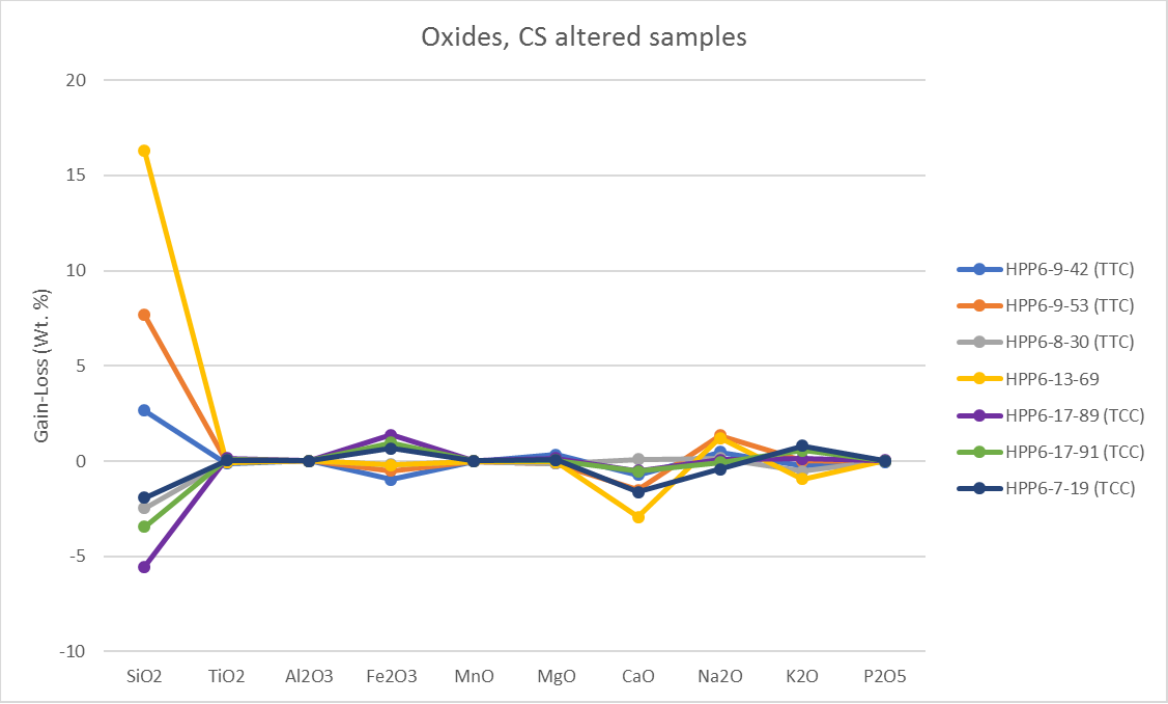

Figure 64: Corrected data for the mass balance of oxides for all CS altered samples. Sample 69 was corrected.

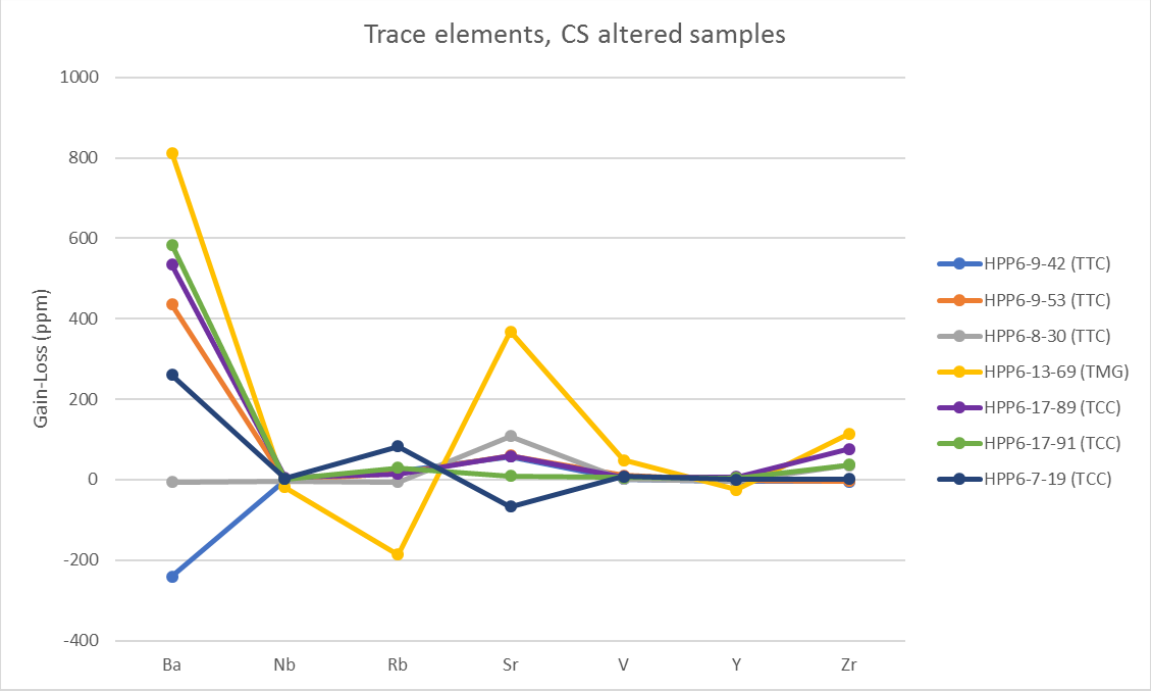

Figure 65: Mass balance data (including samples affected by unit mis-assignment) of trace elements in all the CS altered samples —before corrections and deletions.

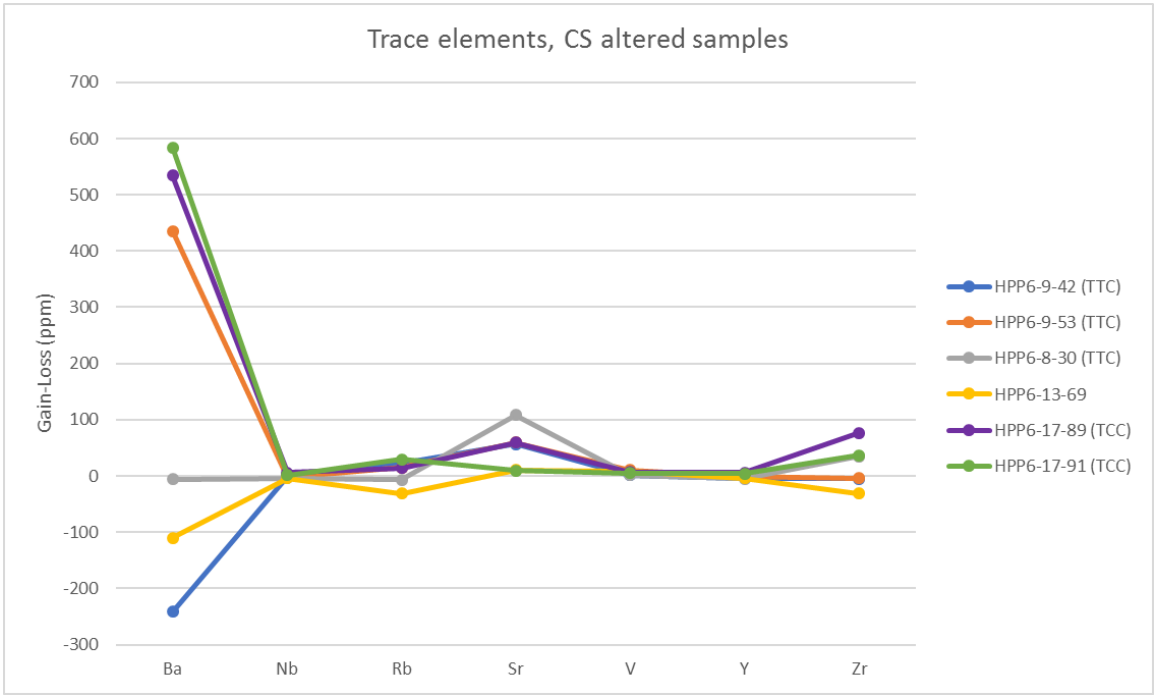

Figure 66: Corrected data for the mass balance of trace elements for all CS altered samples. Sample 19 was removed, and 69 was corrected.

5.3 Fluid flow—Isotope geochemistry of the hydrothermal fluids

Overall, $\delta^{18}O$ values in the quartz separates range from -8 to 18‰, whereas δD values range -189 to -91‰ in biotite, and -199 to -164‰ in chlorite. In combination with fluid temperature estimates from fluid inclusions, these values were used to calculate the isotopic compositions of the hydrothermal fluids responsible for alteration. $\delta^{18}O_{water}$ and δD_{water} values ranged from -12.85 to 12.3‰ and -169 to -31‰ respectively. Data plotted on the δD vs. $\delta^{18}O$ graph produces a curve indicative of interaction between meteoric waters with unusually low δD_{water} (~-160‰ and lower), and magmatic wall rocks. Fluid-wall rock interaction is best displayed in data collected along transects (i.e. in transect 2, the triple contact between epidote rich, CS, and unaltered samples, produces a well-established mixing line between meteoric and magmatic waters (Figure 67)). Furthermore, isotopic data plots in clusters by alteration type, on the δD vs. $\delta^{18}O$ graph. Lastly, finer patterns of fluid infiltration are emphasized by isotopic shifts toward the meteoric water (MW) line, in samples collected near skarn/ limestone pods. The role of limestone assimilation will be discussed in further detail in section 5.4.

On a pluton scale, δD_{water} increases towards the middle of the intrusion, and decreases outwards, while $\delta^{18}O_{water}$ from the center of the HPP overlaps with $\delta^{18}O_{water}$ in samples collected closer to the flanks of the intrusion. Therefore, δD is used to describe pluton scale fluid paths within the HPP intrusion. Lower δD ratios along the flanks of the HPP strongly indicate an interaction with depleted δD_{water}. As meteoric water circulated through the wall rock, and into the flanks of the HPP system, it left hydrous minerals low in δD (~-160‰ and lower). But as water continued to circulate up towards the middle of the HPP, interaction with the granitic rocks gradually produced waters with higher δD

(~-130‰ to -100‰), and shifted isotopic ratios along a reaction curve. By the time the evolved meteoric waters (now devoid of the original depleted δD ratios) reached the center of the system, interaction with magmatic waters left samples with primary magmatic signatures. The geometric distribution of the isotopes throughout the HPP indicates δD and $\delta^{18}O$ imprinted the entire pluton, and that the multiple phases had no effect on isotope distribution. Large scale fluid geometries within the HPP correlate to meteoric paths displayed in porphyry deposits by Seedorff et al. (2008). The large-scale interaction between depleted meteoric waters and the HPP was previously unrecognized in the fluid inclusion isotope data by Gates (2016), as hydrogen data was not obtained.

The geographical distribution of alteration types within the HPP also support the regional fluid paths delineated by δD data. Potassic alteration, typically associated with magmatic fluids (Dilles et al., 1992), occurs in the middle of the HPP, and corresponds to the samples that plot in or near the magmatic box. CS alteration is predominately closer to the flanks of the HPP, and was caused by fluids similar to depleted meteoric waters (Figure 68). Isotopic relationships between the hydrothermal fluids and alteration types are clearly shown on the δD vs. $\delta^{18}O$ graph; samples are differentiated by alteration type, and plot in clusters which correspond to distinct isotopic ranges (Figure 59). Isotopic data of the HPP potassic samples cluster in a similar range and fashion to samples from the Ann Mason Porphyry system, and only differ slightly in δD due to differences in intensity of meteoric signature (Dilles et al., 1992). However, CS isotopic data does not correlate with the data from phyllic/sericite altered rocks from Ann Mason (mixture of magmatic and meteoric fluids), most likely due to the pervasive interaction at the HPP with extremely depleted meteoric waters.

Fluid temperature constraints are consistent with the inferred fluid pathways and alteration geometries. Fluid temperatures were generally hotter near the center of the HPP (marked by potassic alteration) and cooled outward. Although, it should be noted that the western side of the pluton records slightly higher temperatures than the east, as these rocks represent greater depths within the system. The combination of isotopic, alteration, and temperature data, illustrates the large-scale fluid pathways in the HPP as: initial magmatic pulse from below, with concurrent and late circulating depleted meteoric waters along the flanks of the HPP system, which evolve, become heavier in δD, and rise though the center of the system (Figure 68).

The source of the depleted meteoric waters in the RMEHR has been speculated by Fricke et al. (1992) and Wickham et al. (1993). Both studies provide evidence of meteoric infiltration within the RMEHR core complex and mylonitic shear zones. In both studies, the $\delta D_{mineral}$ data from samples that interacted with the low δD waters generally ranged from -175 to -80 ‰. The role of meteoric infiltration is supported by δD in volcanic glass from samples in/near northeastern Nevada, and proved meteoric water in the region was depleted (δD = -179 to -169 ‰) during the Miocene mylonitization event in the Ruby Mountains (17 to 10 Ma) (Mulch et al., 2008). Mulch et. al. (2008) determined the regional isotopic depletion of meteoric waters was caused by orographic and continentality effects. The waters that interacted with the Eocene HPP intrusion after its emplacement are similar to those recorded by Mulch et al. (2008), and geographic landscapes in the Eocene are thus interpreted similar to those of the Miocene.

Extremely low $\delta D_{mineral}$ values (<-165‰) constituted only a minor portion of the data collected by Fricke et al. (1992) and Wickham et al. (1993), whereas low $\delta D_{mineral}$ values dominate in biotite and chlorite separates from the HPP. Unlike data in this study, the rarer occurrences of depleted $\delta D_{mineral}$ (<-165‰) in studies by Fricke et al. (1992) and Wickham et al. (1993), may simply reflect differences in infiltration and volumetric differences of meteoric water between Eocene and Miocene times. Isotopic differences may also indicate fluid conditions, such as temperature, during the HPP emplacement gave larger hydrogen isotope fractionations between micas and water.

Moreover, calculated δD_{water} from HPP samples may also be skewed due to the poorly constrained fractionation factors of micas, displayed as a "kink" in the fractionation curve around 250-350 °C. This "kink", may have caused a ~20‰ decrease in δD, producing the low δD_{water} results. If corrected, values would plot closer to δD_{water} values from Fricke et al. (1992) and Wickham et al. (1993). More work is needed to fully understand and model the fractionation curves of micas.

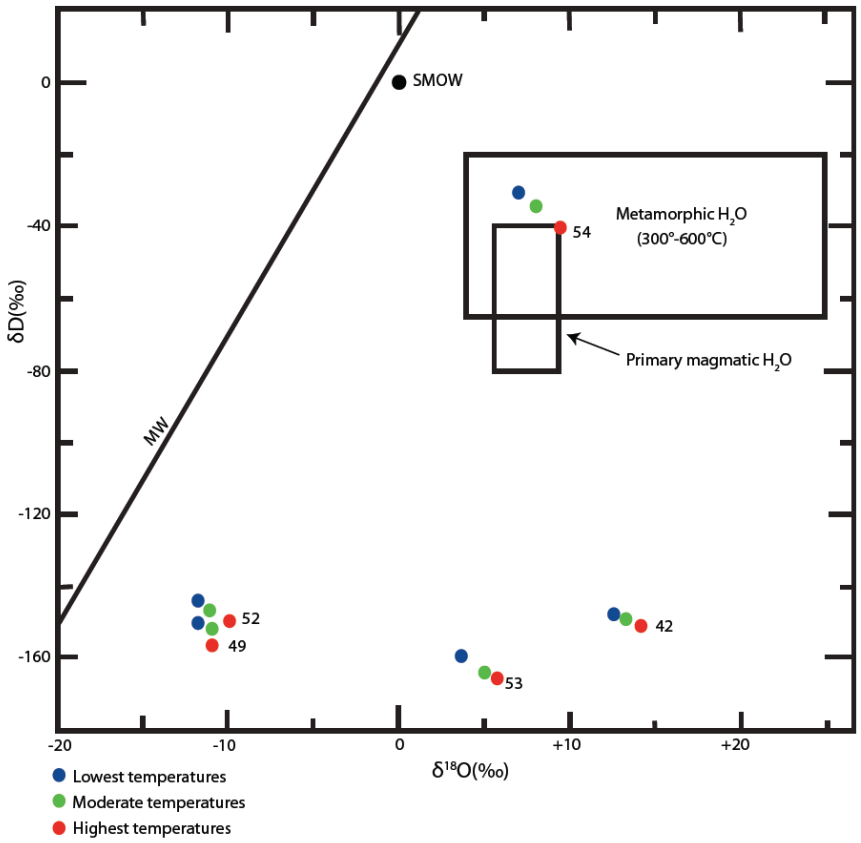

Figure 67: δD and $\delta^{18}O$ ratios of the hydrothermal waters in samples from transect 2. Samples 52 (epidote rich), 53 (CS), and 54 (unaltered) are part of the triple contact in the northwest end of transect two. Sample 42 (CS) and sample 49 (endo-skarn) were collected southeast of the contact.

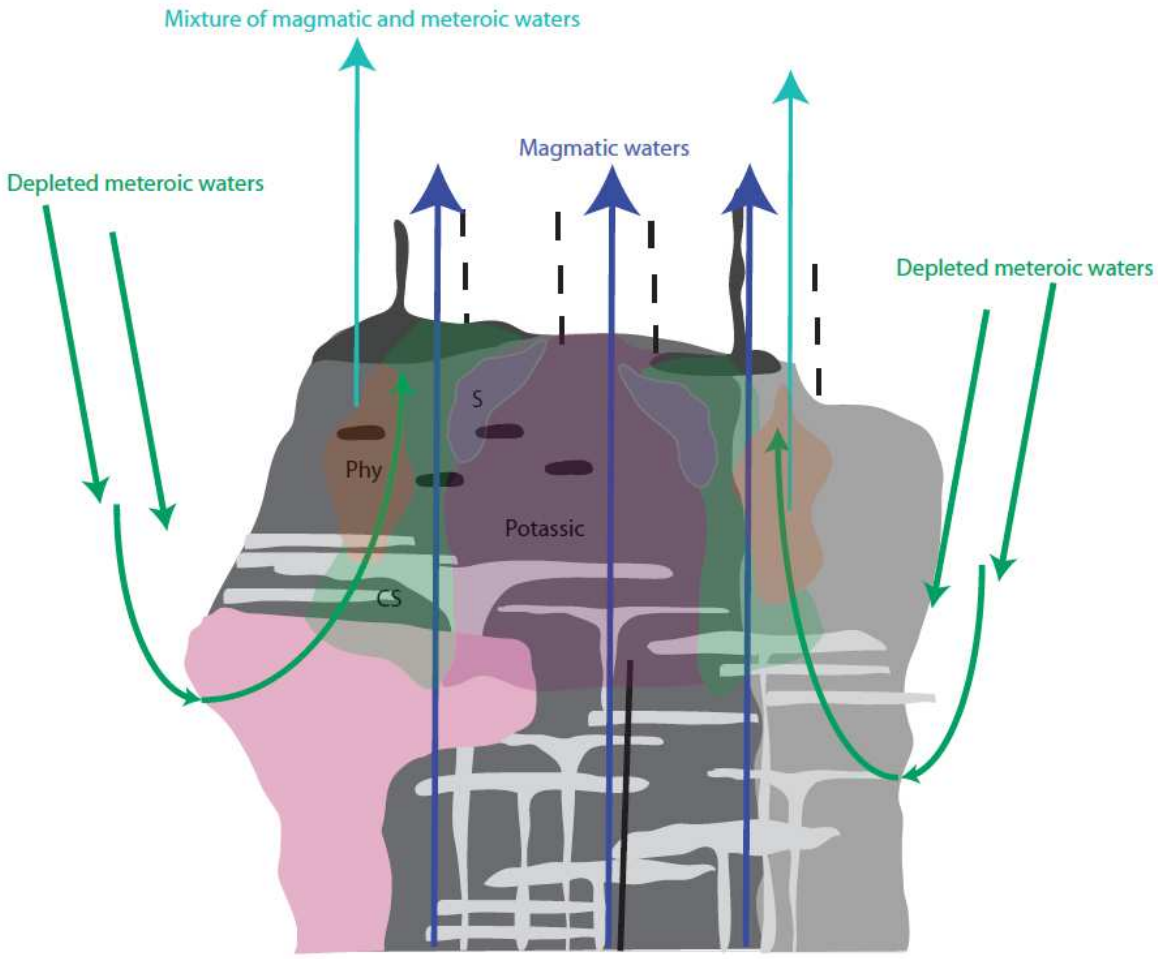

Figure 68: Interpretation of the position of the major alteration types and the pluton scale fluid paths around and within the HPP. Pink=potassic, purple=silicification, green=chlorite sericite, and orange=phyllic.

5.4 Role of carbonate assimilation and skarn alteration

In addition to the pluton scale fluid flow geometries, small fluid pathways (3-20 m) with unusual alterations are due to the interaction between the intrusive units and skarn/ limestone pods scattered within the HPP, and emphasized by REEs, trace element, and isotope data. Local-scale fluid interactions are best interpreted from data differentiated by location. Potassically altered samples in the middle of the Tmg, just south of Toyn Creek (transect 1), were collected at various distances, west along traverse towards an exo-skarn in a xenolith. REEs, CaO, Ba, Sr, Y, and Zr concentrations increased towards the exo-skarn contact, while isotopes shifted from magmatic in signature towards the MW line (decrease in δD and $\delta^{18}O$) (Figures 69-72). Tmg samples near the triple intrusion contact, north of Corral Creek, collected south along a ridge riddled with exo-skarn, endo-skarn, and limestone pods (transect 4), start with magmatic fluid signatures, and shift towards the MW line in samples closer to pod contacts (Figure 71). As opposed to transect 1, REE concentrations increase away from the pods, and are highest in the potassically altered sample, while Ba, Sr, Y, Zr, and TiO_2 (see mass balance results for sample 33 in Appendix 2, Table 4) were mobile (enriched or depleted) during alteration (Figures 73-76). Variances in REE behavior between transect one and four reflect differences in degree of limestone alteration, as limestone xenoliths in transect four were lightly (if at all) altered.

Samples from the isolated southwest Ttc inlier, located south of Pearl Creek within the contact metamorphic aureole (transect 5), record some of the lowest δD and $\delta^{18}O$ ratios in the HPP, while Ba, Rb, Sr, V, Y, Zr, TiO_2, and P_2O_5 (see mass balance results for samples 68 and 69 in Appendix 2, Table 4) were mobilized during alteration (Figures 77-79). These samples, from the small inlier, are interpreted to have reacted with the meta-carbonate

wall rocks upon assimilation, and later with skarn xenoliths within the intrusion. Finally, in samples from the eastern portion of the Tcc unit, southwest of Harrison Pass Creek, and adjacent to the Star mine (transect 7), REE concentrations and δD and $\delta^{18}O$ decrease towards the skarn contact (Figures 80 and 81). Lower REEs, depleted Zr, P2O5, TiO2, and enriched Ba and Sr in the sample adjacent to the skarn xenolith, suggests remobilization of these elements into the skarn (Figures 82 and 83) (see mass balance results for sample 18, 19 and 20 in Appendix 2, Table 4).

The four local fluid pathways (3-20m), identified adjacent to skarn/limestone xenoliths, do not display consistent REE patterns, as REEs either increase or decrease towards the xenoliths. Mobilization of Y, Zr, and lesser amounts of P_2O_5 and TiO_2, remains a consistent pattern within and around the local fluid pathways, however intensity of mobilization varies. Oxygen and hydrogen isotopes consistently decrease progressively in samples closer skarn/limestone xenolith contacts, suggestive of an increased meteoric water interaction around the skarn/limestone pods.

Although fractional crystallization of the HPP cannot be ruled out, the localized mobilization of "immobile" elements, indicate some local interaction between the magma and skarn/limestone pods. A recent study by Van Dongen et al. (2010) proposes Y, Zr, P, Ti, and REEs are mobile under certain conditions such as those in ore-forming magmatic-hydrothermal systems, and can then be precipitated in nearby skarns. Although the salinity of the HPP is lower than that of typical porphyry type systems (Gates, 2016), the fluids were likely both oxidized and hot enough to cause mobilization of otherwise immobile elements. Another clue indicative of limestone interaction with the magma, are the CO_2 rich

fluids encountered by Gates (2016). The fluids were originally speculated to represent later CO_2 rich pulses, however CO_2 fluids could alternatively be a result of reactions between the limestone xenoliths and HPP. Throughout the HPP, skarn/limestone pods may be "invisible", not at surface or eroded away. Although Barnes et al. (2001) mapped a few of the meta-carbonate lenses throughout the eastern and western edges of the Tcc unit, and numerous lenses were identified by the author, the extent and localities of the remaining limestone/skarn xenoliths are unknown. These pods clearly play a role in local scale reactions capable of mobilizing immobile elements. Therefore, depending on the distribution of the skarn/ limestone xenoliths, these alteration patterns can repeat and overprint one another. If skarn/limestone pods are missed, the alteration fingerprints left behind in the adjacent samples may be misinterpreted, or even overlooked.

The possibility of skewed REEs and trace element data due to fluid-limestone+skarn interaction and in various hydrothermally altered samples (Van Dongen et al., 2010), presents an interesting question. Skarn/ limestone xenoliths along with hydrothermal alteration were not mentioned, and only mapped as pods within the Tcc unit, in the study by Barnes et al. (2001). At first glance, especially if not explicitly sought for, most granitic outcrops do not appear hydrothermally altered. However, although difficult to distinguish at times (as shown in this study), many of the granitic outcrops throughout the HPP are hydrothermally altered. Due to the mobility of REEs and trace elements in systems like the HPP, more emphasis should be placed on regional geology (i.e. wall rocks), especially since Ebadi and Johannes (1991) have shown interaction between granitic melts and carbonates affects fractional crystallization of orthoclase and quartz. This may explain why slicification in the HPP is commonly associated with limestone/skarn xenoliths. Addressing how such

parameters could affect geochemical results, is especially important when using REEs to define and distinguish the petrology of multiple evolved magmatic pulses.

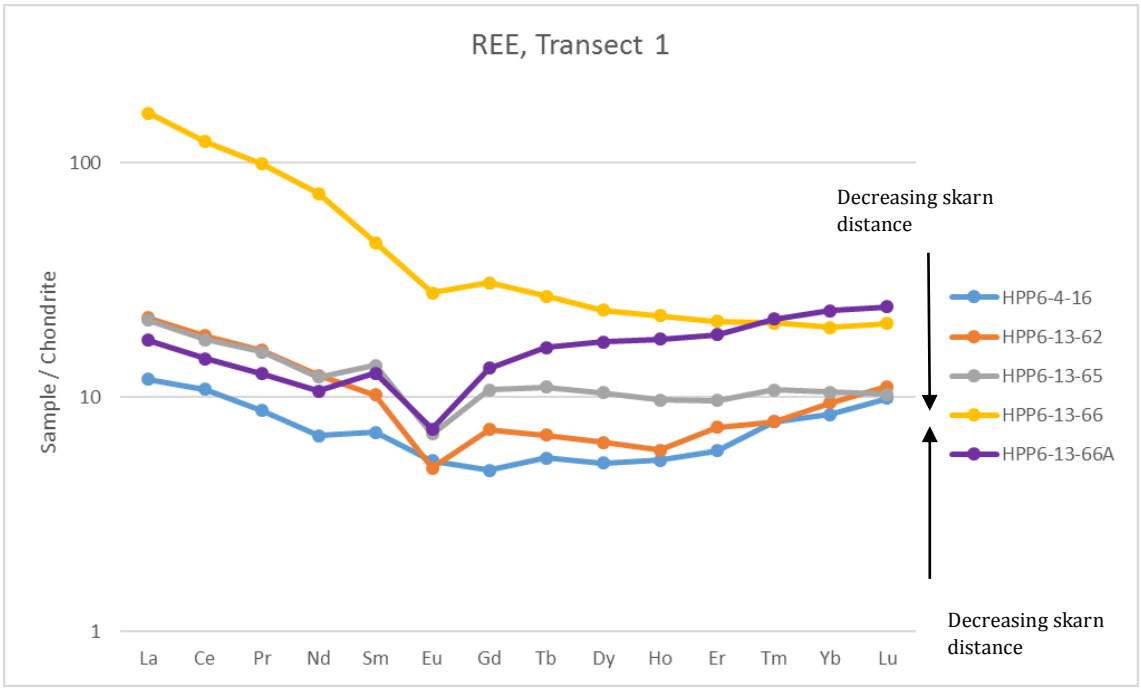

Figure 69: REEs of samples from transect 1. Sample 16 was collected furthest from the skarn xenolith (sample 66), and sample 66 A collected the closest on the opposite (west) side.

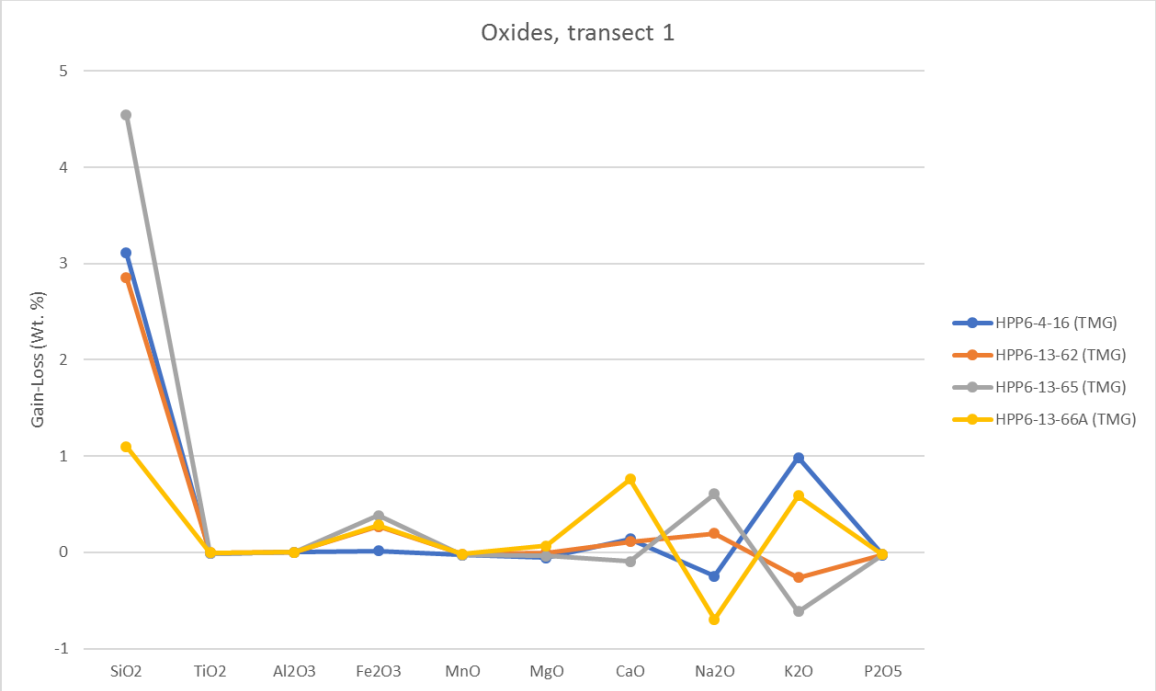

Figure 70: Mass balance of oxides along transect 1. Sample 16 was collected furthest to the skarn contact and 66A closest.

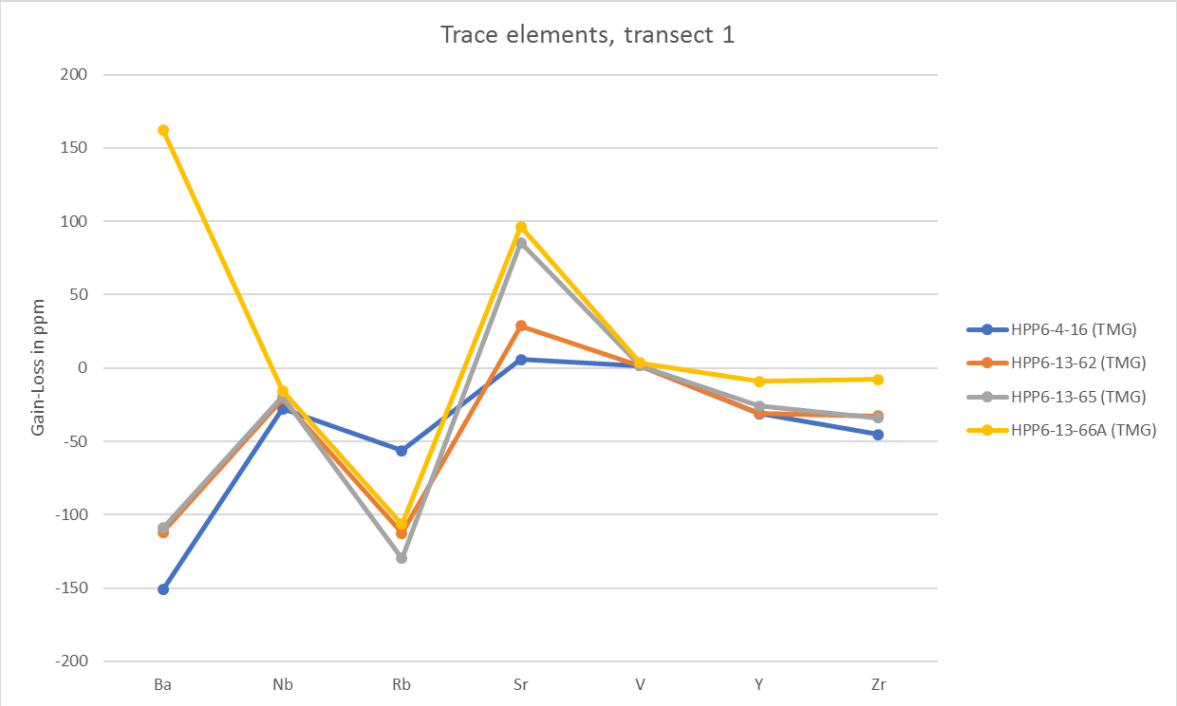

Figure 71: Mass balance of trace elements in samples from transect 1.

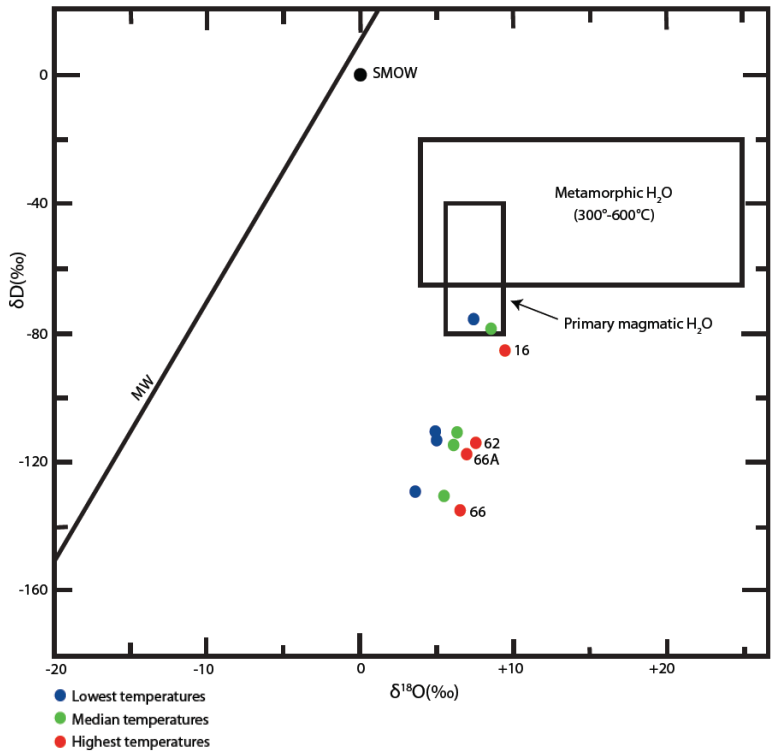

Figure 72: D and $\delta^{18}O$ ratios of the hydrothermal waters in samples from transect 1. Progression of samples: sample 16 was collected furthest from the skarn, 62 in the middle, and 66A directly adjacent to skarn sample 66.

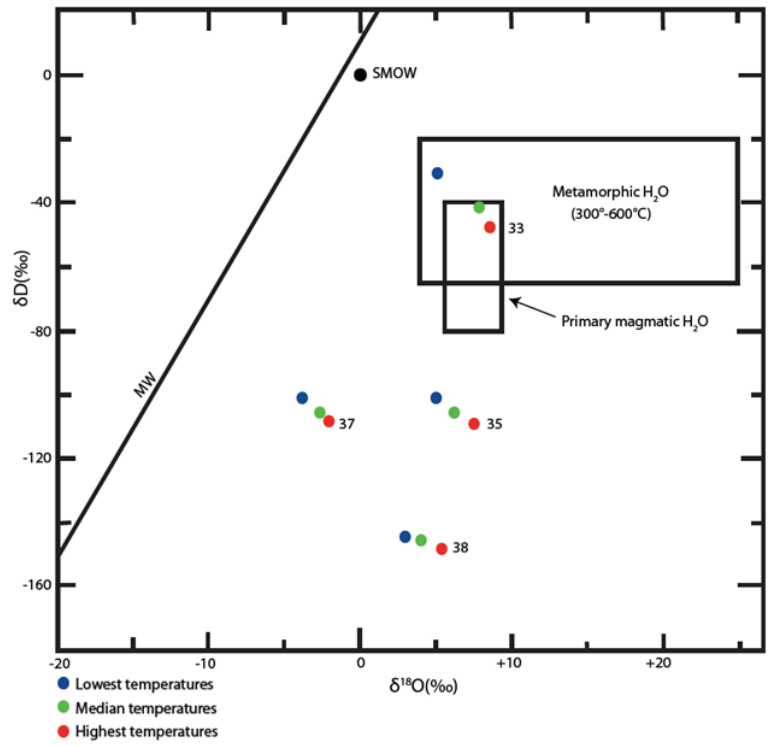

Figure 73: δD and $δ^{18}O$ ratios of the hydrothermal waters in samples from transect 4. Sample 33 was collected furthest from the limestone/skarn xenoliths, while samples 35, 37, and 38 were collected along the ridge riddled with limestone, exo-skarn, and endo-skarn pods.

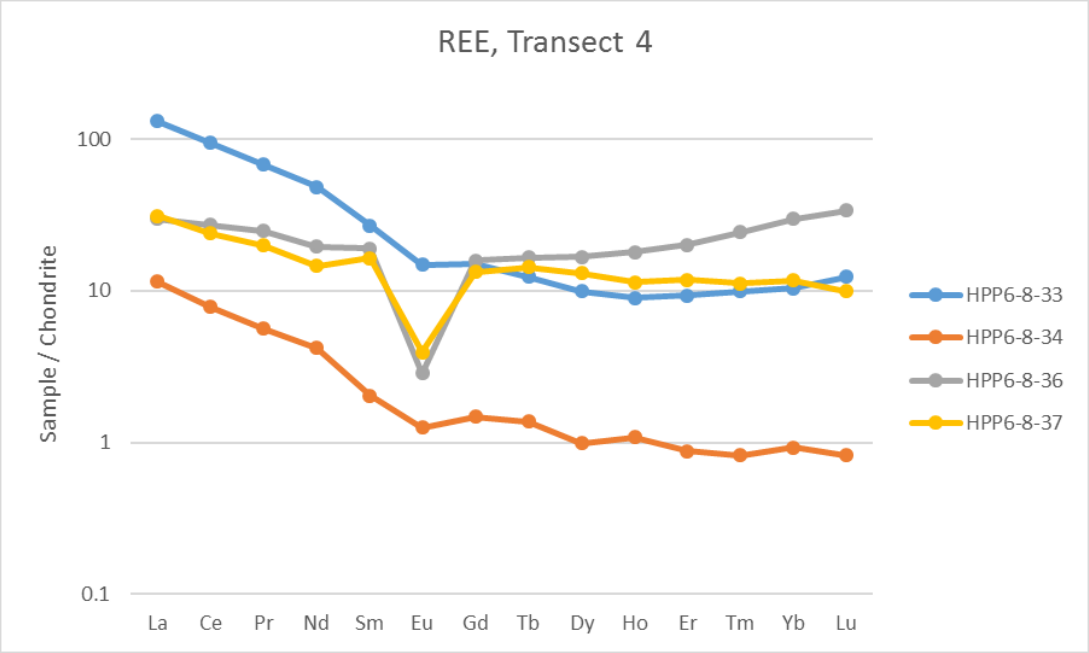

Figure 74: REEs of samples from transect 4 within the TMG. Sample 33 was collected furthest from the skarn/limestone xenolith (sample 34). Samples 36 and 37 were collected in-between.

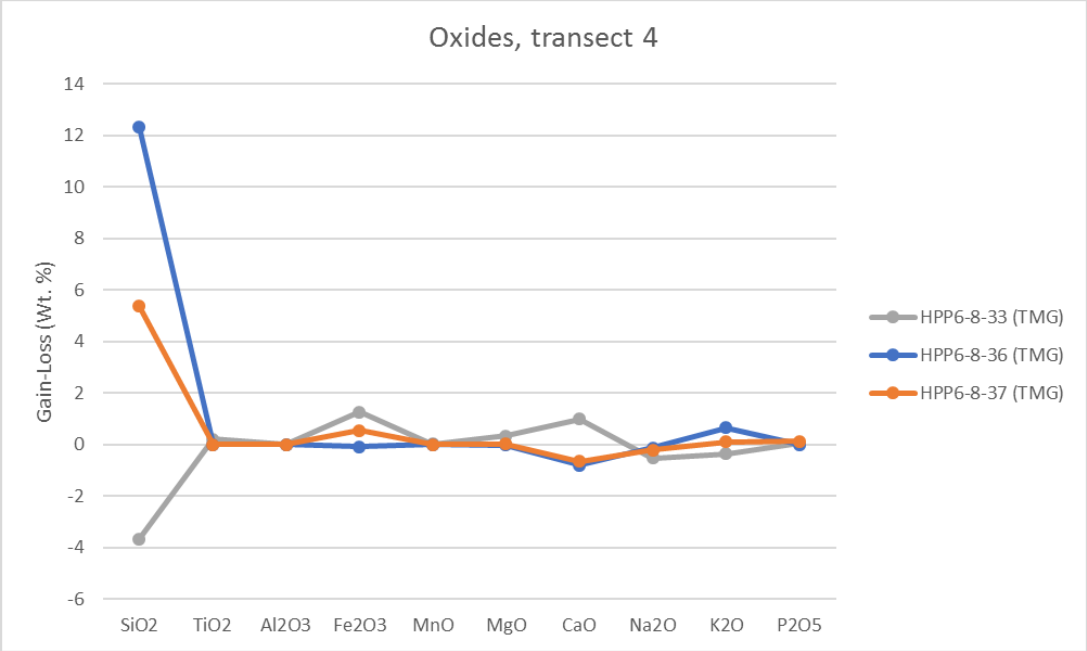

Figure 75: Mass balance of oxides along transect 4. Sample 33 was collected furthest from the skarn/limestone xenolith (sample 34). Samples 36 and 37 were collected in-between. Sample 33 has been re-assigned as Ttc for mass balance calculations.

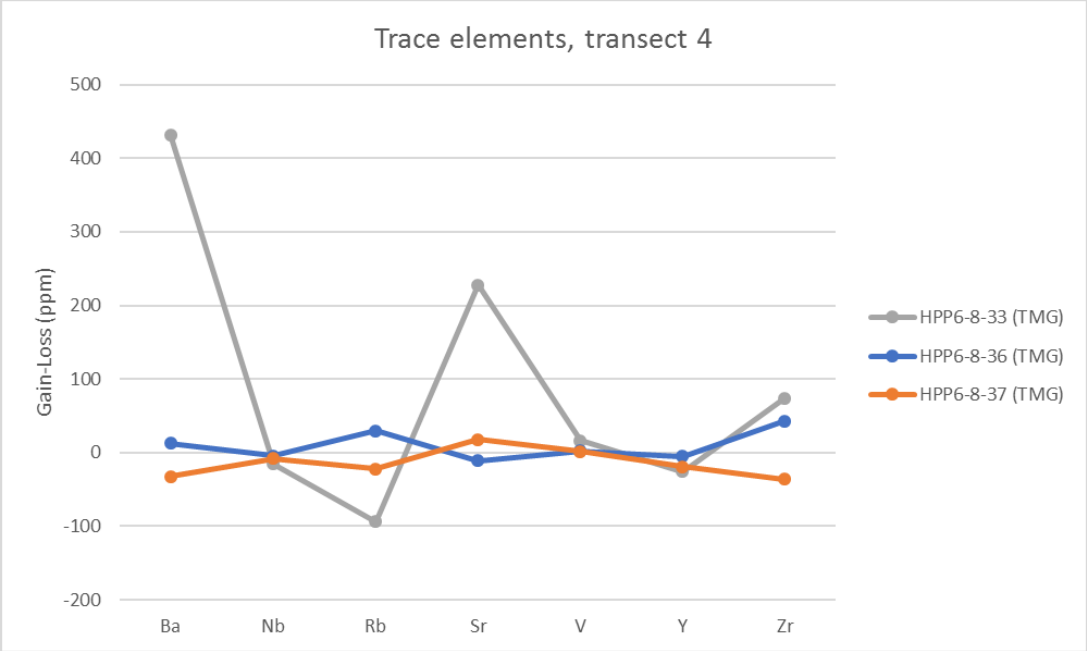

Figure 76: Mass balance of trace elements in samples from transect 4. Sample 33 was collected furthest from the skarn/limestone xenolith (sample 34). Samples 36 and 37 were collected in-between. Sample 33 has been re-assigned as Ttc for mass balance calculations.

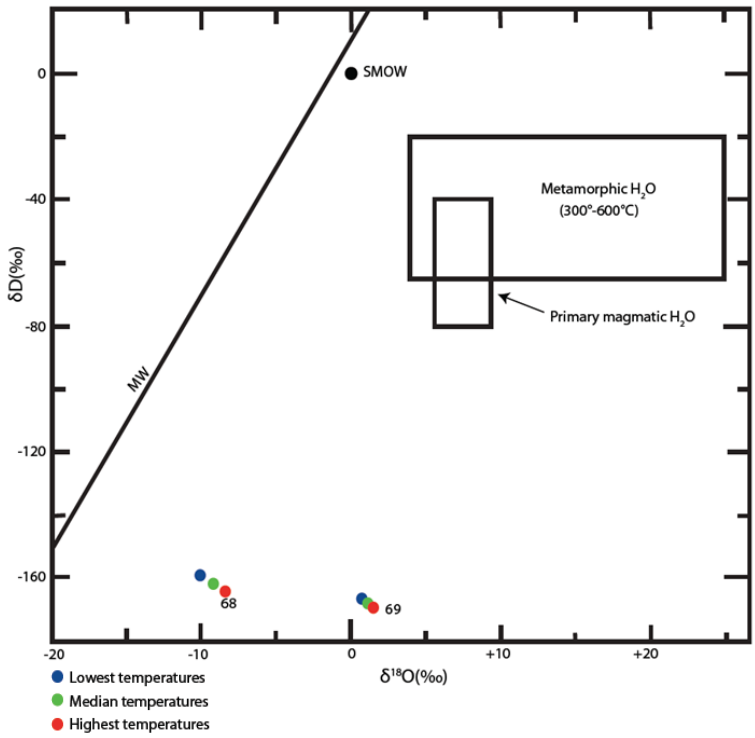

Figure 77: δD and $\delta^{18}O$ ratios of the hydrothermal waters in samples from transect 5. Both samples collected within a Ttc inlier surrounded by meta-carbonates, that contained numerous endo-skarn and limestone xenoliths.

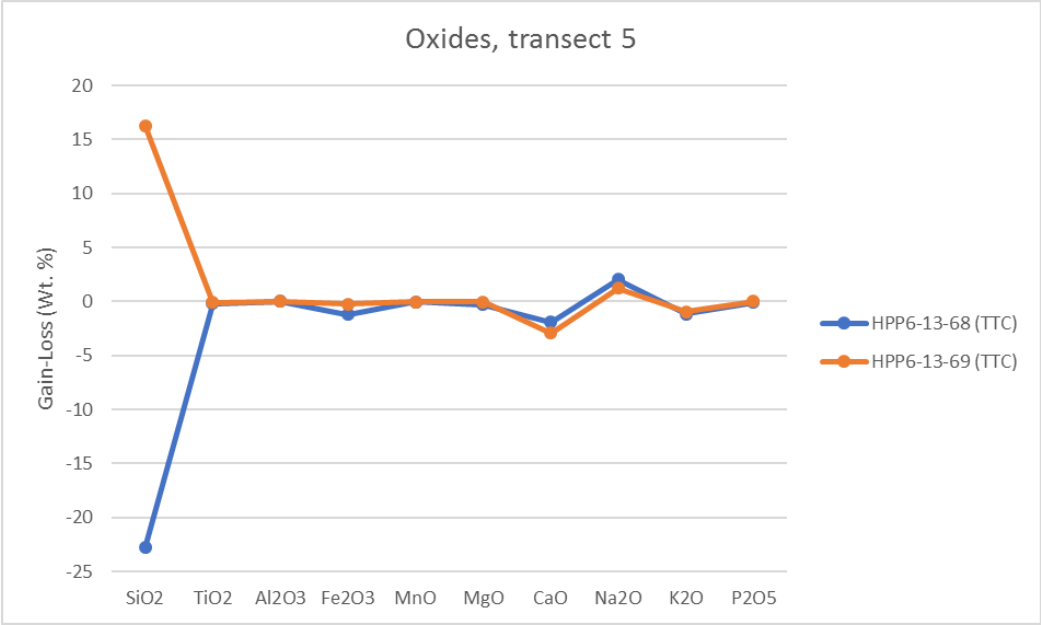

Figure 78: Mass balance of oxides along transect 5. Both samples collected within a Ttc inlier surrounded by meta-carbonates, that contained numerous endo-skarn and limestone xenoliths. Both samples have been re-assigned as Ttc for mass balance calculations.

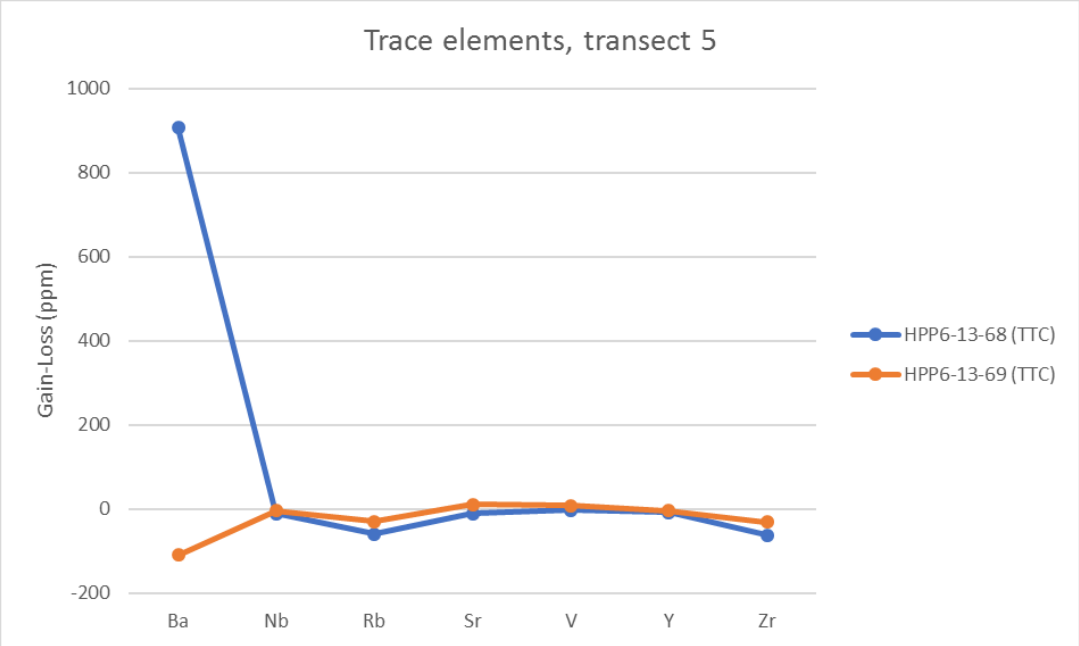

Figure 79: Mass balance data of trace elements in samples from transect 5. Both samples collected within a Ttc inlier surrounded by meta-carbonates, that contained numerous endo-skarn and limestone xenoliths. Both samples have been re-assigned as Ttc for mass balance calculations.

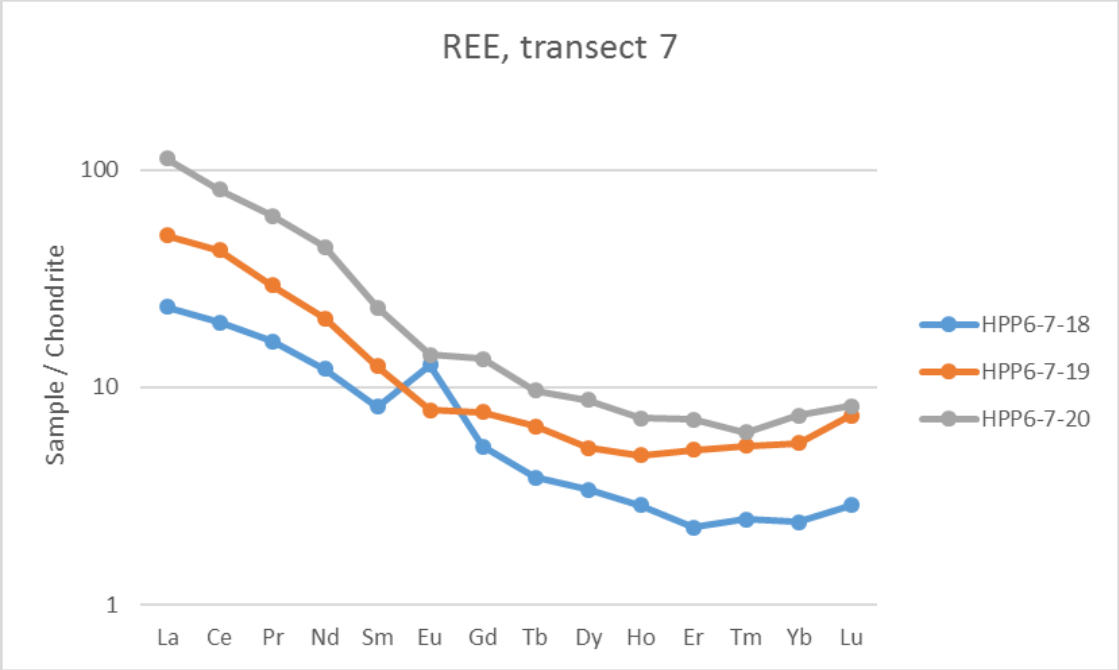

Figure 80: REEs of samples from transect 7 within the TCC. Sample 18 was collected closest to the skarn contact, 19 in-between sample 18 and 20, and sample 20 collected the furthest from the skarn.

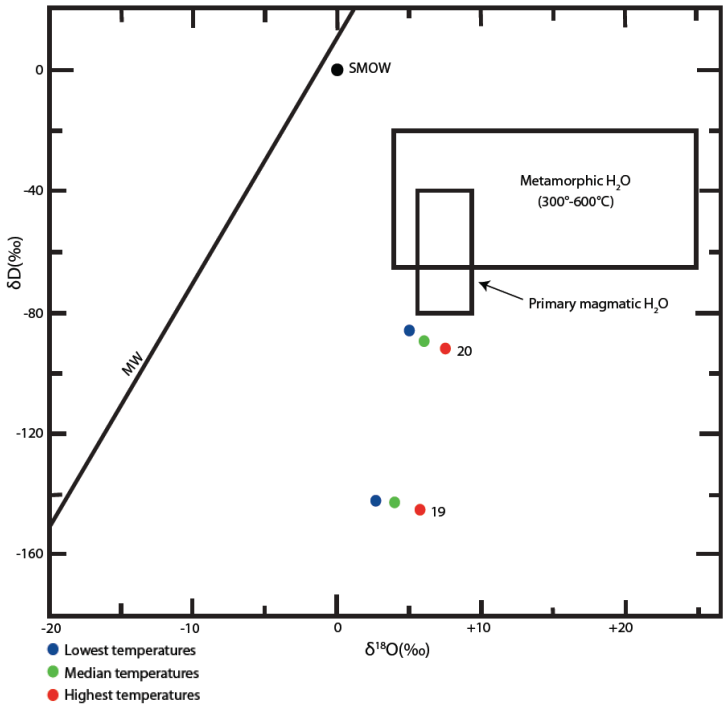

Figure 81: δD and $\delta^{18}O$ ratios of the hydrothermal waters in samples from transect 7. Sample 19 was collected closer to the skarn contact, and sample 20 collected the furthest away.

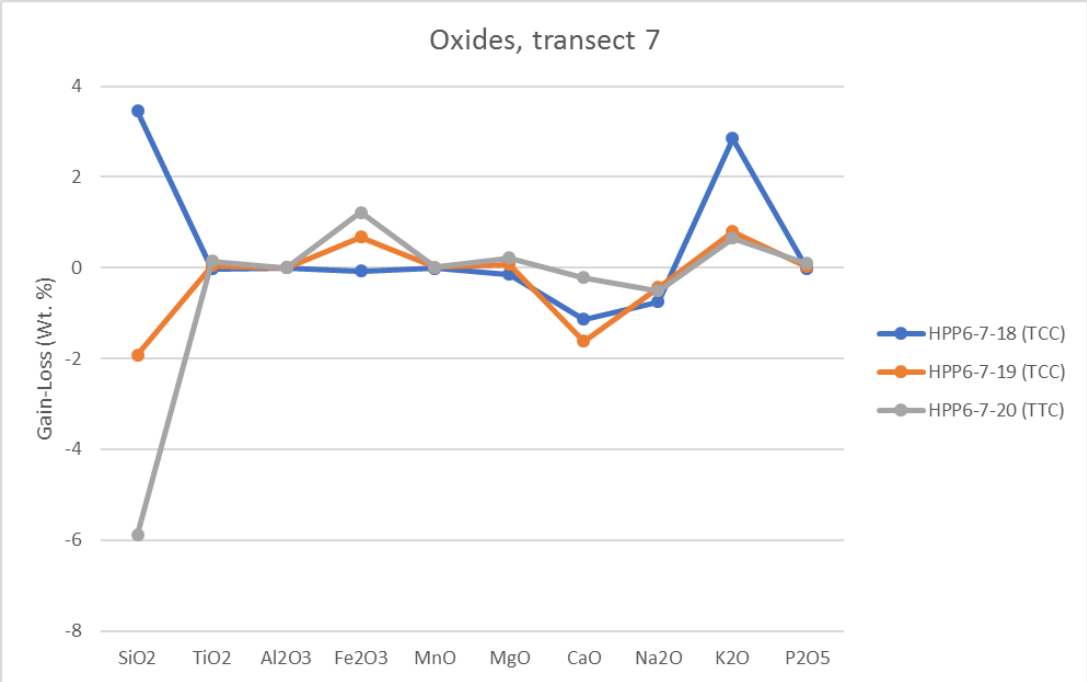

Figure 82: Mass balance of oxides along transect 7. Sample 18 was collected closest to the skarn contact, 19 in-between sample 18 and 20, and sample 20 collected the furthest from the skarn.

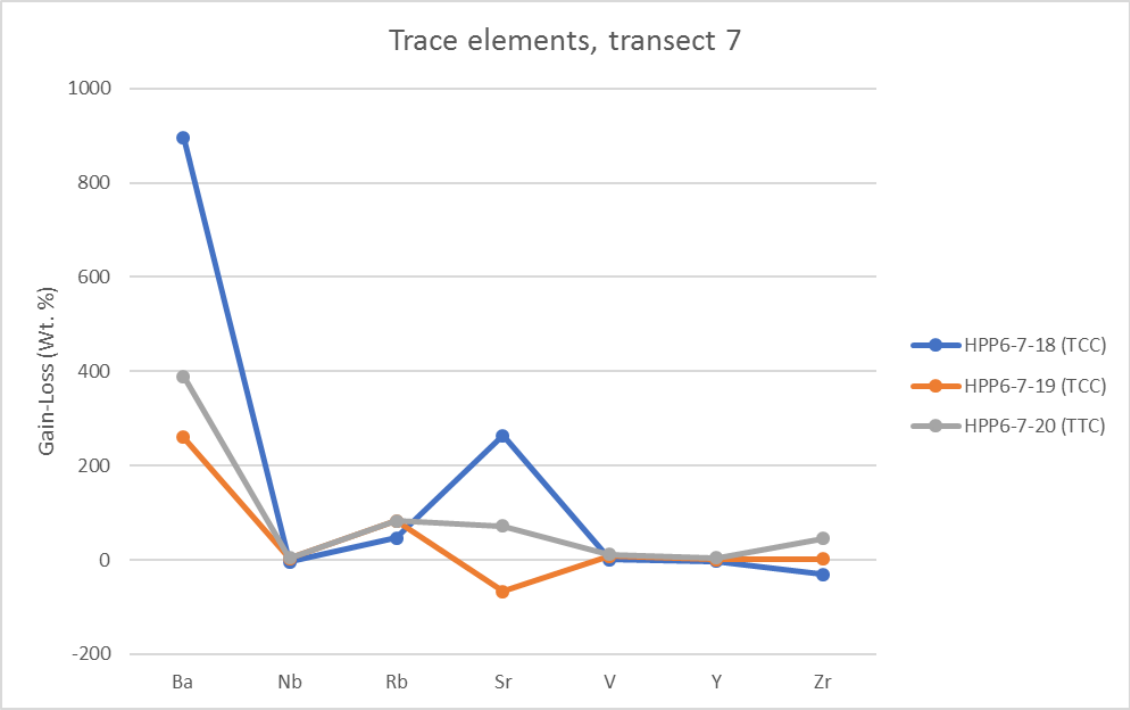

Figure 83: Mass balance of trace elements in samples from transect 7. Sample 18 was collected closest to the skarn contact, 19 in-between sample 18 and 20, and sample 20 collected the furthest from the skarn.

5.5 Implications of a porphyry root

Porphyry root features found within the HPP include: large quartz±feldspar±muscovite aplitic dikes and veins, potassic, CS, phyllic (observed by Musekamp (2011) and Gates (2016)) and endoskarn alteration (alteration similar to the calcic type described by Seedorff et al. (2008)). Alteration types missing within the HPP, typically found in root systems, include sodic and greisen alteration. Other differences include the strong meteoric water signatures within the CS samples, which do not agree with fluid source interpretations by Seedorff et al. (2008) (Figure 4). Geometries of the alteration zones throughout the HPP mimic the depiction of the possible arrangement of alteration types observed by Seedorff et al. (2008) in root zone systems. In both the HPP and model by Seedorff et al. (2008), potassic alteration is situated in the center near the top of the root, with CS and phyllic alteration around the periphery. If the HPP represents the top of a porphyry root system, greisen and sodic alteration may be present at depth.

Estimates of the depth of HPP emplacement range from 4-18 km (Burton, 1997; Barnes et al., 2001; Colgan et al., 2010; Gates, 2016), deep enough to underlie a porphyry ore system. Although metal concentrations within the HPP are low in comparison to mineralized systems, and are not markedly enriched in any alteration type, skarns surrounding the HPP rich in Cu, Pb, and Zn oxides and tungstates, have been exploited along the HPP contact zone. Mineralization around the HPP may be relict of metal rich fluids that continued to rise through the system, leaving the root barren. If metal rich fluids formed an ore body above, depending on the location and orientation of the deposit, either the Ruby detachment fault slid the ore body west or erosion removed the ore eastward into the basin. The HPP shares many characteristics with the porphyry root zones described by

Seedorff et al. (2008), but not enough to with certainty label the HPP as a porphyry root. Results show the importance of increased studies of porphyry root systems and the ability of recognizing these systems, as undiscovered deposits may linger close by.

6 SUMMARY AND CONCLUSION

The HPP is a multiphase granitic pluton in the Central Ruby Mountains, Nevada, emplaced during the Eocene (36 Ma) in two major stages: tonalitic-monzogranite magmas (Ttc and Tcc), and monzogranite (Tmg and Tgm) with sparse mafic dikes. Since the pluton is the only known exposed intrusion coeval and similar in size and shape to the intrusions beneath the Carlin-type (gold only) ore deposits in Nevada, previous studies by Musekamp (2011) and Gates (2016) focused on the fluids that migrated around and within the HPP. A review of the petrological study by Barnes et al. (2001), in addition to alteration data collected by Musekamp (2011) and Gates (2016), emphasized the need to study the chemistry and geometry of hydrothermal alteration zones within the HPP. To understand the effects multiphase plutonic systems have on the geochemistry and fluids responsible for the various alteration types, petrological, whole rock geochemical, fluid inclusion, and isotope studies were conducted. In addition, reconnaissance studies by Musekamp (2011) and Gates (2016) reveal the distribution of alteration types throughout the HPP do not fit alteration geometries typically displayed in and above porphyry systems. The unusual alteration geometries led to the investigation of the HPP as a possible exposure of the roots of a magmatic-hydrothermal system.

Alteration types identified within the HPP include potassic, CS, silicification, endoskarn, and phyllic (identified by both Musekamp (2011) and Gates (2016)). Alteration facies throughout the HPP were mapped and samples were collected from each intrusive unit. Thin sections of forty-seven representative samples were analyzed to confirm hand sample identification of alteration types. Seventeen samples were further selected for fluid

inclusion analysis, and used to determine the temperature and salinity of the hydrothermal fluids responsible for alteration. Results of the whole rock geochemical analysis from altered samples, were used for both the petrological and geochemical analyses. Petrological and geochemical data was first compared to data from Barnes et al. (2001), to evaluate similarities and differences between data. Whole rock geochemical data was then used to quantify the intensity of and identify geochemical trends of each alteration type, by calculating the mass balance of alteration using the EASYGRESGRANT program developed by López-Moro (2011). Quartz, biotite, and chlorite separates were then selected from representative altered samples, and analyzed for oxygen and hydrogen isotope ratios. Calculating δD and $\delta^{18}O$ of the hydrothermal waters shows whether single or multiple fluid types were responsible for the alterations, and is used to infer pluton and local scale fluid pathways.

Petrological data suggest the current geological map of the HPP should be updated to account for the westward extent of the Ttc and eastward extent of lenses of the late Tmg. Multi-element and REE data of samples collected from the isolated Tmg granitic inlier, southwest of the main HPP intrusion, suggest the isolated inlier is instead part of the Ttc. A sample collected along the eastern most extent in the Tmg unit revealed the same results. In addition, petrological data of two Tcc samples, suggest they instead belong to the Tmg unit. The interpretation of the HPP intrusive suites made by Barnes et al. (2001) supports the addition of numerous Ttc and Tmg lenses to the HPP map, as both map and cross-section present the Tmg as sheets and lenses through the Ttc and Tcc units, and contains several more mafic Ttc lenses outcropping in the Tmg unit. The remaining outliers within

the petrological data were interpreted to either indicate 1.) unidentified felsic/mafic pods 2.) new, undescribed intrusive units, or 3.) moderate to pervasive hydrothermal alteration.

Differentiated data by intrusion unit and alteration type, accentuate several samples within the potassic, CS, and endoskarn altered rocks, as geochemically anomalous. Based on REE and multi-element analyses, it was discovered that some samples were compared to incorrect unaltered standards (i.e.: unaltered Ttc, Tcc, or Tmg) for the mass balance of alteration analysis, which caused several of the samples to plot as outliers. On correct comparison to their respective unaltered standard, these samples no longer plotted as anomalies. The remaining outliers were all collected adjacent to skarn/limestone xenoliths, and the compositions interpreted to be attributed to variable fluid conditions between granite-skarn contacts. Additionally, the three exo-skarn samples collected within the Tmg unit clearly illustrate different degrees of alteration plus differences in original lithology of the limestone xenoliths within the HPP.

The remaining data, differentiated by unit, clearly show alteration type signatures vary slightly between each unit. The variations are minor, but within a large data set could produce a wide data spread. The geochemical patterns of each alteration type do not seem to be affected within a few meters of contacts between the intrusive phases, but more data is needed to clearly understand the extent of interaction between intrusive phases. Due to these complexities within the multiphase HPP, identification of alteration types cannot be simplified to the correlation of only one to three trace elements.

Calculated oxygen and hydrogen isotope ratios of the hydrothermal waters ranged from $\delta^{18}O_{water}$ =-12.8 to 14‰ and δD_{water} -169 to -31‰. The fluid-rock interaction curve on

the δD vs. $\delta^{18}O$ graph is indicative of interaction between meteoric waters with unusually low δD_{water} (∼-160‰ and lower), and magmatic wall rocks. On a pluton scale, δD_{water} increases inwards towards the middle of the intrusion, while $\delta^{18}O_{water}$ values overlap throughout the HPP. Lower δD ratios (≤-160‰) along the flanks of the HPP strongly indicates an interaction with depleted δD_{water}, as higher δD ratios (∼-130‰ to -100‰), towards the middle of the pluton suggests mixing/interaction with granitic rocks and magmatic water. In addition, the geometric distribution of the isotopes throughout the HPP indicates δD and $\delta^{18}O$ imprinted the entire pluton, and that the multiple phases had no effect on isotope distribution.

Large scale fluid geometries within the HPP correlates to fluid paths displayed by Seedorff et al. (2008). The geographical distribution of alteration types throughout the HPP (potassic in the middle, and CS on the flanks), and fluid temperature constraints (higher temperature towards the middle, and lower around the flanks), support the regional fluid paths outlined by δD data. The role of depleted meteoric infiltration is supported by low δD (-169 to -179‰) in Miocene volcanic glass from samples in/near northeastern Nevada. The waters that interacted with the Eocene HPP intrusion after emplacement are similar to δD data from Mulch et al. (2008), based off the interpretation that geographic landscapes in the Eocene were similar to those of the Miocene. However, calculated δD_{water} from HPP samples may also be skewed to lower values due to the poorly constrained water-mineral fractionation factors of micas. More work is needed to properly model the fractionation curves of micas.

REE, trace element, and isotope data emphasize small fluid pathways (3-20 m) associated with the skarn/ limestone pods scattered within the HPP. Local-scale fluid interactions are best observed in data differentiated by transects. In general, concentrations of Y, Zr, REEs and δD, $\delta^{18}O$ ratios, and to a lesser extent TiO_2, P_2O_5, are all affected by the presence of skarn/limestone xenoliths (i.e. transport of elements, towards or away xenolith contacts). A recent study suggests relatively immobile elements Y, Zr, P, Ti, and REEs can be mobile under certain conditions (i.e. ore-forming magmatic-hydrothermal systems) and can then be reprecipitated in nearby skarns (Van Dongen et al., 2010). Throughout the HPP, skarn/limestone pods may not be at the surface or be eroded away. Depending on the distribution of the skarn/ limestone xenoliths, these alteration patterns can repeat and overprint one another. Therefore, if skarn/limestone pods are missed, the alteration fingerprints left behind in the adjacent samples may be misinterpreted, or even overlooked. Although fractional crystallization of the HPP units cannot be ruled out as an explanation of these behaviors, localized mobilization of the immobile elements in the HPP, indicate some local interaction between the skarn/limestone xenoliths.

Due to the difficulty of identifying alteration within the HPP and mobility of REEs and trace elements associated with limestone/ skarn pod interaction, more emphasis should be placed on regional geology (i.e. wall rocks). Addressing how such parameters could affect pluton geochemistry, is especially important when attempting to identify and define multiple petrologic phases within a system.

The HPP shares many characteristics with porphyry root zones descried by Seedorff et al. (2008). Features indicative of porphyry root systems found within the HPP include: large quartz±feldspar±muscovite aplitic dikes and veins, potassic, CS, phyllic and endoskarn alteration. Alteration types also typically found in root zones—sodic and greisen— were not found in the HPP. Geometries of the alteration zones throughout the HPP mimic the depiction of the possible arrangement of alteration types observed by Seedorff et al. (2008) in root zone systems. Although metal concentrations within the HPP are low, skarns surrounding the HPP rich in Cu, Pb, Zn oxides and tungstates may be a relic of metal rich fluids that once rose through the system. If metal rich fluids formed an ore body above, the ore body either slid down to the west due to the Ruby detachment fault or eroded ore eastward into the adjacent basin. Although the HPP contains numerous porphyry root characteristics, it is not enough to label the HPP as a porphyry root. Results show the importance and need of increased studies on porphyry root systems, as undiscovered deposits may be close by.

REFERENCES

Anders, Edward and Grevesse, Nicolas, 1989, Abundances of the elements: Meteoritic and solar: Geochimica et Cosmochimica Acta, v. 53, p. 197-214

Barnes, C. G., Burton, B. R., Burling, T. C., Wright, J. E., & Karlsson, H. R., 2001, Petrology and Geochemistry of the Late Eocene Harrison Pass Pluton, Ruby Mountains Core Complex, Northeastern Nevada: Journal of Petrology, v. 42, p. 901–929

Bodnar, R. J., 2003, Introduction to aqueous-electrolyte fluid inclusions. I*n Fluid Inclusions: Analysis and Interpretation: Mineralogical Association of Canada, short course series v. 32, p. 81–100*

Burton, B., 1997, Structural geology and emplacement history of the Harrison Pass pluton, central Ruby Mountains, Elko County, Nevada: Ph.D. thesis, University of Wyoming, Laramie, Wyoming

Clayton, R.N., O'Neil, J.R., and Mayeda, T, 1972, Oxygen isotope exchange between quartz and water: Journal of Geophysical Research, v. 77, p. 3057-3067

Colgan, J. P., Howard, K. A., Fleck, R. J., & Wooden, J. L., 2010, Rapid middle Miocene extension and unroofing of the southern Ruby Mountains, Nevada: Tectonics, v. 29, p. 1-38

Deans, R.L.J., 2010, Trace element and calculated temperature variation in quartz and titanite in the 36 Ma Harrison Pass pluton, Ruby Mountains NE Nevada: M.S. Thesis, Texas Tech University

Dickinson, W.R., 2006, Geotectonic Evolution of the Great Basin: Geosphere, v. 2, p. 353–368

Dilles, J.H., Solomon, G.C., Taylor, H.P., Einaudi, M.T., 1992, Oxygen and Hydrogen Isotope Characteristics of Hydrothermal Alteration at the Ann-Mason Porphyry Copper Deposit, Yerington, Nevada: Economic Geology, v. 87, p. 44-63

Ebadi, A., and Johannes, W., 1991, Beginning of melting and composition of first melts in the system Qz- Ab- Or-H_20- CO_2: Contributions to Mineralogy and Petrology, v. 106, p. 286-295

Fricke, H.C., Wickham, S.M., O'Neil, J.R., 1992, Oxygen and hydrogen isotope evidence of meteoric water infiltration during mylonitization and uplift in the Ruby Mountains-East Humboldt Range core complex, Nevada: Contributions to Mineralogy and Petrology, v. 111, p. 203-221

Feeley, T.C. & Grunder, A.L., 1991, Mantle contribution to the evolution of Middle Tertiary silicic magmatism during early stages of extension: the Egan Range volcanic complex, east-central Nevada: Contributions to Mineralogy and Petrology, v. 106, p. 154-169

Gates, C., 2016, The magmatic-hydrothermal fluid history of the Harrison Pass Pluton, Ruby Mountains, NV: Implications for the Ruby Mountain-East Humboldt Range metamorphic core complex and carlin-type Au deposits: M.S. Thesis, Colorado State University

Henry, C. D., & Boden, D. R., 1998, Eocene magmatism: The heat source for Carlin-type gold deposits of northern Nevada. Geology, v. 26, p. 1067–1070

Horita, J., 2005, Stable isotope thermometry: there is more to it than temperature: Geochemical Journal, v. 39, p. 481-496

Hudec, M. R. (1992). Mesozoic structural and metamorphic history of the central Ruby Mountains metamorphic core complex, Nevada: Geological Society of America Bulletin, v. 104, p. 1086–1100

Humphreys, E., Hessler, E., Dueker, K., Farmer, G. L., Erslev, E., & Atwater, T. (2003). How Laramide-age hydration of North American lithosphere by the Farallon slab controlled subsequent activity in the western United States. International Geology Review, v. 45, p. 575–595

Lapointe, D. D., Tingley, J. V., & Jones, R. B., 1991, Mineral resources of Elko County, Nevada (No. 106). Reno: University of Nevada, Reno

Leitch, C.H.B, and Lentz, D.R., The Gresens approach to mass balance constraints of alteration systems: methods, pitfalls, examples. *In Lentz, D.R. ed., Alteration and Alteration Processes associated with Ore-forming Systems: Geological Association of Canada, Short course notes, v. 11, p. 161-192*

Ligang, Z., Jingxiu, L., Huanbo, Z., and Zhensheng, C., 1989, Oxygen isotope fractionation in the quartz-water-salt system: Economic Geology, v. 84, p. 1643-1650

López-Moro, F. J., 2012, EASYGRESGRANT—A Microsoft Excel spread sheet to quantify volume changes and to perform mass-balance modeling in metasomatic systems: Computers & Geosciences v. 39, p. 191–196

MacCready, T., Snoke, A. W., Wright, J. E., & Howard, K. A., 1997, Mid-crustal flow during Tertiary extension in the Ruby Mountains core complex, Nevada: Geological Society of America Bulletin, v. 109, p. 1576–1594

Mulch, A., Sarna-Wojcicki, A.M., Perkins, M.E., Chamberlain, C.P., 2008, A Miocene to Pleistocene climate and elevation record of the Sierra Nevada (California): PNAS, v. 105, no. 19, p. 6819-6824

Muntean, J. L., Cline, J. S., Simon, A. C., & Longo, A. A., 2011, Magmatic-hydrothermal origin of Nevada's Carlin-type gold deposits: Nature Geoscience, v. 4(2), p. 122–127

Musekamp, C.O., 2011, Field, fluid inclusion and isotope chemistry evidence of fluids circulating around the Harrison Pass Pluton during intrusion: a fluid model for carlin-type deposits: M.S. Thesis, Colorado State University

Nesbitt, B., E., 1996, Applications to oxygen and hydrogen isotopes to exploration of hydrothermal mineralization: SEG Newsletter, no. 27

Pearce, J.A., 1983, role of the sub-continental lithosphere in magma genesis at active continental margins. *In: Rollinson, H., 1993*, *Using geochemical data: evaluation, presentation, and interpretation, p.143,* Singapore: Longmont Singapore Publishers (Pte) Ltd.

Reid, J.B., Murray, D.P., Hermes, O.D., Steig, E.J., 1993, Fractional crystallization in granites of the Sierra Nevada: How important is it?: Geology, v. 21, p. 587-590

Roedder, E., 1984, Fluid Inclusions, Min. Soc. Am. Rev. in Min. v. 12, p. 79-108

Runyon, S.E., Seedorff, E., Steele-Macinnis, M., Lecumberri-Sanchez, P., and Mazdab, F.K., 2016, Greisen alteration in the root zones of porphyry copper systems at Yerington, Nevada: GSA topical session, 2016

Seedorff, E., Barton, M.D., Stavast, W.J.A., Maher, D.J., 2008, Root Zones of Porphyry Systems: Extending the Porphyry Model to Depth: Society of Economic Geology, v. 103, p. 939-956

Snoke, A. W., & Lush, A. P., 1984, Polyphase Mesozoic-Cenozoic deformational history of the northern Ruby Mountains-East Humboldt Range, Nevada: In Western Geological Excursions, prepared for the 1984 Annual Meetings of the Geological Society of America and affiliated societies at Reno, p. 232–260

Stager, H., K., and Tingley, J. V., 1988, Tungsten deposits in Nevada: Nevada Bureau of Mines and Geology, Bulletin 105, p. 256

Stanley, C.R., and Madeisky, H.E., 1994, Lithogeochemical Exploration for Hydrothermal Ore Deposits using Pearce Element Ratio Analysist. *In Lentz, D.R. ed., Alteration and Alteration Processes associated with Ore-forming Systems: Geological Association of Canada, Short course notes, v. 11, p. 193-211*

Taylor, H.P. Jr. 1974, An application of oxygen and hydrogen isotope studies to problems of hydrothermal alteration and ore deposition: Economic Geology, v. 69, p. 843-883

Taylor, H.P., 1997, Oxygen and Hydrogen Isotope Relationships in Hydrothermal Mineral Deposits. *In Barnes, H.L., Geochemistry of Hydrothermal Mineral Deposits, 3rd ed.,* Canada: John Wiley and Sons, Inc.

Thorman, C. H., Ketner, K. B., & Peterson, F. ,1990, The Elko Orogeny-Late Jurassic orogenesis in the Cordilleran miogeocline: Geological Society of America Cordilleran Meeting, Abstracts with Programs, v. 22, no. 3, p. 88

Ulrich, T., and Heinrich, C.A., 2001, Geology and Alteration Geochemistry of the Porphyry Cu-Au Deposit at Bajo de la Alumbrera, Argentina: Economic Geology, v. 96, p. 1719-1742

Van Dongen, M., Weinberg, R.F., Tomkins, A.G., 2010, REE-Y, Ti, and P Remobilization in magmatic rocks by hydrothermal alteration during Cu-Au deposit formation: Economic Geology, v. 105, p. 763-776

Wickham, S. M., Peters, M. T., Fricke, H. C., & O'Neil, J. R., 1993, Identification of magmatic and meteoric fluid sources and upward-and downward-moving infiltration fronts in a metamorphic core complex: Geology, v 21, p. 81–84

Wilkinson, J.J., 2017, Metastable freezing, a new method for the estimation of salinity in aqueous fluid inclusions: Economic Geology, v. 112, p. 185–193

Wright, J. E., & Snoke, A. W., 1993, Tertiary magmatism and mylonitization in the Ruby-East Humboldt metamorphic core complex, northeastern Nevada: U-Pb geochronology and Sr, Nd, and Pb isotope geochemistry: Geological Society of America Bulletin, v. 105, p. 935-95.

APPENDIX 1

Table 1: List of sample numbers, method types, and sample locations.

Sample numbers			Method type:				
TRANSECT 1	Rock type	Alteration type	Isotopes	Whole rock geochemistry	Fluid inclusions	Lattitude (N)	Longitude (W)
HPP6-4-15A	Tmg	Potassic				40.324	-115.557
HPP6-4-S16	Tmg	Potassic	X	X	X	40.324	-115.557
HPP6-13-62	Tmg	Potassic	X	X		40.324	-115.558
HPP6-13-63	Tmg	Potassic				40.326	-115.565
HPP6-13-65	Tmg	Potassic		X	X	40.327	-115.567
HPP6-13-66	Skarn	Skarn	X	X		40.328	-115.569
HPP6-13-66A	Tmg	Potassic	X	X	X	40.328	-115.569
TRANSECT 2							
HPP6-7-22	Ttc	CSS				40.335	-115.474
HPP6-9-42	Ttc	CSS	X	X	X	40.341	-115.472
HPP6-9-43	Ttc	Potassic		X		40.342	-115.472
HPP6-9-44	Ttc	CSS			X	40.343	-115.472
HPP6-9-49	Ttc	Endoskarn	X	X		40.340	-115.481
HPP6-9-52	Ttc	Unaltered-epidote bearing	X	X		40.351	-115.490
HPP6-9-53	Ttc	CSS	X	X	X	40.351	-115.490
HPP6-9-54	Ttc	Unaltered	X	X		40.351	-115.490
TRANSECT 3							
HPP6-8-26	Tmg	Unaltered	X		X	40.339	-115.559
HPP6-8-27	Tmg	Potassic	X	X		40.341	-115.560
HPP6-8-28	Tmg	Potassic		X		40.342	-115.559
HPP6-8-30	Ttc	CSS	X	X	X	40.343	-115.553
HPP6-8-31	Tmg	CSS				40.341	-115.552
TRANSECT 4							
HPP6-8-33	Tmg	Potassic	X	X	X	40.306	-115.528
HPP6-8-34	Tmg	Skarn		X		40.302	-115.530
HPP6-8-35	Tmg	Silicified	X			40.302	-115.530
HPP6-8-36	Tmg	Silicified		X	X	40.302	-115.530
HPP-6-8-37	Tmg	Potassic overprinted by silicification	X	X		40.302	-115.530
HPP6-8-38	Tmg	CSS	X		X	40.303	-115.529
TRANSECT 5							
HPP6-13-68	Tmg	Endoskran	X	X	X	40.245	-115.625
HPP6-13-69	Tmg	CSS	X	X	X	40.244	-115.624
HPP6-13-70	Tmg	Skarn		X		40.244	-115.623
HPP6-13-71	Limestone	Limestone				40.244	-115.622
TRANSECT 6							
HPP6-8-39	Tcc	Potassic	X	X	X	40.312	-115.512
HPP6-17-88	Vuggy qtz vein	Unaltered			X	40.312	-115.511
HPP-6-17-89	Tcc	CSS	X	X		40.312	-115.511
HPP6-17-90	Tcc	CSS				40.312	-115.512
HPP6-17-91	Tcc	CSS	X	X	X	40.312	-115.511
TRANSECT 7							
HPP-6-7-S17	Tcc	Skarn				40.311	-115.476
HPP6-7-S18	Tcc	Potassic		X	X	40.311	-115.476
HPP6-7-S19	Tcc	CSS	X	X		40.310	-115.477
HPP6-7-S20	Tcc	Unaltered	X	X		40.310	-115.479
Greisen?							
HPP6-16-76	Tmg	Greisen		X		40.306	-115.527
Potassic							
HPP6-2-6	Tcc	Potassic		X		40.318	-115.464

Full Transect descriptions

Transect 1

In the mid-western portion of the HPP just south of Toyn Creek, a bleached, protruding, 30m SW trending Tmg outcrop was examined (40.324 N, -115.557 W). Upon closer examination of the outcrop, mineralogy showed that plagioclase has been altered to potassium feldspar. Southwest towards the "apex" of the outcrop, magnetite was found in hand sample and confirmed the alteration type as potassic. The "apex" featured a 0.45-0.6m wide quartz vein cut through the top of the 8m outcrop. Approximately .6 miles west, potassic alteration was still present as small 0.3m wide outcrops, until a skarn-granite contact was encountered (40.328 N, -115.569 W). The skarn outcrop was 1.5m tall and 2.5m wide, with a skarn-granite contact both sides. The skarn alteration was pervasive, including chlorite, hornblende, and minor garnet. The west side of the skarn-granite contact was potassically altered, and continued about 3m west.

Summary of alteration progression: Potassic→mixed potassic/unaltered→skarn → potassic

Transect 2

In the NE corner of the HPP, north of the Harrison Pass Creek, outcrops were significantly fractured, and tinted green. Upon closer look the biotite in the Ttc had altered into chlorite, and displayed the typical mineralogy of chlorite-sericite alteration (CS). Across the valley, on the northern ridge, a bleached, k-feldspar rich sample was collected near a skarn contact. Unaltered Ttc along with light CS altered outcrops were present west along the northern ridge, and were commonly found in contact with skarn, and aplitic pods every 15-30m. Old mine workings were found in a large marble xenolith with

compositional banding trending 280° (40.344 N, -115.479 W). Along the edges of the mine shaft, copper carbonates, and sulphides were present. Samples were collected, but the transect was re-focused north into the adjacent valley. The valley consisted of many CS-quartz vein/endoskarn contacts. At the NW edge of the valley, a 9m tall and 60m wide outcrop (40.351 N, -115.490 W) consisted of a triple contact point between CS altered, epidote rich, and unaltered Ttc. Barnes et al. had discussed the presence of epidote in some of the HPP granites, but a sample was taken for further analysis as epidote made up ≈10% of the sample.

Summary of alteration progression: CS→potassic→unaltered→ CS→ epidote granite

Transect 3

The northern mid-west part of the HPP, just north of Toyn Creek, was explored in order to encounter features present topographically higher in the system (40.339 N, -115.559 W). The elevation at the top of the Tmg peak and ridge trail was ≈2300m, and outcrop was made up of predominately aplites, pegmatites, and quartz veins. Some of the quartz veins contained significant muscovite along the margin, indicating possible greisen alteration. Instead, potassic alteration was found in the Tmg unit, in addition to CS alteration within an isolated Ttc pod. The mylonitic shear zone described by Burton (1997) and others was encountered further south.

Summary of alteration progression: potassic→ potassic→CS

Transect 4

Down in the southern middle portion of the HPP, along the Tcc and Tmg unit boundary, and in between the Corral and Toyn Creeks, a light potassic alteration was found

at the beginning of small ridge (40.306 N, -115.528 W). The area was specifically chosen to be in proximity of the Tmg- Tcc contact. The western part of the ridge, comprised of marble and skarn, was found in direct contact with Tmg granite to the east. The granite was silicified 15-20m north and south of the skarn-granite contact. Quartz veins and relict endoskarn (± diopside) alteration were found scattered throughout the silicified granite to the north.

Summary of alteration progression: potassic→ silicification→ skarn

Transect 5

Located SW of the main HPP intrusion, south of Pearl Creek, a Tmg inlier was chosen as an ideal place for a transect, as earlier data had not been collected at the location (40.245 N, -115.625 W). The isolated Tmg inlier was weathered and covered by foliage 75% of the way up, however small (0.6m tall, 1.5m wide) unweathered, CS and endoskarn outcrops were found littered around the flanks of the intrusion. A skarn contact was encountered, which was relatively unaltered and displayed preserved bedding 40°, 35°E, similar to orientation data collected by Barnes et al. (2001).

Summary of alteration progression: endoskarn→CS→skarn

Transect 6

An the area within the Tcc unit, directly east of transect 4, was chosen as outcrops were located by the triple contact between the Tcc, Ttc, and Tmg phases (40.312 N, -115.511 W). A large, 0.6m wide vuggy quartz vein was found trending N/S, and continued ~4.5m north. The quartz vein outcrop was limited, but trended towards a small

potassically altered Tcc outcrop. North of the potassic alteration, CS alteration was found on either side of the quartz vein trend.

Summary of alteration progression: Quartz vein→light potassic→CS

Transect 7

The Star mine, located on the eastern middle portion of the HPP, just south of the Harrison Pass Creek, was sought for the skarn-granite contact (40.311 N, -115.476 W). The main Star mine shaft dug through the garnet bearing skarn band ≈1.8m wide. The west side of the skarn was in contact with potassically altered Tcc granite. A 4.5m band of CS altered granite was present 30m west of the skarn, and unaltered Tcc 60m further.

Summary of alteration progression: skarn→potassic→CS→unaltered

Petrographic descriptions

Samples below were selected for description in order to encompass all of the major alteration types and features of interest. Petrographic images follow on page 142.

Transect 1

HPP6-13-62 (40.324, -115.558): This sample is a potassically altered biotite monzogranite of the Tmg unit. The sample is composed of quartz (45%), plagioclase (35%), K-feldspar (15%), and biotite (5%), with accessory magnetite, muscovite, allanite, and minor apatite. Quartz is subhedral to anhedral, coarse grained, and displays bulging recrystallization. Plagioclase is coarse grained, subhedral, and locally replaced by minute growths of epidote and sericite. K-Feldspar is medium to coarse grained and subhedral to anhedral. Microcline is commonly found replacing plagioclase, a feature typical of potassic alteration. Biotite is found as long feathery crystals (~0.20-2.5 mm long) inter-grown between quartz and plagioclase, suggestive of hydrothermal biotite. In addition, minor amounts of magnetite blocky and irregular in shape, are found in between grain boundaries-- a typical feature of potassic alteration. The petrographic image is focused a feathery like crystal of hydrothermal biotite, surrounded by slightly sericitized plagioclase.

HPP6-13-66A (40.327, -115.568): This biotite monzogranite sample of the Tmg, is an example of light potassic alteration overprinted by late fluids inducing mild alteration of biotite. Sample 66A was collected right at a Tmg-skarn contact at the end of transect 1. The sample is composed of quartz (35%), plagioclase (35%), K-feldspar (25%), biotite (2%), and chlorite (3%). Accessory minerals include magnetite, and rutile. Two generations of quartz are present: the first is subhedral to anhedral, medium to coarse grained, and the second (product of late fluids) are fine grained, subhedral, and are found in small clusters

or veinlets along grain boundaries. Most quartz grains display bulging recrystallization. Plagioclase is coarse grained, subhedral to anhedral and is commonly replaced by microcline—typical of k-metasomatism. Feldspar is medium to coarse grained and subhedral to anhedral. Biotite and chlorite are found as feathery crystals (~0.07-1.25mm long), and inter-grown between quartz and plagioclase grain boundaries. In addition, biotite shows evidence of chlorite alteration, suggesting the presence of chlorite as product of the secondary fluids. Minor amounts of magnetite, blocky and irregular in shape, are found in between grain boundaries--also a typical feature of potassic alteration. The petrographic image is focused on cross hatched microcline.

Transect 2

HPP6-9-43 (40.341, -115.471): Sample 43 is an example of potassic alteration in the Ttc unit. The sample is composed of intergrown K-feldspar and quartz (70%), quartz (25%), plagioclase (5%), with accessory epidote and minor apatite. The intergrown K-feldspar and quartz is coarse grained, subhedral to anhedral. Two generations of quartz are present: the first is subhedral to anhedral, medium grained, and the second (product of the metasomatic fluids) are fine grained, subhedral, and are found in small clusters or veinlets along grain boundaries. Most quartz grains display bulging recrystallization. The plagioclase is medium grained, subhedral, and typically found surrounded by both generations of quartz. The following petrographic image is centered on a large intergrowth of K-feldspar and quartz.

HPP6-9-52 (40.351, -115.489): Sample 52, is an unaltered mafic endmember of the Ttc, found in contact with CS altered and unaltered Ttc rocks. The sample consists of plagioclase (65%), epidote (20%), quartz (7%), chlorite (7%), and hornblende (1%). Plagioclase is coarse grained (0.5mm-2.5mm), and euhedral to subhedral. Epidote is medium to fine

grained, subhedral, and is present as clinozoisite and zoisite. Quartz is medium grained, subhedral, and is mostly found along plagioclase grain boundaries. Chlorite varies from coarse to fine grained, is subhedral, and appears as a relic of hornblende. Most of the hornblende has been visibly altered into chlorite, however some fine to medium grains are still present in the sample. The Petrographic image is centered on a cluster of epidote surrounded by plagioclase.

HPP6-9-53 (40.351, -115.489): Sample 53 is an example of CS alteration, found next to the unaltered mafic contact in the Ttc. The sample consists of quartz (45%), plagioclase (40%), chlorite (10%), sericite (2%), hornblende (2%), and epidote (1%). Two generations of quartz are present: the first is medium to coarse grained, subhedral, and the second (product the fluids responsible for CS alteration) are fine grained, subhedral, and are found in small clusters around chlorite, sericite, and in some cases epidote. Most quartz grains show signs of bulging recrystallization. Plagioclase is medium to coarse grained, euhedral to subhedral, and in some areas, lightly sericitized. The chlorite is medium to fine grained, subhedral, and is a hydrothermal product of hornblende and biotite. Most of the chlorite gives off a deep blue interference color, indicating iron rich chlorite. Sericite and epidote are fine grained, and commonly found together with the second generation of fine grained quartz. The sericite is a product of plagioclase alteration, whereas the epidote appears magmatic. Hornblende is medium grained, subhedral, and does not appear stable—most of which have altered into chlorite. Petrographic image shows dark blue chlorite, surrounded by plagioclase and small grains of epidote.

Transect 3

HPP6-8-27 (40.340, -115.560): Sample 27 is a potassically altered sample collected in the Tmg unit. The sample has been potassically altered, and consists of quartz (35%), plagioclase (30%), myrmekite (20%), microcline (14%), muscovite (1%), with accessory chlorite, sericite, and magnetite, and minor apatite. Quartz is medium to fine grained, subhedral, and shows signs of bulging recrystallization. Plagioclase is medium to coarse grained, subhedral to anhedral, and trivial amounts replaced by sericite. A larger percent of the plagioclase has been partially replaced by microcline and myrmekite, a characteristic of potassic alteration. The microcline is medium grained, and subhedral to anhedral, whereas the myrmekite is medium to coarse grained. Muscovite is fine grained, subhedral, and found along grain boundaries. The petrographic image is centered on cross hatched microcline, quartz and minor grains of muscovite.

HPP6-8-30 (40.342, -115.552): This sample, part of the Ttc pod found within the Tmg unit, has been CS altered and consists of plagioclase (40%), quartz (35%), biotite (15%), sericite (7%), chlorite (3%), with accessory epidote and minor apatite. Plagioclase is medium to coarse grained, euhedral to subhedral, and over half of the grains have been lightly to pervasively altered to sericite. Quartz is medium to coarse grained, subhedral, and displays grain bulging recrystallization. Biotite is medium grained, euhedral, and in some areas has been altered into chlorite, which is predominately fine to medium grained and subhedral. The petrographic image is focused on grains of biotite, where in some areas has be altered into chlorite, and is surrounded by plagioclase.

Transect 4

HPP6-8-33 (40.305, -115.527): Potassically altered sample 33 was collected in the Tmg unit. The sample is an example of light potassic alteration, and is overprinted by secondary fluids. The sample contains quartz (40%), plagioclase (35%), myrmekite (10%), biotite (8%), microcline (2%), with accessory garnet, chlorite and minor apatite. Two generations of quartz are present: Magmatic quartz is medium to coarse grained and subhedral, while the second generation is fine to medium grained, subhedral, found growing between plagioclase crystals, and is a product of late fluids. Some quartz grains display bulging recrystallization. Plagioclase is medium to coarse grained, subhedral, and a good portion of the zonation textures washed out by the late fluids. Myrmekite, often a product of the initial stage of potassic alteration, is fine to medium grained, and subhedral. Biotite is coarse to fine grained, and subhedral to euhedral. The subhedral biotite displays a prominent shreddy texture, a characteristic feature of potassic alteration. Microcline is medium grained, anhedral, and hard to distinguish as most textures have been washed out by the late fluids.

HPP6-8-36 (40.305, -115.527): The silicified sample 36 was collected in the Tmg, along transect 4. The sample consists of quartz (55%), plagioclase (40%), sericite (4%), and relict biotite (<1%), with minor apatite. Two generations of quartz are present: magmatic quartz is medium to coarse grained and subhedral, while the second generation is fine to medium grained, euhedral to subhedral, and in some cases, grows around/encloses other minerals. Most of the quartz grains display bulging recrystallization. Plagioclase is medium to fine grained, subhedral to anhedral, and has been lightly altered in to sericite. Relict biotite is

found as thin wispy shreds along grain boundaries and looks as though it's been washed out by late fluids. The petrographic image is focused on the two generations of quartz.

Transect 5

HPP6-13-68 (40.244 -115.625): Endoskarn sample 68 was collected along transect 5 from the isolated Tmg inlier to the southwest. The sample consists of plagioclase (45%), calcite (27%), chlorite (15%), muscovite (7%), quartz (5%), biotite (1%), with minor rutile, apatite, and opaques. Plagioclase is medium to coarse grained, subhedral, and in some instances, have been lightly sericitized. The calcite is found along grain boundaries as small veinlets or large clots, and is also seen filling in cracks within the plagioclase. Most of the chlorite gives off a deep blue interference color, and is found alongside the muscovite, between plagioclase and quartz grain boundaries. Quartz is medium to fine grained and displays slight grain bulging recrystallization. Biotite is rare and is found along the boundaries of the chlorite clots, suggestive of a relict mineral. Compared to other samples, sample 68 contains a large amount of rutile, which is found as clots in plagioclase and quarts grains. The petrographic image is centered on calcite, surrounded by chlorite and plagioclase.

HPP6-13-70 (40.243, -115.623): Skarn sample 70, was collected from the isolated Tmg inlier in the southwest portion of the HPP. The sample is fine grained with a granoblastic texture and consists of calcite (35%), quartz (25%), pyroxene (18%), plagioclase (15%), and chlorite (7%), with minor amounts rutile and apatite. Calcite is found along quartz, plagioclase and pyroxene boundaries. Quartz and plagioclase are fine grained, subhedral to anhedral, and are deformed. Pyroxene appears as fined grained, anhedral blobs, commonly surrounded by quartz and feldspar. Chlorite gives off a deep blue interference color, and is

found in small veinlets, along grain boundaries, or replacing pyroxene. The petrographic image is focused on fine grained pyroxene, surrounded by quartz and calcite.

Transect 6

HPP-6-17-89 (40.311, -115.511): The CS altered sample 89 collected in the Tcc unit, and consists of: plagioclase (45%), feldspar (25%), quartz (20%), chlorite (7%), sericite (2%), and biotite (1%), with minor hornblende, opaques, and apatite. Plagioclase and feldspar are medium to coarse grained, and euhedral to subhedral. Plagioclase is also lightly to moderately sericitized. Quartz is medium to coarse grained, subhedral to anhedral, in some cases display grain bulging recrystallization, and sometimes found enclosed by plagioclase grains. Chlorite is found in large clots, replacing biotite between grain boundaries. Biotite is either found in veinlets, along weakened cleavage planed, or as relic remnants around the chlorite clots. The petrographic image is centered on a chlorite clot, surrounded by relic biotite, plagioclase, and quartz.

Petrographic images

HPP6-13-62 potassically altered

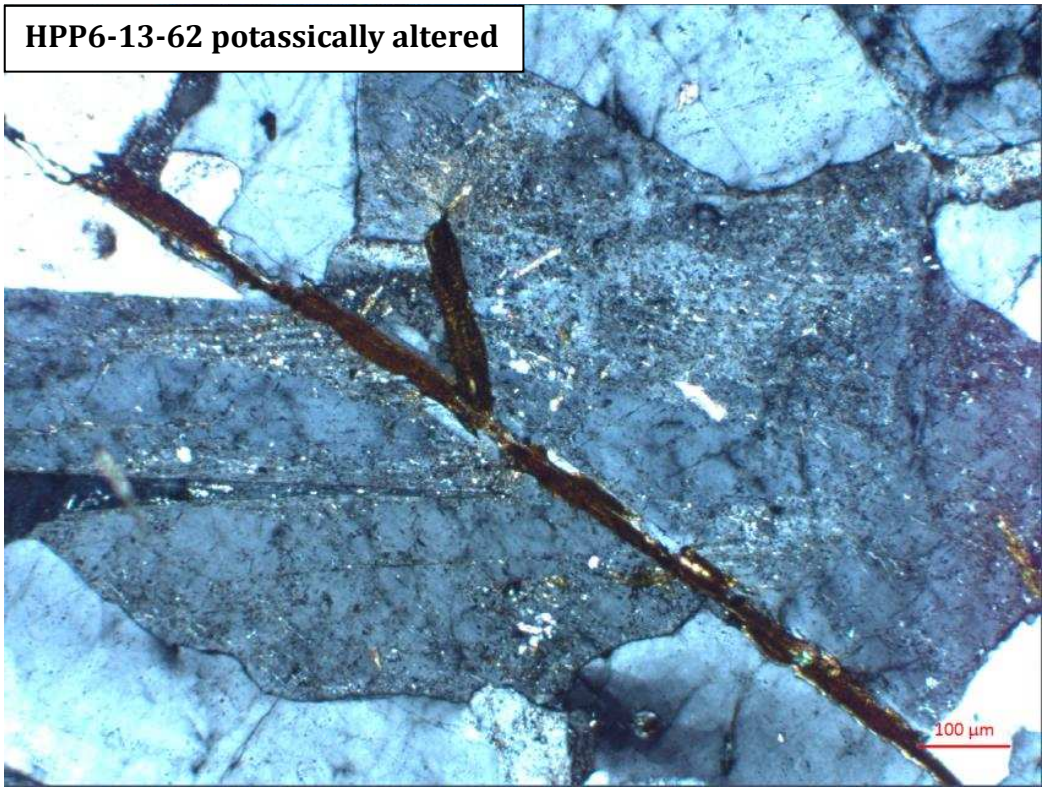

HPP6-13-66A potassically altered

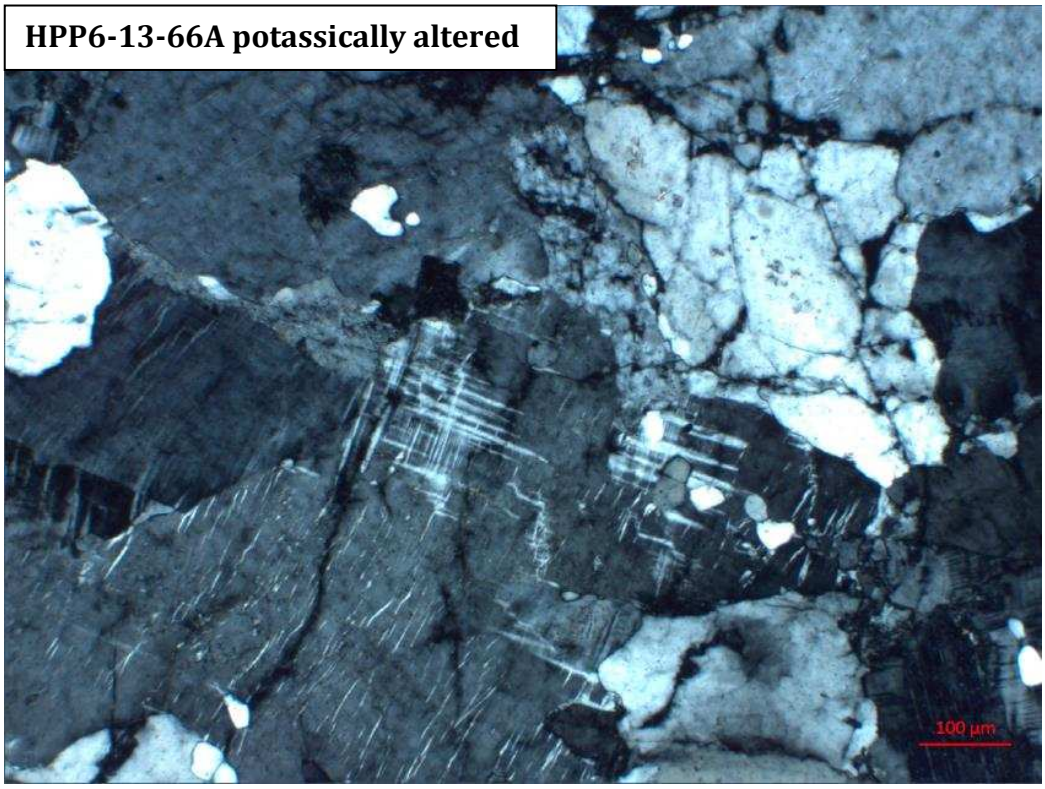

HPP6-9-43 potassically altered

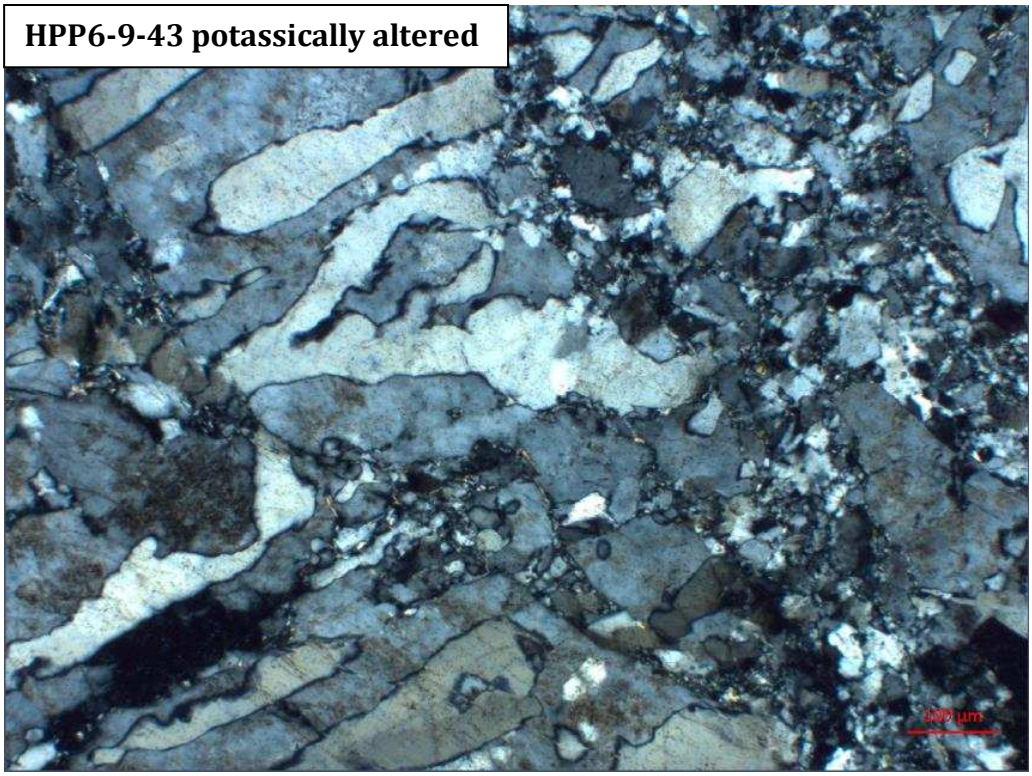

HPP6-9-52 epidote rich sample

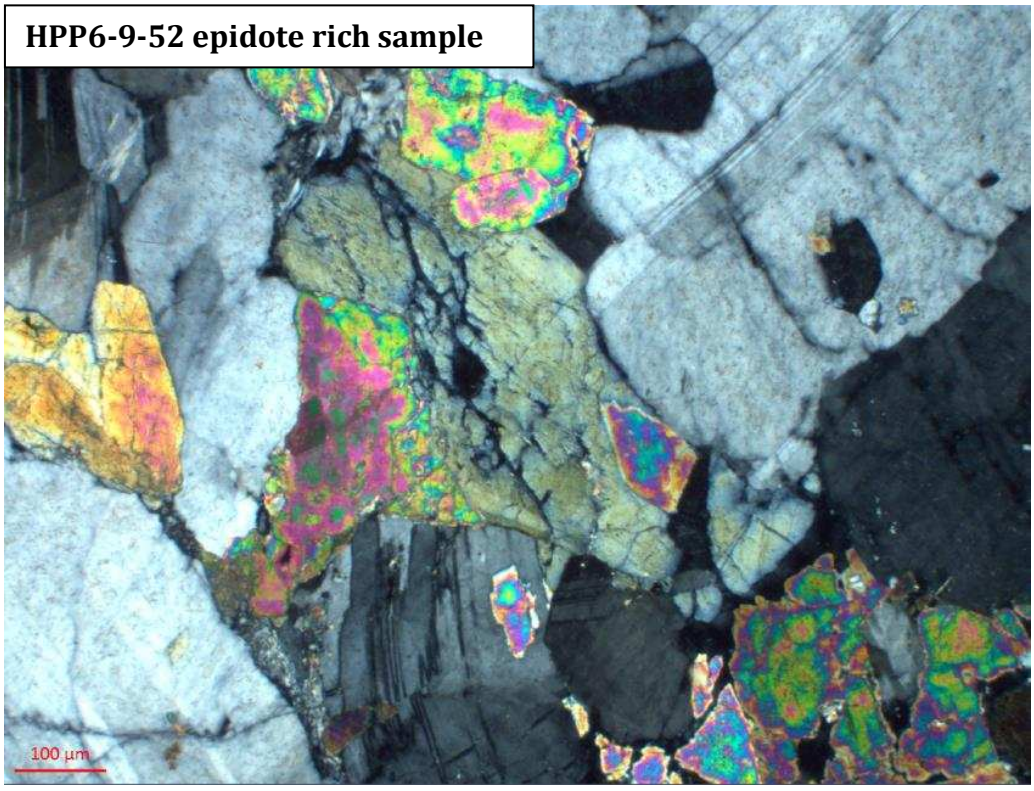

HPP6-9-53 CS altered

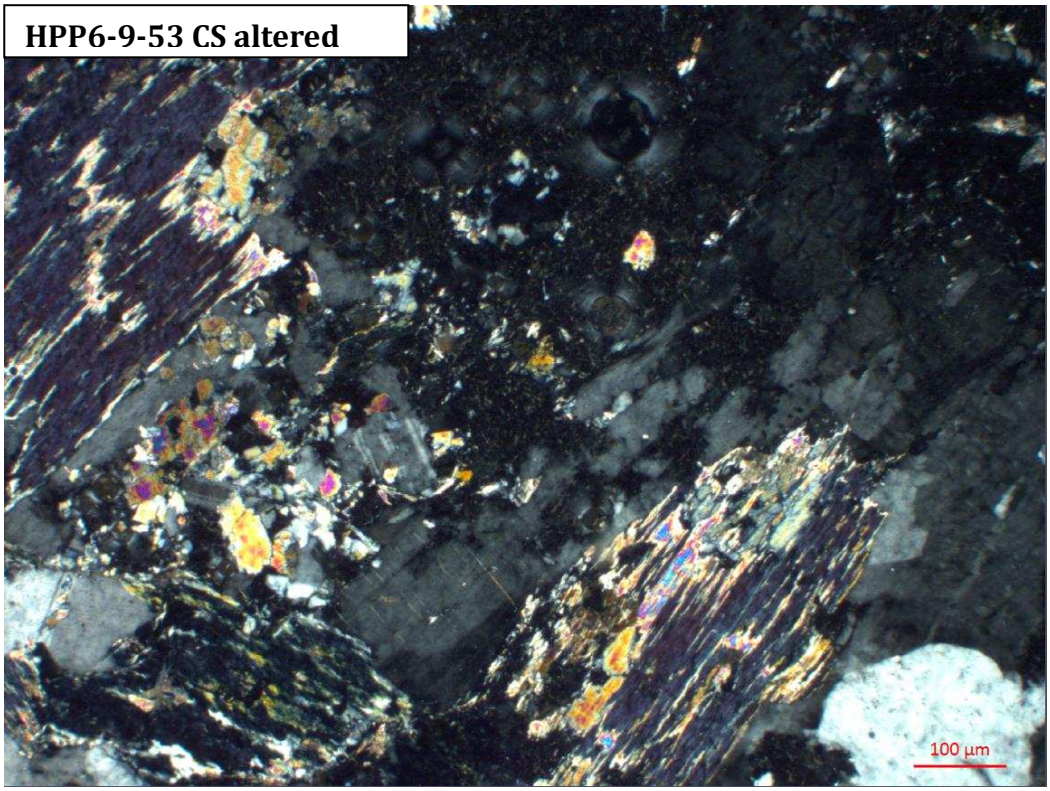

HPP6-8-27 potassically altered

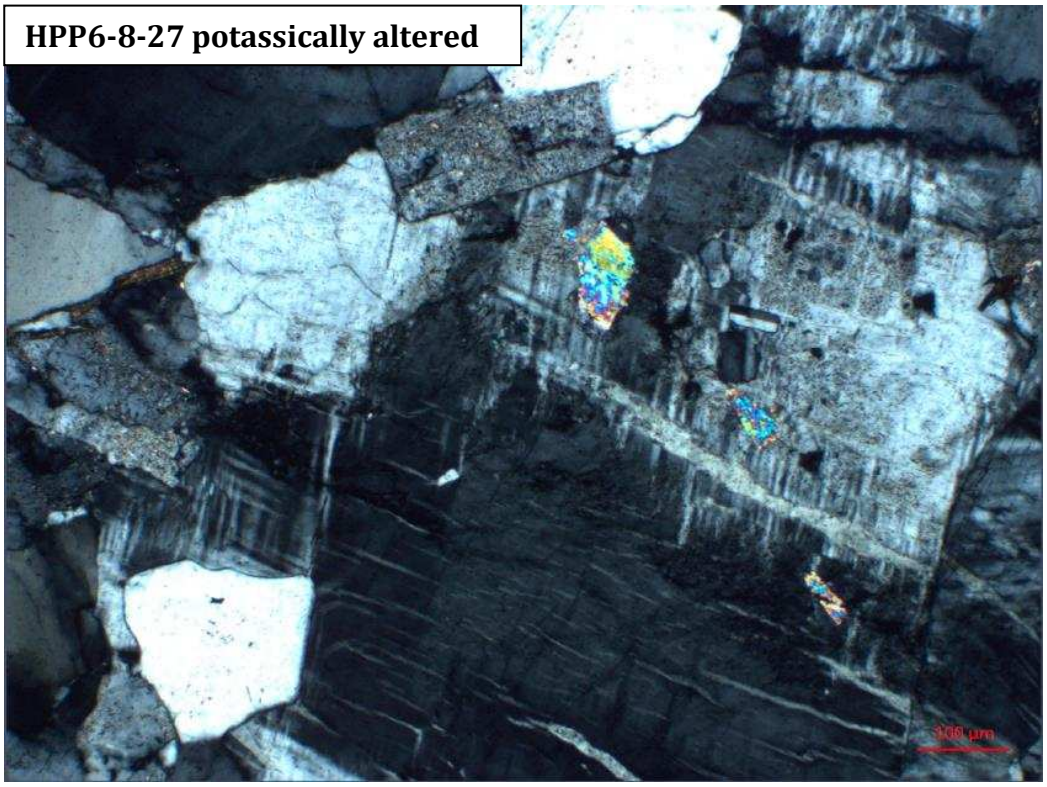

HPP6-8-30 CS altered

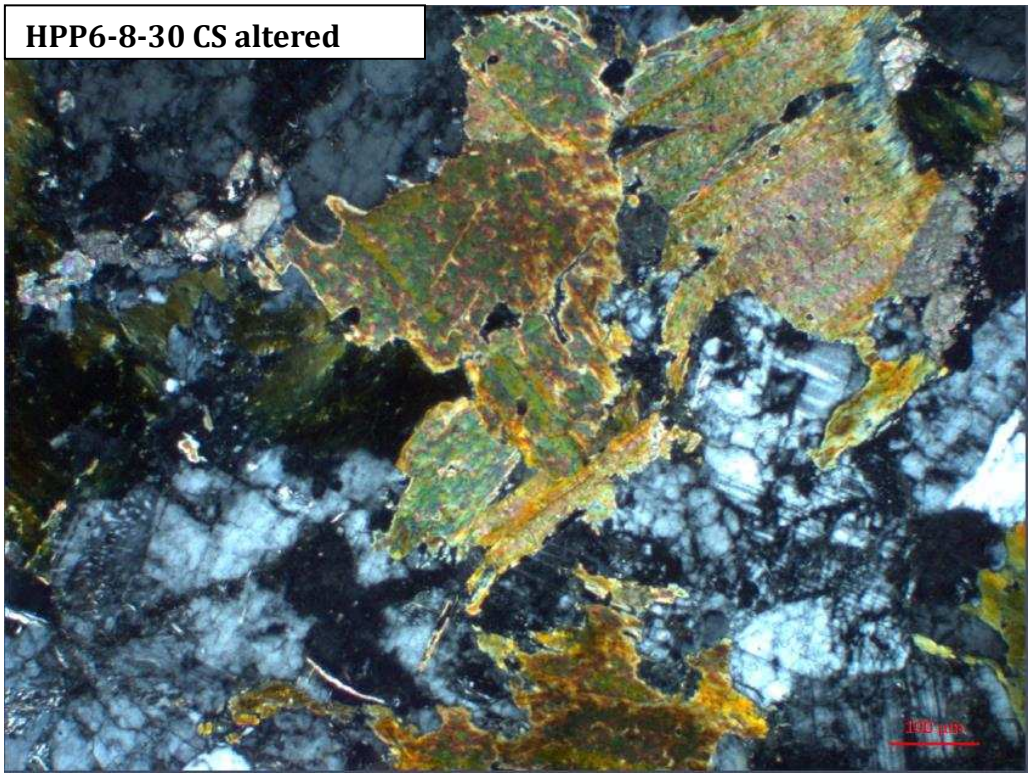

HPP6-8-36 Silicified

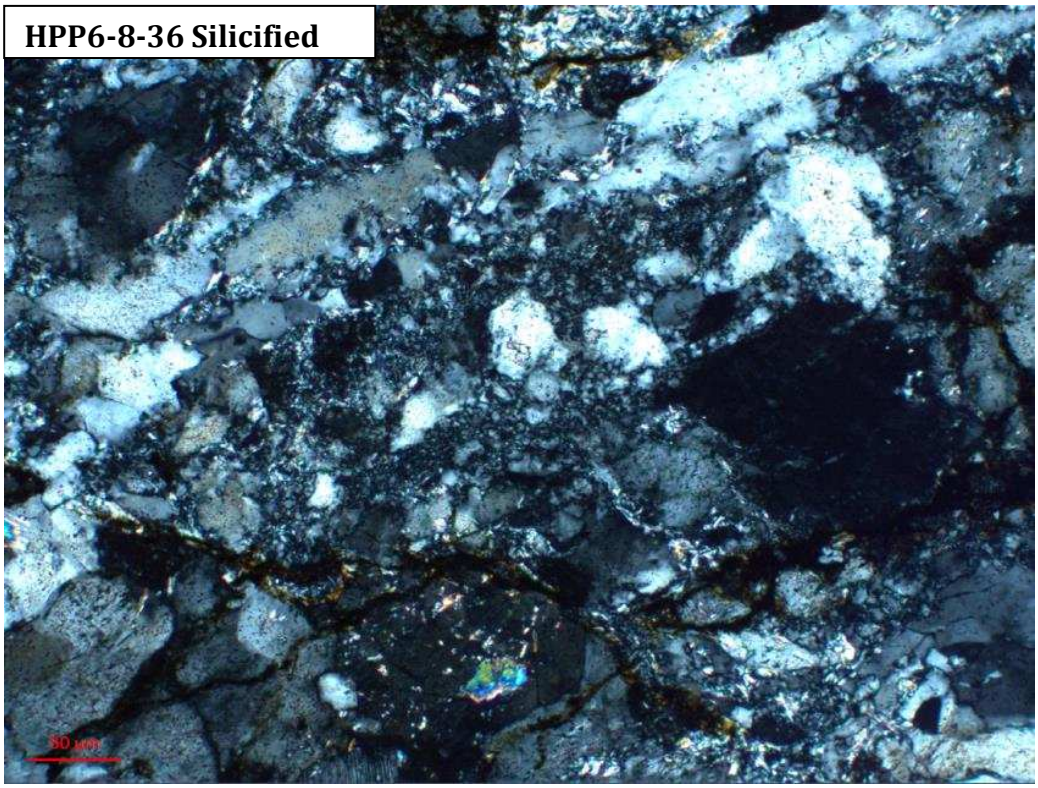

HPP6-13-68 endoskarn

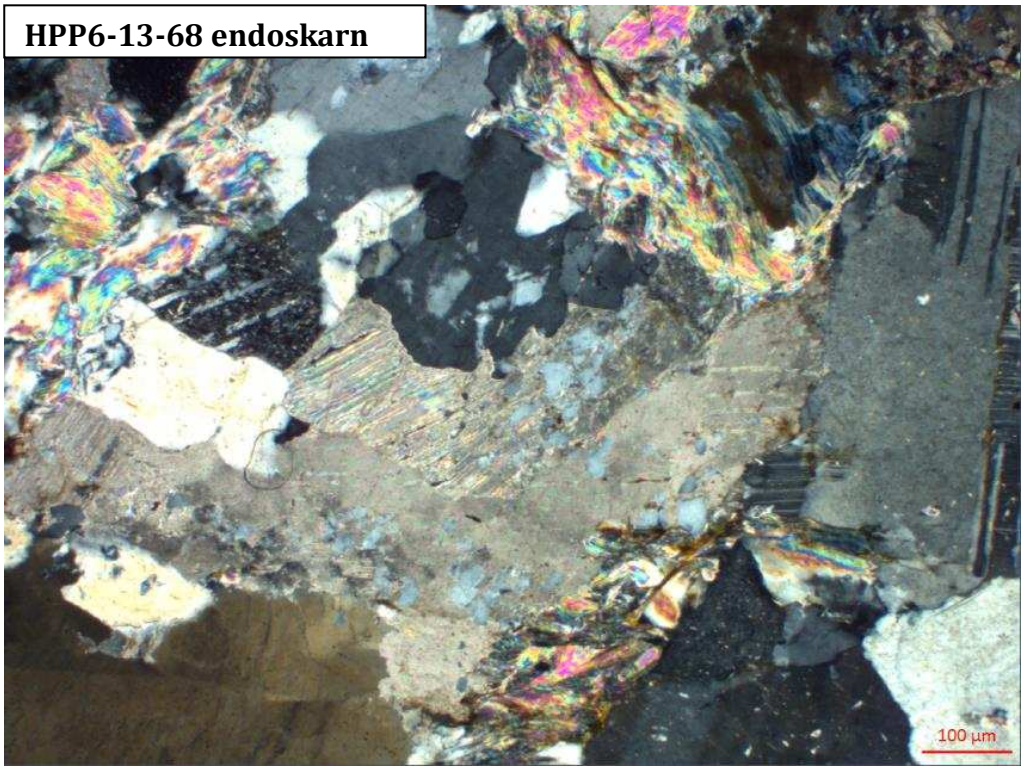

HPP6-13-70 skarn

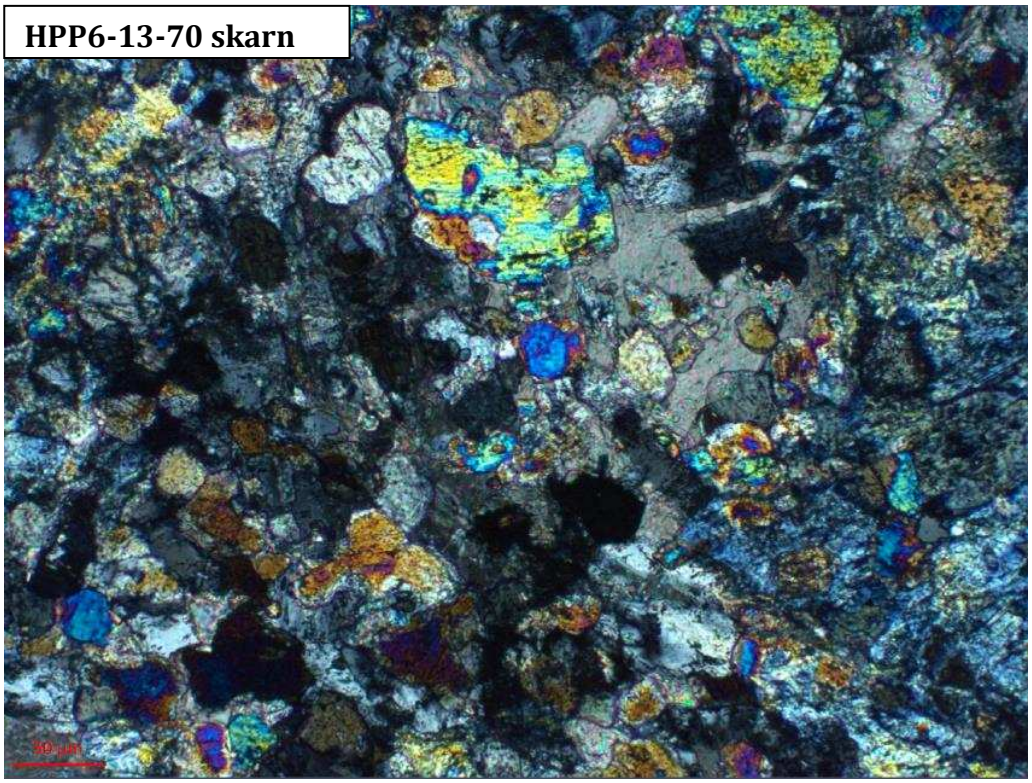

HPP-6-17-89 CS altered

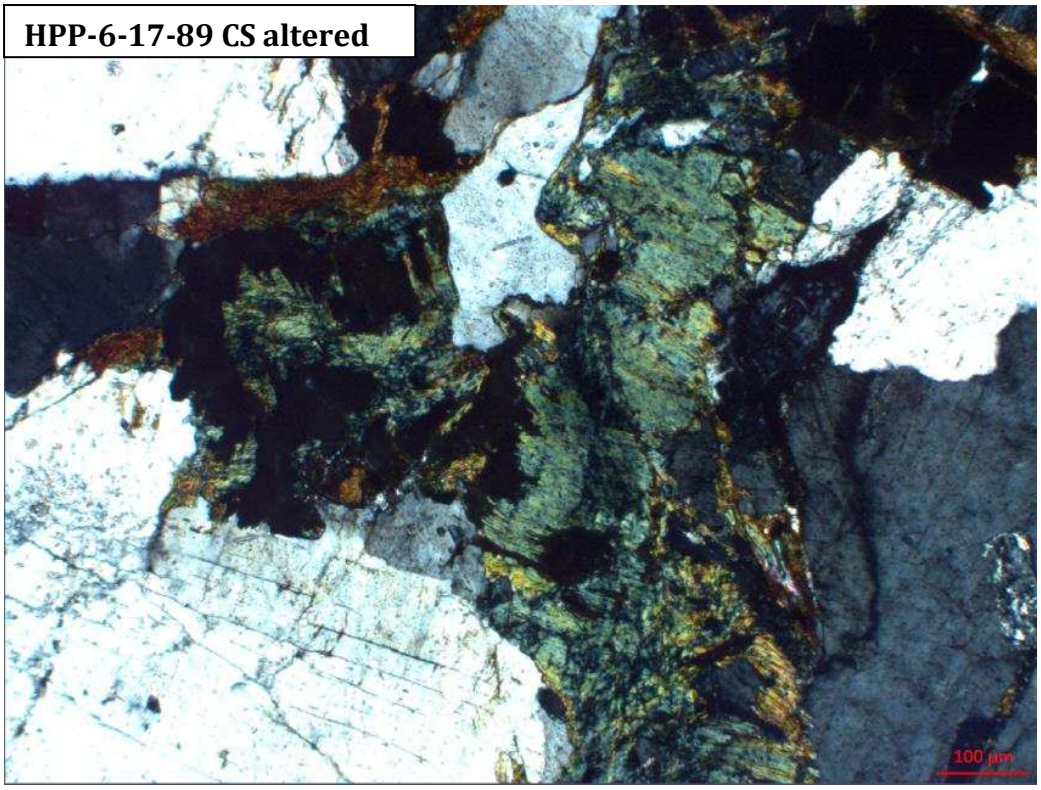

HPP6-9-54- Unaltered Ttc

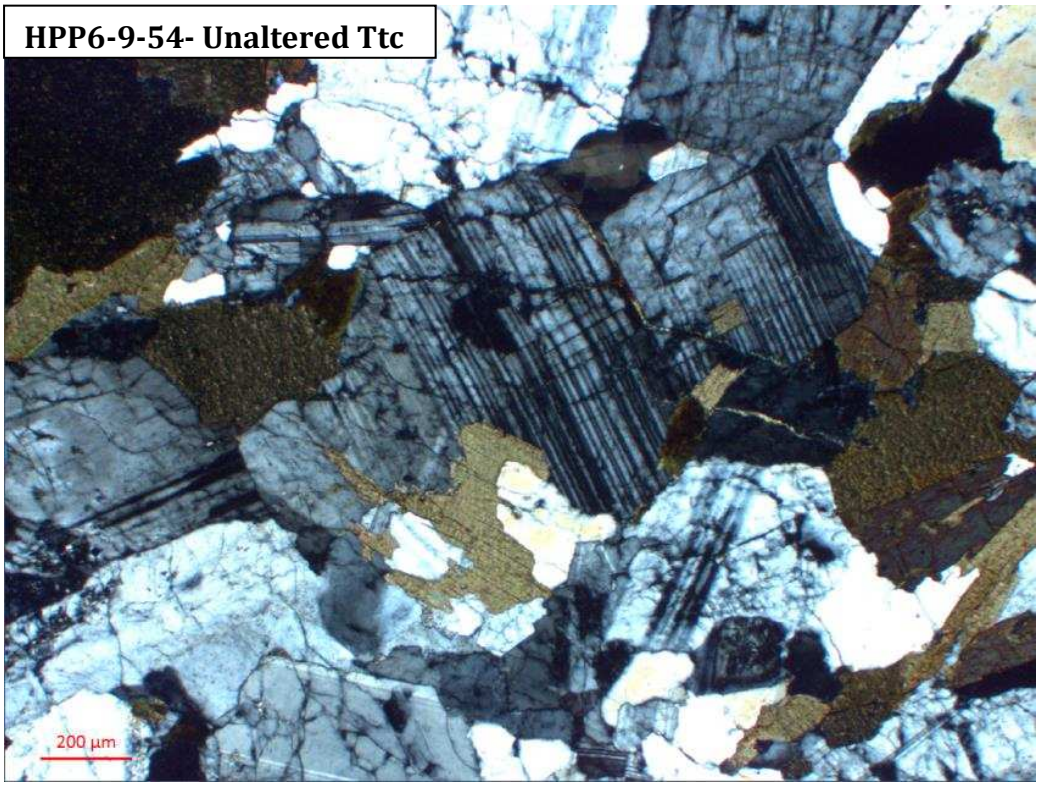

HPP6-7-S20 -Unaltered Tcc

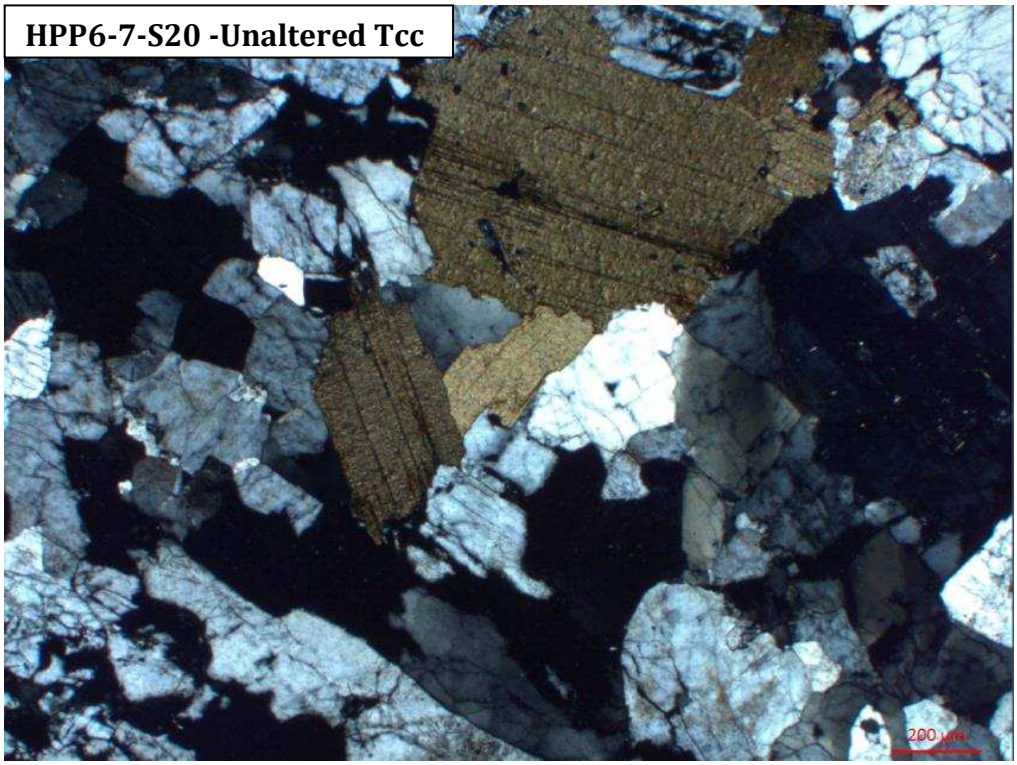

HPP6-16-76-Unaltered Tmg

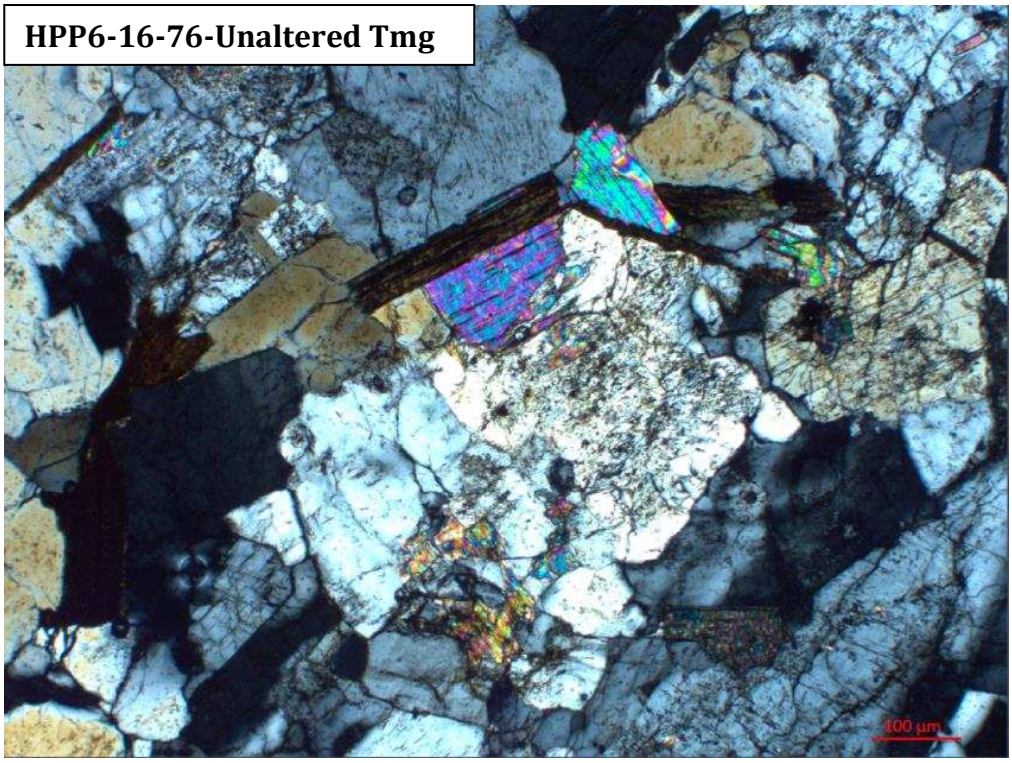

APPENDIX 2

Table 2: Whole rock geochemical results

	Transect 1				Transect 2					
	HPP6-4-16	**HPP6-13-62**	**HPP6-13-65**	**HPP6-13-66A**	**HPP6-9-42**	**HPP6-9-43**	**HPP6-9-52**	**HPP6-9-53**	**HPP6-9-54**	**HPP6-9-49**
Major oxides (wt.%)										
SiO2	76.6	77.8	77.7	75.5	67.7	79	58.6	71	64.6	60
Al2O3	13.25	13.5	13.2	13.4	14.55	11.7	17.9	14.25	16.05	17.6
Fe2O3	0.67	0.93	1.02	0.94	3.08	0.82	5.02	3.46	4.8	3.82
CaO	1.03	1.02	0.8	1.65	2.56	0.2	4.59	1.77	4.19	2.05
MgO	0.03	0.08	0.05	0.15	1.53	0.07	1.51	1.08	1.53	1.2
Na2O	3.28	3.78	4.09	2.88	3.38	3.41	6.33	4.12	3.37	6.65
K2O	5.23	4.1	3.67	4.9	3.17	4.93	2.63	3.36	2.5	3.85
Cr2O3	<0.01	<0.01	<0.01	<0.01	0.01	<0.01	<0.01	<0.01	<0.01	<0.01
TiO2	0.03	0.04	0.03	0.04	0.47	0.06	0.88	0.55	0.69	0.56
MnO	0.01	0.02	0.01	0.02	0.05	0.02	0.07	0.06	0.07	0.05
P2O5	<0.01	0.01	0.01	0.01	0.17	0.01	0.28	0.19	0.26	0.21
SrO	0.01	0.01	0.01	0.02	0.05	0.02	0.1	0.05	0.07	0.1
BaO	<0.01	0.01	0.01	0.03	0.1	0.04	0.14	0.16	0.11	0.2
Trace elements (ppm)										
Ba	16.2	55	56.7	323	916	339	1335	1530	1065	1985
Ce	6.5	11	10.6	8.8	86.5	4.8	147	96.9	120.5	105.5
Cr	<10	<10	10	<10	40	<10	20	10	10	10
Cs	3.62	3.14	1.43	3.19	7.25	2.53	9.18	2.86	2.68	1.84
Dy	1.27	1.56	2.54	4.18	3.32	0.36	7.27	3.87	4.03	3.96
Er	0.94	1.18	1.54	2.94	1.68	0.29	3.58	1.94	2.11	1.94
Eu	0.3	0.28	0.39	0.41	1.28	0.29	2.42	1.49	1.67	1.63
Ga	16.7	18.2	18.2	20.3	16.9	11.2	24.7	20.7	23.6	21.1
Gd	0.96	1.43	2.11	2.61	4.38	0.26	9.19	4.94	5.42	5.35
Hf	1.1	1.7	1.8	2.9	5.7	1.5	8.6	5.6	6.6	6.9
Ho	0.3	0.33	0.54	0.98	0.64	0.07	1.46	0.76	0.74	0.77
La	2.8	5.1	5	4.1	47.9	2.8	77.6	53.1	65.9	57.9
Lu	0.24	0.27	0.25	0.59	0.23	0.1	0.45	0.25	0.27	0.29
Nb	5.9	12.7	14.2	18.2	20.3	7.6	32.7	18.2	18.9	20.4
Nd	3.1	5.6	5.5	4.8	32.2	1.7	61.2	38.4	46	40.2
Pr	0.78	1.41	1.39	1.12	9.21	0.5	16.5	10.55	12.85	11.4
Rb	209	157.5	137.5	162.5	142	186	110.5	133	110	101.5
Sm	1.04	1.5	2.01	1.86	5.49	0.26	11.7	6.56	7.84	6.85
Sn	1	2	1	2	3	2	5	3	3	5
Sr	61	84.9	137.5	150.5	496	219	891	488	654	927
Ta	0.9	1.8	2.4	4.2	1.7	0.5	3	1.5	1.3	1.5
Tb	0.2	0.25	0.4	0.59	0.59	0.05	1.45	0.73	0.75	0.78
Th	10.1	9.51	9.83	10.9	17.15	9.11	28.4	18.75	22.3	26.5
Tm	0.19	0.19	0.26	0.52	0.26	0.07	0.51	0.3	0.28	0.28
U	3.23	2.86	3.4	12.25	3.8	2.02	4.3	2.91	2.36	3.6
V	<5	<5	<5	6	49	<5	76	56	71	34
W	<1	1	1	<1	<1	<1	1	1	<1	4
Y	10	10.6	15	31.6	17.5	2.5	37.4	20.9	21	22
Yb	1.37	1.54	1.71	3.79	1.64	0.56	3.29	1.81	1.69	1.91
Zr	28	41	39	65	227	35	338	223	268	265
Ag	<0.5	<0.5	<0.5	<0.5	<0.5	<0.5	<0.5	<0.5	<0.5	<0.5
As	<5	<5	6	<5	<5	<5	<5	<5	<5	<5
Cd	<0.5	<0.5	<0.5	<0.5	<0.5	<0.5	<0.5	<0.5	<0.5	<0.5
Co	<1	<1	<1	<1	3	<1	6	4	4	5
Cu	2	4	5	9	11	5	5	6	7	7
Li	10	10	<10	10	40	<10	40	40	30	30
Mo	<1	1	<1	<1	<1	1	1	1	1	<1
Ni	1	1	2	<1	16	1	4	4	6	3
Pb	51	43	38	44	19	28	23	19	16	24
Sc	1	1	2	3	6	1	9	6	7	6
Tl	<10	<10	<10	<10	<10	<10	<10	<10	<10	<10
Zn	11	10	9	10	45	13	94	65	85	78

	Transect 3			Transect 4				Transect 5		
	HPP6-8-27	**HPP6-8-28**	**HPP6-8-30**	**HPP6-8-33**	**HPP6-8-34**	**HPP6-8-36**	**HPP6-8-37**	**HPP6-13-68**	**HPP6-13-69**	**HPP6-13-70**
Major oxides (wt.%)										
SiO2	77.6	77.9	68	72.7	11.1	78.4	76.4	58.5	73.8	41.2
Al2O3	13.45	13.4	15.75	13.75	0.55	12.15	12.85	19.6	13.3	12.25
Fe2O3	0.67	0.98	4.14	1.94	0.26	0.53	1.14	3.85	3.47	5.02
CaO	0.96	0.99	3.64	1.91	48.9	0.11	0.25	1.95	0.43	30.7
MgO	0.04	0.03	1.18	0.43	0.55	0.06	0.1	1.25	1.06	4.16
Na2O	3.7	3.67	3.33	3.12	0.07	3.12	3.21	6.58	3.75	0.51
K2O	4.23	4.51	3.16	4.08	0.18	4.5	4.24	3.12	2.3	0.06
Cr2O3	<0.01	<0.01	<0.01	<0.01	<0.01	<0.01	<0.01	<0.01	<0.01	0.01
TiO2	0.04	0.03	0.61	0.26	0.03	0.03	0.04	0.59	0.49	0.49
MnO	0.01	0.02	0.06	0.05	0.02	0.04	0.03	0.06	0.05	0.08
P2O5	0.02	0.01	0.23	0.08	0.11	0.02	0.14	0.19	0.19	0.05
SrO	0.01	<0.01	0.06	0.03	0.04	<0.01	0.01	0.06	0.05	0.08
BaO	<0.01	<0.01	0.13	0.06	<0.01	0.02	0.01	0.29	0.11	0.01
Trace elements (ppm)										
Ba	45.1	24.9	1235	602	28.6	160	127	2710	952	68.6
Ce	3.9	7.1	107	56.7	4.7	16.3	14.4	98.6	76.7	50.4
Cr	<10	10	10	10	10	<10	10	10	10	60
Cs	1.42	2.7	2.83	3.44	0.32	11.2	5.5	2.7	2.55	0.44
Dy	2.28	3.55	3.53	2.4	0.24	4.06	3.17	3.27	2.88	3.58
Er	1.88	2.41	1.81	1.48	0.14	3.18	1.87	1.69	1.42	2.01
Eu	0.28	0.28	1.55	0.83	0.07	0.16	0.22	1.67	1.04	0.82
Ga	18.5	19.7	22.4	19.2	0.8	17.8	23.5	19.7	14.7	16.1
Gd	1.18	2.49	4.93	2.93	0.29	3.1	2.62	4.7	3.85	4.23
Hf	2.1	2.6	7.1	4.7	0.4	5.3	1.5	6.1	4.7	2.1
Ho	0.6	0.8	0.71	0.5	0.06	1	0.63	0.66	0.6	0.75
La	1.6	3.8	57.9	30.7	2.7	7	7.3	54.8	40	26.6
Lu	0.36	0.36	0.24	0.3	0.02	0.82	0.24	0.23	0.22	0.27
Nb	14.8	13.9	18.8	18.3	0.8	26.3	24.3	14.1	15.4	13.1
Nd	1.8	4.9	42.5	21.9	1.9	8.8	6.6	38.8	29.3	23.8
Pr	0.41	1.1	11.75	6.04	0.5	2.2	1.77	10.75	8.21	6
Rb	187.5	218	124.5	179	6.4	268	235	85.3	83.8	3
Sm	0.68	1.89	7.14	3.94	0.3	2.8	2.41	6.45	4.95	4.68
Sn	1	2	3	4	1	3	8	3	3	5
Sr	58.5	49.8	590	286	420	41	70.8	580	413	746
Ta	2.2	1.6	1.3	2.8	0.1	4.7	2.7	0.9	1.1	0.8
Tb	0.29	0.53	0.71	0.45	0.05	0.6	0.52	0.6	0.54	0.66
Th	10.4	10.8	21.4	23.6	0.7	34.4	5.85	16.85	16.2	8.54
Tm	0.34	0.36	0.26	0.24	0.02	0.59	0.27	0.24	0.21	0.27
U	3.51	8.25	5.69	5.72	0.67	10.2	2.67	2.51	2.33	1.38
V	<5	<5	53	19	<5	<5	<5	60	50	77
W	1	<1	<1	<1	<1	1	2	3	2	2
Y	16.4	23.8	18.4	15.5	1.8	32.2	20.6	18.2	16	20
Yb	2.34	2.33	1.57	1.68	0.15	4.85	1.9	1.56	1.47	1.71
Zr	50	61	287	149	16	104	36	231	184	77
Ag	<0.5	<0.5	<0.5	<0.5	<0.5	0.5	<0.5	<0.5	<0.5	<0.5
As	<5	<5	<5	6	5	<5	<5	7	<5	5
Cd	<0.5	<0.5	<0.5	<0.5	<0.5	<0.5	<0.5	<0.5	<0.5	0.9
Co	<1	<1	3	1	<1	<1	<1	5	4	11
Cu	11	5	6	5	4	6	5	6	4	7
Li	10	<10	50	60	<10	10	10	20	20	<10
Mo	<1	1	1	1	<1	<1	1	<1	<1	1
Ni	1	1	3	<1	<1	<1	2	5	3	26
Pb	48	46	18	38	3	41	39	15	17	6
Sc	2	1	6	3	<1	2	3	6	6	9
Tl	<10	<10	<10	<10	<10	<10	<10	<10	<10	<10
Zn	103	11	79	46	6	21	17	61	57	106

	Transect 6			Transect 7			Potassic sample	Greisen?
	HPP6-8-39	**HPP6-17-89**	**HPP6-17-91**	**HPP6-7-18**	**HPP6-7-19**	**HPP6-7-20**	**HPP6-2-6**	**HPP6-16-76**
Major oxides (wt.%)								
SiO2	76.7	74.4	74.9	77.7	76.2	73.5	76.4	76.4
Al2O3	13.1	13.6	13.3	12.6	13.25	13.5	12.65	14.05
Fe2O3	1.18	2.35	1.87	0.76	1.57	2.17	1.08	1.03
CaO	0.68	1.33	1.28	0.61	0.15	1.62	0.69	0.73
MgO	0.08	0.37	0.25	0.05	0.27	0.43	0.02	0.07
Na2O	3.69	3.49	3.28	2.44	2.89	2.87	3.62	3.34
K2O	4.83	4.11	4.48	6.47	4.71	4.64	4.85	5.29
Cr2O3	<0.01	<0.01	<0.01	<0.01	<0.01	<0.01	<0.01	<0.01
TiO2	0.05	0.26	0.18	0.08	0.15	0.26	0.04	0.05
MnO	0.02	0.05	0.04	0.01	0.03	0.04	0.01	0.02
P2O5	0.02	0.08	0.05	<0.01	0.05	0.13	0.02	0.09
SrO	0.02	0.03	0.02	0.05	0.01	0.03	<0.01	0.01
BaO	0.03	0.08	0.09	0.12	0.05	0.07	<0.01	0.01
Trace elements (ppm)								
Ba	257	763	797	1060	462	606	19	141
Ce	19.5	68.2	53.6	12	25.7	49	13.4	13.8
Cr	10	10	<10	10	10	10	10	<10
Cs	4.68	4.74	5.81	3.09	5.36	6.58	5.95	6.6
Dy	2.91	2.52	2.11	0.82	1.28	2.12	0.88	3.08
Er	1.79	1.38	1.07	0.36	0.82	1.13	0.74	1.88
Eu	0.35	0.9	0.77	0.71	0.44	0.79	0.11	0.32
Ga	16.1	17.4	16.7	11.8	17.1	18.5	22.3	22.6
Gd	2.59	3.65	2.77	1.05	1.51	2.66	0.83	2.6
Hf	2.3	4.9	3.8	1.9	2.9	4.2	5.9	1.6
Ho	0.56	0.5	0.42	0.16	0.27	0.4	0.22	0.65
La	10	36	28.4	5.5	11.7	26.5	4.2	7.1
Lu	0.34	0.21	0.17	0.07	0.18	0.2	0.3	0.29
Nb	15.7	18.5	13.3	7.4	15.3	16.8	21.2	26.7
Nd	8.6	27.5	21.2	5.5	9.4	20	4.1	6.2
Pr	2.26	7.57	5.98	1.45	2.63	5.48	1.14	1.64
Rb	215	162.5	174	181.5	228	232	286	266
Sm	2.48	5.01	3.94	1.2	1.84	3.42	1.01	2.13
Sn	3	4	3	1	3	5	3	8
Sr	141.5	263	206	443	127.5	274	17.2	75
Ta	2.7	1.5	1.1	0.8	1.6	1.5	12.4	2.3
Tb	0.48	0.49	0.43	0.14	0.24	0.35	0.16	0.53
Th	18.2	23.6	16.3	6.01	17.2	16.4	24.3	7.23
Tm	0.3	0.2	0.17	0.06	0.13	0.15	0.15	0.27
U	6.22	4.38	4.19	1.01	5.7	4.15	6.99	3.04
V	<5	14	12	7	15	19	<5	<5
W	<1	1	1	12	3	1	<1	1
Y	19.1	14.1	11.9	4	7.9	11.7	6.4	20.5
Yb	2.05	1.3	1.13	0.39	0.9	1.21	1.37	1.78
Zr	46	171	127	54	90	138	67	32
Ag	<0.5	<0.5	<0.5	<0.5	<0.5	<0.5	<0.5	<0.5
As	<5	<5	<5	<5	<5	<5	<5	<5
Cd	<0.5	<0.5	<0.5	<0.5	<0.5	<0.5	<0.5	<0.5
Co	<1	1	<1	<1	1	1	<1	<1
Cu	8	10	6	4	9	9	4	9
Li	10	40	20	10	20	50	20	20
Mo	<1	<1	<1	1	1	1	1	1
Ni	2	2	2	1	3	1	<1	2
Pb	39	30	23	25	31	41	58	54
Sc	1	3	2	2	2	3	2	3
Tl	<10	<10	<10	<10	<10	<10	<10	<10
Zn	15	64	40	5	26	42	8	17

Table 3: Unaltered data, and averages used for the mass balance calculations, from Barnes et al. (2001)

	Ttc	Ttc	Ttc	Ttc	
Sample I.D.	**44-95**	**27-95**	**32-95**	**14-95**	**AVG Ttc**
Major oxides (wt. %)					
SiO2	70.08	65.14	67.07	70.63	68.23
TiO2	0.53	0.78	0.7	0.51	0.63
Al2O3	14.9	15.99	15.56	14.48	15.2325
Fe2O3	3.29	5.32	4.67	3.49	4.1925
MnO	0.06	0.08	0.07	0.06	0.0675
MgO	0.93	1.71	1.46	0.97	1.2675
CaO	2.97	3.95	3.73	3.01	3.415
Na2O	3.22	3.04	3.01	3.01	3.07
K2O	3.41	3.6	3.83	3.47	3.5775
P2O5	0.21	0.23	0.21	0.19	0.21
Trace elements (ppm)					
Ba	956	1623	1184	1038	1200.25
Ce	83	111.1	75.6	101.7	92.85
Cr	4	6	8	6	6
Cs	3.46	2.85	3.4	3.62	3.3325
Eu	1.19	1.69	1.06	1.17	1.2775
Hf	5.6	7.23	7.19	6.05	6.5175
La	43.7	59.6	40.6	55.1	49.75
Lu	N/A	0.31	0.26	0.21	0.26
Nb	23	23	21	21	22
Nd	29	50	28	41	37
Rb	129	119	122	137	126.75
Sm	6.03	8.19	5.63	6.16	6.5025
Sr	424	517	478	430	462.25
Ta	1.6	1.35	0.94	1.13	1.255
Tb	0.58	0.88	0.64	0.54	0.66
Th	19.57	21.4	14.2	24.04	19.8025
U	2.97	2.86	2.29	2.69	2.7025
V	34	70	60	35	49.75
Y	19.4	29.2	23.3	19.1	22.75
Yb	1.49	2.24	1.6	1.39	1.68
Zr	211	310	257	191	242.25
Cu	1	1	2	2	1.5

Table 3 continued:

	Tcc	Tcc	Tcc	
Sample I.D.	**195**	**197**	**37-95**	**AVG Tcc**
Major oxides (wt. %)				
SiO2	76.66	76.34	75.78	76.26
TiO2	0.06	0.1	0.15	0.103333
Al2O3	13.28	12.56	12.94	12.92667
Fe2O3	0.65	0.82	1.09	0.853333
MnO	0.02	0.02	0.03	0.023333
MgO	0.12	0.17	0.3	0.196667
CaO	2.26	1.32	1.72	1.766667
Na2O	4.23	2.42	3.12	3.256667
K2O	1.78	5.47	4.13	3.793333
P2O5	0.02	0.02	0.04	0.026667
Trace elements (ppm)				
Ba	34	207	331	190.6667
Ce	N/A	N/A	22.7	22.7
Cr	13	1	3	5.666667
Cs	N/A	N/A	4.2	4.2
Eu	N/A	N/A	0.54	0.54
Hf	N/A	N/A	3.18	3.18
La	N/A	N/A	11.9	11.9
Lu	N/A	N/A	0.27	0.27
Nb	12	12	11	11.66667
Nd	N/A	N/A	7.6	7.6
Rb	61	193	166	140
Sm	N/A	N/A	1.79	1.79
Sr	130	228	215	191
Ta	N/A	N/A	0.85	0.85
Tb	N/A	N/A	0.29	0.29
Th	N/A	N/A	26.3	26.3
U	N/A	N/A	11.02	11.02
V	3	7	9	6.333333
Y	9.7	4.4	7.6	7.233333
Yb	N/A	N/A	0.8	0.8
Zr	98	79	82	86.33333
Cu	N/A	N/A	1	1

Table 3 continued:

	Tmg	Tmg	Tmg	
Sample I.D.	**102-94**	**28-95**	**8-95**	**AVG Tmg**
Major oxides (wt. %)				
SiO2	76.34	74.76	77.01	76.03667
TiO2	0.04	0.07	0.02	0.043333
Al2O3	13.19	14.58	13.3	13.69
Fe2O3	0.63	0.94	0.46	0.676667
MnO	0.03	0.03	0.06	0.04
MgO	0.06	0.14	0.06	0.086667
CaO	0.87	0.73	1.17	0.923333
Na2O	3.76	3.56	3.59	3.636667
K2O	4.52	5	3.74	4.42
P2O5	0.01	0.06	0.03	0.033333
Trace elements (ppm)				
Ba	64	413	26	167.6667
Ce	N/A	48.8	N/A	48.8
Cr	N/A	3	2	2.5
Cs	N/A	7.36	N/A	7.36
Eu	N/A	0.55	N/A	0.55
Hf	N/A	3.46	N/A	3.46
La	N/A	25.6	N/A	25.6
Lu	N/A	0.346	N/A	0.346
Nb	21	41	40	34
Nd	N/A	24	N/A	24
Rb	224	357	236	272.3333
Sm	N/A	4.14	N/A	4.14
Sr	55	86	31	57.33333
Ta	N/A	4.15	N/A	4.15
Tb	N/A	0.63	N/A	0.63
Th	N/A	24.3	N/A	24.3
U	N/A	6.23	N/A	6.23
V	N/A	4	1	2.5
Y	32.1	33.2	58.9	41.4
Yb	N/A	2.52	N/A	2.52
Zr	51	95	77	74.33333
Cu	2	3	6	3.666667

Table 4: Mass balance of alteration results. Samples identified in section 5.1 as mis-assigned, have results from both the original assignment, and the reassignment.

			Overall mass change (%)	3.321
			Slope	0.968
	Unaltered	Altered	Gain/Loss relative to Ci0	Gain/Loss in wt.% or ppm
Sample	TMG	HPP6-4-16	ΔCi/Ci0	ΔCi
Oxides (Wt.%)				
SiO2	76.037	76.600	0.041	3.107
TiO2	0.043	0.030	-0.285	-0.012
Al2O3	13.690	13.250	0.000	0.000
Fe2O3	0.677	0.670	0.023	0.016
MnO	0.040	0.010	-0.742	-0.030
MgO	0.087	0.030	-0.642	-0.056
CaO	0.923	1.030	0.153	0.141
Na2O	3.637	3.280	-0.068	-0.248
K2O	4.420	5.230	0.223	0.984
P2O5	0.033	0.005	-0.845	-0.028
Trace elements (ppm)				
Ba	167.667	16.200	-0.900	-150.929
Ce	48.800	6.500	-0.862	-42.084
Cr	2.500	9.000	2.720	6.799
Cs	7.360	3.620	-0.492	-3.620
Eu	0.550	0.300	-0.436	-0.240
Hf	3.460	1.100	-0.672	-2.323
La	25.600	2.800	-0.887	-22.707
Lu	0.346	0.240	-0.283	-0.098
Nb	34.000	5.900	-0.821	-27.904
Nd	24.000	3.100	-0.867	-20.797
Rb	272.333	209.000	-0.207	-56.393
Sm	4.140	1.040	-0.740	-3.065
Sr	57.333	61.000	0.099	5.692
Ta	4.150	0.900	-0.776	-3.220
Tb	0.630	0.200	-0.672	-0.423
Th	24.300	10.100	-0.571	-13.865
U	6.230	3.230	-0.464	-2.893
V	2.500	4.000	0.653	1.633
Y	41.400	10.000	-0.750	-31.068
Yb	2.520	1.370	-0.438	-1.105
Zr	74.333	28.000	-0.611	-45.404
Cu	3.667	2.000	-0.436	-1.600

			Overall mass change (%)	1.407
			Slope	0.986
	Unaltered	Altered	Gain/Loss relative to Ci0	Gain/Loss in wt.% or ppm
Sample	TMG	HPP6-13-62	ΔCi/Ci0	ΔCi
Oxides (Wt.%)				
SiO2	76.037	77.800	0.038	2.858
TiO2	0.043	0.040	-0.064	-0.003
Al2O3	13.690	13.500	0.000	0.000
Fe2O3	0.677	0.930	0.394	0.266
MnO	0.040	0.020	-0.493	-0.020
MgO	0.087	0.080	-0.064	-0.006
CaO	0.923	1.020	0.120	0.111
Na2O	3.637	3.780	0.054	0.197
K2O	4.420	4.100	-0.059	-0.262
P2O5	0.033	0.010	-0.696	-0.023
Trace elements (ppm)				
Ba	167.667	55.000	-0.667	-111.893
Ce	48.800	11.000	-0.771	-37.645
Cr	2.500	9.000	2.651	6.627
Cs	7.360	3.140	-0.567	-4.176
Eu	0.550	0.280	-0.484	-0.266
Hf	3.460	1.700	-0.502	-1.736
La	25.600	5.100	-0.798	-20.428
Lu	0.346	0.270	-0.209	-0.072
Nb	34.000	12.700	-0.621	-21.121
Nd	24.000	5.600	-0.763	-18.321
Rb	272.333	157.500	-0.414	-112.617
Sm	4.140	1.500	-0.633	-2.619
Sr	57.333	84.900	0.502	28.762
Ta	4.150	1.800	-0.560	-2.325
Tb	0.630	0.250	-0.598	-0.376
Th	24.300	9.510	-0.603	-14.656
U	6.230	2.860	-0.534	-3.330
V	2.500	4.000	0.623	1.556
Y	41.400	10.600	-0.740	-30.651
Yb	2.520	1.540	-0.380	-0.958
Zr	74.333	41.000	-0.441	-32.756
Cu	3.667	4.000	0.106	0.390

			Overall mass change (%)	3.712
			Slope	0.964
	Unaltered	Altered	Gain/Loss relative to Ci0	Gain/Loss in wt.% or ppm
Sample	TMG	HPP6-13-65	ΔCi/Ci0	ΔCi
Oxides (Wt.%)				
SiO2	76.037	77.700	0.060	4.548
TiO2	0.043	0.030	-0.282	-0.012
Al2O3	13.690	13.200	0.000	0.000
Fe2O3	0.677	1.020	0.563	0.381
MnO	0.040	0.010	-0.741	-0.030
MgO	0.087	0.050	-0.402	-0.035
CaO	0.923	0.800	-0.101	-0.094
Na2O	3.637	4.090	0.166	0.605
K2O	4.420	3.670	-0.139	-0.614
P2O5	0.033	0.010	-0.689	-0.023
Trace elements (ppm)				
Ba	167.667	56.700	-0.649	-108.862
Ce	48.800	10.600	-0.775	-37.807
Cr	2.500	10.000	3.148	7.871
Cs	7.360	1.430	-0.798	-5.877
Eu	0.550	0.390	-0.265	-0.146
Hf	3.460	1.800	-0.460	-1.593
La	25.600	5.000	-0.797	-20.414
Lu	0.346	0.250	-0.251	-0.087
Nb	34.000	14.200	-0.567	-19.273
Nd	24.000	5.500	-0.762	-18.296
Rb	272.333	137.500	-0.476	-129.729
Sm	4.140	2.010	-0.496	-2.055
Sr	57.333	137.500	1.487	85.271
Ta	4.150	2.400	-0.400	-1.661
Tb	0.630	0.400	-0.342	-0.215
Th	24.300	9.830	-0.580	-14.105
U	6.230	3.400	-0.434	-2.704
V	2.500	4.000	0.659	1.648
Y	41.400	15.000	-0.624	-25.843
Yb	2.520	1.710	-0.296	-0.747
Zr	74.333	39.000	-0.456	-33.886
Cu	3.667	5.000	0.414	1.519

			Overall mass change (%)	2.164
			Slope	0.979
	Unaltered	Altered	Gain/Loss relative to Ci0	Gain/Loss in wt.% or ppm
Sample	TMG	HPP6-13-66A	ΔCi/Ci0	ΔCi
Oxides (Wt.%)				
SiO2	76.037	75.500	0.014	1.097
TiO2	0.043	0.040	-0.057	-0.002
Al2O3	13.690	13.400	0.000	0.000
Fe2O3	0.677	0.940	0.419	0.284
MnO	0.040	0.020	-0.489	-0.020
MgO	0.087	0.150	0.768	0.067
CaO	0.923	1.650	0.826	0.762
Na2O	3.637	2.880	-0.191	-0.694
K2O	4.420	4.900	0.133	0.586
P2O5	0.033	0.010	-0.694	-0.023
Trace elements (ppm)				
Ba	167.667	323.000	0.968	162.324
Ce	48.800	8.800	-0.816	-39.810
Cr	2.500	9.000	2.678	6.695
Cs	7.360	3.190	-0.557	-4.101
Eu	0.550	0.410	-0.238	-0.131
Hf	3.460	2.900	-0.144	-0.497
La	25.600	4.100	-0.836	-21.411
Lu	0.346	0.590	0.742	0.257
Nb	34.000	18.200	-0.453	-15.406
Nd	24.000	4.800	-0.796	-19.096
Rb	272.333	162.500	-0.390	-106.317
Sm	4.140	1.860	-0.541	-2.240
Sr	57.333	150.500	1.682	96.424
Ta	4.150	4.200	0.034	0.141
Tb	0.630	0.590	-0.043	-0.027
Th	24.300	10.900	-0.542	-13.164
U	6.230	12.250	1.009	6.285
V	2.500	6.000	1.452	3.630
Y	41.400	31.600	-0.220	-9.116
Yb	2.520	3.790	0.537	1.352
Zr	74.333	65.000	-0.107	-7.927
Cu	3.667	9.000	1.508	5.528

			Overall mass change (%)	4.691
			Slope	0.955
	Unaltered	Altered	Gain/Loss relative to Ci0	Gain/Loss in wt.% or ppm
Sample	TTC	HPP6-9-42	ΔCi/Ci0	ΔCi
Oxides (Wt.%)				
SiO2	68.230	67.700	0.039	2.646
TiO2	0.630	0.470	-0.219	-0.138
Al2O3	15.233	14.550	0.000	0.000
Fe2O3	4.193	3.080	-0.231	-0.968
MnO	0.068	0.050	-0.225	-0.015
MgO	1.268	1.530	0.264	0.334
CaO	3.415	2.560	-0.215	-0.735
Na2O	3.070	3.380	0.153	0.469
K2O	3.578	3.170	-0.072	-0.259
P2O5	0.210	0.170	-0.153	-0.032
Trace elements (ppm)				
Ba	1200.250	916.000	-0.201	-241.283
Ce	92.850	86.500	-0.025	-2.293
Cr	6.000	40.000	5.979	35.876
Cs	3.333	7.250	1.278	4.258
Eu	1.278	1.280	0.049	0.063
Hf	6.518	5.700	-0.084	-0.550
La	49.750	47.900	0.008	0.397
Lu	0.260	0.230	-0.074	-0.019
Nb	22.000	20.300	-0.034	-0.748
Nd	37.000	32.200	-0.089	-3.290
Rb	126.750	142.000	0.173	21.911
Sm	6.503	5.490	-0.116	-0.755
Sr	462.250	496.000	0.123	57.016
Ta	1.255	1.700	0.418	0.525
Tb	0.660	0.590	-0.064	-0.042
Th	19.803	17.150	-0.093	-1.848
U	2.703	3.800	0.472	1.276
V	49.750	49.000	0.031	1.548
Y	22.750	17.500	-0.195	-4.429
Yb	1.680	1.640	0.022	0.037
Zr	242.250	227.000	-0.019	-4.602
Cu	1.500	11.000	6.677	10.016

			Overall mass change (%)	30.192
			Slope	0.768
	Unaltered	Altered	Gain/Loss relative to Ci0	Gain/Loss in wt.% or ppm
Sample	TTC	HPP6-9-43	ΔCi/Ci0	ΔCi
Oxides (Wt.%)				
SiO2	68.230	79.000	0.507	34.622
TiO2	0.630	0.060	-0.876	-0.552
Al2O3	15.233	11.700	0.000	0.000
Fe2O3	4.193	0.820	-0.745	-3.125
MnO	0.068	0.020	-0.614	-0.041
MgO	1.268	0.070	-0.928	-1.176
CaO	3.415	0.200	-0.924	-3.155
Na2O	3.070	3.410	0.446	1.370
K2O	3.578	4.930	0.794	2.841
P2O5	0.210	0.010	-0.938	-0.197
Trace elements (ppm)				
Ba	1200.250	339.000	-0.632	-758.898
Ce	92.850	4.800	-0.933	-86.601
Cr	6.000	9.000	0.953	5.717
Cs	3.333	2.530	-0.012	-0.039
Eu	1.278	0.290	-0.704	-0.900
Hf	6.518	1.500	-0.700	-4.565
La	49.750	2.800	-0.927	-46.105
Lu	0.260	0.100	-0.499	-0.130
Nb	22.000	7.600	-0.550	-12.105
Nd	37.000	1.700	-0.940	-34.787
Rb	126.750	186.000	0.911	115.408
Sm	6.503	0.260	-0.948	-6.164
Sr	462.250	219.000	-0.383	-177.129
Ta	1.255	0.500	-0.481	-0.604
Tb	0.660	0.050	-0.901	-0.595
Th	19.803	9.110	-0.401	-7.942
U	2.703	2.020	-0.027	-0.073
V	49.750	4.000	-0.895	-44.542
Y	22.750	2.500	-0.857	-19.495
Yb	1.680	0.560	-0.566	-0.951
Zr	242.250	35.000	-0.812	-196.683
Cu	1.500	5.000	3.340	5.010

			Overall mass change (%)	-14.902
			Slope	1.175
	Unaltered	Altered	Gain/Loss relative to Ci0	Gain/Loss in wt.% or ppm
Sample	TTC	HPP6-9-52	ΔCi/Ci0	ΔCi
Oxides (Wt.%)				
SiO2	68.230	58.600	-0.269	-18.363
TiO2	0.630	0.880	0.189	0.119
Al2O3	15.233	17.900	0.000	0.000
Fe2O3	4.193	5.020	0.019	0.079
MnO	0.068	0.070	-0.118	-0.008
MgO	1.268	1.510	0.014	0.017
CaO	3.415	4.590	0.144	0.491
Na2O	3.070	6.330	0.755	2.317
K2O	3.578	2.630	-0.374	-1.339
P2O5	0.210	0.280	0.135	0.028
Trace elements (ppm)				
Ba	1200.250	1335.000	-0.053	-64.195
Ce	92.850	147.000	0.347	32.244
Cr	6.000	20.000	1.837	11.020
Cs	3.333	9.180	1.344	4.479
Eu	1.278	2.420	0.612	0.782
Hf	6.518	8.600	0.123	0.801
La	49.750	77.600	0.327	16.286
Lu	0.260	0.450	0.473	0.123
Nb	22.000	32.700	0.265	5.827
Nd	37.000	61.200	0.408	15.080
Rb	126.750	110.500	-0.258	-32.717
Sm	6.503	11.700	0.531	3.454
Sr	462.250	891.000	0.640	295.971
Ta	1.255	3.000	1.034	1.298
Tb	0.660	1.450	0.870	0.574
Th	19.803	28.400	0.220	4.365
U	2.703	4.300	0.354	0.957
V	49.750	76.000	0.300	14.924
Y	22.750	37.400	0.399	9.077
Yb	1.680	3.290	0.666	1.120
Zr	242.250	338.000	0.187	45.380
Cu	1.500	5.000	1.837	2.755

			Overall mass change (%)	6.895
			Slope	0.935
	Unaltered	Altered	Gain/Loss relative to Ci0	Gain/Loss in wt.% or ppm
Sample	TTC	HPP6-9-53	ΔCi/Ci0	ΔCi
Oxides (Wt.%)				
SiO2	68.230	71.000	0.112	7.665
TiO2	0.630	0.550	-0.067	-0.042
Al2O3	15.233	14.250	0.000	0.000
Fe2O3	4.193	3.460	-0.118	-0.494
MnO	0.068	0.060	-0.050	-0.003
MgO	1.268	1.080	-0.089	-0.113
CaO	3.415	1.770	-0.446	-1.523
Na2O	3.070	4.120	0.435	1.334
K2O	3.578	3.360	0.004	0.014
P2O5	0.210	0.190	-0.033	-0.007
Trace elements (ppm)				
Ba	1200.250	1530.000	0.363	435.239
Ce	92.850	96.900	0.116	10.731
Cr	6.000	10.000	0.782	4.689
Cs	3.333	2.860	-0.083	-0.275
Eu	1.278	1.490	0.247	0.315
Hf	6.518	5.600	-0.082	-0.531
La	49.750	53.100	0.141	7.011
Lu	0.260	0.250	0.028	0.007
Nb	22.000	18.200	-0.116	-2.545
Nd	37.000	38.400	0.109	4.048
Rb	126.750	133.000	0.122	15.420
Sm	6.503	6.560	0.078	0.510
Sr	462.250	488.000	0.128	59.396
Ta	1.255	1.500	0.278	0.348
Tb	0.660	0.730	0.182	0.120
Th	19.803	18.750	0.012	0.240
U	2.703	2.910	0.151	0.408
V	49.750	56.000	0.203	10.111
Y	22.750	20.900	-0.018	-0.409
Yb	1.680	1.810	0.152	0.255
Zr	242.250	223.000	-0.016	-3.875
Cu	1.500	6.000	3.276	4.914

			Overall mass change (%)	-5.093
			Slope	1.054
	Unaltered	Altered	Gain/Loss relative to Ci0	Gain/Loss in wt.% or ppm
Sample	TTC	HPP6-9-54	ΔCi/Ci0	ΔCi
Oxides (Wt.%)				
SiO2	68.230	64.600	-0.101	-6.920
TiO2	0.630	0.690	0.039	0.025
Al2O3	15.233	16.050	0.000	0.000
Fe2O3	4.193	4.800	0.087	0.363
MnO	0.068	0.070	-0.016	-0.001
MgO	1.268	1.530	0.146	0.185
CaO	3.415	4.190	0.164	0.562
Na2O	3.070	3.370	0.042	0.128
K2O	3.578	2.500	-0.337	-1.205
P2O5	0.210	0.260	0.175	0.037
Trace elements (ppm)				
Ba	1200.250	1065.000	-0.158	-189.495
Ce	92.850	120.500	0.232	21.512
Cr	6.000	10.000	0.582	3.491
Cs	3.333	2.680	-0.237	-0.789
Eu	1.278	1.670	0.241	0.307
Hf	6.518	6.600	-0.039	-0.254
La	49.750	65.900	0.257	12.793
Lu	0.260	0.270	-0.014	-0.004
Nb	22.000	18.900	-0.185	-4.063
Nd	37.000	46.000	0.180	6.657
Rb	126.750	110.000	-0.176	-22.353
Sm	6.503	7.840	0.144	0.938
Sr	462.250	654.000	0.343	158.439
Ta	1.255	1.300	-0.017	-0.021
Tb	0.660	0.750	0.078	0.052
Th	19.803	22.300	0.069	1.362
U	2.703	2.360	-0.171	-0.463
V	49.750	71.000	0.354	17.634
Y	22.750	21.000	-0.124	-2.820
Yb	1.680	1.690	-0.045	-0.076
Zr	242.250	268.000	0.050	12.100
Cu	1.500	7.000	3.429	5.143

			Overall mass change (%)	-13.452
			Slope	1.155
	Unaltered	Altered	Gain/Loss relative to Ci0	Gain/Loss in wt.% or ppm
Sample	TTC	HPP6-9-49	ΔCi/Ci0	ΔCi
Oxides (Wt.%)				
SiO2	68.230	60.000	-0.239	-16.301
TiO2	0.630	0.560	-0.231	-0.145
Al2O3	15.233	17.600	0.000	0.000
Fe2O3	4.193	3.820	-0.211	-0.886
MnO	0.068	0.050	-0.359	-0.024
MgO	1.268	1.200	-0.181	-0.229
CaO	3.415	2.050	-0.480	-1.641
Na2O	3.070	6.650	0.875	2.685
K2O	3.578	3.850	-0.069	-0.245
P2O5	0.210	0.210	-0.135	-0.028
Trace elements (ppm)				
Ba	1200.250	1985.000	0.431	517.734
Ce	92.850	105.500	-0.017	-1.542
Cr	6.000	10.000	0.442	2.655
Cs	3.333	1.840	-0.522	-1.740
Eu	1.278	1.630	0.104	0.133
Hf	6.518	6.900	-0.084	-0.546
La	49.750	57.900	0.007	0.361
Lu	0.260	0.290	-0.035	-0.009
Nb	22.000	20.400	-0.197	-4.344
Nd	37.000	40.200	-0.060	-2.208
Rb	126.750	101.500	-0.307	-38.903
Sm	6.503	6.850	-0.088	-0.574
Sr	462.250	927.000	0.736	340.053
Ta	1.255	1.500	0.034	0.043
Tb	0.660	0.780	0.023	0.015
Th	19.803	26.500	0.158	3.133
U	2.703	3.600	0.153	0.413
V	49.750	34.000	-0.409	-20.324
Y	22.750	22.000	-0.163	-3.709
Yb	1.680	1.910	-0.016	-0.027
Zr	242.250	265.000	-0.053	-12.897
Cu	1.500	7.000	3.039	4.558

			Overall mass change (%)	1.784
			Slope	0.982
	Unaltered	Altered	Gain/Loss relative to Ci0	Gain/Loss in wt.% or ppm
Sample	TMG	HPP6-8-27	ΔCi/Ci0	ΔCi
Oxides (Wt.%)				
SiO2	76.037	77.600	0.039	2.948
TiO2	0.043	0.040	-0.060	-0.003
Al2O3	13.690	13.450	0.000	0.000
Fe2O3	0.677	0.670	0.008	0.005
MnO	0.040	0.010	-0.746	-0.030
MgO	0.087	0.040	-0.530	-0.046
CaO	0.923	0.960	0.058	0.054
Na2O	3.637	3.700	0.036	0.129
K2O	4.420	4.230	-0.026	-0.115
P2O5	0.033	0.020	-0.389	-0.013
Trace elements (ppm)				
Ba	167.667	45.100	-0.726	-121.762
Ce	48.800	3.900	-0.919	-44.830
Cr	2.500	9.000	2.664	6.661
Cs	7.360	1.420	-0.804	-5.915
Eu	0.550	0.280	-0.482	-0.265
Hf	3.460	2.100	-0.382	-1.323
La	25.600	1.600	-0.936	-23.971
Lu	0.346	0.360	0.059	0.020
Nb	34.000	14.800	-0.557	-18.936
Nd	24.000	1.800	-0.924	-22.168
Rb	272.333	187.500	-0.299	-81.488
Sm	4.140	0.680	-0.833	-3.448
Sr	57.333	58.500	0.039	2.211
Ta	4.150	2.200	-0.460	-1.911
Tb	0.630	0.290	-0.531	-0.335
Th	24.300	10.400	-0.564	-13.714
U	6.230	3.510	-0.427	-2.657
V	2.500	4.000	0.629	1.571
Y	41.400	16.400	-0.597	-24.707
Yb	2.520	2.340	-0.055	-0.138
Zr	74.333	50.000	-0.315	-23.441
Cu	3.667	11.000	2.054	7.530

			Overall mass change (%)	2.164
			Slope	0.979
	Unaltered	Altered	Gain/Loss relative to Ci0	Gain/Loss in wt.% or ppm
Sample	TMG	HPP6-8-28	ΔCi/Ci0	ΔCi
Oxides (Wt.%)				
SiO2	76.037	77.900	0.047	3.549
TiO2	0.043	0.030	-0.293	-0.013
Al2O3	13.690	13.400	0.000	0.000
Fe2O3	0.677	0.980	0.480	0.325
MnO	0.040	0.020	-0.489	-0.020
MgO	0.087	0.030	-0.646	-0.056
CaO	0.923	0.990	0.095	0.088
Na2O	3.637	3.670	0.031	0.113
K2O	4.420	4.510	0.042	0.188
P2O5	0.033	0.010	-0.694	-0.023
Trace elements (ppm)				
Ba	167.667	24.900	-0.848	-142.228
Ce	48.800	7.100	-0.851	-41.546
Cr	2.500	10.000	3.087	7.716
Cs	7.360	2.700	-0.625	-4.602
Eu	0.550	0.280	-0.480	-0.264
Hf	3.460	2.600	-0.232	-0.804
La	25.600	3.800	-0.848	-21.718
Lu	0.346	0.360	0.063	0.022
Nb	34.000	13.900	-0.582	-19.799
Nd	24.000	4.900	-0.791	-18.994
Rb	272.333	218.000	-0.182	-49.615
Sm	4.140	1.890	-0.534	-2.209
Sr	57.333	49.800	-0.113	-6.456
Ta	4.150	1.600	-0.606	-2.515
Tb	0.630	0.530	-0.141	-0.089
Th	24.300	10.800	-0.546	-13.266
U	6.230	8.250	0.353	2.199
V	2.500	4.000	0.635	1.587
Y	41.400	23.800	-0.413	-17.085
Yb	2.520	2.330	-0.055	-0.140
Zr	74.333	61.000	-0.162	-12.013
Cu	3.667	5.000	0.393	1.442

			Overall mass change (%)	-3.286
			Slope	1.034
	Unaltered	Altered	Gain/Loss relative to Ci0	Gain/Loss in wt.% or ppm
Sample	TTC	HPP6-8-30	ΔCi/Ci0	ΔCi
Oxides (Wt.%)				
SiO2	68.230	68.000	-0.036	-2.464
TiO2	0.630	0.610	-0.064	-0.040
Al2O3	15.233	15.750	0.000	0.000
Fe2O3	4.193	4.140	-0.045	-0.189
MnO	0.068	0.060	-0.140	-0.009
MgO	1.268	1.180	-0.100	-0.126
CaO	3.415	3.640	0.031	0.105
Na2O	3.070	3.330	0.049	0.151
K2O	3.578	3.160	-0.146	-0.521
P2O5	0.210	0.230	0.059	0.012
Trace elements (ppm)				
Ba	1200.250	1235.000	-0.005	-5.829
Ce	92.850	107.000	0.115	10.634
Cr	6.000	10.000	0.612	3.671
Cs	3.333	2.830	-0.179	-0.595
Eu	1.278	1.550	0.173	0.222
Hf	6.518	7.100	0.054	0.349
La	49.750	57.900	0.126	6.248
Lu	0.260	0.240	-0.107	-0.028
Nb	22.000	18.800	-0.174	-3.818
Nd	37.000	42.500	0.111	4.104
Rb	126.750	124.500	-0.050	-6.341
Sm	6.503	7.140	0.062	0.403
Sr	462.250	590.000	0.234	108.364
Ta	1.255	1.300	0.002	0.002
Tb	0.660	0.710	0.040	0.027
Th	19.803	21.400	0.045	0.894
U	2.703	5.690	1.036	2.801
V	49.750	53.000	0.030	1.509
Y	22.750	18.400	-0.218	-4.955
Yb	1.680	1.570	-0.096	-0.162
Zr	242.250	287.000	0.146	35.320
Cu	1.500	6.000	2.869	4.303

			Overall mass change (%)	-0.436
			Slope	1.004
	Unaltered	Altered	Gain/Loss relative to Ci0	Gain/Loss in wt.% or ppm
Sample	TMG	HPP6-8-33	ΔCi/Ci0	ΔCi
Oxides (Wt.%)				
SiO2	76.037	72.700	-0.048	-3.654
TiO2	0.043	0.260	4.974	0.216
Al2O3	13.690	13.750	0.000	0.000
Fe2O3	0.677	1.940	1.854	1.255
MnO	0.040	0.050	0.245	0.010
MgO	0.087	0.430	3.940	0.341
CaO	0.923	1.910	1.060	0.978
Na2O	3.637	3.120	-0.146	-0.530
K2O	4.420	4.080	-0.081	-0.358
P2O5	0.033	0.080	1.390	0.046
Trace elements (ppm)				
Ba	167.667	602.000	2.575	431.706
Ce	48.800	56.700	0.157	7.653
Cr	2.500	10.000	2.983	7.456
Cs	7.360	3.440	-0.535	-3.935
Eu	0.550	0.830	0.503	0.276
Hf	3.460	4.700	0.352	1.219
La	25.600	30.700	0.194	4.966
Lu	0.346	0.300	-0.137	-0.047
Nb	34.000	18.300	-0.464	-15.780
Nd	24.000	21.900	-0.091	-2.196
Rb	272.333	179.000	-0.346	-94.114
Sm	4.140	3.940	-0.052	-0.217
Sr	57.333	286.000	3.967	227.419
Ta	4.150	2.800	-0.328	-1.362
Tb	0.630	0.450	-0.289	-0.182
Th	24.300	23.600	-0.033	-0.803
U	6.230	5.720	-0.086	-0.535
V	2.500	19.000	6.567	16.417
Y	41.400	15.500	-0.627	-25.968
Yb	2.520	1.680	-0.336	-0.847
Zr	74.333	149.000	0.996	74.016
Cu	3.667	5.000	0.358	1.312

Recalculated with correct unaltered sample			Overall mass change (%)	10.782
			Slope	0.903
	Unaltered	Altered	Gain/Loss relative to Ci0	Gain/Loss in wt.% or ppm
Sample	TTC	HPP6-8-33	ΔCi/Ci0	ΔCi
Oxides (Wt.%)				
SiO2	68.230	72.700	0.180	12.308
TiO2	0.630	0.260	-0.543	-0.342
Al2O3	15.233	13.750	0.000	0.000
Fe2O3	4.193	1.940	-0.487	-2.043
MnO	0.068	0.050	-0.179	-0.012
MgO	1.268	0.430	-0.624	-0.791
CaO	3.415	1.910	-0.380	-1.299
Na2O	3.070	3.120	0.126	0.386
K2O	3.578	4.080	0.263	0.942
P2O5	0.210	0.080	-0.578	-0.121
Trace elements (ppm)				
Ba	1200.250	602.000	-0.444	-533.343
Ce	92.850	56.700	-0.323	-30.037
Cr	6.000	10.000	0.846	5.078
Cs	3.333	3.440	0.144	0.478
Eu	1.278	0.830	-0.280	-0.358
Hf	6.518	4.700	-0.201	-1.311
La	49.750	30.700	-0.316	-15.740
Lu	0.260	0.300	0.278	0.072
Nb	22.000	18.300	-0.078	-1.727
Nd	37.000	21.900	-0.344	-12.739
Rb	126.750	179.000	0.564	71.549
Sm	6.503	3.940	-0.329	-2.138
Sr	462.250	286.000	-0.315	-145.414
Ta	1.255	2.800	1.472	1.847
Tb	0.660	0.450	-0.245	-0.161
Th	19.803	23.600	0.320	6.342
U	2.703	5.720	1.345	3.634
V	49.750	19.000	-0.577	-28.701
Y	22.750	15.500	-0.245	-5.579
Yb	1.680	1.680	0.108	0.181
Zr	242.250	149.000	-0.319	-77.185
Cu	1.500	5.000	2.693	4.039

			Overall mass change (%)	12.675
			Slope	0.888
	Unaltered	Altered	Gain/Loss relative to Ci0	Gain/Loss in wt.% or ppm
Sample	TMG	HPP6-8-36	ΔCi/Ci0	ΔCi
Oxides (Wt.%)				
SiO2	76.037	78.400	0.162	12.300
TiO2	0.043	0.030	-0.220	-0.010
Al2O3	13.690	12.150	0.000	0.000
Fe2O3	0.677	0.530	-0.117	-0.079
MnO	0.040	0.040	0.127	0.005
MgO	0.087	0.060	-0.220	-0.019
CaO	0.923	0.110	-0.866	-0.799
Na2O	3.637	3.120	-0.033	-0.121
K2O	4.420	4.500	0.147	0.650
P2O5	0.033	0.020	-0.324	-0.011
Trace elements (ppm)				
Ba	167.667	160.000	0.075	12.613
Ce	48.800	16.300	-0.624	-30.434
Cr	2.500	9.000	3.056	7.641
Cs	7.360	11.200	0.715	5.260
Eu	0.550	0.160	-0.672	-0.370
Hf	3.460	5.300	0.726	2.512
La	25.600	7.000	-0.692	-17.713
Lu	0.346	0.820	1.670	0.578
Nb	34.000	26.300	-0.128	-4.367
Nd	24.000	8.800	-0.587	-14.085
Rb	272.333	268.000	0.109	29.635
Sm	4.140	2.800	-0.238	-0.985
Sr	57.333	41.000	-0.194	-11.137
Ta	4.150	4.700	0.276	1.146
Tb	0.630	0.600	0.073	0.046
Th	24.300	34.400	0.595	14.460
U	6.230	10.200	0.845	5.263
V	2.500	4.000	0.803	2.007
Y	41.400	32.200	-0.124	-5.119
Yb	2.520	4.850	1.169	2.945
Zr	74.333	104.000	0.576	42.849
Cu	3.667	6.000	0.844	3.094

			Overall mass change (%)	6.537
			Slope	0.939
	Unaltered	Altered	Gain/Loss relative to Ci0	Gain/Loss in wt.% or ppm
Sample	TMG	HPP6-8-37	ΔCi/Ci0	ΔCi
Oxides (Wt.%)				
SiO2	76.037	76.400	0.070	5.358
TiO2	0.043	0.040	-0.017	-0.001
Al2O3	13.690	12.850	0.000	0.000
Fe2O3	0.677	1.140	0.795	0.538
MnO	0.040	0.030	-0.201	-0.008
MgO	0.087	0.100	0.229	0.020
CaO	0.923	0.250	-0.712	-0.657
Na2O	3.637	3.210	-0.060	-0.217
K2O	4.420	4.240	0.022	0.097
P2O5	0.033	0.140	3.475	0.116
Trace elements (ppm)				
Ba	167.667	127.000	-0.193	-32.365
Ce	48.800	14.400	-0.686	-33.459
Cr	2.500	10.000	3.261	8.154
Cs	7.360	5.500	-0.204	-1.500
Eu	0.550	0.220	-0.574	-0.316
Hf	3.460	1.500	-0.538	-1.862
La	25.600	7.300	-0.696	-17.823
Lu	0.346	0.240	-0.261	-0.090
Nb	34.000	24.300	-0.239	-8.112
Nd	24.000	6.600	-0.707	-16.969
Rb	272.333	235.000	-0.081	-21.971
Sm	4.140	2.410	-0.380	-1.572
Sr	57.333	70.800	0.316	18.095
Ta	4.150	2.700	-0.307	-1.274
Tb	0.630	0.520	-0.121	-0.076
Th	24.300	5.850	-0.744	-18.068
U	6.230	2.670	-0.543	-3.385
V	2.500	4.000	0.705	1.761
Y	41.400	20.600	-0.470	-19.453
Yb	2.520	1.900	-0.197	-0.496
Zr	74.333	36.000	-0.484	-35.980
Cu	3.667	5.000	0.453	1.660

			Overall mass change (%)	-30.153
			Slope	1.432
	Unaltered	Altered	Gain/Loss relative to Ci0	Gain/Loss in wt.% or ppm
Sample	TMG	HPP6-13-68	ΔCi/Ci0	ΔCi
Oxides (Wt.%)				
SiO2	76.037	58.500	-0.463	-35.176
TiO2	0.043	0.590	8.510	0.369
Al2O3	13.690	19.600	0.000	0.000
Fe2O3	0.677	3.850	2.974	2.012
MnO	0.040	0.060	0.048	0.002
MgO	0.087	1.250	9.074	0.786
CaO	0.923	1.950	0.475	0.439
Na2O	3.637	6.580	0.264	0.959
K2O	4.420	3.120	-0.507	-2.241
P2O5	0.033	0.190	2.981	0.099
Trace elements (ppm)				
Ba	167.667	2710.000	10.289	1725.185
Ce	48.800	98.600	0.411	20.069
Cr	2.500	10.000	1.794	4.485
Cs	7.360	2.700	-0.744	-5.474
Eu	0.550	1.670	1.121	0.616
Hf	3.460	6.100	0.231	0.801
La	25.600	54.800	0.495	12.676
Lu	0.346	0.230	-0.536	-0.185
Nb	34.000	14.100	-0.710	-24.152
Nd	24.000	38.800	0.129	3.101
Rb	272.333	85.300	-0.781	-212.754
Sm	4.140	6.450	0.088	0.365
Sr	57.333	580.000	6.066	347.779
Ta	4.150	0.900	-0.849	-3.521
Tb	0.630	0.600	-0.335	-0.211
Th	24.300	16.850	-0.516	-12.531
U	6.230	2.510	-0.719	-4.477
V	2.500	60.000	15.763	39.408
Y	41.400	18.200	-0.693	-28.688
Yb	2.520	1.560	-0.568	-1.430
Zr	74.333	231.000	1.171	87.013
Cu	3.667	6.000	0.143	0.524

Recalculated with			Overall mass change (%)	-22.283
correct unaltered sample			Slope	1.287
	Unaltered	Altered	Gain/Loss relative to Ci0	Gain/Loss in wt.% or ppm
Sample	TTC	HPP6-13-68	ΔCi/Ci0	ΔCi
Oxides (Wt.%)				
SiO2	68.230	58.500	-0.334	-22.766
TiO2	0.630	0.590	-0.272	-0.171
Al2O3	15.233	19.600	0.000	0.000
Fe2O3	4.193	3.850	-0.286	-1.200
MnO	0.068	0.060	-0.309	-0.021
MgO	1.268	1.250	-0.234	-0.296
CaO	3.415	1.950	-0.556	-1.900
Na2O	3.070	6.580	0.666	2.044
K2O	3.578	3.120	-0.322	-1.153
P2O5	0.210	0.190	-0.297	-0.062
Trace elements (ppm)				
Ba	1200.250	2710.000	0.755	905.876
Ce	92.850	98.600	-0.175	-16.221
Cr	6.000	10.000	0.295	1.772
Cs	3.333	2.700	-0.370	-1.234
Eu	1.278	1.670	0.016	0.020
Hf	6.518	6.100	-0.273	-1.777
La	49.750	54.800	-0.144	-7.161
Lu	0.260	0.230	-0.313	-0.081
Nb	22.000	14.100	-0.502	-11.042
Nd	37.000	38.800	-0.185	-6.846
Rb	126.750	85.300	-0.477	-60.458
Sm	6.503	6.450	-0.229	-1.490
Sr	462.250	580.000	-0.025	-11.492
Ta	1.255	0.900	-0.443	-0.556
Tb	0.660	0.600	-0.293	-0.194
Th	19.803	16.850	-0.339	-6.707
U	2.703	2.510	-0.278	-0.752
V	49.750	60.000	-0.063	-3.120
Y	22.750	18.200	-0.378	-8.606
Yb	1.680	1.560	-0.278	-0.468
Zr	242.250	231.000	-0.259	-62.724
Cu	1.500	6.000	2.109	3.163

			Overall mass change (%)	2.932
			Slope	0.972
	Unaltered	Altered	Gain/Loss relative to Ci0	Gain/Loss in wt.% or ppm
Sample	TMG	HPP6-13-69	ΔCi/Ci0	ΔCi
Oxides (Wt.%)				
SiO2	76.037	73.800	-0.001	-0.073
TiO2	0.043	0.490	10.639	0.461
Al2O3	13.690	13.300	0.000	0.000
Fe2O3	0.677	3.470	4.278	2.895
MnO	0.040	0.050	0.287	0.011
MgO	0.087	1.060	11.589	1.004
CaO	0.923	0.430	-0.521	-0.481
Na2O	3.637	3.750	0.061	0.223
K2O	4.420	2.300	-0.464	-2.053
P2O5	0.033	0.190	4.867	0.162
Trace elements (ppm)				
Ba	167.667	952.000	4.844	812.249
Ce	48.800	76.700	0.618	30.149
Cr	2.500	10.000	3.117	7.793
Cs	7.360	2.550	-0.643	-4.735
Eu	0.550	1.040	0.946	0.520
Hf	3.460	4.700	0.398	1.378
La	25.600	40.000	0.608	15.573
Lu	0.346	0.220	-0.346	-0.120
Nb	34.000	15.400	-0.534	-18.148
Nd	24.000	29.300	0.257	6.159
Rb	272.333	83.800	-0.683	-186.076
Sm	4.140	4.950	0.231	0.955
Sr	57.333	413.000	6.415	367.777
Ta	4.150	1.100	-0.727	-3.018
Tb	0.630	0.540	-0.118	-0.074
Th	24.300	16.200	-0.314	-7.625
U	6.230	2.330	-0.615	-3.832
V	2.500	50.000	19.586	48.966
Y	41.400	16.000	-0.602	-24.931
Yb	2.520	1.470	-0.400	-1.007
Zr	74.333	184.000	1.548	115.062
Cu	3.667	4.000	0.123	0.451

Recalculated with correct unaltered sample			Overall mass change (%)	14.530
			Slope	0.873
	Unaltered	Altered	Gain/Loss relative to Ci0	Gain/Loss in wt.% or ppm
Sample	TTC	HPP6-13-69	ΔCi/Ci0	ΔCi
Oxides (Wt.%)				
SiO2	68.230	73.800	0.239	16.293
TiO2	0.630	0.490	-0.109	-0.069
Al2O3	15.233	13.300	0.000	0.000
Fe2O3	4.193	3.470	-0.052	-0.218
MnO	0.068	0.050	-0.152	-0.010
MgO	1.268	1.060	-0.042	-0.053
CaO	3.415	0.430	-0.856	-2.923
Na2O	3.070	3.750	0.399	1.225
K2O	3.578	2.300	-0.264	-0.943
P2O5	0.210	0.190	0.036	0.008
Trace elements (ppm)				
Ba	1200.250	952.000	-0.092	-109.924
Ce	92.850	76.700	-0.054	-5.005
Cr	6.000	10.000	0.909	5.453
Cs	3.333	2.550	-0.124	-0.412
Eu	1.278	1.040	-0.068	-0.086
Hf	6.518	4.700	-0.174	-1.135
La	49.750	40.000	-0.079	-3.938
Lu	0.260	0.220	-0.031	-0.008
Nb	22.000	15.400	-0.198	-4.362
Nd	37.000	29.300	-0.093	-3.443
Rb	126.750	83.800	-0.243	-30.774
Sm	6.503	4.950	-0.128	-0.833
Sr	462.250	413.000	0.023	10.759
Ta	1.255	1.100	0.004	0.005
Tb	0.660	0.540	-0.063	-0.042
Th	19.803	16.200	-0.063	-1.249
U	2.703	2.330	-0.013	-0.034
V	49.750	50.000	0.151	7.515
Y	22.750	16.000	-0.195	-4.425
Yb	1.680	1.470	0.002	0.004
Zr	242.250	184.000	-0.130	-31.515
Cu	1.500	4.000	2.054	3.081

			Overall mass change (%)	-1.323
			Slope	1.013
	Unaltered	Altered	Gain/Loss relative to Ci0	Gain/Loss in wt.% or ppm
Sample	TCC	HPP6-8-39	ΔCi/Ci0	ΔCi
Oxides (Wt.%)				
SiO2	76.260	76.700	-0.008	-0.575
TiO2	0.103	0.050	-0.523	-0.054
Al2O3	12.927	13.100	0.000	0.000
Fe2O3	0.853	1.180	0.365	0.311
MnO	0.023	0.020	-0.154	-0.004
MgO	0.197	0.080	-0.599	-0.118
CaO	1.767	0.680	-0.620	-1.096
Na2O	3.257	3.690	0.118	0.385
K2O	3.793	4.830	0.256	0.973
P2O5	0.027	0.020	-0.260	-0.007
Trace elements (ppm)				
Ba	190.667	257.000	0.330	62.933
Ce	22.700	19.500	-0.152	-3.458
Cr	5.667	10.000	0.741	4.201
Cs	4.200	4.680	0.100	0.418
Eu	0.540	0.350	-0.360	-0.195
Hf	3.180	2.300	-0.286	-0.910
La	11.900	10.000	-0.171	-2.032
Lu	0.270	0.340	0.243	0.066
Nb	11.667	15.700	0.328	3.826
Nd	7.600	8.600	0.117	0.886
Rb	140.000	215.000	0.515	72.155
Sm	1.790	2.480	0.367	0.657
Sr	191.000	141.500	-0.269	-51.372
Ta	0.850	2.700	2.134	1.814
Tb	0.290	0.480	0.633	0.184
Th	26.300	18.200	-0.317	-8.341
U	11.020	6.220	-0.443	-4.882
V	6.333	4.000	-0.377	-2.386
Y	7.233	19.100	1.606	11.614
Yb	0.800	2.050	1.529	1.223
Zr	86.333	46.000	-0.474	-40.942
Cu	1.000	8.000	6.894	6.894

Recalculated with correct unaltered sample			Overall mass change (%)	4.504
			Slope	0.957
	Unaltered	Altered	Gain/Loss relative to Ci0	Gain/Loss in wt.% or ppm
Sample	TMG	HPP6-8-39	ΔCi/Ci0	ΔCi
Oxides (Wt.%)				
SiO2	76.037	76.700	0.054	4.118
TiO2	0.043	0.050	0.206	0.009
Al2O3	13.690	13.100	0.000	0.000
Fe2O3	0.677	1.180	0.822	0.556
MnO	0.040	0.020	-0.477	-0.019
MgO	0.087	0.080	-0.035	-0.003
CaO	0.923	0.680	-0.230	-0.213
Na2O	3.637	3.690	0.060	0.220
K2O	4.420	4.830	0.142	0.628
P2O5	0.033	0.020	-0.373	-0.012
Trace elements (ppm)				
Ba	167.667	257.000	0.602	100.908
Ce	48.800	19.500	-0.582	-28.422
Cr	2.500	10.000	3.180	7.950
Cs	7.360	4.680	-0.335	-2.469
Eu	0.550	0.350	-0.335	-0.184
Hf	3.460	2.300	-0.305	-1.056
La	25.600	10.000	-0.592	-15.150
Lu	0.346	0.340	0.027	0.009
Nb	34.000	15.700	-0.517	-17.593
Nd	24.000	8.600	-0.626	-15.013
Rb	272.333	215.000	-0.175	-47.650
Sm	4.140	2.480	-0.374	-1.548
Sr	57.333	141.500	1.579	90.540
Ta	4.150	2.700	-0.320	-1.328
Tb	0.630	0.480	-0.204	-0.128
Th	24.300	18.200	-0.217	-5.280
U	6.230	6.220	0.043	0.270
V	2.500	4.000	0.672	1.680
Y	41.400	19.100	-0.518	-21.440
Yb	2.520	2.050	-0.150	-0.378
Zr	74.333	46.000	-0.353	-26.262
Cu	3.667	8.000	1.280	4.694

			Overall mass change (%)	-4.951
			Slope	1.052
	Unaltered	Altered	Gain/Loss relative to Ci0	Gain/Loss in wt.% or ppm
Sample	TCC	HPP6-17-89	ΔCi/Ci0	ΔCi
Oxides (Wt.%)				
SiO2	76.260	74.400	-0.073	-5.544
TiO2	0.103	0.260	1.392	0.144
Al2O3	12.927	13.600	0.000	0.000
Fe2O3	0.853	2.350	1.618	1.380
MnO	0.023	0.050	1.037	0.024
MgO	0.197	0.370	0.788	0.155
CaO	1.767	1.330	-0.284	-0.503
Na2O	3.257	3.490	0.019	0.061
K2O	3.793	4.110	0.030	0.113
P2O5	0.027	0.080	1.851	0.049
Trace elements (ppm)				
Ba	190.667	763.000	2.804	534.557
Ce	22.700	68.200	1.856	42.123
Cr	5.667	10.000	0.677	3.838
Cs	4.200	4.740	0.073	0.305
Eu	0.540	0.900	0.584	0.315
Hf	3.180	4.900	0.465	1.477
La	11.900	36.000	1.875	22.318
Lu	0.270	0.210	-0.261	-0.070
Nb	11.667	18.500	0.507	5.917
Nd	7.600	27.500	2.439	18.538
Rb	140.000	162.500	0.103	14.455
Sm	1.790	5.010	1.660	2.972
Sr	191.000	263.000	0.309	58.979
Ta	0.850	1.500	0.677	0.576
Tb	0.290	0.490	0.606	0.176
Th	26.300	23.600	-0.147	-3.868
U	11.020	4.380	-0.622	-6.857
V	6.333	14.000	1.101	6.974
Y	7.233	14.100	0.853	6.169
Yb	0.800	1.300	0.545	0.436
Zr	86.333	171.000	0.883	76.200
Cu	1.000	10.000	8.505	8.505

			Overall mass change (%)	-2.807
			Slope	1.029
	Unaltered	Altered	Gain/Loss relative to Ci0	Gain/Loss in wt.% or ppm
Sample	TCC	HPP6-17-91	ΔCi/Ci0	ΔCi
Oxides (Wt.%)				
SiO2	76.260	74.900	-0.045	-3.462
TiO2	0.103	0.180	0.693	0.072
Al2O3	12.927	13.300	0.000	0.000
Fe2O3	0.853	1.870	1.130	0.964
MnO	0.023	0.040	0.666	0.016
MgO	0.197	0.250	0.236	0.046
CaO	1.767	1.280	-0.296	-0.523
Na2O	3.257	3.280	-0.021	-0.069
K2O	3.793	4.480	0.148	0.561
P2O5	0.027	0.050	0.822	0.022
Trace elements (ppm)				
Ba	190.667	797.000	3.063	583.961
Ce	22.700	53.600	1.295	29.395
Cr	5.667	9.000	0.544	3.081
Cs	4.200	5.810	0.345	1.447
Eu	0.540	0.770	0.386	0.208
Hf	3.180	3.800	0.161	0.513
La	11.900	28.400	1.320	15.703
Lu	0.270	0.170	-0.388	-0.105
Nb	11.667	13.300	0.108	1.260
Nd	7.600	21.200	1.711	13.005
Rb	140.000	174.000	0.208	29.116
Sm	1.790	3.940	1.139	2.039
Sr	191.000	206.000	0.048	9.218
Ta	0.850	1.100	0.258	0.219
Tb	0.290	0.430	0.441	0.128
Th	26.300	16.300	-0.398	-10.458
U	11.020	4.190	-0.630	-6.948
V	6.333	12.000	0.842	5.330
Y	7.233	11.900	0.599	4.333
Yb	0.800	1.130	0.373	0.298
Zr	86.333	127.000	0.430	37.102
Cu	1.000	6.000	4.832	4.832

			Overall mass change (%)	2.593
			Slope	0.975
	Unaltered	Altered	Gain/Loss relative to Ci0	Gain/Loss in wt.% or ppm
Sample	TCC	HPP6-7-18	ΔCi/Ci0	ΔCi
Oxides (Wt.%)				
SiO2	76.260	77.700	0.045	3.454
TiO2	0.103	0.080	-0.206	-0.021
Al2O3	12.927	12.600	0.000	0.000
Fe2O3	0.853	0.760	-0.086	-0.074
MnO	0.023	0.010	-0.560	-0.013
MgO	0.197	0.050	-0.739	-0.145
CaO	1.767	0.610	-0.646	-1.141
Na2O	3.257	2.440	-0.231	-0.753
K2O	3.793	6.470	0.750	2.844
P2O5	0.027	0.005	-0.808	-0.022
Trace elements (ppm)				
Ba	190.667	1060.000	4.704	896.815
Ce	22.700	12.000	-0.458	-10.389
Cr	5.667	10.000	0.810	4.593
Cs	4.200	3.090	-0.245	-1.030
Eu	0.540	0.710	0.349	0.188
Hf	3.180	1.900	-0.387	-1.231
La	11.900	5.500	-0.526	-6.257
Lu	0.270	0.070	-0.734	-0.198
Nb	11.667	7.400	-0.349	-4.075
Nd	7.600	5.500	-0.258	-1.957
Rb	140.000	181.500	0.330	46.206
Sm	1.790	1.200	-0.312	-0.559
Sr	191.000	443.000	1.380	263.485
Ta	0.850	0.800	-0.034	-0.029
Tb	0.290	0.140	-0.505	-0.146
Th	26.300	6.010	-0.766	-20.134
U	11.020	1.010	-0.906	-9.984
V	6.333	7.000	0.134	0.848
Y	7.233	4.000	-0.433	-3.130
Yb	0.800	0.390	-0.500	-0.400
Zr	86.333	54.000	-0.358	-30.933
Cu	1.000	4.000	3.104	3.104

			Overall mass change (%)	-2.440
			Slope	1.025
	Unaltered	Altered	Gain/Loss relative to Ci0	Gain/Loss in wt.% or ppm
Sample	TCC	HPP6-7-19	ΔCi/Ci0	ΔCi
Oxides (Wt.%)				
SiO2	76.260	76.200	-0.025	-1.919
TiO2	0.103	0.150	0.416	0.043
Al2O3	12.927	13.250	0.000	0.000
Fe2O3	0.853	1.570	0.795	0.678
MnO	0.023	0.030	0.254	0.006
MgO	0.197	0.270	0.339	0.067
CaO	1.767	0.150	-0.917	-1.620
Na2O	3.257	2.890	-0.134	-0.437
K2O	3.793	4.710	0.211	0.802
P2O5	0.027	0.050	0.829	0.022
Trace elements (ppm)				
Ba	190.667	462.000	1.364	260.059
Ce	22.700	25.700	0.105	2.373
Cr	5.667	10.000	0.722	4.089
Cs	4.200	5.360	0.245	1.029
Eu	0.540	0.440	-0.205	-0.111
Hf	3.180	2.900	-0.110	-0.351
La	11.900	11.700	-0.041	-0.486
Lu	0.270	0.180	-0.350	-0.094
Nb	11.667	15.300	0.279	3.260
Nd	7.600	9.400	0.207	1.571
Rb	140.000	228.000	0.589	82.436
Sm	1.790	1.840	0.003	0.005
Sr	191.000	127.500	-0.349	-66.611
Ta	0.850	1.600	0.836	0.711
Tb	0.290	0.240	-0.193	-0.056
Th	26.300	17.200	-0.362	-9.520
U	11.020	5.700	-0.495	-5.459
V	6.333	15.000	1.311	8.301
Y	7.233	7.900	0.066	0.474
Yb	0.800	0.900	0.098	0.078
Zr	86.333	90.000	0.017	1.470
Cu	1.000	9.000	7.780	7.780

			Overall mass change (%)	-4.247
			Slope	1.044
	Unaltered	Altered	Gain/Loss relative to Ci0	Gain/Loss in wt.% or ppm
Sample	TCC	HPP6-7-20	ΔCi/Ci0	ΔCi
Oxides (Wt.%)				
SiO2	76.260	73.500	-0.077	-5.881
TiO2	0.103	0.260	1.409	0.146
Al2O3	12.927	13.500	0.000	0.000
Fe2O3	0.853	2.170	1.435	1.225
MnO	0.023	0.040	0.641	0.015
MgO	0.197	0.430	1.094	0.215
CaO	1.767	1.620	-0.122	-0.215
Na2O	3.257	2.870	-0.156	-0.509
K2O	3.793	4.640	0.171	0.650
P2O5	0.027	0.130	3.668	0.098
Trace elements (ppm)				
Ba	190.667	606.000	2.043	389.597
Ce	22.700	49.000	1.067	24.219
Cr	5.667	10.000	0.690	3.909
Cs	4.200	6.580	0.500	2.101
Eu	0.540	0.790	0.401	0.216
Hf	3.180	4.200	0.265	0.842
La	11.900	26.500	1.132	13.475
Lu	0.270	0.200	-0.291	-0.078
Nb	11.667	16.800	0.379	4.420
Nd	7.600	20.000	1.520	11.551
Rb	140.000	232.000	0.587	82.147
Sm	1.790	3.420	0.829	1.485
Sr	191.000	274.000	0.374	71.363
Ta	0.850	1.500	0.690	0.586
Tb	0.290	0.350	0.156	0.045
Th	26.300	16.400	-0.403	-10.596
U	11.020	4.150	-0.639	-7.046
V	6.333	19.000	1.873	11.860
Y	7.233	11.700	0.549	3.970
Yb	0.800	1.210	0.448	0.359
Zr	86.333	138.000	0.531	45.806
Cu	1.000	9.000	7.618	7.618

			Overall mass change (%)	2.187
			Slope	0.979
	Unaltered	Altered	Gain/Loss relative to Ci0	Gain/Loss in wt.% or ppm
Sample	TCC	HPP6-2-6	ΔCi/Ci0	ΔCi
Oxides (Wt.%)				
SiO2	76.260	76.400	0.024	1.811
TiO2	0.103	0.040	-0.604	-0.062
Al2O3	12.927	12.650	0.000	0.000
Fe2O3	0.853	1.080	0.293	0.250
MnO	0.023	0.010	-0.562	-0.013
MgO	0.197	0.020	-0.896	-0.176
CaO	1.767	0.690	-0.601	-1.062
Na2O	3.257	3.620	0.136	0.443
K2O	3.793	4.850	0.307	1.163
P2O5	0.027	0.020	-0.234	-0.006
Trace elements (ppm)				
Ba	190.667	19.000	-0.898	-171.251
Ce	22.700	13.400	-0.397	-9.007
Cr	5.667	10.000	0.803	4.552
Cs	4.200	5.950	0.448	1.880
Eu	0.540	0.110	-0.792	-0.428
Hf	3.180	5.900	0.896	2.849
La	11.900	4.200	-0.639	-7.608
Lu	0.270	0.300	0.135	0.037
Nb	11.667	21.200	0.857	9.997
Nd	7.600	4.100	-0.449	-3.410
Rb	140.000	286.000	1.088	152.255
Sm	1.790	1.010	-0.423	-0.758
Sr	191.000	17.200	-0.908	-173.424
Ta	0.850	12.400	13.907	11.821
Tb	0.290	0.160	-0.436	-0.127
Th	26.300	24.300	-0.056	-1.469
U	11.020	6.990	-0.352	-3.877
V	6.333	4.000	-0.355	-2.246
Y	7.233	6.400	-0.096	-0.693
Yb	0.800	1.370	0.750	0.600
Zr	86.333	67.000	-0.207	-17.868
Cu	1.000	4.000	3.087	3.087

Recalculated with correct unaltered sample			Overall mass change (%)	8.221
			Slope	0.924
	Unaltered	Altered	Gain/Loss relative to Ci0	Gain/Loss in wt.% or ppm
Sample	TMG	HPP6-2-6	ΔCi/Ci0	ΔCi
Oxides (Wt.%)				
SiO2	76.037	76.400	0.087	6.644
TiO2	0.043	0.040	-0.001	0.000
Al2O3	13.690	12.650	0.000	0.000
Fe2O3	0.677	1.080	0.727	0.492
MnO	0.040	0.010	-0.729	-0.029
MgO	0.087	0.020	-0.750	-0.065
CaO	0.923	0.690	-0.191	-0.177
Na2O	3.637	3.620	0.077	0.281
K2O	4.420	4.850	0.187	0.829
P2O5	0.033	0.020	-0.351	-0.012
Trace elements (ppm)				
Ba	167.667	19.000	-0.877	-147.105
Ce	48.800	13.400	-0.703	-34.298
Cr	2.500	10.000	3.329	8.322
Cs	7.360	5.950	-0.125	-0.921
Eu	0.550	0.110	-0.784	-0.431
Hf	3.460	5.900	0.845	2.925
La	25.600	4.200	-0.822	-21.055
Lu	0.346	0.300	-0.062	-0.021
Nb	34.000	21.200	-0.325	-11.057
Nd	24.000	4.100	-0.815	-19.563
Rb	272.333	286.000	0.137	37.180
Sm	4.140	1.010	-0.736	-3.047
Sr	57.333	17.200	-0.675	-38.719
Ta	4.150	12.400	2.234	9.269
Tb	0.630	0.160	-0.725	-0.457
Th	24.300	24.300	0.082	1.998
U	6.230	6.990	0.214	1.335
V	2.500	4.000	0.732	1.829
Y	41.400	6.400	-0.833	-34.474
Yb	2.520	1.370	-0.412	-1.037
Zr	74.333	67.000	-0.025	-1.825
Cu	3.667	4.000	0.181	0.662

APPENDIX 3

Table 5: Microthermometric analysis data. $T_{ice-gas}$=temperature of which the gas bubble freezes.

Sample #	Tmf	T ice-gas	Te	Tm-ice	Th	Size of gas bubble %
16	-38		-12	2	210	50
16	-38	-70	-50	3	225	50
16	-30	-80	-55	1.5	230	
16	-30		-10	0	207	
16	-43		-11	0	200	
16	-40		-9	2	217	
16	-43		-10	0	215	
16	-37		-4	0	204	
16	-33		-3	2.5	220	
16	-42		-3	2.5	220	
16	-39		-5	1.5	215	
65	-31		-4	1.5	233	
65	-38		-4	3.5	235	
65	-30		-7	3.5	234	
65	-32		-7	0	238	
65	-34		-7	3	240	
65	-32		-1	2	244	
65	-40	-72	-52	5	219	5
65	-32		-7.8	2	240	
65	-32		-3	2	245	
65	-40		-1	0	231	
65	-36		-3	0	236	
65	-38		-1	3	239	
65	-38		-7	3	244	
44	-38.5		-0.5	2	190	
44	-36		-0.5	5	192	
44	-37		-1	2	192	
44	-36		-1	2	199	
44	-40		-1	2	210	
44	-37		0	2	200	
44	-36		-1.3	0	215	
44	-35		-5	0	150	
44	-35		-3	2.7	185	
44	-34		-3	3.6	190	
44	-33		-5	2	155	
53	-38		-1.5	0	147	
53	-32		-3.8	-1	150	
53	-31		-5	-2.2	155	
53	-34		-1	0	150	
53	-35		-3.4	0	210	
53	-35		-2.6	2	215	
53	-36		-9	-0.2	214	

Sample #	Tmf	T ice-gas	Te	Tm-ice	Th	Size of gas bubble %
26	-45		-2.4	0	202	
26	-48		-2.4	0	205	
26	-45		-2	2.5	205	
26	-48	-70	-2	0.8	200	50
26	-43		-2.9	0	215	
26	-43		-8	-2	215	
26	-36		-5	0	219	
26	-36		-7	0	222	
26	-40		-7	0	218	
30	-40.9		-3	-1	231	
30	-47		-4	0	221	
30	-40		-3	0	221	
30	-41.7	-56	-2	0	244	50
30	-36		-5	0	229	
30	-44		-3.6	0	227	
30	-35.5		-3.6	-0.6	217	
30	-39.5		-6	0	217	
30	-43.7		-5	0	200	
30	-43		-6	2	214	
30	-46		-6	0	226	
30	-46		-6	2	229	
30	-46		-6	0	229	
30	-45		-6	0	229	
33	-42		-1	1.8	158	
33	-42		-1	2	174	
33	-45		-1.9	2.2	176	
33	-43		0	2.5	177	
33	-40		-4	3	180	
36	-32		0	3	176	
36	-34		0	0	175	
36	-35		0	3	174	
36	-35		-1	0	176	
36	-36		-2	0	180	
36	-36.4		-6.2	3	187	
36	-37.4		-10	2.8	200	
36	-35		-1.8	3.5	174	
36	-39		-1	2.4	210	
36	-42		-2.6	3	184	
36	-35		-4.3	3.2	207	
36	-34.7		-4	0	198	
38	-39		-2	0	165	
38	-38		-1.8	1.5	170	
38	-40		-0.8	2	160	
38	-40		-1	0	190	
38	-39		0	2.6	192	

Sample #	Tmf	T ice-gas	Te	Tm-ice	Th	Size of gas bubble %
68	-35		-0.8	0	169	
68	-36		-6	0	200	
68	-37		-2	2.4	230	
68	-37		-2.6	2.4	230	
68	-44		-4	2.5	250	
68	-43		-4	2.5	250	
68	-38		-7	3	230	
68	-38		-3.9	2	230	
68	-38		-3.9	2.3	244	
68	-32		-2	5	175	
69	-38		-2	3	230	
69	-37		-7	2	168	
69	-38		-7	4	220	
69	-36		-4.9	2.5	230	
69	-40		-4.3	3.5	236	
69	-41		-4	0	230	
69	-45		-4.1	2.5	230	
69	-45		-1.8	0	240	
69	-45		-0.58	4	240	
69	-40		-6	2	250	
69	-45		-5	3	250	
69	-43		-4.6	5	247	
69	-45		-4.4	2.5	245	
69	-44		-4	3	248	
39	-40		-0.2	3	174	
39	-39		-0.1	3.4	155	
39	-39		0	0	148	
39	-38		0	0	160	
88	-39		7.2	1.5	150	
88	-35.5		8.7	3	142	
88	-39.8		6.7	0	150	
88	-39		9	0	145	
88	-37		8	3.5	144	
88	-39.5		10	3	152	
88	-36		2.3	0	156	
88	-37.9		10	2	150	
88	-38		-0.3	2.2	165	
88	-36		6.3	2	149	
88	-34.7		0	2.2	130	
88	-33		10	3	153	
88	-31		7	0	155	
88	-38		8	0	153	
88	-40		10	3	175	
88	-40		10	3	175	

Sample #	Tmf	T ice-gas	Te	Tm-ice	Th	Size of gas bubble %
18	-39		1.3	1	110	
18	-38		3	1	125	
18	-39.8		-1	0	148	
18	-43		-1	1.5	175	
18	-43		-1	0	170	
18	-30.8		-0.5	0	143	
18	-36		-1	2	165	
18	-40		-0.5	1.5	175	
18	-33.8		-2	0	171	
18	-40		-1	0	165	
18	-39		-0.5	1	180	
18	-38		-2	1	177	
18	-39		-1	0	175	
18	-31		0	0	170	

Table 6: Lab results of $\delta D_{mineral}$ and $\delta^{18}O_{mineral}$.

Alteration type	Transect	Sample I.D.	Mica type	δD corrected	δ18O corrected
potassic	T1	HPP6-4-16	biotite	-144.85	11.56
	T1	HPP6-4-16-DUP	biotite	-146.18	
	T1	HPP6-4-16-TRIP	biotite	-145.11	
potassic	T1	HPP6-13-62	biotite	-171.43	9.74
	T1	HPP6-13-62-DUP	biotite	-171.61	9.76
	T1	HPP6-13-62-TRIP	biotite	-172.27	
potassic	T1	HPP6-13-66a	biotite	-172.21	9.16
	T1	HPP6-13-66A-DUI	biotite	-168.16	
	T1	HPP6-13-66A-TRI	biotite	-169.51	
exo-skarn	T1	HPP6-13-66	chlorite	-168.22	8.58
	T1	HPP6-13-66-DUP	chlorite	-164.38	
	T1	HPP6-13-66-TRIP	chlorite	-164.98	
CSS	T2	HPP6-9-42	chlorite	-183.65	18.19
	T2	HPP6-9-42-DUP	chlorite	-185.10	
	T2	HPP6-9-42-TRIP	chlorite	-184.64	
CSS	T2	HPP6-9-53	chlorite	-194.44	8.88
	T2	HPP6-9-53-DUP	chlorite	-195.19	
unaltered--epidote bearing sample	T2	HPP6-9-52	chlorite	-178.67	-8.08
unaltered	T2	HPP6-9-54	biotite	-91.09	11.89
	T2	HPP6-9-54-DUP	biotite	-92.15	11.64
endo-skarn	T2	HPP6-9-49	chlorite	-187.51	-6.58
	T2	HPP6-9-49-DUP	chlorite	-187.69	
unaltered	T3	HPP6-8-26	biotite	-158.60	10.47
CSS	T3	HPP6-8-30	chlorite	-176.13	11.09
	T3	HPP6-8-30-DUP	chlorite	-175.19	
potassic	T3	HPP6-8-27	biotite	-164.69	7.97
potassic	T4	HPP6-8-33	biotite	-102.81	10.93
silicified	T4	HPP6-8-37	biotite	-169.40	1.85
	T4	HPP6-8-37-DUP	biotite	-169.61	
silicified	T4	HPP6-8-35	biotite	-169.55	11.06
	T4				11.33
CSS	T4	HPP6-8-38	chlorite	-181.09	9.69
endo-skarn	T5	HPP6-13-68	chlorite	-192.09	-6.14
	T5	HPP6-13-68-DUP	chlorite	-193.15	
CSS	T5	HPP6-13-69	chlorite	-198.68	4.84
CSS	T6	HPP6-17-89	chlorite	-177.26	10.03
CSS	T6	HPP6-17-91	chlorite	-181.32	9.35
	T6	HPP6-17-91-DUP	chlorite	-182.12	
potassic	T6	HPP6-8-39	biotite	-187.98	9.45
	T6	HPP6-8-39-DUP	biotite	-189.03	
CSS	T7	HPP6-7-19	chlorite	-177.97	9.31
unaltered	T7	HPP6-7-20	biotite	-146.17	10.80
	T7	HPP6-7-20-DUP	biotite	-148.55	11.19

Table 7: Calculated δD_{water} and $\delta^{18}O_{water}$ at various hydrothermal temperatures.

	Sample I.D.	mica type	temperature	δDwater	δ18Owater	temperature	δDwater	δ18Owater	temperature	δDwater	δ18Owater
T1	HPP6-4-16	biotite	400	-76.40	7.50	450	-79.17	8.50	500	-82.84	9.31
T1	HPP6-4-16-DUP	biotite	400	-77.84		450	-80.61		500	-84.28	
T1	HPP6-4-16-TRIP	biotite	400	-76.68		450	-79.45		500	-83.12	
T1	HPP6-13-62	biotite	400	-109.58	5.68	450	-111.36	6.68	500	-114.90	7.49
T1	HPP6-13-62-DUP	biotite	400	-109.76	5.70	450	-111.54	6.70	500	-115.09	7.51
T1	HPP6-13-62-TRIP	biotite	400	-110.48		450	-112.26		500	-115.80	
T1	HPP6-13-66	biotite	400	-134.28	4.52	450	-136.87	5.52	500	-140.32	6.32
T1	HPP6-13-66-DUP	biotite	400	-130.27		450	-132.88		500	-136.34	
T1	HPP6-13-66-TRIP	biotite	400	-130.91		450	-133.51		500	-136.97	
T1	HPP6-13-66a	chlorite	400	-113.96	5.11	450	-116.61	6.10	500	-120.14	6.91
T1	HPP6-13-66A-DUI	chlorite	400	-109.63		450	-112.30		500	-115.84	
T1	HPP6-13-66A-TRII	chlorite	400	-111.07		450	-113.74		500	-117.28	
T2	HPP6-9-42	chlorite	330	-147.78	12.30	360	-148.64	13.16	400	-151.19	14.13
T2	HPP6-9-42-DUP	chlorite	330	-149.30		360	-150.15		400	-152.69	
T2	HPP6-9-42-TRIP	chlorite	330	-148.82		360	-149.67		400	-152.22	
T2	HPP6-9-52	chlorite	370	-143.43	-12.85	435	-147.71	-11.42	500	-151.11	-10.33
T2	HPP6-9-53	chlorite	370	-159.88	4.11	410	-163.24	5.04	450	-164.91	5.81
T2	HPP6-9-53-DUP	chlorite	370	-160.67		410	-164.02		450	-165.69	
T2	HPP6-9-54	biotite	370	-31.02	7.12	435	-35.86	8.55	500	-39.70	9.63
T2	HPP6-9-54-DUP	biotite	370	-32.15	6.87	435	-36.98	8.30	500	-40.82	9.39
T2	HPP6-9-49	chlorite	330	-151.81	-12.47	365	-152.66	-11.48	450	-157.73	-11.48
T2	HPP6-9-49-DUP	chlorite	330	-152.00		365	-152.84		450	-157.91	
T3	HPP6-8-26	biotite	380	-89.44	5.95	440	-94.88	7.23	500	-97.59	8.22
T3	HPP6-8-27	biotite	387	-96.93	3.62	443	-102.33	4.78	500	-104.13	5.72
T3	HPP6-8-30	chlorite	410	-142.51	7.24	430	-145.08	7.65	450	-145.93	8.02
T3	HPP6-8-30-DUP	chlorite	410	-141.52		430	-144.10		450	-144.95	
T4	HPP6-8-33	biotite	330	-33.90	5.04	415	-41.60	7.20	500	-47.33	8.68
T4	HPP6-8-35	biotite	330	-102.18	5.17	365	-104.87	6.16	400	-107.55	7.00
T4		biotite			5.44			6.43			7.27
T4	HPP6-8-37	biotite	320	-101.12	-4.36	360	-103.81	-3.18	400	-107.39	-2.21
T4	HPP6-8-37-DUP		320	-101.35		360	-104.04		400	-107.62	
T4	HPP6-8-38	chlorite	320	-145.11	3.49	360	-145.97	4.66	400	-148.52	5.64
T5	HPP6-13-68	chlorite	410	-159.11	-9.98	455	-161.63	-9.12	500	-164.98	-8.40
T5	HPP6-13-68-DUP	chlorite	410	-160.22		455	-162.74		500	-166.08	
T5	HPP6-13-69	chlorite	410	-165.97	1.00	430	-168.47	1.40	450	-169.30	1.78
T6	HPP6-8-39	chlorite	300	-119.47	2.56	400	-127.36	5.39	500	-131.71	7.20
T6	HPP6-8-39-DUP	chlorite	300	-120.61		400	-128.49		500	-132.84	
T6	HPP6-17-89	chlorite	300	-140.26	3.14	350	-141.97	4.73	400	-144.54	5.97
T6	HPP6-17-91	biotite	300	-144.49	2.46	350	-146.20	4.04	400	-148.76	5.29
T6	HPP6-17-91-DUP	biotite	300	-145.33		350	-147.04		400	-149.59	
T7	HPP6-7-19	chlorite	330	-141.86	3.42	365	-142.71	4.41	400	-145.28	5.25
T7	HPP6-7-20	biotite	330	-84.26	4.91	365	-86.09	5.90	400	-89.73	6.74
T7	HPP6-7-20-DUP	biotite	330	-86.81	5.30	365	-88.64	6.29	400	-92.28	7.13